

Epigraph

Something about measuring the distance between *here* and *there* cast off the mystery of what lay between, and since I was a child with limited empirical evidence, the unknown of what might just lie between *here* and *there* could be terrifying. I, like most children, had never been *there*. I had barely even been *here*.

- The Selected Works of T.S. Spivet

by Reif Larsen

University of Alberta

Kirkpatrick-Baez Microscope for Hard X-Ray Imaging of Fast Ignition Experiments

by

Hal Joseph Friesen

A thesis submitted to the Faculty of Graduate Studies and Research
in partial fulfillment of the requirements for the degree of

Master of Science

in

Photonics and Plasmas

Department of Electrical & Computer Engineering

©Hal Joseph Friesen
Fall 2011
Edmonton, Alberta

Permission is hereby granted to the University of Alberta Libraries to reproduce single copies of this thesis and to lend or sell such copies for private, scholarly or scientific research purposes only.

Where the thesis is converted to, or otherwise made available in digital form, the University of Alberta will advise potential users of the thesis of these terms.

The author reserves all other publication and other rights in association with the copyright in the thesis and, except as herein before provided, neither the thesis nor any substantial portion thereof may be printed or otherwise reproduced in any material form whatsoever without the author's prior written permission.

Abstract

Fast ignition (FI) decouples the compression and ignition in normal Inertial Confinement Fusion schemes, and can rely on hot electron transport to ignite the compressed core. In order to study electron transport, characteristic K_α X-ray emission from copper tracer layers is often employed. A Kirkpatrick-Baez X-ray microscope was constructed using grazing incidence platinum mirrors and characterized to image Cu K_α emission in high intensity Fast Ignition experiments. The broad spectral window from 4 to 9 keV enables imaging of both the copper K_α emission as well as the emitted Bremsstrahlung radiation from the high intensity interaction spot. A resolution of 30 μm or less over a 300 μm field of view has been confirmed experimentally. Results from cone-wire experiments are presented where the emission from the high intensity interaction spot and the copper K_α emission from the copper wire tip were analysed as a function of prepulse energy.

Contents

1	Introduction	1
1.1	Energy Demands and Possible Sources	1
1.2	Fusion's Potential Role	4
1.3	Status of Fusion Research	8
1.4	Outline	11
2	Fast Ignition Fusion	13
2.1	Plasmas	13
2.2	Thermonuclear Fusion	14
2.3	Hydrodynamic Behaviour of a Plasma	19
2.4	Critical Density	23
2.5	The Ponderomotive Force	23
2.6	The Raman Instability	26
2.7	Fast Ignition Fusion	28
2.8	Studying Hot Electrons	32
3	Laser Plasma Interactions and other Physical Phenomena	33
3.1	Laser Absorption	33
3.2	Basic Absorption	34
3.3	Ionization and Plasma Formation	35
3.4	Inverse Bremsstrahlung: Collisional Absorption	36
3.5	Collision frequency scaling	37
3.6	Resonance Absorption	38
3.7	Vacuum Heating	40
3.8	$J \times B$ Heating	42
3.9	Hole-Boring	43
3.10	Laser Beam Self-focusing and Filamentation	44

3.11	Ion Beams and Hydrodynamic Expansion	45
3.12	Cold Return Current	46
3.13	Ionization	51
3.14	Heating	53
3.15	Electron Scattering	55
4	X-ray imaging Background and Diagnostic Challenges	59
4.1	X-ray Reflection	59
4.2	Imaging X-rays	61
4.3	KB Microscope	64
4.4	Resolution Requirements	65
4.5	Aberration analysis and correction	66
4.6	Coatings	67
4.7	Multilayers	70
4.8	Improving the KB	76
4.9	Other Advances	78
5	Design and Characterization	81
5.1	Re-entrant assembly	81
5.2	Mirrors and Coating Results	83
5.3	Shielding	85
5.4	Measuring incident angles	85
5.5	Adjusting the alignment	88
5.6	Alignment	88
5.7	Moxtek X-ray Tube	91
5.8	Resolution	100
5.9	Incident Angle and Reflectivity	120
5.10	Adjustment of Focal Length by Bending the Second Mirror	133
	5.10.1 Transducer Calibrations	135
	5.10.2 Mirror Bending tests	136
6	Prepulse Scan on Titan	148
6.1	Fast Ignition Experimental Setup	148
6.2	Laser History	149
6.3	Titan Description	150
6.4	Laser Diagnostics	150
6.5	Diagnostic Techniques	152
	6.5.1 Image Plates	152
	6.5.2 University of Alberta IP Reader	154

6.5.3	Princeton CCD Cameras	155
6.6	Prepulse Formation	156
6.7	Experimental Parameters	156
6.8	FLYCHK	157
6.9	Bremsstrahlung	163
6.10	Analysis Steps	163
6.11	Background Subtraction	164
6.11.1	KB Linearity	168
6.11.2	Image Rotation	168
6.11.3	Gaussian Blur	169
6.11.4	Reflectivity Correction	170
6.12	Wire Transport	174
6.13	Preplasma scaling	182
6.14	Preplasma emission from other targets	188
7	Current Developments and Future Work	194
7.1	Mirror Bender and Multilayer Mirrors	194
7.2	Next Generation KB	197
7.3	Conclusions	198
	References	201
	Appendices	212
A.1	Rolling Ball Algorithm	212
A.2	List of Shots and Parameters where Preplasma Emission was observed	218
A.3	Alignment Guide	222
A.3.1	Initial Setup	222
A.3.2	Alignment at air	223
A.3.3	Preparing for vacuum	224
A.3.4	Adjusting the alignment	225
A.4	Other Alignment Techniques	226
A.4.1	First Alignment Scheme	226
A.4.2	Second Alignment Scheme	227
A.4.3	Third Alignment Scheme	228
A.4.4	Fourth Alignment Scheme	229
A.4.5	Fifth Alignment Scheme	231
A.5	Instrument Dimensions and Vacuum Shifts Measured	232
A.5.1	Instrument Dimensions	232

A.5.2	Vacuum Shifts	233
A.5.3	Port Information	234
A.6	ZEMAX Simulations	234
A.6.1	Imaging Ta Foil	234
A.7	Layout of Titan Ports	239

List of Tables

4.1	Common K emission lines [24, 40, 74, 81, 84, 90, 91, 92]	71
4.2	Multilayer Coating Specifications	74
4.3	Various Wolter-I mirror parameters used at the Wonkwang University Institute for Radiological Imaging Science [104]. These examples have an aspect ratio of 2 (i.e., mirror length/intersection diameter=2). . .	79
4.4	Design Specifications of SIX Mirror Systems [105]	80
4.5	PIXEL Mirror Parameters [105]	80
5.1	PIN diode measurements vs. Amptek results	100
5.2	Summary of Bending Results	141
6.1	Experimental Parameters for Prepulse Scan on Titan.	158
6.2	Rate Coefficients in Collisional-Radiative Model [65].	161
6.3	The percentage of emission in different bandwidths (in keV) for differ- ent Au plasma temperatures. Generated in FLYCHK.	174

List of Figures

1.1	Four shots taken during the early National Ignition Campaign in 2009 [8]. The initial capsule diameter was 1.8 mm, and the emitting region 33X smaller than capsule diameter, which is consistent with a 10-15 mass compression ratio. The symmetric implosion exhibits a P_2 of 7%.	9
2.1	The binding energy per nucleon increases toward the iron group of isotopes around mass number 62 [14]. A higher binding energy means a deeper potential well and a lower energy state for the nucleus. Therefore transitions toward this plateau of stability release excess energy (mass defect), whether they be fission or fusion.	16
2.2	A time sequence of density maps simulated using CALE (C-based Arbitrary Lagrangian-Eulerian) software [22]. The code mimicked the 200 eV heating of a foam-gold target by the 1 ns NOVA laser. The foam had a density of 0.15 g/cc, and a typical pore size was 5 μm . A 50 μm wide section was modeled.	21
2.3	Density iso-contour surfaces of 45 g/cm ³ at 15.65 ns into a 3D HYDRA simulation of a section of an implosion [23] (peak implosion occurs at 15.55 ns). The capsule simulated had a beryllium ablator doped with 0.9% copper (135 μm thick), followed by a layer of DT ice (80 μm thick) and a core of DT gas with a full capsule radius of 1085 μm . It is driven by a shaped pulse with a peak temperature of 300 eV produced by the 192 beams of NIF. The ice surface perturbations were initialized from previous results.	21
2.4	A temperature and areal density map showing where ignition (Gain=1) will occur, and the regions which NIF hopes to access in comparison to older experiments on the OMEGA laser [8].	22
2.5	The three stages of the hole-boring fast ignition concept: (i) Compression (ii) Hole-boring (iii) Ignition (redrawn from [15]).	29
2.6	Two type of fast ignition: cone guided and proton fast ignition [32].	30
2.7	The Fast Ignition concept has a much higher gain for the same driver energy as other fusion schemes [15].	31

3.1	A plot of the resonant absorption coefficient versus angle for two different values of kL , illustrating that it is maximized at an intermediate angle of incidence.	40
3.2	A plot of the Brunel absorption coefficient versus angle for two different values of a_0 , illustrating that it is maximized at an intermediate grazing incidence angle.	42
3.3	The magnetic switchyard concept. The plot on the left is initial electron density, and the middle and right plots are hot electron densities at different times during the pulse [63].	51
3.4	The spectral changes in a plasma with temperature. The vertical bars represent the energy aperture of a typical Bragg crystal imager used in Fast Ignition experiments [70]. The vertical axes are in arbitrary units.	56
4.1	Differentially filtered images obtained using an X-ray pinhole camera during a Titan experiment.(2009.08.13.shot#2)	63
4.2	The transmission curves for a Ross filter pair designed for Cu K_α	63
4.3	Overlapped lineouts of the different filtered regions. Linewidth=5 pixels.	63
4.4	The lineout obtained by subtracting the two different filtered regions.	63
4.5	Two grazing-incidence mirrors will focus in both planes and enable formation of an X-ray image with good spatial resolution [41]. Such a design is called a KB microscope.	65
4.6	Resolution of a KB microscope as a function of position from best focus.The solid line is the predicted resolution from ray tracing, whereas the dotted lines are measured by backlighting a Cu-mesh using a dc X-ray source [84].	66
4.7	Definition of variables for the KB microscope setup.	67
4.8	The response or point-spread function (PSF) of the KB microscope, traced using ZEMAX, compared to a gaussian function of the same rms. The image settings were $p=94.6$ mm, $q=1232$ mm, $i=8.73$ mrad (0.5°), $R=20$ m, with a mirror diameter of 25.4 mm.	68
4.9	The maximum grazing angle for which total reflection occurs as a function of wavelength. For short X-ray wavelengths, higher Z (i.e. denser) reflectors are desired [41].	69
4.10	Left: measured and calculated reflectivity for gold-coated mirrors used in OMEGA for an angle of incidence of 0.70° . Right: Predicted reflectivities for single-metal coatings for an angle of incidence of 0.70° [40].	70
4.11	Constructive interference and the Fresnel reflection are combined in multilayer coatings (inspired by [73]). Refraction is ignored for simplicity.	71

4.12	Spectral windows and throughput for multilayers vs. single metal coatings [81]. All coatings were designed for a grazing incident angle of 36.5 mrad (2.1°). The Ir coating consisted of 300 Å of Ir on 100 Å of Cr. The Ni/BN mirror had 60 layers with 1.4nm/3.5nm thicknesses. The Pt/C mirror had 100 layers with 0.79nm/2.13nm thicknesses.	72
4.13	The KB design parameters for mirrors used in ESRF beamlines [42]. .	73
4.14	Reflectivity R, and throughput T (reflectivity times source spectrum, which is the bremsstrahlung emission from a laser plasma source with a rhenium target, from 12-25 nm) vs. energy (top) and coating thicknesses for Mo/Si multilayered mirrors (bottom) [97].	75
4.15	KBA Design [102].	76
4.16	Theoretical Resolution comparison of KB and KBA microscopes [102].	76
4.17	The double mirror design in KBA leads to identical angular change for two different incident rays. That is, the difference between AO_1 and O_2A' is the same (2η) as the difference between BO_1 and O_2B' [102]. This roughly means that their focal distance is the same.	77
4.18	Example of two rays on a singlet lens being deflected by the same angle as a result of the fixed focal length.	77
4.19	A Wolter type I optic for NASA's Advanced X-ray Astrophysics Facility (AXAF), with ellipsoidal followed by hyperboloidal mirrors [103].	78
4.20	The 8-image toroidal mirror design of the Ligne d'Intégration Laser (LIL) facility [83].	78
5.1	Outline of the re-entrant KB microscope.	82
5.2	Lineouts of the roughness measured with the white-light interferometer (ZYGO) for mirrors 1 and 2. The lineout on the right is high-pass filtered.	84
5.3	3D surface plot of the area seen in the white-light interferometer (ZYGO) for mirror 2.	84
5.4	How the KB microscope forms images.	86
5.5	The geometry involved in inferring incident angle from the image separation from the zero-order image. The zero axis is chosen for convenience and the down direction is positive.	87
5.6	The fiber optic alignment setup used to serve as a point source at Target Chamber Center (TCC).	90
5.7	The X-ray copper reflection tube (Moxtek) along with the 40 kV power supply and controller [107].	91

5.8	A sample image of the Moxtek X-ray source formed using the KB microscope. The first mirror focused vertically ($p=108.3\text{mm}$, $q=1354.5\text{mm}$, $M=9.94$) and the second mirror focused horizontally ($p=133.7\text{mm}$, $q=1329.1\text{mm}$, $M=12.51$). At these settings each mirror focuses at 10.03 mrad and 12.14 mrad respectively. This image was at 8.05 mrad and 10.23 mrad with FWHM $171 \times 112\mu\text{m}$, with wings extending to $322 \times 168\mu\text{m}$. The source size was much larger than the resolution so images a little out of focus were still limited by the source size. The Moxtek tube was set at 15 kV, $100 \mu\text{A}$ for a 17 min. exposure and a 51 minute decay on BAS-MS IP#4. Exposure #4 on 2011.05.08.	92
5.9	The X-ray box with and without the lids on.	93
5.10	A schematic of the X-ray box to shield the Moxtek X-ray source. The larger box typically contained the source and optics, and the smaller box contained the detector.	93
5.11	Plot of transmission and absorption of Be, air and CdTe versus energy.	95
5.12	Effect of transmission on the observed X-ray spectra. The solid red curve is the original spectrum obtained on the Amptek. The dashed green curve is the spectrum after taking all transmission factors into account. Spectrum #16 on Nov. 17, 2010. 15 kV $10 \mu\text{A}$ for 60 s. at a distance of 99.6 cm. RTD ON, threshold 150, gain 6. 500 um pinhole on Amptek.	96
5.13	Flux of K_α (red triangles) and K_β (blue squares) photons for various tube voltages.	97
5.14	Final corrected spectra for the output of the Moxtek cw X-ray source.	97
5.15	The transmission of 111 mm of air and the photoabsorptive efficiency of $250 \mu\text{m}$ Si versus energy.	99
5.16	The setup for the linearity test using the HOPG crystal done on 2010.10.15.	101
5.17	The results from the HOPG voltage scan done on 2010.10.15. Fluxes are based on preliminary calibration values.	101
5.18	The results from the IP linearity test done on 2010.10.15. Fluxes are based on preliminary calibration values. The standard deviation of the fit is 1.4×10^9 photons/srad/ μA , or 12% of the average photon signal.	101
5.19	The target shot for 2011.06.01 shot#3 on Titan. The fluor depth is $100 \mu\text{m}$	103
5.20	Left: Experimental image and lineouts (linewidth=5) obtained with the KB microscope on 2011.06.01 shot#3 on Titan. The KB diagnostic was run by Mianzhen Mo and Shaun Kerr for this experiment. Zero-order and 1D image orientation shown in bottom right. Right: Theoretical image and lineouts obtained using ZEMAX with a $10 \mu\text{m}$ diameter source and the same angles in the image on the left.	104

5.21	A plot of the vertical lineouts (experimental and theoretical) through the images in Figure 5.20. The ZEMAX lineout has been scaled arbitrarily.	104
5.22	How the edge spread function (ESF) is related to the point spread function (PSF). [112]	105
5.23	How the edge spread function (ESF) is related to the line spread function (LSF). [112]	106
5.24	How the tantalum foil was positioned relative to the mirrors.	107
5.25	A sample ESF, LSF and MTF measured for M1. Image plate #7 was used, and the X-ray tube was set at 15 keV, 100 μ A. The exposure was 41 mins. and the delay before scanning was 28 mins., scanned on the FLA-5000. The FWHM of the LSF is 17 μ m. The MTF reaches the value of 0.1 at 0.0456 μ m ⁻¹ which corresponds to a resolution of 22 μ m. The green curve on the MTF shows how well the interpolation function matches the output. This is the edge obtained for the image shown at the far right of Figure 7.20, at 8.58 mrad.	109
5.26	A sample LSF and the gaussian fit for the image shown at the far right of Figure 7.20, at 8.58 mrad. The FWHM is 17 μ m.	110
5.27	Resolution of the KB microscope using a Ta edge and the calculated MTF.	111
5.28	Effective size of the mirror versus angle for different threshold reflectivities, assuming a flat 25.4 mm diameter mirror for simplicity.	112
5.29	The spot sizes of the KB microscope obtained during fast electron experiments on Titan, compared against that predicted by ZEMAX.	113
5.30	Two pictures of Gold mesh used for qualitative image testing, at different magnifications. Pictures taken using light microscope.	113
5.31	X-ray mesh images obtained using M1 and M3 during the qualitative resolution angular scan. Lineouts taken with linewidth=4 pixels. M1 is closer to the source.	115
5.32	X-ray mesh images obtained using M2 and M4 during the qualitative resolution angular scan. Lineouts taken with linewidth=4 pixels. M2 is closer to the source.	116
5.33	The mesh transmission functions for 2 μ m and 5 μ m Au, after taking a weighted average of the source spectrum and looking up the tabulated transmission of Au.	117
5.34	The gold transmission curves multiplied by a 180 μ m FWHM gaussian function to represent the X-ray source.	117
5.35	A sample exponential fit of the PSF for 8.73 mrad angle of incidence. The raw PSF was generated in ZEMAX. The curve fit had an R=0.82.	117
5.36	The ideal PSF (from ZEMAX) and the average PSF obtained by doubling its lateral size.	117

5.37	The increase in 1/e scalelength and tail length observed by changing the position in the field of view by 200 μm in each direction from best focus.	118
5.38	The lineshape obtained by convolving Figure 5.34 with the ideal PSF. The maximum contrast is 2.0 and 4.3 for the 2 μm and 5 μm cases, respectively.	118
5.39	The lineshape obtained by convolving Figure 5.34 with the average PSF. The maximum contrast is 1.5 and 2.3 for the 2 μm and 5 μm cases, respectively.	118
5.40	Reflectivity at 8.05 keV of the platinum coated mirrors according to Fresnel theory. The solid line depicts an arbitrarily scaled reflectivity times angular aperture for a fixed diameter mirror (25.4 mm), showing that there is an optimal region around 0.5° angle of incidence.	121
5.41	The reflection versus grazing incident angle for different X-ray energies, in keV.	121
5.42	The decay of the BAS-MS type Fujifilm IP versus time. The dashed curve represents the double exponential fit, and the dot-dash curve represents the single exponential fit. Data collected by Mianzhen Mo, 2010.	123
5.43	The tungsten rods and the rear mirror surfaces define the size of the zero-order as well as the size of the 1D images in the unfocused dimension.	125
5.44	Transmission curves for the materials in the reflectivity calibration. The solid (blue) curve is for 20 μm of aluminum. The dash-dot (green) curve is for 15 μm nickel. The dashed (red) curve is for 144.9 cm of air at 760 torr, 298 K.	126
5.45	The photon flux before and after air, nickel and aluminum transmission. The dashed curve is the total transmission scaled by 2×10^5 for visibility. The edge above 8 keV corresponds to the K edge of Ni and serves to filter a significant amount of the K_β radiation at 8.9 keV.	127
5.46	The size of the zero-order (FWHM) versus incident angle, measured on images where the 1D reflection was not embedded. The vertical magnification was 12.51, and the horizontal magnification was 9.94.	129
5.47	A zero-order background taken from another image is scaled horizontally using the results from Figure 5.46 and vertically (arbitrarily) to provide an adequate background for subtraction (left). The image on the right shows the result of subtraction (taken on 2011.05.09 #5, for M2 focusing vertically as first mirror).	129
5.48	A sample image obtained during the reflectivity measurements (2011.05.09 exposure #5). In this case the 2D image is embedded in the horizontal reflection from M4 since the angle for M2 is too small – in such cases the lineout was taken through the unaffected region.	130

5.49	Sample fit of the reflected lineshape for the M4H reflection given in Figure 5.48.	131
5.50	Experimentally obtained reflectivity versus angle, compared to Fresnel theory. The other curves are modified versions of Fresnel assuming, respectively, 0.55 Å rms roughness, and 80% Platinum solid density.	134
5.51	Calibration curves for the transducers.	135
5.52	Setup for bending the 2nd mirror.	137
5.53	A plot of maximum deflection (y_M) versus applied uniform force calculated using Equation 5.29, along with inferred radius of curvature using Equation 5.27 and assuming the mirror bends into a spherical shape.	138
5.54	A sample image obtained during the bending tests where M2 is the second mirror focusing vertically. There is evidence of multiple image shadows which are pronounced enough to produce two peaks in the LSF. The image corresponds to a measured applied force of 410 ± 10 N (92 ± 2 lbs.). The image was obtained using IP #6, with X-ray tube settings of 15 kV, 100 μ A for a 1 hour long exposure, and 90 minute decay.	140
5.55	Two peaks are found in the LSF from Figure 5.54, likely due to mechanical shifting during the time-integrated exposure resulting in two edges in the ESF. The worst peak from the LSF in Figure 5.54 is fit with a Gaussian function to give a FWHM of 44 ± 10 μ m.	140
5.56	Experimental results for bending the 2nd mirror. The theoretical curves for the various radii of curvature were calculated using ZEMAX, and the details about each point are given in Table 5.2.	141
5.57	Calibration for number of screw turns versus pounds of force.	143
5.58	1D images of gold mesh obtained during the bending test.	145
5.59	The best mesh image obtained during the bending test, exposure #5 on 2011.05.16. The inferred mesh period is $31 \mu\text{m} \pm 5 \mu\text{m}$, and the predicted radius of curvature at this force is 21.2 m, which would have a theoretical resolution of approximately 50 μ m.	146
6.1	Titan Laser in the Jupiter Laser Facility at LLNL [115].	151
6.2	A sample focal spot on Titan using the 16-bit camera [115].	152
6.3	Schematic Diagram of the University Alberta IP reader. The CCD camera and lenses are on the left, and the image plate is on the right attached to a magnetic backing to hold it in place. The LED array and filters are in between. Figure courtesy of Mianzhen Mo 2011.	155
6.4	A typical Titan prepulse [131].	157

6.5	The layout of relevant diagnostics in the Titan chamber. The large blue beam is the laser pulse. The KB microscope was mounted on port TS4 on the roof of the chamber pointing down at TCC with a 40° angle with respect to horizontal.	158
6.6	A cone-wire used in the prepulse scan [129].	159
6.7	KB microscope image (2009.10.18 shot #2) after background subtraction using the Fourier filter in ImageJ for structures down to 100 pixels (left), and the rolling ball algorithm using a pixel radius of 50 pixels (right).	166
6.8	Comparison of lineouts (2009.10.18 shot #2) after background subtraction using the Fourier filter and the rolling ball algorithm. Left: The raw lineouts reveal that the Fourier filter leaves a substantial background, but it is still flat. Right: After shifting the lineouts to overlap, the Fourier filtered image has a faster fall-off for the signal from the wire region.	166
6.9	Sample KB microscope image of a gold-cone copper wire shot using the Titan Laser at LLNL. Shot number 2 on August 18, 2009.	167
6.10	Sample region of interest of a KB microscope image of a gold-cone copper wire shot using the Titan Laser at LLNL. Shot number 2 on August 18, 2009. The plot shows a lineout of emission intensity along the central axis of the cone (linewidth=10 pixels).	167
6.11	Background using ImageJ's rolling ball algorithm (r=300 pixels, no smoothing). Shot number 2 on August 18, 2009.	167
6.12	KB microscope image after background subtraction using rolling ball algorithm. Shot number 2 on August 18, 2009.	167
6.13	KB microscope image region of interest after background subtraction using rolling ball algorithm. Note the removal of the non-uniform background and the clarity of the image. The lower portion of the plot is a lineout (linewidth=10 pixels) through the central axis of the cone.	168
6.14	KB microscope linearity with respect to the HOPG, with a least-squares curve fit passing through zero. The fit had a 6% error.	169
6.15	KB microscope image region of interest after background subtraction and reflectivity correction assuming 8 keV X-rays. Shot number 2 on August 18, 2009.	170
6.16	The comparison of bound-bound, bound-free and free-free radiation from a 10 keV gold plasma at $n_e=10^{21}cm^{-3}$. The radiation is that is viewable by the KB microscope after transmission through 23.7 μm Au and two mirror reflections at 0.4°.	172
6.17	The emissivity of two plasmas versus energy. The sharp peak on the left is cold copper, and the rest of the spectrum is hot gold. They both have the same hot electron population of $10^{20}cm^{-3}$	173

6.18	The difference in reflectivity over the lineout of the image from 8 keV (dashed, R) to the weighted reflectivity calculated using FLYCHK spectra (line, R_{sum}). R_{sum} is the Fresnel reflectivity using the weighting 4.8% 9.5 keV reflectivity, 84.9% 10.5 keV reflectivity, and 9.7% 11.5 keV reflectivity. The ratio of 8 keV to the weighted reflectivity (R/R_{sum}) is plotted as well (dash-dot, Ratio).	175
6.19	The final axial lineout (top) after correcting for background, reflectivity and the specific reflectivity of the preplasma region. The lower curve is the axial lineout prior to the weighted reflectivity correction. . . .	175
6.20	The corrected image and lineout (10 pixel linewidth) for shot #2 on 2009.08.18, for an intrinsic prepulse of 7 mJ in 1.5 ns.	176
6.21	The corrected image and lineout (10 pixel linewidth) for shot #6 on 2009.08.18, for an injected prepulse of 30 mJ in 3 ns.	176
6.22	The corrected image and lineout (10 pixel linewidth) for shot #2 on 2009.08.17, for an injected prepulse of 100 mJ in 3 ns.	177
6.23	The corrected image and lineout (10 pixel linewidth) for shot #3 on 2009.08.17, for an injected prepulse of 500 mJ in 3 ns.	178
6.24	The corrected image and lineout (10 pixel linewidth) for shot #4 on 2009.08.17, for an injected prepulse of 1000 mJ in 3 ns.	179
6.25	The final corrected lineouts from the prepulse scan on Titan.	180
6.26	Coupling into the copper wire for different prepulse energies.	181
6.27	Comparison of the KB microscope $1/e$ scalelengths to those obtained by the Bragg crystal imager	181
6.28	The original critical density distances from the target surface obtained through 1D HYADES simulations. The dashed line is a power law fit with a scaling of $\approx E^{1/6}$	183
6.29	The scale length of preplasma versus prepulse energy. Experimental is compared against 2D HYDRA modeling and extended 1D modeling (from both Mora's model and HYADES), which provide upper and lower bounds. The dashed line through the 2D data is a power law fit of $1/3$ scaling, and the dashed line through the 1D data is a power law fit of $1/12$ scaling.	186
6.30	The 2D cylindrical HYDRA code simulation results for 8 mJ prepulse and 1J prepulse, showing evidence of a plasma jet along the central axis [143].	187
6.31	One of the targets shot during the Z effect study on Titan [64].	188
6.32	The vectors defining target normal (A) and the view of the KB microscope (B).	190
6.33	The target as seen by the KB microscope on Titan Port TS1. The grey circles indicate where front surface emission is positioned relative to layer emission for electrons traveling normal to the target surface. Generated using visrad by Hiroshi Sawada (UCSD).	192

6.34	The double emission seen by the KB microscope for shot 6 on May 18, 2010. The plot is a lineout 5 pixels wide taken through the two peaks at an angle of 48°	192
6.35	The double emission seen by the KB microscope for shot 6 on May 18, 2010 overlain on the image generated using visrad. The emission lies roughly within the circles predicted by visrad.	193
7.1	Concept of the mirror bender (modified from [145]).	195
7.2	First mirror bender design.	196
7.3	Interferometer used to measure mirror bending. All mirrors are flat. M1 is 25.4 mm diameter. M2 is 190.5 mm diameter. M3 and BS are 127 mm diameter. The lens has a focal length of 80 cm and a diameter of 101.6 mm. The lens sets the vertical size limit and the beamsplitter sets the horizontal size limit.	197
7.4	Structuring elements used for erosion and dilation [137].	212
7.5	Sample binary image A [137].	213
7.6	Result after first erosion of A by B1 [137].	214
7.7	Result after second erosion of A by B2 : denote this as C [137].	214
7.8	Result after first dilation of C by B2 [137].	215
7.9	Result after second dilation of C by B1 [137].	216
7.10	Net result of 2 erosions and 2 dilations of image A. We can remark that the entire process is identical to placing the structure element $B = B1 \oplus B2$ inside the region and only retaining those portions where it fits [137].	216
7.11	Application of the rolling ball algorithm to a gray-scale image is akin to using a three-dimensional structure element and rolling it across the umbra (cubical pixels in a 3D volume) [137].	217
7.12	Picture taken during August 2009 experiments showing back of KB microscope, outside the Titan target chamber.	223
7.13	The Quad Photodiode (QPD) used to track alignment. The differential voltage between two opposing quadrants was zeroed in order center the beam on the detector [146].	228
7.14	The response function of the QPD used [146].	228
7.15	Measurements of the KB microscope.	232
7.16	Dimensions of the mirror pins used to define a reproducible surface on the KB microscope.	233
7.17	The cosine exponent Cn controls the distribution of rays around a polar axis. The graph on the right shows functions $(\cos \theta)^{Cn}$ for different values of Cn , and shows that as Cn is increased, the angular spread of the cone of rays decreases. The image on the left shows a 3-dimensional view of what these spreads imply for the source emission.	235

7.18	ZEMAX output images for various cases. (a): The image produced by a 300 μm diameter source. (b) & (c): The images produced as the tantalum foil is moved further and further into the incident beam. (d): The Ta foil is blocking so much of the beam we do not have an ESF for either mirror. The cross pattern is from the foil taking the place of the tungsten rod for the edge cutoff of the zero-order.	236
7.19	The ZEMAX output image for the experimental situation where one mirror's image was well-clipped forming a nice ESF, but the other was still imaging normally.	238
7.20	The ZEMAX output images demonstrating that as the tantalum is moved further into the beam in (a) through (d) in one dimension only, the edge of the zero-order stays in the same position because it is dependent on the source. The image in (e) was obtained during the experiment.	238
7.21	The layout of ports on the Titan chamber.	239

Glossary of Acronyms

ADC: Analog to Digital Converter
AFM: Atomic Force Microscope
CALE: C-based Arbitrary Lagrangian-Eulerian (code)
CCD: Charge-coupled Device
CHS: Central Hot Spot
CID: Charge-injection device.
CPA: Chirped Pulse Amplification
CR: collisional radiative
DT: Deuterium-Tritium
EHP: electron hole pair
EMP: electromagnetic pulse
ESF: Edge spread function
ESRF: European Synchrotron Radiation Facility
FI: Fast Ignition
GRIN: Gradient Index
HOPG: Highly-oriented pyrolytic graphite
ICF: Inertial Confinement Fusion
IP: image plate
JLF: Jupiter Laser Facility
KB: Kirkpatrick-Baez
KBA: KB “amelioore” (improved)
LED: light-emitting diode
LLNL: Lawrence Livermore National Laboratory
LPI: Laser-Plasma Interaction(s)
LSF: Line spread function
LTE: Local Thermal Equilibrium
MCA: Multi-Channel Analyzer
MCF: Magnetic Confinement Fusion
MTF: Modulation transfer function
NA: Numerical Aperture
NIF: National Ignition Facility
NIST: National Institute of Standards and Technology
PET: polyethyleneterephthalate
PFI: proton fast ignition
PMT: photomultiplier tube
PSL: Photostimulated Luminescence
QL: Quantum Level
QPD: Quad Photodiode
RTI: Rayleigh-Taylor Instability
SNR: signal-to-noise ratio

TCC: Target Chamber Center
TLA: Three-Letter Acronym
TNSA: Target-normal sheath acceleration
UTA: Unresolved transition array
RTD: Rise Time Discrimination
ZPL: ZEMAX programming language

Web Sites

Here is a list of useful websites that are related to this work:

FLYCHK web site:

<http://nlte.nist.gov/FLY>

Filter transmission (solids):

http://henke.lbl.gov/optical_constants/filter2.html

X-ray Interactions with Matter:

http://henke.lbl.gov/optical_constants/

X-ray Form Factor, etc.:

<http://physics.nist.gov/PhysRefData/FFast/html/form.html>

ACFEI:

<http://www.ece.ualberta.ca/~acfei/>

NIF:

<https://lasers.llnl.gov/>

LMJ:

<http://www-lmj.cea.fr/>

HIPER:

<http://www.hiper-laser.org/>

Chapter 1

Introduction

1.1 Energy Demands and Possible Sources

In the last two centuries, the world population increased six times, the life expectancy two times and energy use 35 times [1]. The energy use is expected to increase to nearly 800 exojoules by 2030 [2]. By the end of this century the population of the world is expected to rise from 7 billion to 10 billion. The energy has primarily been supplied by fossil fuels, and is expected to continue that way as the energy demand increases. The increasing energy demand arises from population increase, industrialization, implementation of modern agricultural techniques and rising standards of living in developing and transitional countries [2].

According to the U.S. DOE in the year 2003 the world marketed energy was 444 EJ [2], 165 of which were used by industrial sector, 90 in transportation, 53 in residential use and 26 in commercial sector. By the year 2030 these numbers are expected to increase to 315 EJ (industrial) 132 EJ (transportation) 82 EJ (residential) and 41 EJ (commercial), with a total of 570 EJ.

We need more energy – it is evident everywhere and on a massive scale. Even

if effective energy saving measures are put into practice, that will not decrease the energy consumption to a sustainable level.

The main reasons to push for new energy technologies include [2]:

1. Need to address global warming
2. Growth in global energy demand (particularly in Asia)
3. Limited capacity for carbon sequestration
4. Eventual depletion of fossil fuels

The current energy supply relies to a large extent on fossil fuels – coal, oil and natural gas [2]. Coal is abundant, but it creates polluting gases and soot, causing acid rain and air pollution. It also produces carbon dioxide, a major contributor to global warming. Oil is another fuel, having the advantages of being easily transportable and refinable to many different grades. However, there is a finite supply and it too pollutes a great deal with CO₂ and other gases. Natural gas burns cleanly, is transportable, but again, it produces CO₂ and there's a limited supply.

We may need fossil fuels for the near-term until a suitable replacement is found, but they are limited in the long-term due to resource limits, geopolitical tensions from non-uniform distribution of resources and increasing need of energy by developing nations, and environmental effects [2].

The use of fossil fuels is already bringing about specific strategies to minimize the environmental impact, such as hybrid cars. Carbon sequestration is a potential solution but has a number of significant unaddressed problems such as the fuel burned to sequester the carbon in the first place, the impact on saline aquifers and availability of sequestration sites near major power plants. If we continue to make fuels from the oil sands as supplies become scarce and toward mid-century, process heat is required

for extraction, and hydrogen is needed for upgrading heavy oil [2]. As tougher green house gas regulations begin to be put in place, there is a strong need for a cleaner alternative for the source of process heat and hydrogen in order to marginally retain fossil fuels as an acceptable solution. It will likely be the case that the stiff regulations on greenhouse gas emissions force companies to seek alternatives faster than the governments themselves.

Another energy alternative is that of nuclear fission, splitting atoms and capitalizing on the mass defect. While providing a vast amount of energy that does not directly emit CO₂, nuclear fission results in some emission from mining and processing the necessary uranium ore. The fuel supply for traditional non-breeding reactors is limited, and the storage of long-term radioactive waste is nontrivial. Fission reactions also rely on unstable chain reactions that need to be maintained at a stable operating point. Although the safety of nuclear reactors has increased tremendously and the safe storage of radioactive waste is progressing, the limited amount of uranium ore deposits makes it undesirable as a total solution to the world's energy needs. The useful lifetime of available ores can be extended by an order of magnitude by switching to breeder reactors, but that produces more weapons-grade material that is geopolitically dangerous.

Renewable energy sources are further potential candidates for greenhouse gas free energy supply. Hydroelectric energy is the most used form of renewable energy [3]. It is clean, but is geographically limited by the locations of water flow. Wind energy is starting to be implemented more, and again is very clean. However, a huge number of wind turbines is necessary and again restricted geographically. The other renewable sources, geothermal and solar, share the same traits: clean, but geographically limited with a huge number of required cells [3]. They do, however,

offer continually replenished fuel supplies.¹ and do not require the construction of large facilities. They have a minimal environmental impact and diversity.

While much more reasonable for sustainability, the renewable sources are unpredictable, relying on appropriate weather conditions such as wind and sunlight. It is difficult to see how they can meet the energy needs for an industrialized society – most quoted figures for renewables treat only the amount of household energy needs that can be met. The reality is that half the energy consumption of an industrialized world is by industry, and a quarter is by transportation [2]. These needs will have to be met by some alternative energy source. The newer renewable energy technologies are not centralized, and cannot meet the demands of massive power grids.

There is no blanket cure-all to the current energy crisis. Multiple avenues and solutions need to be investigated and implemented in order to develop a sustainable world for generations to come.

1.2 Fusion's Potential Role

Fusion energy, described in detail in Chapter 2 is a very promising solution to the world's energy needs, with minimal environmental impact, weather-independent, centralized and huge energy reserve.

The two fuels for fusion are deuterium and tritium. Deuterium is in plentiful supply. It is found in lakes and seawater with a natural abundance of 0.016% [4]. It can be found everywhere on earth. Tritium is a radioactive isotope of hydrogen with a short 12.3 year half-life, so is not found naturally anywhere. However, it can be bred on-site from lithium reacting with neutrons from the fusion reactions themselves and tritium is found in plentiful supply in the earth's crust. At any given time there would

¹Geothermal energy is an exception; it will only replenish if the area is reheated.

only be a small amount of tritium on the reactor site. It is used in many biology labs around the world as a tracer, so its safe handling procedures are well-established.

Fusion is also extremely energy-efficient. For a GW power plant, 1 tonne (cubic metre) of heavy water and 10 tonnes of lithium fuel would be required for an entire year [4]. This is in contrast to 30 tonnes of UO_2 for fission, 1,300,000 tonnes (or 10,000,000 barrels) of oil, or 2,000,000 tonnes (21,010 railcar loads) of coal [3]. Thus a shipment in one supply truck would last an entire year at a fusion reactor. It would also be a centralized power plant that could be located anywhere since ocean water is practically ubiquitous and the required deuterium and lithium easy to transport, making it available to the entire world.

It is important to emphasize that fusion is *not* the same as fission. Fusion does not produce long-lived radioactive waste – its byproduct is helium and a neutron. As long as appropriate materials are chosen for the reactor construction, there would be a modest level of activation from the neutrons in a fusion reactor. Furthermore, fusion reactions are so difficult to make happen in the first place that there is no chance whatsoever of a runaway reaction. The number of conditions that are needed to ensure the reactions can occur mean that if a system were to fail then the reactions would stop. Therefore, in contrast to fission, fusion cannot have reactor meltdowns or chain reactions.

Finally, fusion reactors could not only generate electricity, but could furnish high quality heat for oil sand extraction and other industrial processes. More importantly, it could be the stepping stone toward a hydrogen economy. Currently fuel cell cars, which operate on hydrogen and produce water, are not a viable alternative since the means of producing the hydrogen involves burning fossil fuels. However, with a fusion infrastructure, hydrogen could be produced as fuel for cars and the global economy would be hydrogen-based. Alternatively, the vast amount of energy provided

by fusion could be used for fleets of electric cars as well. It would bring humanity closer to becoming true stewards of the Earth to control climate change, benefiting and living from a deep understanding of the workings of the universe.

The basic science for fusion has been proven but it needs to be scaled up to reactor-size conditions, and energy gain needs to be demonstrated [5]. There are many schemes to try and realise this, all with their challenges and advantages. Fusion is arguably the most technically and scientifically challenging problem humanity has ever faced.

Since the invention of the laser, light was thought of as an ideal way to confine and heat the fusion reactants in order to produce net gain. There are several more specific approaches that have evolved since then, such as central hot spot, indirect drive, and fast ignition.

Central hot spot is the original conception of laser fusion: multiple laser beams compress and heat a spherical pellet from all sides. It has very strict symmetry requirements and has a reasonable gain compared to other methods. Assuming a perfectly symmetrical compression, with 10 kJ of laser energy coupled to the core and a temperature of 10 M K, the required density is 200 g/cc (1000 times liquid density) [3].

Furthermore, during the implosion, the plasma formed behaves like a fluid, and has instabilities inherent to fluids (discussed in Chapter 2). For ignition to occur without the incapacitating effect of these instabilities, a 1% radiation uniformity is required around the pellet. The pellet itself needs to be symmetric to within a percent as well. This is not a trivial fabrication task.

The interaction of the laser with the plasma is also quite complex, as will be discussed in Chapter 3. Many instabilities that were poorly understood in the past can be dealt with more readily thanks to a great deal of work in simulation and

experiment.

As far as an actual reactor goes, a fusion reaction needs to occur often enough to make steam for turbine electricity generation. This requires a megajoule-class laser which can fire at 5-10 Hz. Advances in laser technology have brought about a few possible candidates such as thin slab glass or ceramic-based Nd or Yb-doped material. The targets must also be inexpensive and able to be fired into the chamber with high positional accuracy.

These are only a few of the issues within laser fusion. Another proposed solution, indirect drive, manages to produce the extreme symmetry requirements for implosion. It exploits the fact that high intensity lasers create a hot plasma which then produces jets of X-ray radiation. These X-rays then heat their surroundings including the outer surface of a fuel capsule which subsequently implodes. Therefore the scheme is to use a cm-sized cylindrical kiln known as a hohlraum to produce X-rays to heat a pellet to ignition temperatures. It is being investigated at the National Ignition Facility (NIF) as discussed below.

Another method proposed in 1994 by Max Tabak is known as Fast Ignition, and is the principal Fusion method investigated in this thesis. It essentially separates the compression and heating phases by using two separate beams (whether they are laser or ion beams) [6]. It is analogous to using a spark plug as opposed to traditional diesel-engine compression. One pulse is longer, to compress the target fuel mass, and the second beam is a short laser pulse that heats up the compressed pellet to the critical temperature for fusion. There are much lower symmetry requirements (the ignition can happen anywhere in the pellet, not just the core), allowing greater flexibility in the beam and target quality. Furthermore, there is a higher gain for the same amount of input energy [6]. There are a few different schemes for fast ignition which will be discussed in turn in Chapter 2. They revolve around a central problem,

which is the fact that the second laser cannot penetrate into the pre-compressed core. Instead, the laser energy must be converted into an intermediate carrier of energy such as a jet of hot electrons by a short-pulse laser. These hot electrons can couple the energy necessary to achieve ignition, and their characterization is the principal application of the diagnostic described in this thesis.

The hot electrons required for fast ignition are energetic enough to knock out inner shell electrons, after which the atoms de-excite by emitting X-rays known as K_α radiation. An image of these X-rays provides a means of tracking the number and position of hot electrons within a given target, and exactly how this is done will be discussed in Chapter 4.

1.3 Status of Fusion Research

The National Ignition Facility in Livermore, California, is the world's largest laser, (the first MJ class laser) commissioned on March 10, 2009 in the UV range [7]. It has 192 beamlines amplified over three football fields to enter a 10 m diameter chamber from all sides [7]. It heats matter to temperatures greater than $10^8 K$, densities greater than 10^3 g/cm^3 and pressures greater than 10^{11} atm [8]. It is the culmination of a long line of laser systems, and a \$ 4 billion investment made it possible. A comparable system is the Laser Mégajoule in France, which is a 2 MJ laser in construction (near-completion at the time of writing) near Bordeaux France. It will have 240 beamlines and provide another avenue to push forward in fusion energy research [3].

The National Ignition Campaign is underway with collaborations from laboratories across the US. It started ignition experiments this year, and aims to demonstrate proof-of-principle laser fusion for indirect drive as well as a reliable and repeatable ignition platform. It will access the extreme conditions needed for ignition.

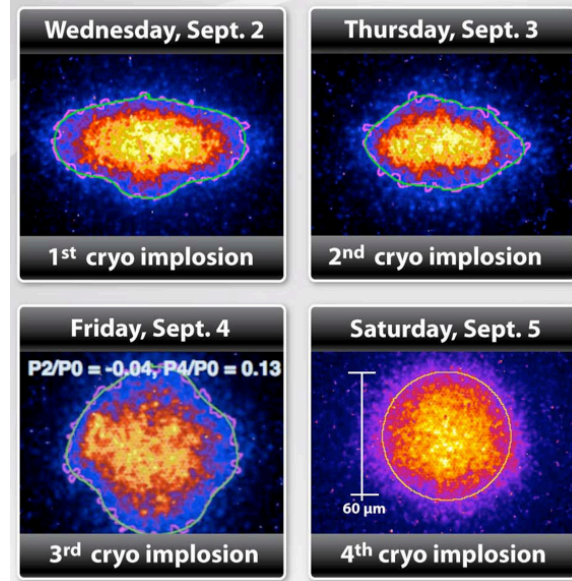


Figure 1.1: Four shots taken during the early National Ignition Campaign in 2009 [8]. The initial capsule diameter was 1.8 mm, and the emitting region 33X smaller than capsule diameter, which is consistent with a 10-15 mass compression ratio. The symmetric implosion exhibits a P_2 of 7%.

The implosions to date have shown good symmetry at lower temperatures, as the series of shots in Figure 1.1 shows. In 4 shots they tuned the laser parameters in order to achieve a symmetrical implosion with a P_2 of 7%. This term is the second-order Legendre pressure asymmetry which is related to the spatial distortion $a_n(\tau)$ by [9] (where the P_n are expressed as ratios to the zeroth order pressure moment P_0)

$$a_n(\tau) = -\frac{1}{2} \int v P_n(t) dt = -\frac{1}{2} a_0(\tau) P_n \text{ (for constant } P_n). \quad (1.1)$$

The NIF scientific team achieved such symmetry by tuning the wavelength of some of the beam cones, capitalizing on crossed-beam energy transfer from the laser plasma interaction [8]. This was all modeled through advances in computer simulation and physics understanding.

They have made tremendous progress, recently reporting 1 MJ laser energy on target [10] with remarkable symmetry which is being tuned to meet implosion requirements. Current calculations put ignition at 1.2 MJ. Initial yields are predicted to be of the order of 20 MJ. Eventually yields greater than 100 MJ may be possible depending on the performance of the hohlraums – that’s a factor of 50 gain in energy.

The end goal of the National Ignition Campaign is to develop a robust burning plasma platform by the end of 2012, with careful tuning of all parameters over the next year. Scientists are taking necessary precautions, however, since all aspects of the system have to demonstrate they can handle the optical loading and radiation damage from the tests.

Achieving ignition on NIF will be a defining moment for the world’s energy future, but as Steven Chu, the U.S. Secretary of Energy put it, we should “not wait for NIF ignition to start such planning”. And they have been planning.

Laser-induced Fusion Energy (LIFE) is a “credible extension of NIF” to build an engineering demo reactor. The early concept for this was to basically initiate a lower-yield fusion reaction whose neutrons can induce fission reactions in a blanket of surrounding material [8]. This hybrid concept would not only allow for lower beam energy, but it could help dispose of nuclear waste from fission reactors. However, they have recently shifted away from the hybrid design and focused on developing a near-term lower-gain pure fusion reactor [11]. It aims to provide a form of fusion ready for use around the world, and would provide valuable materials science for future high-gain pure-fusion reactors.

Although the development of NIF has met with a large amount of success, some key physics issues remain unresolved. For example, it may turn out that the loss from Stimulated Raman Scattering may be larger than expected, resulting in intolerable levels of target preheating from fast electrons generated during the compression.

Other approaches are therefore still being investigated. There are several fast ignition experiments underway around the world. FIREX is a 10 kJ laser energy Fast Ignition Realization Experimental Facility in Osaka, Japan. There is potential for an upgrade to FIREX II which will provide 50 kJ in 3 ns for implosion and 50 kJ in 10 ps for heating, and it will focus heavily on fast ignition. The funding of FIREX II will depend on the success of FIREX and the results from NIF. In Rochester, New York, the OMEGA-EP laser will carry out fast ignition experiments in integrated experiments including fuel pellet implosion and compression.

HiPER is a European High Power laser Energy Research facility that plans to demonstrate the feasibility of fusion as an energy source (i.e. a fusion power plant) [12]. It will focus on fast ignition or shock ignition. It will be a billion Euro investment with collaborators from all over the European Union (25 institutions from 11 nations) [12]. The proposed beam implosion energy is 200 kJ in 5 ns, and the PW beam for fast ignition is 70 kJ in 10 ps at 2ω [3], which may be revised as results from NIF and ongoing fast ignition experiments come in. There are still major hurdles to minimize target and laser costs in addition to the primary physics obstacles.

1.4 Outline

The outline of the thesis is as follows. The physical basis for fast ignition fusion will be discussed along with hot electron generation and X-ray emission. An outline of laser plasma interactions will be given to provide the background necessary to interpret hot electron behaviour. An overview of X-ray imaging methods and the status of other KB microscope designs will provide context for the design presented in subsequent chapters. The microscope design will be presented, followed by experimental applications on the Titan laser system at the Lawrence Livermore National Labora-

tory (LLNL). Current developments and future improvements will then be presented to give a picture of what the diagnostic's role will be in coming years.

Chapter 2

Fast Ignition Fusion

This chapter provides context and motivation for the development of the KB microscope. Basic fusion processes will be discussed up to and including the promising Fast Ignition scheme, discussing some of the challenges and strengths inherent in each proposed scheme. At the end of the chapter it will be evident how the KB microscope can contribute to studying some of the issues which need to be resolved in order to reach the breakeven point for fusion energy.

2.1 Plasmas

A plasma is the fourth state of matter, occurring at higher temperatures than gases. Basically a plasma consists of an ionized gas, and the extent of ionization can vary widely. Plasmas in fact account for 99% of the matter in the visible universe [13], and understanding the physics of how plasmas interact is essential not only to this thesis but to a large number of real-world applications.

2.2 Thermonuclear Fusion

In the burning ionized gases of the Sun, with temperatures of a million degrees Kelvin and pressures on the order of megabars (a million atmospheres), atoms are pushed close enough to one another that the Coulomb repulsive barrier can be overcome in order to form a new nucleus. This process, nuclear fusion, is the way that heavier elements are generated from the abundant hydrogen in the universe. There are many different fusion reactions that can occur in this chain called nucleosynthesis, and a few are listed below [140].

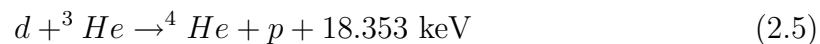


The energy released is related to Einstein's famous equation, $E = mc^2$. Figure 2.1 shows the binding energy per nucleon versus atomic number [14]. As you climb the curve toward higher binding energy per nucleon, this corresponds to a lower potential well (since the binding energy is negative). The excess energy corresponds to the amount the mass decreases (aka. the mass defect), and Einstein's equation indicates that this little bit of mass is equivalent to a large amount of energy. One of the lowest threshold fusion reactions is



The nuclear reaction of combining deuterium and tritium to form helium and a neutron, products with a net energy of 17.3 MeV [15], is one that occurs on the sun and is the goal of many clean-energy minded scientists. Huge output energy, non-toxic

byproducts, plentiful supply of deuterium in the ocean and tritium that can be bred on-site are just a few of the reasons why the desire to reproduce fusion on Earth is so strong. Of other interest is the reaction with Helium-3,



which has a slightly higher ignition temperature but produces no nuclear activation of the chamber if the protons are decelerated in magnetic fields and the energy extracted directly in electric currents [16]. It is partly for this reason, in fact, that Russia and China hope to land on the moon by 2020 [17] and an argument put forth by NASA as well [18]. The moon's surface is blasted by space weather and captures Helium-3 which cannot form naturally on Earth.ⁱ Thus the moon is a Helium-3 mine.

Currently there are two broad categorizations of approaches to create fusion energy, separated by the way in which the fuel is kept together: magnetic confinement fusion (MCF) and inertial confinement fusion (ICF). The basic idea behind magnetic confinement is to use magnetic fields confine the fuel for long periods of time and thus maintain the close proximity necessary for fusion while preventing it from cooling by contacting the walls. The idea behind inertial confinement is to push the fuel together to fuse faster than it can separate, capitalizing on the fact that the pellet has an inertial mass that will require a finite time to disassemble.

A common criterion for fusion reactions is the Lawson Criterion, which was first derived by J.D. Lawson and reported in his article "Some Criteria for a Power Producing Thermonuclear Reactor" [19]. The basic idea is intuitive: for a fusion reaction to occur sufficient reagents have to be close enough for a sufficiently long time for the net fusion energy released to be larger than the energy used to heat the fuel.

ⁱThankfully because the hordes of bombarding charged particles are stopped by the atmosphere before making it to the Earth.

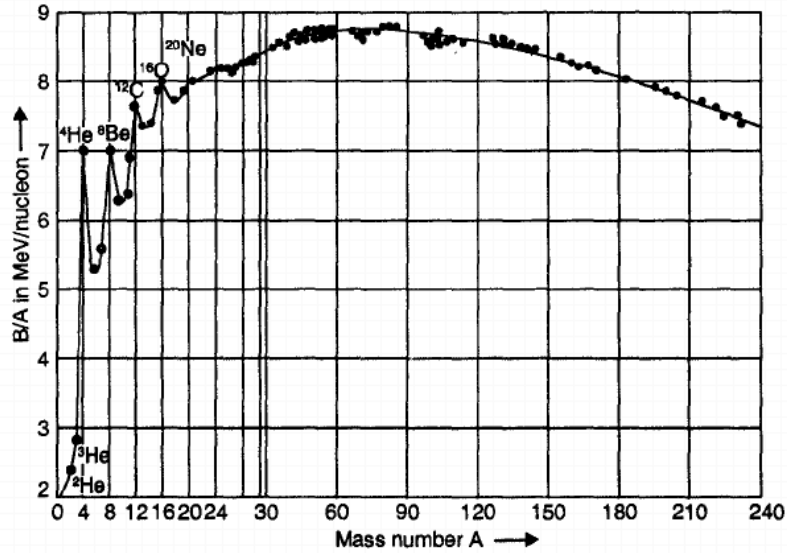


Figure 2.1: The binding energy per nucleon increases toward the iron group of isotopes around mass number 62 [14]. A higher binding energy means a deeper potential well and a lower energy state for the nucleus. Therefore transitions toward this plateau of stability release excess energy (mass defect), whether they be fission or fusion.

Specifically, it is a product of density (enough reagents close enough) and time. For a reacting temperature of 5-10 keV, $n\tau = 10^{14} - 10^{15} s \cdot cm^{-3}$ [15] (the lower values are for MCF). The magnetic confinement fusion approach is to basically have a lower-density plasma circulate for a long time. MCF confines a deuterium-tritium plasma in a toroidal magnetic structure such as a Tokamak or a stellarator in order to achieve this goal. ICF takes the opposite approach, encasing deuterium and tritium in a microscopic glass or plastic pellet. Lasers and/or particle beams are used to compress and heat the pellet to very high densities for a very short time. In addition to the Lawson criterion in ICF is the requirement for a minimum value of ρR , also known as the areal density [20] (the reason for this convention will be explained shortly). Before continuing, however, it should be mentioned that neither fusion approach has

yet been physically realized with ignition or net gain.ⁱⁱ

We start with the reaction rate equation for a D-T reaction [20]:

$$\frac{dn_T}{dt} = -n_T n_D \langle \sigma_{DT} v \rangle \quad (2.6)$$

When the species are equal in density, we can write $n_T = n_D = n/2$ and the equation becomes

$$\frac{dn}{dt} = -\frac{n^2}{2} \langle \sigma v \rangle \quad (2.7)$$

By integrating the value of $1/n^2$ from a start time (set to zero) until the inertial disassembly time τ_d , we get

$$\int_0^{\tau_d} \frac{1}{n^2} \frac{dn}{dt} dt = - \int_0^{\tau_d} \frac{\langle \sigma v \rangle}{2} dt \Rightarrow \frac{1}{n} - \frac{1}{n_0} = \frac{\tau_d}{2} \langle \sigma v \rangle \quad (2.8)$$

In order to get the confinement or disassembly time, an argument by Rosen [21] is followed. First we use the hydrodynamic concept that a plasma surrounded by vacuum will have rarefaction waves that propagate at the speed of sound from the vacuum into the plasma core C_s . At each point r' in the sphere the disassembly will begin when the rarefaction wave passes (this is where we define confinement to be lost). The time at which this occurs is

$$\tau_d(r') = \frac{R - r'}{C_s} \quad (2.9)$$

To get the global confinement time for the entire spherical pellet of radius R and

ⁱⁱSee Section 1.3 for most current ICF developments.

uniform density ρ , we take a weighted average using the mass:

$$\tau_d = \int_0^R \rho[(R - r')/C_s] 4\pi r'^2 dr' / [(4/3)\pi\rho R^3] \quad (2.10)$$

$$= (3/C_s R^3) [(Rr'^3/3 - (r'^4/4)]_0^R = R/4C_s \quad (2.11)$$

We extend this by considering the fraction of unused fuel, n/n_0 . The fraction of burned fuel is

$$f_b = 1 - \frac{n}{n_0} \quad (2.12)$$

Using the above equations along with $n_0 = \rho/\langle m \rangle$ where $\langle m \rangle$ is the average of D and T nuclear masses, we get

$$f_b = \frac{\rho R}{\rho R + \beta(T)} \quad (2.13)$$

where $\beta(T) = 8C_s \langle m \rangle / \langle \sigma v \rangle$. It is a function of temperature because for a plasma the speed of sound is given by

$$C_s = \left(\frac{\gamma Z k_B T_e}{m_i} \right)^{1/2} \quad (2.14)$$

where T_e is the electron temperature and m_i is the ion mass [13]. The value of $\beta(T)$ takes on a maximum value of about 6.0 g/cm² for optimal burns at 30 keV [21]. A reasonable burn fraction of 1/3 requires a ρR of about 3 g/cm². This is a much more convenient way of expressing the confinement achieved, since it will directly indicate the expected burn yield. For MCF this term is not very meaningful, since theoretically a fusion reactor would have the plasma circulate long enough so the burn fraction of a given sample of fuel approaches one. Converting the ρR criterion to the density-time notation used for MCF, the criterion is $2 \times 10^{15} \text{ s} \cdot \text{cm}^{-3}$ [21], indicating that ICF has a higher confinement requirement than MCF mainly because the fuel assembly in ICF introduces a plethora of loss mechanisms and challenges to overcome.

Although a complete derivation and description is beyond the scope of this work, it is worthwhile to mention a few loss mechanisms that diminish the amount of useful energy and are hindrances to successful ignition [20]. Heat conduction serves to carry energy away from the hot spot, and raises the required amount of input energy to reach ignition. Electron motion in a plasma whose temperature is above a few keV results in Bremsstrahlung (“braking radiation”) which is emitted as the plasma electrons are slowed down via the Coulomb force of nearby ions.ⁱⁱⁱ Optical thickness also plays a role, determining how much of the radiation will be reabsorbed in the plasma or escape, in either case altering the dynamics of the implosion.

Beyond these loss mechanisms, there are other physical processes and instabilities that play a role in ICF schemes. The two broad categories are hydrodynamic instabilities which arise because of a plasma’s behaviour as a fluid, and laser-plasma interactions (LPI) which arise because of the strong fields, high power and high intensities of the laser drivers used [20].

2.3 Hydrodynamic Behaviour of a Plasma

The formation of a dense hot spot that meets the Lawson criterion requires high symmetry in the implosion. Convergence ratio is defined as $C_h = R_0/R_h$, R_h being the hot spot radius and R_0 the initial fuel pellet radius [20]. The detailed calculations can be found elsewhere, but for example, for a convergence ratio of $C_h \approx 30$, the deviations in the ablation pressure should not be larger than 1%. The symmetry requirements become more and more strict as the convergence ratio increases [20]. This is influenced by the increased area as perturbations in the surface uniformity and smoothness of the sphere become more prominent, and other instabilities such

ⁱⁱⁱBremsstrahlung is also produced from hot electrons which will be described shortly, along with the very-important K_α radiation.

as the Rayleigh-Taylor Instability (RTI).

The Rayleigh-Taylor Instability is a phenomenon that occurs at the interfaces of fluids of different densities [20]. Basically if the surface is accelerated toward the denser fluid, a small perturbation can grow exponentially in time. There are two stages of ICF where this can occur [20]. The first is at the ablating surface of the thin shell encasing the fuel, which can have nonuniformities from heating and result in an amplifying asymmetry that renders ignition impossible. The other stage is near the end of the implosion, when the highly compressed fuel slows down the incoming shell. The instability at this stage leads to mixing of the fuel with the shell, reducing the temperature at the edges and thus reducing the size of the hot spot that can ignite [20]. The RTI plays a major role in determining the symmetry bounds of a given implosion, and calculations of the perturbations which result can be found in Figures 2.2 & 2.3.

Although these symmetry requirements are less stringent for lower convergence ratios, the pulse energy required can be shown to have the following scaling [20]:

$$E \propto \frac{(\rho R)^3}{\rho^2} \quad (2.15)$$

where ρR is the fuel's areal density and ρ is the fuel density (a uniform coupling efficiency is assumed). The required laser energy decreases as the pellet is compressed to a higher density for a given value of ρR , which requires a higher convergence ratio [20]:

$$E \propto C_h^{-6} \quad (2.16)$$

This equation assumes a uniform fuel sphere density in the beginning and after compression. Thus a balance must be struck between the achievable convergence ratio

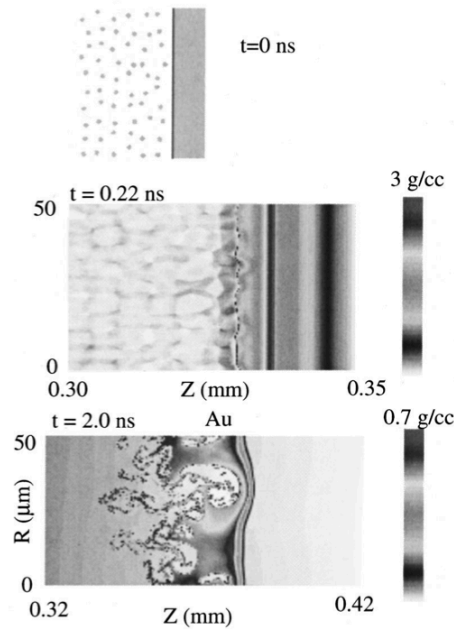


Figure 2.2: A time sequence of density maps simulated using CALE (C-based Arbitrary Lagrangian-Eulerian) software [22]. The code mimicked the 200 eV heating of a foam-gold target by the 1 ns NOVA laser. The foam had a density of 0.15 g/cc, and a typical pore size was 5 μm . A 50 μm wide section was modeled.

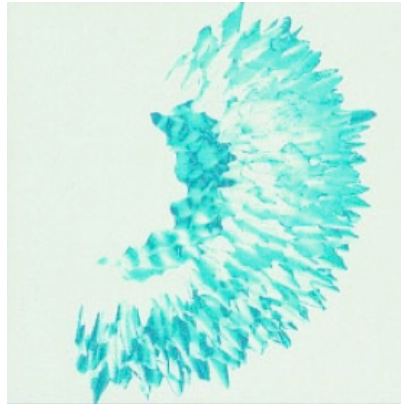


Figure 2.3: Density iso-contour surfaces of 45 g/cm³ at 15.65 ns into a 3D HYDRA simulation of a section of an implosion [23] (peak implosion occurs at 15.55 ns). The capsule simulated had a beryllium ablator doped with 0.9% copper (135 μm thick), followed by a layer of DT ice (80 μm thick) and a core of DT gas with a full capsule radius of 1085 μm . It is driven by a shaped pulse with a peak temperature of 300 eV produced by the 192 beams of NIF. The ice surface perturbations were initialized from previous results.

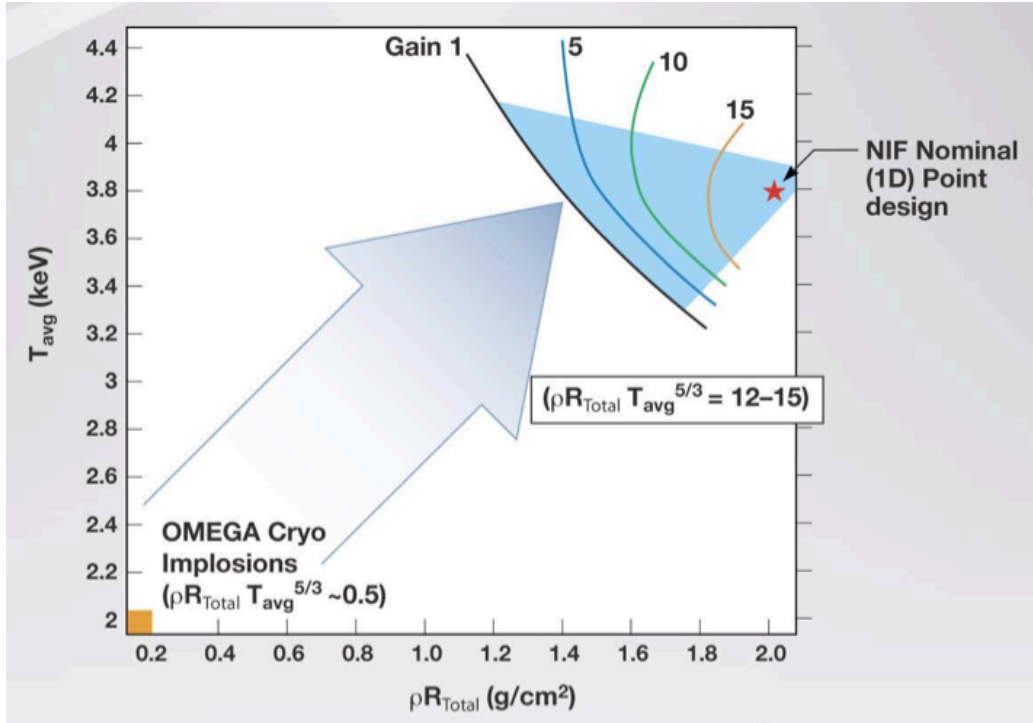


Figure 2.4: A temperature and areal density map showing where ignition (Gain=1) will occur, and the regions which NIF hopes to access in comparison to older experiments on the OMEGA laser [8].

and reasonable pulse energies.

We will end the discussion of symmetrical implosions with a curve showing the regions where ignition can occur in Figure 2.4. Hopefully at this point it has been stressed that successful thermonuclear ignition is very difficult to achieve, and there are many parameters and factors that play a role in determining that success. The method described above is the traditional or “central hot spot” (CHS) approach to fusion, where compression and ignition go hand in hand. Another approach which is part of the focus of this work is Fast Ignition (FI) which decouples the compression and ignition stages, and has promising advantages over traditional CHS fusion [24].

2.4 Critical Density

As an electromagnetic wave travels with angular frequency ω and wavevector \mathbf{k} in an unmagnetized plasma, it obeys the following dispersion equation [13]:

$$k^2 c^2 = \omega^2 - \omega_p^2 \quad (2.17)$$

where ω_p is the plasma frequency. We see that the wavenumber of the propagating wave becomes imaginary when $\omega < \omega_p$. The boundary point when $\omega = \omega_p$ corresponds to a particular density of the plasma called critical density:

$$n_c = \frac{m_e \epsilon_0 \omega^2}{e^2} \quad (2.18)$$

The inclusion of the relativistic mass adds a γ factor to the equation, and allows the laser to penetrate further into the plasma ($n_{cr} = \gamma n_c$ [25]). This density is commonly used as a density scale in all types of modeling and calculations. The imaginary \mathbf{k} vector at densities higher than the critical density results in a skin depth δ over which the wave will decay exponentially [13].

2.5 The Ponderomotive Force

The ponderomotive force is experienced by electrons in the presence of intense oscillating electromagnetic fields related to gradients in the field intensity. In order to calculate this force a derivation from Chen [13] is followed for nonrelativistic plasmas.

We start with the Lorentz equation:

$$m \frac{d\vec{v}}{dt} = -e[\vec{E}(\vec{r}) + \vec{v} \times \vec{B}(\vec{r})] \quad (2.19)$$

We take the laser to be linearly polarized with

$$\vec{E} = \vec{E}_s(\vec{r}) \cos \omega t \quad (2.20)$$

Taking the standard approach to linearization, we recognize that the $\vec{v} \times \vec{B}$ term is second order for nonrelativistic plasmas, so to first order it can be neglected. We therefore have, at the initial position r_0 ,

$$m \frac{d\vec{v}_1}{dt} = -e \vec{E}(\vec{r}_0) \quad (2.21)$$

$$\vec{v}_1 = -(e/m\omega) \vec{E}_s \sin \omega t = d\vec{r}_1/dt \quad (2.22)$$

$$\delta\vec{r}_1 = (e/m\omega^2) \vec{E}_s \cos \omega t \quad (2.23)$$

giving the first order particle oscillation in the applied field. E_s contains the spatial dependence. We have what we need to go to second-order, where we expand $\vec{E}(\vec{r}_0)$ about \vec{r}_0 in a Taylor series:

$$\vec{E}(\vec{r}) = \vec{E}(\vec{r}_0) + (\delta\vec{r}_1 \cdot \vec{\nabla}) \vec{E}|_{r=r_0} + \dots \quad (2.24)$$

To include the $v_1 \times B_1$ term, we use Maxwell's equation:

$$\vec{\nabla} \times \vec{E} = \partial \vec{B} / \partial t \quad (2.25)$$

$$\vec{B}_1 = -(1/\omega) \vec{\nabla} \times \vec{E}_1|_{r=r_0} \sin \omega t \quad (2.26)$$

Using the above equations we can write the second-order contribution to the equation of motion:

$$m d\vec{v}_2/dt = -e[(\delta r_1 \cdot \vec{\nabla})\vec{E} + \vec{v}_1 \times \vec{B}_1] \quad (2.27)$$

$$m \left\langle \frac{d\vec{v}_2}{dt} \right\rangle = -\frac{e^2}{m\omega^2} \frac{1}{2} [(\vec{E}_s \cdot \vec{\nabla})\vec{E}_s + \vec{E}_s \times (\vec{\nabla} \times \vec{E}_s)] = \vec{f}_{NL} \quad (2.28)$$

Finally, recalling that [26]

$$A \times (B \times C) = B(A \cdot C) - C(A \cdot B) \quad (2.29)$$

we can cancel some terms and take the time average over one cycle to get the final expression for the nonlinear force:

$$\vec{F}_{NL} = -\frac{1}{4} \frac{e^2}{m\omega^2} \vec{\nabla} E_s^2 = -\frac{\omega_p^2}{\omega^2} \vec{\nabla} \frac{\langle \epsilon_0 E^2 \rangle}{2} \quad (2.30)$$

where we have used the fact that $E_s^2 = 2\langle E^2 \rangle$ where $\langle E^2 \rangle$ is a time averaged quantity. This force is called the ponderomotive force [13]. Since energy density is proportional to E^2 , and is equivalent to pressure, the ponderomotive force is the result of gradients in light pressure [27]. This force is essentially the result of electrons oscillating (at the “quiver velocity”) in the E field experiencing the $v \times B$ force along the direction of k . At relativistic intensities, the quiver velocity is limited to a maximum value of c , but the push forward from the $v \times B$ or more appropriately for the numerous electrons to which this occurs given by $j \times B$, is significant. The ponderomotive force is therefore sometimes called the $j \times B$ force [28]. This asymmetrical oscillation results in an accumulation of charge. By applying Newton’s law we see that the force of the space charge in these accumulation regions will eventually balance or equal the

force exerted on it [13]. A similar derivation can be carried out for relativistic motion (see [28] or Section 3.14) , giving the following ponderomotive potential energy solved numerically for linear polarization:

$$U_p = m_0 c^2 \left(\sqrt{1 + \frac{I_{W/cm^2} \lambda_{\mu m}^2}{1.37 \times 10^{18}}} - 1 \right) \quad (2.31)$$

This force acts primarily on electrons, but since the gradient of the field squared is typically a slowly changing function, the low-frequency motion can eventually transfer to the ions [13].

A nonuniform field will have the strongest gradients, and so the ponderomotive acceleration of electrons (i.e. heating) will be greatest when the field is very intense [30]. This occurs in high-intensity pulses, which have a very short amplitude rise time, which corresponds to a steep gradient in the intensity [30]. This absorption of energy to push electrons aside is conventionally known as ponderomotive heating, but sometimes called absorption by a “third body” which is the field irregularity [30].

The ponderomotive force has an extra effect: when there is sufficient time for the ions to be drawn out of the laser beam by the Coulomb attraction from the expelled electrons, it is the cause of self-focusing of laser light in a plasma as the electrons are pushed out of high field regions and cause a higher refractive index on axis (for more information, see [13]). Generally this can impact the absorption mechanism and effective intensity as the laser moves through the material.

2.6 The Raman Instability

The Raman instability is the resonant decay of an incident photon into a scattered photon and an electron plasma wave (plasmon) [27]. The minimum frequency of light

that can travel in a plasma is given by the plasma frequency, ω_{pe} (related to the critical density), and since we have the conservation of energy condition that requires

$$\omega_0 = \omega_s + \omega_{pe} \quad (2.32)$$

where ω_0 is the incident EM wave frequency and ω_s is the scattered EM wave frequency. We can show that, since $\omega_s \geq \omega_{pe}$, for the Raman instability a necessary condition is $\omega_0 \geq 2\omega_{pe}$. Basically a light wave propagating causes a density fluctuation which results in a transverse current. If the wave numbers and frequencies are matched appropriately, a scattered light wave is generated. This wave generates a spatial variation in the electric field through interference with the incident wave (i.e. a ponderomotive force) that, as we just discussed, generates its own density fluctuation. Thus a feedback loop is created, and this instability can grow, transferring energy from the laser pulse to plasma waves, creating larger and larger density fluctuations or plasmons and a growing scattered wave [27].

It can be shown that a small amplitude plasmon is damped only by particles close to its velocity which is called Landau damping [27]. An interacting electron can be brought into resonance with the field when

$$v_e = \frac{eE}{m\omega_0} \approx \frac{\omega_{pe}}{k_p} \quad (2.33)$$

where v_e is the electron velocity, ω_0 is the frequency of the incident EM wave and ω_{pe} the frequency of the plasma wave or the oscillating electrons. Many electrons can be brought into resonance, effectively damping the plasmon while being accelerated. This amplitude is where wave breaking occurs in a plasma. The Raman instability occurs up to about $n_c/4$ (where $\omega_{pe} = \omega_0/2$) then it is damped as a beam of highly-

energetic electrons are generated. These so-called hot electrons can preheat the core in a fusion experiment, and because of this the Raman Instability must be minimized in most approaches to ICF. In Fast Ignition, these hot electrons are likely not desirable since they arise from the underdense plasma region and are generally too hot to be of interest. The useful Fast Ignition hot electrons mostly arise from the ponderomotive heating described in Section 2.5.

2.7 Fast Ignition Fusion

The basic idea behind Fast Ignition, originally conceived in 1994 by Tabak, Muro and Lindl [6] is to use one driver (that can be a laser, a heavy ion beam, or a magnetically compressed wire cage known as a Z-pinch) to create a dense fuel mass and another ultraintense laser beam to ignite the pre-compressed core [24]. The idea became feasible after the development of high-power, short-pulse lasers which were possible after the Chirped Pulse Amplification (CPA) scheme was invented [31]. CPA allowed laser pulses to be stretched, amplified, then recompressed immediately prior to final focusing, increasing the achievable amplification while still remaining below the damage threshold for the optics as well as the gain media.

The main idea is illustrated in Figure 2.5. A long laser pulse on the order of ns is used to compress the fuel pellet (i), then a second short laser pulse is used to ignite the core (iii). The method for bringing the second pulse closer to the core varies, but in (ii) a laser pulse is used to bore a hole through the coronal plasma. The ignitor pulse in (iii) cannot penetrate beyond the plasma critical density, as discussed earlier, so another means must be used to transport energy to the high density core. In addition to the hole-boring scheme mentioned above, hot electrons generated at the plasma critical density provides a way to transport energy to the preheated core

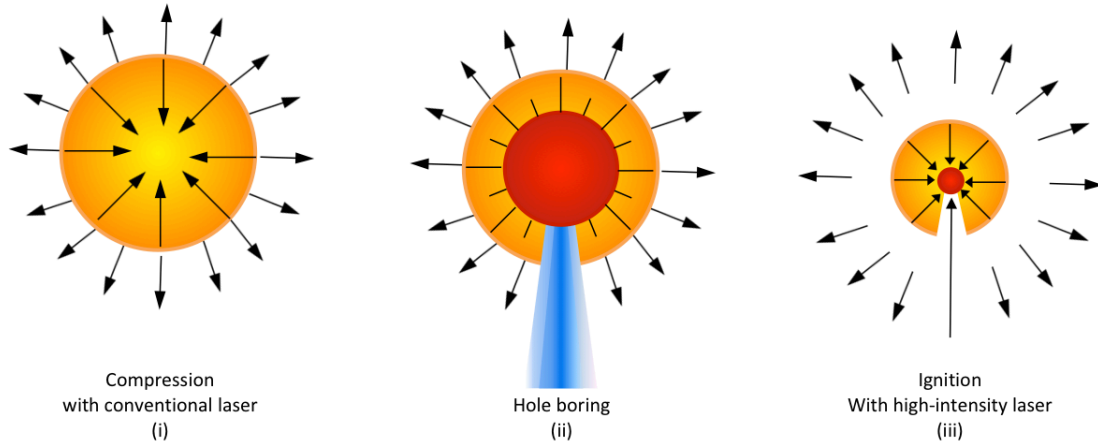


Figure 2.5: The three stages of the hole-boring fast ignition concept: (i) Compression (ii) Hole-boring (iii) Ignition (redrawn from [15]).

region. Generated by a second short-pulse laser, they can couple energy and succeed in igniting the core.

The original concept was called hole-boring, using two fast ignition pulses. The first bores a hole by using light pressure (ponderomotive pressure) to literally push the plasma out of the way, and the second pulse drives in after it to couple into a high density region close to the core (see Figure 2.5). Hole-boring allows for simple compressed target geometries which are simple to align. However, the hole-boring laser requires a considerable amount of energy. Currently the most common form of Fast Ignition is to use a cone attached to the side of the spherical pellet of DT fuel, to minimize the amount of plasma the hot electrons have to travel through and avoid a hole-boring laser. Another method for Fast Ignition involves the use of protons generated from a thin high density shell near the outside of the cone opening. Both of these methods are shown in Figure 2.6. We will not go into detail here, but one mechanism of generating protons is called Target-Normal Sheath Acceleration (TNSA) [33]. As the beam of hot electrons penetrate through and leave the back

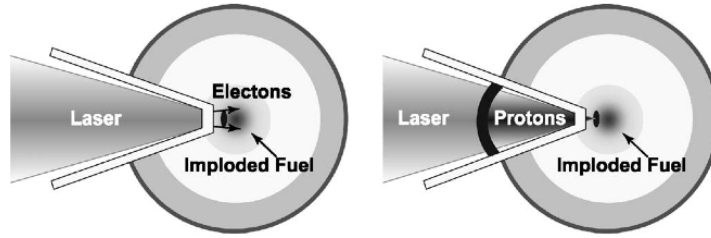


Figure 2.6: Two type of fast ignition: cone guided and proton fast ignition [32].

surface of the thin foil, that surface is strongly positively charged and there is a very large electric field that can extract a beam of protons to trail behind the electrons. This scheme is called Proton Fast Ignition (PFI), and has the advantage of short deposition range and good penetration capacity in the high density core. However, the relatively low conversion efficiency into protons is a big challenge to overcome, as well as how to focus the protons and prevent the beam from electrostatically and ballistically spreading.

Since Fast Ignition separates compression and ignition, the initial compression driver input energy is lower, relaxing some of the requirements on symmetry and enabling more flexible target fabrication [15]. Theoretically one can obtain higher efficiency (i.e. for the same amount of energy, greater gain than CHS fusion). For example, in FI the target gain could be 200 compared to a gain of 100 in the direct drive case, and 30 for the indirect drive case [15].

In contrast to the CHS approach, the FI approach is not in pressure equilibrium. In the CHS method the pressure equilibrium is necessary to ensure a symmetrical implosion. This in turn implies that the hot-spot density must be 10 times lower than the main fuel density [15]. Since Fast Ignition does not have this density requirement, a much higher areal density (ρR) can be employed, implying a much higher burn mass, or a smaller laser energy for an equivalent amount of gain (see Figure 2.7).

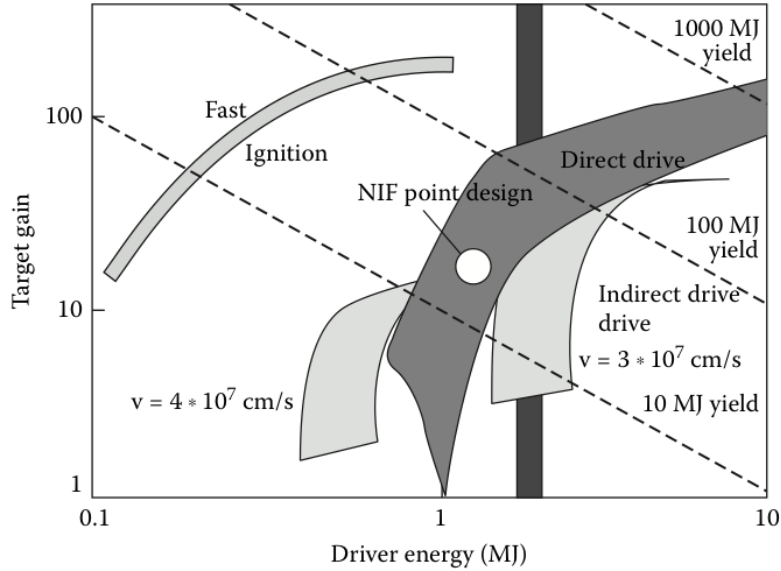


Figure 2.7: The Fast Ignition concept has a much higher gain for the same driver energy as other fusion schemes [15].

Since the fast ignition pulse is incident upon a plasma, and is in general of sufficient intensity to generate a plasma regardless, the penetration is limited to the underdense region and overcritical region up to the skin depth, where it is typically absorbed via inverse bremsstrahlung (photon absorption by an electron colliding with a nucleus in the underdense plasma region) and nonlinear wave-particle interaction in the critical density region [34]. This occurs in a region far from the core because the laser light cannot penetrate past the critical plasma density. In this critical density region, a resonant plasma wave is generated that can then be absorbed via collisionless or collisional mechanisms [25] and other wave particle acceleration mechanisms that lead to the heating of hot electrons. These electrons have sufficient energy (on the order of 1 MeV [35]) to penetrate into the dense compressed core and heat it to achieve ignition. These hot electrons, previously an undesired side-effect for CHS fusion, are essential to fast ignition fusion.

2.8 Studying Hot Electrons

In order to track the hot electrons, and see how efficient the energy conversion is for various schemes, they must be observed indirectly. Such highly energetic electrons can collide with and knock out an electron in the inner shell (1s) of an atom. A 2p electron then drops down to fill the hole, and such an energetic transition can produce an X-ray. This radiation is known as K_α emission [25]. The conversion of laser energy into GA (giga-ampere) fast electron currents [36] is approximately 10-30% for intensities on the order of $10^{19}W/cm^2$ [37], and the overall conversion of laser energy into K_α X-rays is generally on the order of $10^{-4} - 10^{-5}$ [38] [39].

Therefore, one diagnostic for the study of fast ignition processes has involved using X-ray-producing tracer layers embedded in the target. In general X-ray diagnostics can be used to determine such data as imploded target size, symmetry, temperature and areal density [40], all of which are essential to evaluating whether the laser fusion process can ultimately function and be fashioned to produce a viable source of greatly-needed energy. The imaging of the X-ray emission involves the application of imaging techniques that had been theoretically investigated over fifty years ago [41], but only pushed to their practical limits for less than three decades [42].

Chapter 3

Laser Plasma Interactions and other Physical Phenomena

In this chapter we will discuss the interactions of a laser with a plasma, discussing absorption mechanisms as well as instabilities and other pertinent phenomena.

3.1 Laser Absorption

The powerful and coherent electromagnetic fields of a laser beam opened the door into new physical regimes that require new theories of absorption more complex than traditional methods of ionization or stimulated transitions. The strength of the field determines the motion of an atom's electron. In general, an electron embedded in a laser field, which is inherently oscillatory, will execute a corresponding oscillatory motion [30]. When the field intensity becomes high enough, the induced motion of the electron can become relativistic, often referred to as the relativistic laser regime [30]. It is this regime, which corresponds to intensities greater than $10^{18}W/cm^2$ [43], which is of interest in the experimental work of this thesis. The interactions that play a role

in the relativistic regime are significantly different from the non-relativistic case.

Understanding laser absorption is important for Inertial Confinement Fusion (ICF), which requires great control and understanding of how the incident high-intensity laser beam is transmitted and absorbed in the deuterium-tritium rich target [44]. In any laser application, there are many ways of coupling the laser energy to a given material, but *where* it couples makes a great difference in terms of the end result: whether the laser energy creates thermal electrons, hot electrons or hot ions [25]. The species generated, and the properties of its propagation such as divergence and energy spread, are critical parameters in determining if the reaction will succeed.

The outline of this section is as follows. A discussion of the effects of prepulse will lead into the primary interaction of interest in the high-intensity regime: that of plasma absorption [30]. From there we will investigate collisional effects, which dominate the lower-intensity regime but are still present relativistically [43]. We will present corrections and additional effects in order of importance as the intensity is increased. Throughout the discussion the influence of prepulse, plasma profile, plasma density, pulse length, polarization and angle of incidence will be discussed in order to try and glean an overall understanding of the global absorption behaviour.

3.2 Basic Absorption

The Drude model for metals basically applies the kinetic theory of gases to the electrons in a metal, treating them as free [45]. In a metal these unbound electrons are typically formed through the release or promotion of valence electrons into what is known as the conduction band, where the electrons essentially move under no potential influence and behave as though they were a free electron gas moving against a background of immobile ions [45].

This purely collisional model is remarkably successful at modeling basic absorption of light incident on a metal as well as a metal. The result for the conductivity when a time dependent electric field of frequency ω is incident upon a material is [45]

$$\sigma(\omega) = \frac{\sigma_0}{1 - i\omega\tau} \quad (3.1)$$

where $\sigma_0 = ne^2\tau/m$, and τ is the relaxation time or the mean time between collisions, typically on the order of $10^{-14} - 10^{-15}$ seconds.

Inserting this result into Maxwell's equations and evaluating the permittivity gives

$$\epsilon = 1 - \frac{\omega_{pe}^2}{\omega^2 + i\frac{\omega}{\tau}}. \quad (3.2)$$

The first important result is that, for frequencies larger than the plasma frequency, the plasma is transparent to the radiation. The second is that for frequencies smaller than the plasma frequency, the wave will not propagate but will decay and be absorbed with a characteristic skin depth which can be calculated from the above equation.

3.3 Ionization and Plasma Formation

At moderately high intensities ($10^9 - 10^{14}W/cm^2$), multiphoton ionization leads to the creation of free electrons which are accelerated in the EM field generating new collisional electrons in an avalanche process. The laser beam alters the cold material into an ionized plasma and transparent dielectric materials such as quartz will demonstrate much higher absorption under these irradiation conditions [47] [48] [49]. However, when the intensity is increased beyond $10^{15}W/cm^2$, the reflectivity becomes much higher [47].

The reason for the rapid change of behaviour as intensity is increased (absorption

decreasing and reflectivity increasing) is that the oscillating electrons have a very high velocity and low collisionality. For ns pulses and low Z materials at intensities greater than $10^{15}\text{W}/\text{cm}^2$, the laser is essentially distorting the electron distribution and thus changing the collision frequency. This is known as non-linear inverse Bremsstrahlung [29].

Even if the pulse is short often the accompanying prepulseⁱ is intense enough to form a plasma [30]. What this implies is that, for very high-intensity laser pulses, there is generally no strict laser-solid interaction; it is primarily laser-plasma interactionⁱⁱ. As discussed earlier, a plasma will reflect radiation at its critical density, which is why the behaviour changes so markedly. There are various schemes such as plasma mirrors, second harmonic frequency conversion and nonlinear frequency conversion schemes to reduce the prepulse (see [50]).

Absorption in a plasma up to the relativistic regime occurs through inverse-bremsstrahlung together with resonant coupling mechanisms (resonant absorption, the Brunel effect, and parametric decays, to name a few) [25].

3.4 Inverse Bremsstrahlung: Collisional Absorption

The dominant absorption mechanism at lower intensities is due to collisions of electrons and ions which is just the inverse of the Bremsstrahlung emission process. Bremsstrahlung radiation occurs when an electron is decelerated when colliding with an ion, and literally translated from German means “braking radiation” [34]. Inverse bremsstrahlung is therefore the process by which a photon is absorbed by an electron

ⁱSee Chapter 6 for a more in-depth description.

ⁱⁱFor a discussion of heating and plasma formation, see [51].

in the midst of a collision [34]. A rigorous treatment of this effect can be carried out in a number of ways such as quantum mechanically using the Time-Dependent Schrödinger equation (TDSE) [54] or kinetically using the Vlasov equationⁱⁱⁱ (which takes into account the evolution of the distribution function for ions and electrons) [25]. There are variations on pure collisional absorption such as the anomalous skin effect and sheath-inverse bremsstrahlung where either the spatial field gradients or the spatial density gradients play a significant role in the interaction [25], but as we shall see at relativistic intensities other effects predominate.

3.5 Collision frequency scaling

For absorbed intensities above $10^{15}W/cm^2$, the plasma temperature rises fast enough that collisions become ineffective. The classical Coulomb collision frequency scales as

$$\nu_{ei} \propto T^{-3/2} \quad (3.3)$$

Thus, assuming a self-similar scaling model for plasma temperature, [25]

$$T_e \propto I_a^{4/9} t^{2/9} \quad (3.4)$$

one obtains a collision frequency scaling of

$$\nu_{ei} \approx I_a^{-2/3} t^{-1/3}. \quad (3.5)$$

Here I_a is the absorbed laser intensity and t is the laser pulse duration.

Another limitation that arises as the intensity is increased is when the electron

ⁱⁱⁱ $\frac{\partial f}{\partial t} + \mathbf{v} \cdot \nabla f + \frac{q}{m}(\mathbf{E} + \mathbf{v} \times \mathbf{B}) \cdot \frac{\partial f}{\partial \mathbf{v}} = 0$ [13].

quiver (oscillatory motion) becomes comparable to the thermal velocity: the same reduction in collision frequency occurs due to the oscillatory velocity of the electron [25]. The effective collision frequency can be written as

$$\nu_{eff} \approx \nu_{ei} \frac{v_{te}^3}{(v_{os}^2 + v_{te}^2)^{3/2}} \quad (3.6)$$

To give an idea where this effect starts to become prominent, consider the following example. For a temperature of 1 keV, the thermal velocity is roughly 0.05 c, which corresponds to an oscillatory motion provided by an irradiance $I\lambda^2 \geq 10^{15} W cm^{-2} \mu m^{-2}$ [25]. Therefore in the high-intensity regime absorption is *not* dominated by collisional processes, and other phenomena tend to dominate. The most prominent is resonance absorption [25].

3.6 Resonance Absorption

Resonance absorption was first studied in the 1970s and 80s with two-dimensional particle-in-cell (PIC) codes [52, 53]. This absorption occurs for p-polarized light, and is present when an incident laser strikes a plasma at nonzero angle of incidence [34]. There is a singularity in the magnitude of the oscillating electric field in the plasma, and this electric field can drive an electron plasma wave. The original laser wave tunnels through to the critical surface, then generates a plasma wave that grows over several laser periods [25]. The plasma wave can then be damped in a collisional or collisionless manner, so that this mechanism will be present even at low collision frequencies [34].

At very high intensities, the plasma waves can be damped by particle trapping and wave breaking [25]. Particle trapping is when the amplitude of the field is strong

enough that the potential experienced by the particle is greater than its thermal energy, preventing it from moving outside the wave's trough [13]. The trapped particles can then extract energy from the wave. Wavebreaking is like ocean waves on a beach, when high-amplitude waves disperse rapidly, converting most of their energy into thermal energy. This absorption mechanism is dominant over inverse bremsstrahlung for high plasma temperatures (which correspond to higher laser intensities), long wavelengths (which give a lower critical density) and short plasma scale lengths [34]. Under the right conditions, resonance absorption can account for up to roughly 50% of the total absorption [34]. The angular dependence is given approximately by [25]

$$\alpha_{ra} = \frac{1}{2}\phi^2(\xi) \quad (3.7)$$

where α_{ra} is the absorption coefficient, $\phi(\xi) \approx 2.3\xi \exp(-2\xi^2/3)$ and $\xi = (kL)^{1/3} \sin \theta$, with θ angle of incidence [25] (plotted in Figure 3.1). It is clear from Figure 3.1 that resonant absorption is maximized at some intermediate angle of incidence, when the transverse fields are partially aimed into the plasma.

The main observable difference between inverse bremsstrahlung heating and resonance absorption is that inverse bremsstrahlung heats all electrons equally, whereas the absorption of the plasma wave results in a minority of electrons gaining a large amount of energy (so called “hot electrons”) [34].

The equations given above cannot describe the generation of hot electrons. For precise details, kinetic approaches are needed such as the Vlasov equation or PIC simulations [25]. Even then, resonance absorption modeling does not adequately explain absorption for very steep density gradients. This is because in a sharp profile the gradient is steep enough that adequate field growth over several periods at resonance cannot occur. For these plasma profiles, a new mechanism occurs.

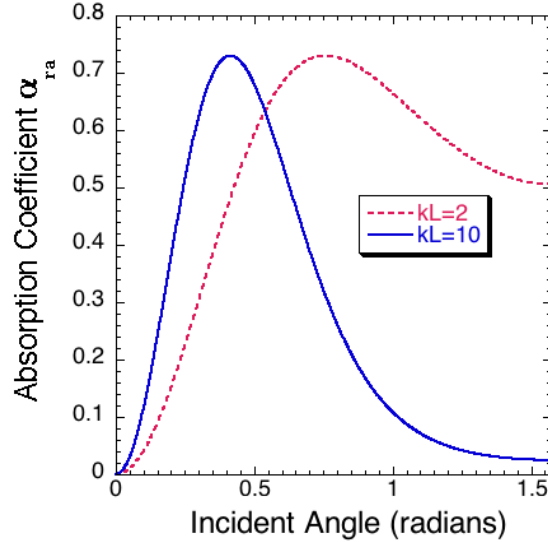


Figure 3.1: A plot of the resonant absorption coefficient versus angle for two different values of kL , illustrating that it is maximized at an intermediate angle of incidence.

3.7 Vacuum Heating

At a steep or abrupt interface between vacuum and a plasma, the electrons near the edge are directly exposed to the laser fields [25]. These electrons experiencing the powerful electric fields can be dragged out violently beyond the Debye sheath length. When the oscillating field switches directions, these electrons are then shot back into the plasma.

If the plasma is very overdense, Debye shielding limits the laser field penetration to a very thin skin depth. Thus the electron experiences no field once injected into the high density region and moves as a nearly-free particle through the plasma, where it can then be absorbed through collisional effects [25]. Brunel was the first to describe this mechanism in 1987, and thus vacuum heating is sometimes called the Brunel effect [55].

To first-order, this mechanism can be modeled by a “capacitor approximation”

[25] where the magnetic field is ignored and the electric field pulls electrons in an oscillatory manner from their equilibrium positions [25]. A standing wave is set up, and we can solve for the final velocity of the electrons and assume they are all absorbed. Adding some corrections to account for imperfect field reflection and adding relativistic speed limitation, the absorption coefficient is given by [25]

$$\alpha_B = \frac{1}{\pi a_0} f [(1 + f^2 a_0^2 \sin^2 \theta)^2 - 1] \frac{\sin \theta}{\cos \theta} \quad (3.8)$$

where $a_0 = v_{os}/c$, $f = 1 + (1 - \alpha_a)^{1/2}$ (field amplification factor), α_a is the fractional rate of absorption [25]:

$$\alpha_a = \frac{4}{\pi} a_0 \frac{\sin^3 \theta}{\cos \theta} \quad (3.9)$$

and v_{os} is defined as

$$v_{os} = \frac{eE_0}{m\omega}. \quad (3.10)$$

The absorption coefficient is plotted in Figure 3.2. Similar to resonance absorption, this heating mechanism is largest at intermediate grazing incidence angles, when the laser field is directed into the plasma. For high intensities and short scale-lengths, the absorption is limited to about 10-15%, but intermediate intensities can reach as high as 70% [25]. The above model does not demonstrate this limit, but there are in fact surface DC currents that are set up by the non-zero magnetic field, which can deflect the returning electrons and prevent them from penetrating the plasma. Brunel proposed two geometrically opposed lasers to produce cancelation of the surface currents [25] (confirmed in PIC simulations). The transition region from resonance absorption to vacuum heating, however, is fairly complex (investigated by Gibbon & Bell in 1992) [25].

PIC simulations with mobile ions give different behaviour [25]. The strong space-

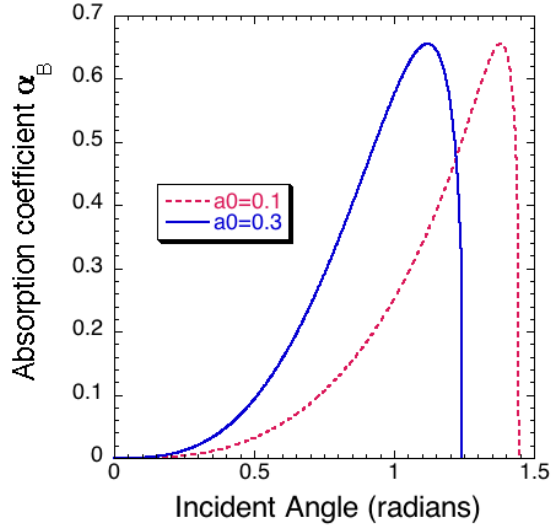


Figure 3.2: A plot of the Brunel absorption coefficient versus angle for two different values of a_0 , illustrating that it is maximized at an intermediate grazing incidence angle.

charge fields generated by the removed electrons tend to pull out an “ion shelf” that can significantly alter the absorption process [25]. Ion effects will be discussed later, but first we move to an effect similar to vacuum heating, which is produced by the magnetic field rather than the electric field.

3.8 $J \times B$ Heating

Like vacuum heating, in this mechanism electrons near the surface of a vacuum-plasma interface or steep gradient are accelerated by the laser field. In this case, however, the driving term is the $v \times B$ term of the Lorentz force. For a linearly polarized wave, for example, there is a resulting longitudinal force term (i.e. into the plasma) [25]:

$$f = -\frac{m}{4} \frac{\partial v_{os}^2(x)}{\partial x} (1 - \cos 2\omega t) \quad (3.11)$$

The first term is the ponderomotive force (proportional to the gradient of the squared electric field, basically when a high-frequency field induces a slow timescale force [34]. This will be discussed shortly.). The second term produces an effect very similar to the oscillating electric field in vacuum heating [25]. Contrary to vacuum heating, however, this force will be maximized at normal incidence. This mechanism contributes a small portion to the absorption mechanism, but increases with laser intensity and was shown by Gamliy and Dragila to produce very anisotropic plasma distribution functions [25]. The current understanding is that $J \times B$ heating is dominant at relativistic intensities [25].

3.9 Hole-Boring

Hole-boring occurs when the light pressure is greater than that exerted by the plasma [25]. Essentially it is a result of this pressure imbalance, and the laser pulse pushes the plasma inwards with a maximum strength at the center of the spot. There is then a density discontinuity that travels into the target (called a “bow-shock”) [25].

Hole-boring, or any surface deformation for that matter, modifies the interaction geometry [25]. As we saw previously, the angle of incidence will determine what mechanism is dominant, and so hole-boring can arrange so that vacuum heating occurs along the sides of the hole, and $J \times B$ heating can occur at the end [25]. It occurs for extreme irradiances (greater than $10^{18} \text{Wcm}^{-2} \mu\text{m}^{-2}$) and tightly focused light. The hole can generally extend several wavelengths deep over sub-ps timescales [25].

Typically hole-boring is detected by red-shift of the reflected light [25]. Hole-boring was first studied by Wilks in PIC simulations in 1992 [56] where an expression

for boring velocity of

$$\frac{u}{c} = \left(\frac{n_c}{2n_{pe}} \frac{Zm}{M} \frac{I_{W/cm^2} \lambda_\mu^2}{1.37 \times 10^{18}} \right)^{1/2} \quad (3.12)$$

was given as an estimation by balancing the momentum flux of mass flow with the light pressure. n_c is the critical density, n_{pe} is the electron plasma density, u is the ion velocity, M the ion mass, and Z the charge state. The absorption through generation of the moving density discontinuity from hole-boring becomes important as a major absorption mechanisms at intensities above $10^{20} W/cm^2$ [43]. Such intensities are possible by focusing the latest generation of petawatt (PW) laser pulses [43].

3.10 Laser Beam Self-focusing and Filamentation

When we consider that the relativistic oscillation of an electron in a high-intensity field gives rise to a fluctuating mass, some other effects also arise [30]. A high-intensity laser beam self-focuses due to the induced relativistic increase in refractive index on axis of the material through which it propagates, and is more severe if there are any nonuniformities in the wave front. The beam then splits into several parts with higher intensities than the initial pulse [30]. It originates in the dispersion relation, which is altered with the electron mass oscillation in such a way that the phase velocity of the beam is a minimum where the intensity is maximized [30]. The wavefront then flexes as different phase speeds cause it to bend, and the beam acts as a lens for itself, focusing and breaking into filaments [30]. Again, although we will not discuss *all* laser-plasma interactions, this effect changes the intensity of the beam and correspondingly the dominant absorption mechanism(s), the electron energy and the spectra produced.

3.11 Ion Beams and Hydrodynamic Expansion

For sufficiently high-strength fields or for picosecond timescales, ions can no longer be treated as fixed (requires fields strengths of order GV/m) [25]. The ion motion is generally driven by space charge fields set up by the electrons, when many electrons are displaced from their initial positions [25]. The slower inertial response of the ions is due to their much larger mass ($M/m \geq 1800$), causing a much smaller quiver velocity with respect to the electrons [25].

Generally, hot electrons escaping from the plasma form a Debye sheath which tugs on the ions. The strength of the Coulomb field generated by the hot electrons is directly proportional to their temperature [25]. The field can be shown to exhibit the following dependence [25]:

$$E \approx \frac{T_h}{L_h} \quad (3.13)$$

where L_h is the density scale-length of hot electrons and T_h is their temperature. The momentum equations for ions can be written as

$$\frac{\partial v_i}{\partial t} + v_i \frac{\partial v_i}{\partial x} = -C_h^2 \frac{1}{n_i} \frac{\partial n_i}{\partial x} \quad (3.14)$$

where $C_h = (ZT_h/M)^{1/2}$ is the hot ion sound speed. The maximum ion speed can be shown to be

$$v_{max} = C_h [1 + 2 \ln(\omega_{pi0} t_f)] \quad (3.15)$$

where ω_{pi0} is the initial ion plasma frequency at the initial density and t_f is the time of interaction with the hot electron field [25]. This equation reveals that even highly relativistic electrons will generate ions that are still non-relativistic (eg. $T_h = 10$ MeV, $C_h \approx 0.1$ c) [25]. To generate relativistic protons, for example, requires $I\lambda^2 \geq 10^{24} W cm^{-2} \mu m^{-2}$ [25], so the general treatment of considering only electron

expansion in the plasma is fairly reasonable for most intensity regimes.

Experiments for fast-ion generation from ps and subps pulses were carried out by the Rochester group and Meyerhofer et al. showed, in 1993, that p-polarized light influenced the ion energies, demonstrating that grazing incidence resonance absorption was a dominant mechanism [25]. Further work in this area, generating proton beams adequate to heat pellet cores in fast ignition fusion, led to the pursuit of the proton fast ignition (PFI) concept [25].

3.12 Cold Return Current

As mentioned previously, hot electrons are generated in high-intensity absorption. These electrons can flow into the target or along the surface, in either case generating a very strong magnetic field [25]. This flow is eventually balanced by an electronic return current in the background plasma [25].

Hannes Alfvén's original work on the motion of cosmic rays in interstellar space [57] investigated how the self-generated field of a given current will eventually lead to particles turning back toward the source. This phenomenon sets an upper limit on the allowed current of a wave propagating in a vacuum [58], known as the Alfvén limit:

$$J_A = \frac{4\pi}{e\mu_0} p \quad (3.16)$$

where e is the electron charge and p is the electron momentum. The following estimates for electron beam currents relevant to fast ignition follow from an article by J.R. Davies [58]. If the coupled energy for ignition is 3 kJ, with a mean hot electron energy of 1 MeV and a beam duration of 10 ps impinging upon a DT fuel density of $3 \times 10^5 \text{ kg m}^{-3}$ (300 g/cc), the required ignition current is 0.3 GA (as calculated by

Tabak et al. [6]). Atzeni carried out a more detailed calculation [59] and estimated a higher ignition energy of 18 kJ and a longer beam duration of 20 ps, resulting in a net raised current requirement of 0.9 GA. The Alfvén limit for these 1 MeV electrons is 47.5 kA, 1.9×10^4 lower than the requirement [58]. This initially appears to be a show-stopper for fast ignition, but in fact this limit is on the *net* current, not the forward current. Thankfully in fast ignition there is a background plasma which can provide a return current.

The return current is, however, still limited. A calculation on the limit for fast ignition follows from [58]. Since the beam current is significantly higher than the Alfvén limit, almost all of the forward current density \mathbf{j} must be balanced, so $j_p \approx j$. Faraday's law predicts the growth of the magnetic field as

$$\frac{\partial \mathbf{B}}{\partial t} = \nabla \times \eta \mathbf{j} \quad (3.17)$$

Working with the assumption of constant resistivity and current density, the magnetic field is approximately

$$B \approx \frac{\eta j t}{R} \quad (3.18)$$

where R is the beam radius of a cylindrical beam. The net current J_{net} is $2\pi R B \mu_0$ with a beam current J of $\pi R^2 j$, giving

$$J_{net} \approx 2 \frac{t}{t_D} J \quad (3.19)$$

where

$$t_D = \frac{\mu_0 R^2}{\eta} \quad (3.20)$$

is the characteristic time for the decay of the return current. The assumed current

balance in the target is only valid much earlier than this time, and the time at which the net current breaks the Alfvén limit, the magnetic inhibition time, is [58]

$$t_I \approx \frac{t_D}{2J/J_A}. \quad (3.21)$$

With a radius of 20 μm , Spitzer resistivity at the ignition T of 10 keV ($\approx 1 n\Omega m$), the current decay time (t_D) is 50.3 μs [58]. Taking J/J_A to be at least 1.9×10^4 , the ratio of the inhibition time to the beam time (t_B) is ≈ 0.65 , which means the beam cannot be maintained for the required time. A more rigorous derivation gives results which are qualitatively similar [58]. The implication of the Alfvén limit is to prevent hot electron beam propagation and alter the fast ignition requirements originally envisaged by Tabak et al. [6] and later Atzeni [59]. Davies proposed the following methods to meet the ignition requirement: increasing the hot electron temperature by decreasing the beam radius and duration, using multiple beams, and using annular beams which have a higher Alfvén limit.

The Alfvén limit imposed by magnetic fields is one hurdle to hot electron propagation, but in the above derivation it was assumed that the target had enough background charge to balance the forward-going current. That assumption is not necessarily correct, and can be investigated by looking at energy balance and mean free paths of electrons.

The mean free path is based on collisional energy losses, and no other effects are included. A simple estimate of the current-generated magnetic field is as follows from [60]. We assume a pulse length τ of 1 ps, an absorbed laser intensity I_{abs} of 10^{18} W/cm^2 , a laser wavelength of 1 μm and a spot diameter of $2r_{spot}=30 \mu m$. If the target is aluminum with a solid density of 2.7 g/cc, the absorbed energy is 7.1 J (if 100% absorbed) and the characteristic hot electron temperature (assumed to

be approximately Maxwellian) is $T_0=200$ keV [61]. The number of electrons heated during the pulse is then 1.5×10^{14} , with a characteristic time between collisions of $\tau_{ee}=4.6$ ps and a collisional stopping distance in Al of $215 \mu m$. The characteristic time for angular scattering is inversely proportional to Z , i.e. τ_{ee}/Z and the fast electron RMS range is $R_e = 60 \mu m$. The current carried by the hot electrons is then 24 MA, and if one assumes the hot electrons are entering in a cylinder of the same diameter as the spot size, then the magnetic field at the cylinder surface is $B_{cyl}=3200$ MG. If this magnetic field penetrates $60 \mu m$ into the target (R_e), then the energy in the magnetic field would be on the order of

$$\left(\frac{B_{cyl}^2}{2\mu_0}\right) (\pi r_{spot}^2) R_e (2 \log (R_e/r_{spot})) = 5kJ. \quad (3.22)$$

Obviously from energy arguments this magnetic field cannot be generated. It therefore must be opposed by an electric field which confines the electrons closer to the surface of the target, or the target itself must provide an opposing return current so that an energetically impossible magnetic field is not generated. We have the same requirement as earlier where $j_{net} = j_{fast} + j_{thermal} \approx 0$. The continuity equation for fast electrons, using a maxwellian distribution, gives [60]

$$\frac{\partial n}{\partial t} = \nabla \cdot \left(\frac{\sigma T_0}{en} \nabla n \right) \quad (3.23)$$

where n is the number density of hot electrons, and σ is the conductivity of the thermal background plasma. The dependence on the cold electron density is expressed indirectly through σ . Equation 3.23 is essentially a diffusion equation with a diffusion coefficient $D = \sigma T_0/en$. The number density of hot electrons increases as the pulse arrives at the target (linearly if a top hat pulse [60]). Therefore at the beginning

of the pulse the hot electrons penetrate far into the target because their number density is relatively small, and the diffusion coefficient is large. The equation for the characteristic penetration length can be written as [60]

$$z_0 = \left(\frac{T_0}{200 \text{ keV}} \right)^2 \left(\frac{\sigma}{10^6 \Omega^{-1} m^{-1}} \right) \left(\frac{I_{abs}}{10^{18} \text{ W cm}^{-2}} \right)^{-1} 12 \mu m \quad (3.24)$$

The conductivities measured experimentally (from 0.5×10^6 to $1 \times 10^6 \Omega^{-1} m^{-1}$, measured by Milchberg et al [62]) give a penetration distance of approximately $10 \mu m$, which suggests that the target is incapable of supplying the balancing return current, and that the penetration of hot electrons is as much as six times less than what would be predicted collisionally. The above equation is the penetration during the laser pulse, and it can be shown that the adiabatic expansion into the target after the pulse is insignificant compared to z_0 , since the penetration distance increases as $L \propto t^{3/5}$, and the electron temperature goes as $T \propto t^{-2/5}$ [60].

The resistivity is the key parameter here, and an accurate value or model for the resistivity must be used depending upon the experiment. Simulations that assume a preheated plasma might not, therefore, accurately reflect experimental results since the preheated plasma has a disproportionately large conductivity [60]. Many schemes are under investigation to exploit the effects of resistivity on hot electron transport. One such scheme is called a magnetic switchyard, where structured filaments of different materials are used and the effects of resistivity gradients exploited in order to allow the hot electron beam not only to be collimated, but to penetrate further into the target [63]. A simulation of the scheme can be seen in Figure 3.3, where preliminary investigations seem promising. It remains to be seen whether such a target, once constructed, can survive the fuel assembly during the long pulse compression.

Resistivity effects on hot electrons are a very current topic, with recent work

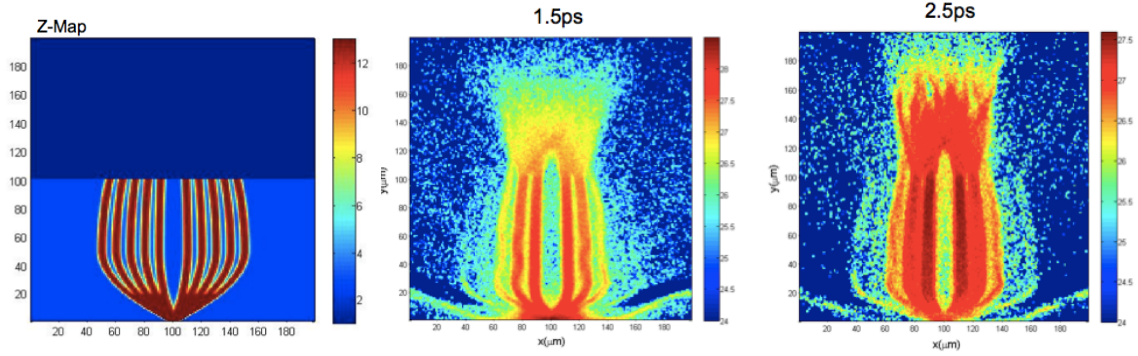


Figure 3.3: The magnetic switchyard concept. The plot on the left is initial electron density, and the middle and right plots are hot electron densities at different times during the pulse [63].

studying the impact on electron transport [64] (the KB microscope was in fact used during this experiment). The preliminary results indicate that an increase in Z lowers the net energy of hot electrons, but that different Z materials exhibit no observable trend for spot size. This supports the notion that resistive fields play a larger role than pure scattering effects [64], and further simulations are underway.

3.13 Ionization

The relative population densities of various ion levels in thermal equilibrium are given by the Saha equation [65]:

$$n_{0z} = \frac{n_{0z+1} n_e}{2} \frac{g_{0z}}{g_{0z+1}} \left[\frac{h^2}{2\pi m_e kT} \right]^{3/2} \exp \left[-\frac{E_{Iz}}{kT} \right] \quad (3.25)$$

where n_{0z} and n_{0z+1} are the number densities of ions in ionization states z and $z+1$, respectively. g_{0z} and g_{0z+1} are the statistical weights assigned to z and $z+1$, respectively, based on the number of degenerate states in each level. It can be derived from the Einstein transition probabilities, the Planck function and the Maxwell-Boltzmann

distribution [66]. This is an accurate description of the ionization state of a plasma in what is called Local Thermal Equilibrium (LTE), where all processes are more or less in balance, and the collision frequency is high enough that any imbalances are negligible [67]. There are minimal radiation losses and collisional transitions provide the primary pathways for energy transfer. This is the simplest way to view plasma ionization. On the other extreme is the Coronal model, which applies for relatively sparse plasmas where collisional transitions are minimal and radiation dominates.

In the middle regime where both collisional and radiation transitions occur, a new more general model is used. The non-local thermal equilibrium (non-LTE) model is also called a collisional-radiative (CR) model. The population distribution is calculated from a balancing of collisional processes which are local and radiative processes which are non-local [65]. The output of a CR code is heavily influenced by the quality of the atomic data [65]. CR modeling is used predominantly in X-ray spectroscopy for laser-produced plasmas, which makes it relevant for the KB microscope, since it images such a broad spectrum of X-ray energies. It is significantly more difficult to calculate since the population distribution at any point is not determined by bulk plasma parameters like the other two models [65]. For example, population spatial gradients can develop even though there may not be gradients in temperature or density. For some of the equations used in the CR model, see Chapter 6.

In many simulations and models of laser-plasma interactions, the ionization state of the plasma is fixed for the duration of the interaction. In high-intensity experiments, however, this is inaccurate since the absorbed laser energy is significant even during the pedestal of the pulse. A more accurate simulation will include dynamic ionization, which computes the ionization states at each time step and simulates the physics accordingly. The effects of dynamic ionization are on the forefront of current research primarily because it is complex and computationally intensive to implement.

3.14 Heating

As described in Section 2.5, the hot electrons are heated by the ponderomotive force of the laser, and here we describe the relativistic derivation from [28]. The equation of motion for an electron fluid element in a plasma, near the vacuum plasma interface is

$$\frac{\partial \vec{p}}{\partial t} + \vec{v} \cdot \vec{\nabla} \vec{p} = -e \left[\vec{E} + \frac{\vec{v} \times \vec{B}}{c} \right]. \quad (3.26)$$

where $\vec{p} = \gamma m_0 \vec{v}$ and

$$\gamma = \frac{1}{\sqrt{1 - \frac{\bar{p}^2}{\gamma^2}}} \quad (3.27)$$

with $\bar{p}^2 = p_{osc}^2/m_e^2 c^2$. Writing Equation 3.26 in terms of \bar{p} and a vector potential \vec{A} allows for the derivation of the equation for the longitudinal electron fluid momentum:

$$\frac{\partial \vec{p}_L}{\partial t} = e \vec{\nabla} \phi - m_0 c^2 \vec{\nabla}^2 (\gamma - 1) \quad (3.28)$$

The first term is an electrostatic force term, and the second is due to the relativistic ponderomotive force. If it is assumed that the hot electrons gain their longitudinal energy from this ponderomotive potential, then their temperature scales as [28]

$$T_{hot} \approx \left(\sqrt{1 + \frac{I_{W/cm^2} \lambda_{\mu m}^2}{2.8 \times 10^{18}}} - 1 \right) 511 \text{ keV}. \quad (3.29)$$

This general dependence that $T_{hot} \propto (I\lambda^2)^{1/2}$, called ponderomotive scaling, is often used in calculations estimating hot electron temperature, although it doesn't completely reproduce the results from experiments.

A compilation of results obtained on the CPA beamline of the VULCAN Nd:glass laser at 1053 nm revealed a different intensity scaling known as Beg scaling [61]. The

pulse energies on target were up to 30 J, and pulse lengths from 700 fs to 1.3 ps. The general dependence is $T_{hot} \propto (I\lambda^2)^{1/3}$, and the full least-square fit to their data for maximum ion energy (which is directly related to hot electron temperature) is

$$E_{max} = 1.2 \pm (0.3) \times 10^{-2} [I/W \text{ cm}^{-2}]^{0.313 \pm 0.03} \text{ keV}. \quad (3.30)$$

This scaling is also used frequently in estimations of hot electron temperatures. However, unlike ponderomotive scaling no theoretical basis or derivation has yet been provided to justify why the hot electron temperature should exhibit such dependence.

Separate from the heating of the hot electrons for fast ignition is the effect of the background plasma temperature through which the electrons will travel. The deposited energy in the target at high intensities results in a hot plasma, which has different emission spectra than a cold atom. Simulating this laser-produced plasma emission is challenging because the plasma is in a transient non-equilibrium state. There are also two electron fractions (background plasma and hot electrons) in a non-equilibrium state, and this requires a wide range of computed plasma emission energies in whichever CR model is applied [68].

There are several emission mechanisms which play a role in the final observed spectra. Spontaneous radiative decay is probably the most well-known, with a line transition of an excited electron falling from a higher energy state to a lower energy state. Autoionization, where an atom ejects an electron, can occur when an electron drops down to fill a hole in the electron shell transferring its energy to an escaping electron (known as the Auger effect) [68]. Electron collisions play a large role in the above processes and particularly for hot electron beams. Hot electrons also generate strong fields which can lead to heating of the target [69]. Recombination of a free electron into an atomic shell is another emission process of importance [68].

Excited electronic states of atoms or ions give rise to a whole new series of line transitions which are slightly shifted from the original cold spectra, and these are called satellites [68]. The appearance of these satellites is the most significant factor when a plasma is heated, resulting in a reshaping of the spectrum as seen in Figure 3.4. Another major effect is opacity (resonant self-absorption by the target), which can alter the line shape significantly as well.

A significant advantage of the KB microscope over the traditional Bragg crystal imager is its insensitivity to such changes in lineshape and emission shifts due to plasma heating. The broadband nature of the platinum mirrors employed means that it will image emission from a 100 eV plasma nearly just as well as a cold plasma. In contrast, the Bragg crystal imager has a bandwidth on the order of 10 eV, and such high temperature plasmas will emit predominantly outside the bandwidth of the crystal imager, and a weaker image will be formed [70]. The window of energies viewable by a Bragg crystal imager is shown in the vertical lines in Figure 3.4. As laser systems move closer to full-scale ignition shots, the KB microscope is more suitable for the task of imaging the emission from the increasingly hot plasmas.

3.15 Electron Scattering

The scattering or divergence of a hot high current electron beam in a solid target is not entirely understood because of the multitude of physics processes that are involved as well as the computational limitations restricting accurate simulation. However, in the past decade or so of research some progress has been made, but it is still not a complete picture.

A preliminary estimate of the divergence of a beam of hot electrons is found by applying conservation of momentum in the target plane for a normally-incident beam.

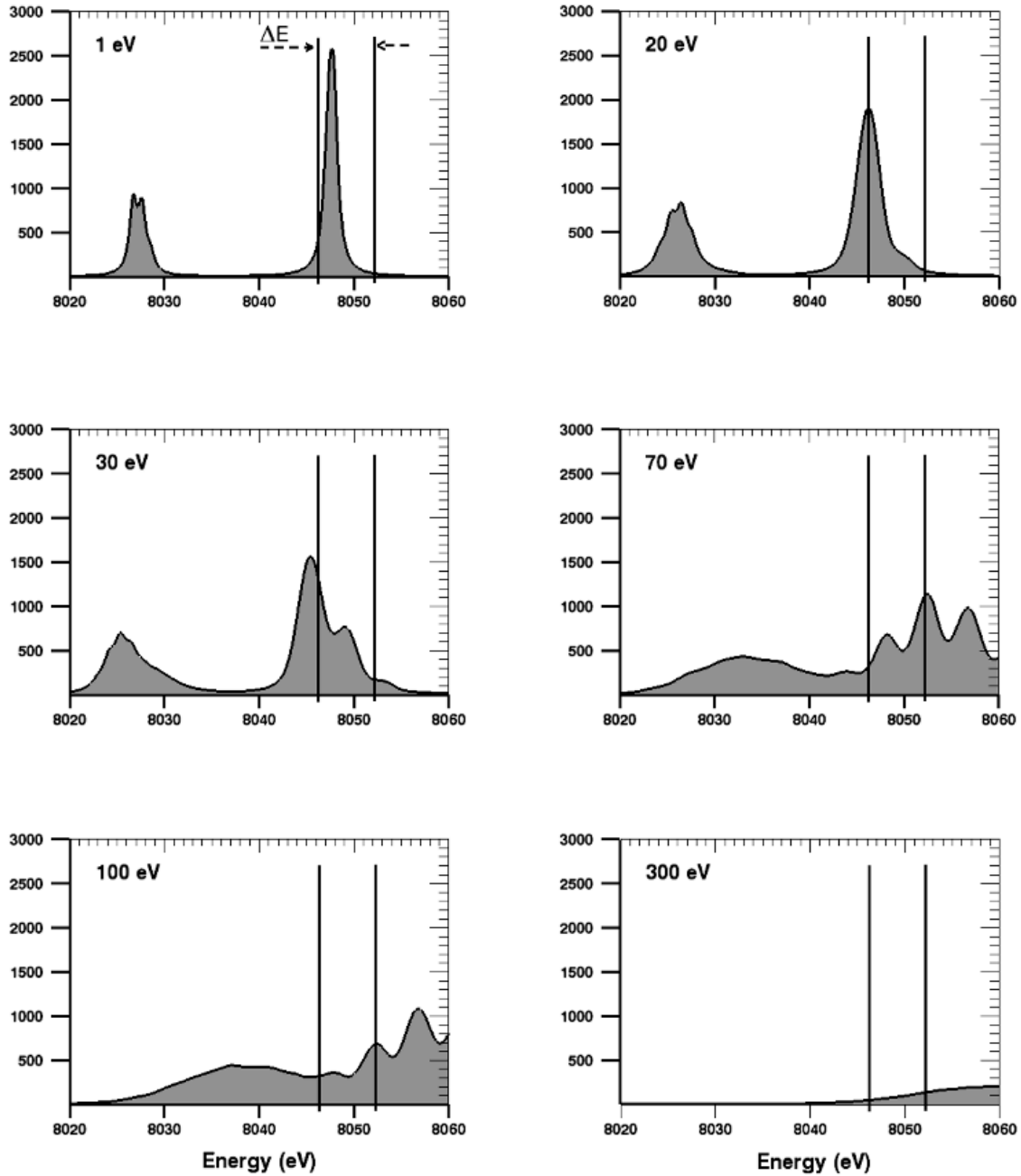


Figure 3.4: The spectral changes in a plasma with temperature. The vertical bars represent the energy aperture of a typical Bragg crystal imager used in Fast Ignition experiments [70]. The vertical axes are in arbitrary units.

In such a case the electron ejection angle is related to its energy by

$$\theta = \tan^{-1} \sqrt{2/(\gamma - 1)} \quad (3.31)$$

where γ is the relativistic Lorentz factor [71]. This equation (ponderomotive dispersion) predicts a decrease in electron divergence with energy.

An additional effect missed by ponderomotive dispersion is the effect of the fields of the reflected laser, especially in a solid target. In addition for a high current beam, there are perturbations in the electron trajectories that can grow via the Weibel instability [13] producing large magnetic field modulations on a micron scalelength. Some simulations use random magnetic fields in a thin layer behind the absorption region to explain the observed electron divergence [71]. Such a model is accurate in reproducing the local electron divergence in the laser plasma interaction region, but cannot completely account for the observed macroscopic divergence throughout the larger solid target.

The profile and non-uniformity of the laser spot also results in electrons being accelerated with a velocity component transverse to the beam depending on their radial position within the focal spot [71]. This makes it difficult for the self-generated magnetic fields to collimate the hot electron beam, and many simulations underestimate the energy required to achieve ignition for a given electron beam since they do not accurately account for this effect.

The most current understanding is that the Weibel instability as well as the transverse ponderomotive force are responsible for hot electron divergence [71]. In order to control the Weibel instability and minimize divergence, high electron densities and low intensities should be used. Ironically, this tends to increase the collisionality of the plasma, but as it turns out the field effects are much stronger for divergence.

The scalelength of preplasma is significant as well, since the preplasma tends to make the Weibel instability stronger. Additionally, it tends to broaden the sources of self-generated magnetic fields, further reducing any collimation effects. Energy estimates for Fast Ignition based on this newly-considered transverse ponderomotive force are under development [71].

Chapter 4

X-ray imaging Background and Diagnostic Challenges

4.1 X-ray Reflection

In 1922, Compton discovered that X-rays could be reflected at grazing incidence [72]. It can be understood via total internal reflection, but in the case of X-rays, the phenomenon occurs externally and so is termed total external reflection. We begin with Snell's Law [73]:

$$n_1 \sin \theta_1 = n_2 \sin \theta_2 \tag{4.1}$$

where θ is the angle relative to surface normal. Total internal reflection occurs when the transmitted angle is $\pi/2$, and if we assume the incident medium number 1 is air, we get

$$\sin \theta_1 = n_2 \tag{4.2}$$

If we write in terms of the grazing angle of incidence $i = \pi/2 - \theta_1$, and recall the formula for the refractive index of a plasma, we get

$$\sin(\pi/2 - \theta_1) = \cos i = n_2 = \sqrt{1 - \frac{\omega_p^2}{\omega^2}} \quad (4.3)$$

Using, $\omega = 2\pi c/\lambda$ where c is the vacuum speed of light, and the definition of plasma frequency $\omega_p^2 = n_e e^2 / (\epsilon_0 m_e)$ [13] yields a condition for the the cutoff wavelength that will be reflected:

$$\cos^2 i = 1 - \frac{\omega_p^2}{\omega^2} \quad (4.4)$$

$$\sin^2 i = \frac{n_e e^2}{\epsilon_0 m_e \omega^2} \quad (4.5)$$

$$\sin^2 i = \frac{n_e e^2 (\lambda)^2}{(2\pi c)^2 \epsilon_0 m_e} \quad (4.6)$$

$$\Rightarrow \lambda = \frac{2\pi c i}{e} \sqrt{\frac{\epsilon_0 m_e}{n_e}} \quad (4.7)$$

where we have used the small angle approximation $\sin i \approx i$ which is valid because we are working at grazing angles of incidence. This gives a condition for energies or wavelengths of light that are reflected at a given angle of incidence. Since $\lambda \propto i$ we see that we can reflect larger wavelengths for larger angles of incidence. However, as we go to higher and higher energy X-rays (shorter wavelengths), we have to go to increasingly small angles of incidence. Typically this effect is compensated by maximizing the electron density to increase the angle of incidence to a point where the solid angle and throughput of the X-ray mirror reaches an acceptable level. It is for this reason that X-ray mirrors are typically coated with a high-density, high-Z material such as iridium, platinum or gold [40]. The material density is typically used in calculating the reflectivity or the critical angle, which is a good first-order

approximation. However, a more exact calculation takes into account some tightly bound K-shell electrons which are not free. This effect is taken into account in tabulated indices of refraction.

4.2 Imaging X-rays

X-ray imaging is very different from optical imaging. The reason is that, for most materials, the X-ray refractive index, n , is less than one by a factor δ typically of the order of 10^{-4} to 10^{-5} .

$$n = 1 - \delta \tag{4.8}$$

For example, nickel has $\delta=2.4\times 10^{-5}$ at 0.154 nm, 1.4×10^{-2} at 4.48 nm [74].ⁱ Because harder and harder X-rays (i.e. more energetic) are being used as a hot electron diagnostic (in order to be able to pass through denser plasmas), the option of using longer wavelength X-rays is out. At such refractive indices, a theoretical X-ray lens would have a focal length so large that a very thick graded index lens would be required to bring the focal length down to the order of meters [41].

Bragg reflection is one option that applies for light of any wavelength; it is constructive interference that occurs at a specific angle for a given crystal spacing [73]. By nature it is very sensitive to angle, but the reflection is efficient enough (typically of the order of a few percent [75]) for X-rays. Crystals such as highly-oriented pyrolytic graphite (HOPG) [40] or crystal quartz are used in K_α imagers, normally bent into spherical shape to enable focusing [24]. However, the angular dependence implies a very narrow bandwidth of reflected energies, such that if the target tracer layers are ionized, the resulting shift in the K_α line will not be reflected, leading to incorrect detection of K_α yield [24].

ⁱ $\delta \propto \lambda^2$, but absorption is proportional to λ^3 , making larger δ challenging to work with [41].

Another technique that has been employed is that of pinhole imaging. Smaller pinholes enable greater spatial resolution at a sacrifice of brightness [41]. The manner by which data are extracted is by using Ross filter pairs that have K-edges above and below the desired wavelength region [76] as shown in Figure 4.2, leading to images which are then subtracted to obtain the difference signal of interest. The trouble with this technique is that the signal-to-noise ratio (SNR) is typically less than desired.

An example is given in Figures 4.1-4.4. The pinhole images were produced using a 10 X 10 array of 30 μm Ta pinholes which were 500 μm thick. Some pinholes had 22 μm Ni filtering, and some had 25 μm Co filtering to produce a Ross filter pair. The image magnification was 4.7. The target was a 25 μm copper foil shot with 158.8 J in 0.7 ps and 10 μm focal spot size on the Titan laser. There was 6 mJ of prepulse energy in 1.5 ns, and the target was viewed from the front. Aside from the Ross filter pair the pinholes were filtered with a 50 μm mylar blast shield, 500 μm Be window, and 25 μm Al foil. A sample lineout of 5 pixel width is shown in Figure 4.3, illustrating the signal difference arising from the difference in filtering. Upon subtracting the aligned lineouts, the final image in Figure 4.4 is an image of the band between the K-edges of Ni and Co, but as is evident the noise is amplified undesirably.

Other X-ray imaging techniques include Fresnel-Zone-Plates (FZPs) which reach a resolution of 30 nm in the hard X-ray region [77] but are strongly chromatic, which is disadvantageous in such thermally-shifted plasmas particularly if the degree of lineshift is unknown. Aspherical reflecting surfaces provide perfect imaging, but are very hard to manufacture (such as the Wolter microscope which is aspheric and axially symmetric [78]).

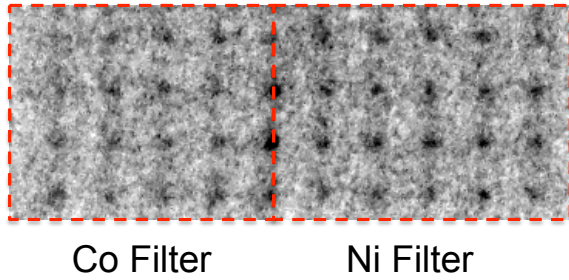


Figure 4.1: Differentially filtered images obtained using an X-ray pin-hole camera during a Titan experiment. (2009.08.13.shot#2)

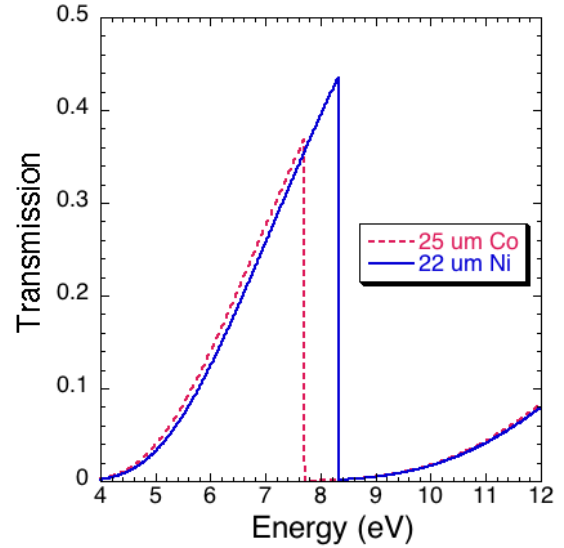


Figure 4.2: The transmission curves for a Ross filter pair designed for Cu K_{α} .

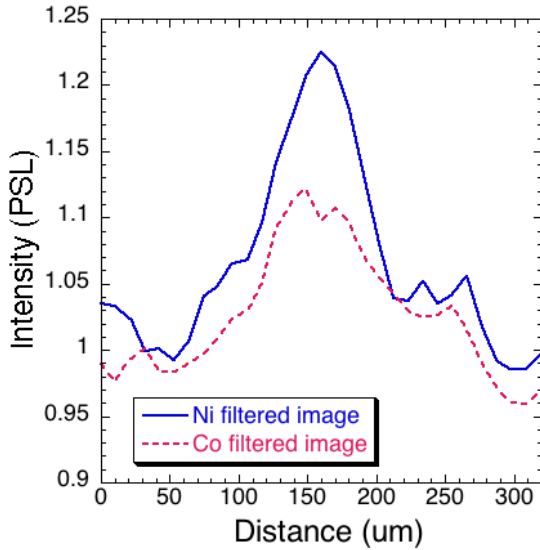


Figure 4.3: Overlapped lineouts of the different filtered regions. Linewidth=5 pixels.

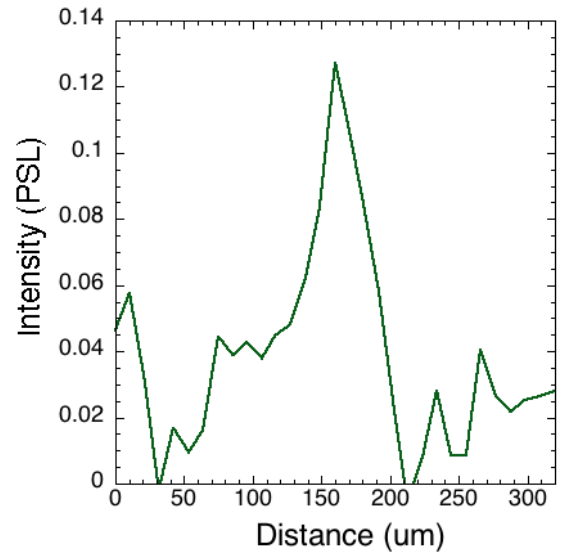


Figure 4.4: The lineout obtained by subtracting the two different filtered regions.

4.3 KB Microscope

The alternative solution, which is the type this thesis focuses on, is grazing-incidence reflection. In 1948, P. Kirkpatrick and A.V. Baez published a paper exploring the formation of X-ray images by using curved surfaces at grazing incidence [41]. In the paper they highlight how there is a critical angle of total reflection as given by Equation 4.7.

Kirkpatrick and Baez showed that the focal length of a spherical mirror in the meridian plane (plane containing the radius of curvature at the point of incidence) is

$$f_m = \frac{R \sin i}{2} \quad (4.9)$$

where R is the radius of curvature and i is the grazing angle. They also showed that the sagittal focal length (plane normal to meridian) is

$$f_s = \frac{R}{2 \sin i}. \quad (4.10)$$

The astigmatic difference is substantial (nearly 10,000 for some cases of interest), and it is clear that the lack of focusing in the sagittal direction means that the mirror essentially behaves as a cylindrical surface [41]. Kirkpatrick and Baez had the idea to use two perpendicular mirrors in succession in order to obtain an X-ray image. Such a design is depicted in Figure 4.5, and is the microscope that bears their names or initials.

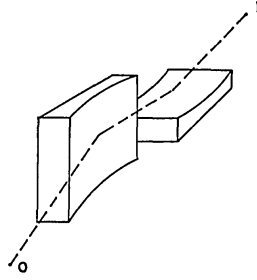


Figure 4.5: Two grazing-incidence mirrors will focus in both planes and enable formation of an X-ray image with good spatial resolution [41]. Such a design is called a KB microscope.

4.4 Resolution Requirements

The ultimate KB resolution limit is $\sim \lambda/2i$, given by the diffraction limit. However, for a typical practical system ($R=20$ m, $i=7 \times 10^5 \lambda$ (in cm),ⁱⁱ object distance $p=10$ cm), the resolution is of the order of 340 nm [79]. For current laser fusion experiments, the resolution required to investigate and image the micron-scale instabilities [80] is better than 5 microns at photon energies greater than 4 keV [40]. Pinhole cameras are known to diminish in contrast and resolution at high energies, and as discussed before, bragg crystals have a bandwidth too small to detect the K_α emission that is shifted in thermal plasmas. Therefore the KB seems to be a promising diagnostic for K_α imaging.

The KB describes the imaging half of the diagnostic, and can be coupled with many different detectors: image plates, CCD cameras, CID cameras, framing cameras and streak cameras [40].

It should be noted that, since the focal length has strong angular dependence, the resolution of the KB microscope degrades rapidly as the source moves laterally from the optimal position. Figure 4.6 shows both the theoretical and measured resolution

ⁱⁱThis is the maximum angle for platinum metals, obtained from Equation 4.7.

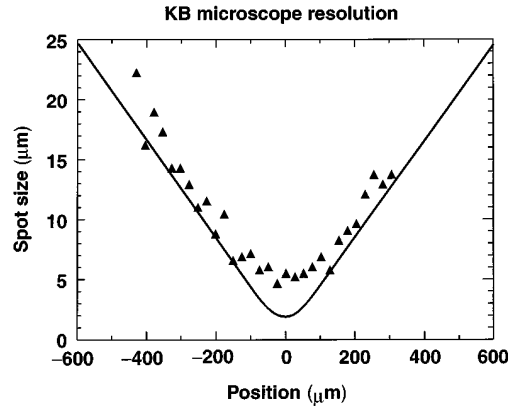


Figure 4.6: Resolution of a KB microscope as a function of position from best focus. The solid line is the predicted resolution from ray tracing, whereas the dotted lines are measured by backlighting a Cu-mesh using a dc X-ray source [84].

of a KB microscope as a function of lateral displacement out of best focus. In theory if the response of the microscope is well-known and characterized one can deconvolve the data taking into account the calculated point spread function (PSF) versus angle.ⁱⁱⁱ For this reason the resolution of the KB is typically reported as a function of field of view, such as a 5 micron resolution over a 200 micron field of view in the OMEGA iridium-coated KB [81]. The hot dense plasmas generated in ICF have dimensions of hundreds of microns, so optimizing the resolution over a large field of view is desired [80].

4.5 Aberration analysis and correction

Field obliquity is very high in the KB, meaning the focal surface is strongly inclined relative to the normal of the principal ray [82]. This obliquity can be reduced by placing an aperture stop before the mirrors, but such a solution may significantly

ⁱⁱⁱIt is a nontrivial problem, however, since because of the change with angle the conventional definition of convolution cannot be used.

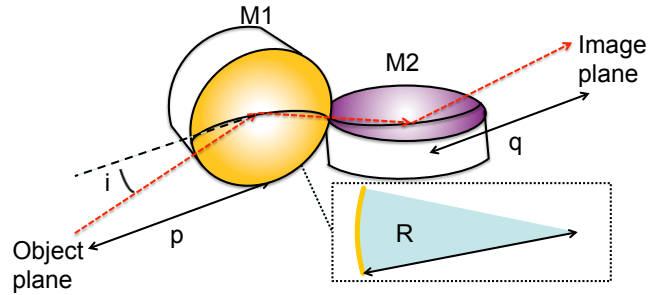


Figure 4.7: Definition of variables for the KB microscope setup.

reduce the collection efficiency to that already achieved by pinholes.

Spherical aberration is always present in any spherical mirror, and can be corrected through the use of elliptical or parabolic mirrors. Early calculations done by Dyson [82] showed that the resolution cannot be increased by greater than a factor of two over the spherical case. However, such an increase in resolution may be necessary in increasingly demanding experiments.

Regardless of whether or not aspherical mirrors are used, field aberrations will still be present, namely coma and curvature of field. The response or point-spread function (PSF) of the KB microscope in one dimension is plotted in Figure 4.8, along with a Gaussian function with the same rms (the variables are defined in Figure 4.7). Also, the different magnification of each mirror (called anamorphotism [102]) will introduce some distortion that can be accounted for. In principle, at least, these aberrations can be corrected after data collection.

4.6 Coatings

Surface irregularities which cause scattering increase in importance as wavelength decreases [41], so the mirrors typically have to be super-polished to an rms roughness of a few angstroms [81]. Indeed, one of the most accurate measurements of surface

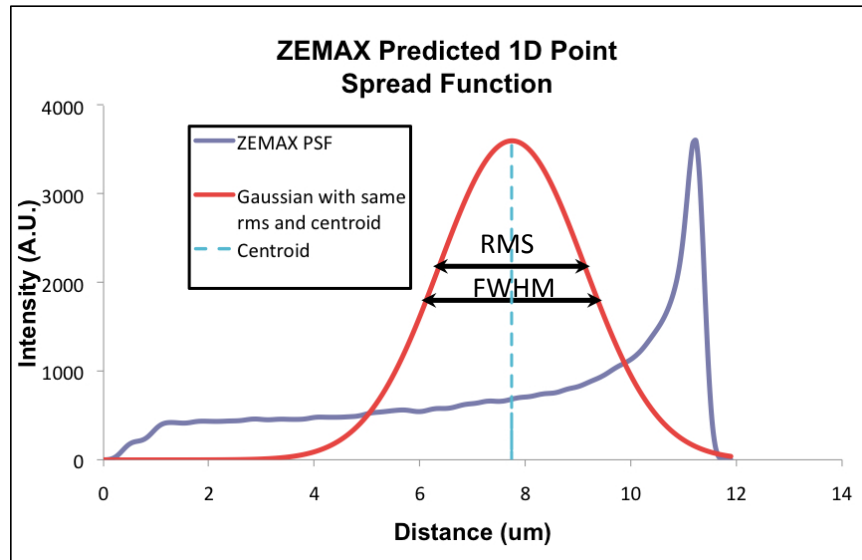


Figure 4.8: The response or point-spread function (PSF) of the KB microscope, traced using ZEMAX, compared to a gaussian function of the same rms. The image settings were $p=94.6$ mm, $q=1232$ mm, $i=8.73$ mrad (0.5°), $R=20$ m, with a mirror diameter of 25.4 mm.

roughness is by using X-rays [41], meaning that the most accurate analysis of a KB mirror's roughness may be to test it in an experiment or on an X-ray source if available. Atomic Force Microscopes (AFM) can also obtain the required measurement accuracy needed.

If one returns to Equation 4.7, one sees that for a given wavelength, the incident angle can be increased if the electron density is increased. An increase in the incident angle is beneficial for two reasons. First of all, the field of view is increased by increasing the effective solid angle of the mirrors, which increases the sensitivity and diminishes brightness requirements. Secondly, Kirkpatrick and Baez showed that the focus wanders greatly for a larger angular difference between the ray striking the mirror center and the ray striking the mirror edge. In order to minimize this angular difference and hence diminish this field obliquity aberration, a higher incident angle is desired.

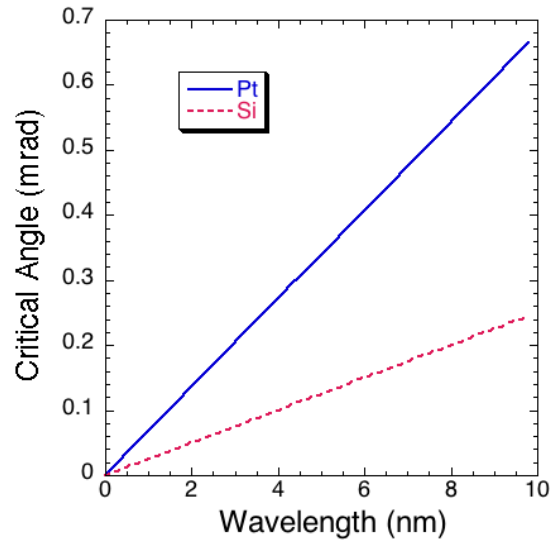


Figure 4.9: The maximum grazing angle for which total reflection occurs as a function of wavelength. For short X-ray wavelengths, higher Z (i.e. denser) reflectors are desired [41].

In order to maximize the imaging capabilities, the mirrors must be coated with a high-Z material. Typical choices are nickel, silicon, platinum [83], gold and iridium [84]. Sputtering seems to be the method of choice to achieve the minimum roughness necessary [85], and has even been used to coat a spherical mirror into an elliptical shape [88]. Other methods that have been used to coat X-ray mirrors include pulsed chemical vaporization machining (PCVM) which achieved a flatness of 22.5 nm [87], and various wet chemical deposition processes [86]. Figure 4.10 shows some measured and calculated reflectivities for various energies.

The K_α emitter of choice for tracer layers is currently copper at 8.05 keV, and may be switched to zirconium at 15.8 keV or silver at 22.2 keV for higher-energy NIF experiments [89]. Typical K_α emission lines are listed in Table 4.1. As Figure 4.10 shows, the copper K_α emission of 8.05 keV will barely be imaged by the single metal coatings discussed above. For these higher energies, a different type of mirror

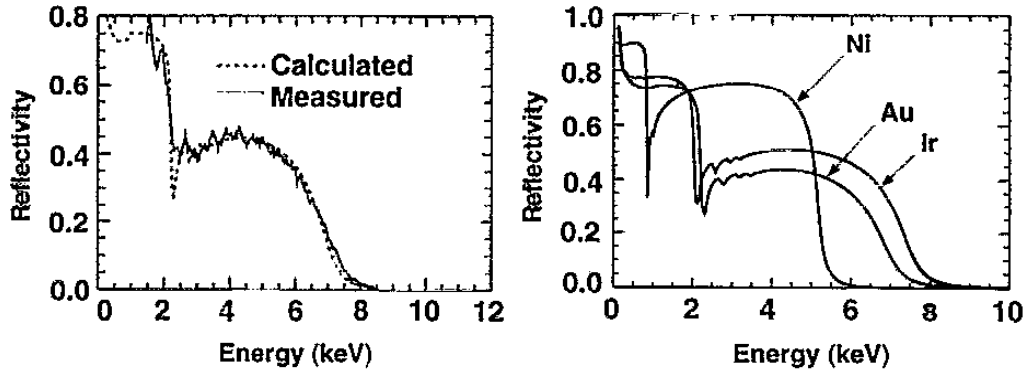


Figure 4.10: Left: measured and calculated reflectivity for gold-coated mirrors used in OMEGA for an angle of incidence of 0.70° . Right: Predicted reflectivities for single-metal coatings for an angle of incidence of 0.70° [40].

is necessary.

4.7 Multilayers

Multilayer coatings apply coherent addition of multiple grazing incidence Fresnel reflections from step changes in refractive index to give a large reflected signal similar to Bragg reflection from a crystal. By having alternating coatings of high-Z and low-Z materials, the X-rays are afforded multiple occasions to reflect each time they cross and interface between the high and low Z materials. Highly developed deposition techniques allow fabrication with appropriate spacing for constructive interference of X-rays from the layers, with thicknesses on the order of a few nanometers [81]. Figure 4.11 illustrates the principle of multibeam interference that is employed in such multilayer coatings to give enhanced reflectivity. Figure 4.12 shows an example of the new reflectivity obtained with multilayers.

This reflection technique, since now dependent upon layer spacing, allows feasible X-ray reflection at near-normal incidence for soft X-rays [74]. However, for harder X-

Table 4.1: Common K emission lines [24, 40, 74, 81, 84, 90, 91, 92]

Element	K_α		K_β^a	
	E (keV)	λ (nm)	E (keV)	λ (nm)
C	0.277	4.48	-	-
Al	1.49	0.836	1.557	0.797
Ti	4.51	0.275	4.932	0.252
Cu	8.048	0.153	8.905	0.1395
Zn	8.639	0.144	9.572	0.1298
Zr	15.7	0.0791	17.7	0.0702
Ag	22.16	0.05606	24.94	0.0498

^aThis corresponds to a transition from 3p to 1s [93].

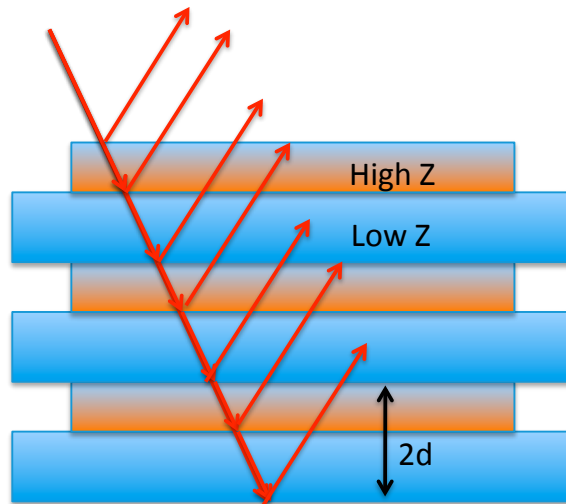


Figure 4.11: Constructive interference and the Fresnel reflection are combined in multilayer coatings (inspired by [73]). Refraction is ignored for simplicity.

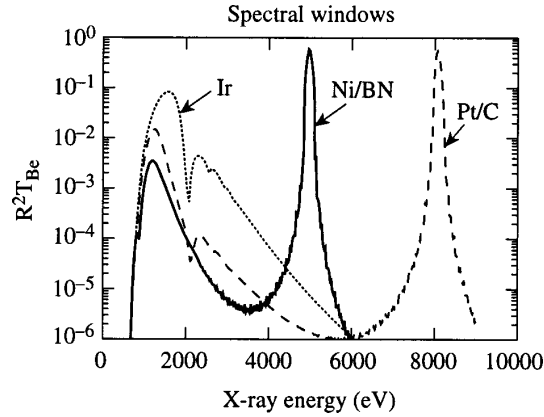


Figure 4.12: Spectral windows and throughput for multilayers vs. single metal coatings [81]. All coatings were designed for a grazing incident angle of 36.5 mrad (2.1°). The Ir coating consisted of 300 Å of Ir on 100 Å of Cr. The Ni/BN mirror had 60 layers with 1.4nm/3.5nm thicknesses. The Pt/C mirror had 100 layers with 0.79nm/2.13nm thicknesses.

rays at near-normal incidence, the layer spacing approaches atomic separation, which is what is done in Bragg crystal imagers. Though still limited to grazing incidence, multilayer coatings for hard X-rays allow for substantial reflection of much higher energy X-rays which would have previously been reflected only at vanishingly small angles. Table 4.2 summarizes some of the multilayer coatings used by various synchrotron and ICF groups around the world, and Figure 4.13 summarizes the parameters for KB mirrors used in the European Synchrotron Radiation Facility (ESRF) (synchrotron facilities have in fact been using KB microscopes considerably longer than the ICF community).

		Em in KeV	E _{max} KeV	Source dist m	Focus dist m	Incident angle max mrad	Dimensions L-t-w1- w2 mm	Source size μ m	design spec focus FWHM μ m	Coating material	Mirror central Radius m
		KeV	KeV	m	m			μ m			
ID15	Vert	30	90	50.5	2.2	8.9	300-15-40	24	8	WB ₄ C	474
MPI	Hor	16.5	16.5	14.2	0.3	13.2	170-6-30-18	30	1	NiB ₄ C	45
	Vert	16.5	16.5	42.3	0.58	3.8	170-8-30	60	1.3	Pt	301
ID22	Hor	8	18	41	0.19	3.5	92-5-46-19	700	3.5	Rh	108
	Vert	8	18	41	0.39	3.5	170-8-42-33	24	1.5	Rh	221
ID28	Hor	15.81	21.74	100	2	10.5	300-15-40	900	20	RuB ₄ C	373
ID30	Hor	30	80	30.3	0.55	8.5	170-6-30	900	17.0	Ir Al ₂ O ₃	127
	Vert	30	80	30	0.85	8.5	170-9-30	24	3.5	Ir Al ₂ O ₃	194
ID13	Hor	13	21	46	0.095	4.2	96-8-42-10	134	0.5	Pt	45
	Vert	13	21	46	0.28	4.2	170-8-30-17	24	0.5	Pt	133
BM5	Hor	7	20	58	0.15	14	92-5-40-12	296	1	ML	21
	Vert	7	20	58	0.345	14	170-8-40-18	87	1	ML	49
ID19	Hor	15	30	150	0.088	5.6	96-8-40-18	134	0.15	Pt	31
	Vert	15	30	150	0.28	14	170-9-30-?	24	0.15	ML	40

Figure 4.13: The KB design parameters for mirrors used in ESRF beamlines [42].

Table 4.2: Multilayer Coating Specifications

Coating	i (mrad)	Range (keV)	E peak (keV)	dx_1	dx_2	Total layers	Ref.
W/ B_4C	12.22	7-9	~ 8	2.5nm	4.5nm	-	[94]
	36.65	FWHM = 0.3	4.950	3.5nm	3.5nm	25	[95]
	7 & 2.9	15-20.5	20.5	d=4.7nm ctr, 140nm tot. ^a			[96]
	42	-	8.05	35%d	65%d, d=1.7-2.19nm	200	[92]
Ir/Cr	36.65	FWHM 0.4 keV	1.5	30nm	bind. layer	2	[81, 85]
Si/Mo	-	0.065-0.095	-	4-8nm	2-4nm	60	[97]
Ni/BN	36.65	-	4.95	1.4nm	2.1nm	60	[81]
Pt/C	36.65	-	8.05	0.788nm	1.34nm	100	[81]
W/C	$\sim 1000\pi/2$	-	0.277	0.765 nm	1.510nm	76	[74]
	8.73-15.7	-	8.05	~ 3 nm	~ 3 nm	-	[98]
W/Si	1.66	-	70	3.33-29.6nm	3.33-29.6nm	150	[99]
	40.1 ^b	0.6	3.4	10-50nm	10-50nm	~ 20	[80]
Cr/Sc	104.7 ^c	0.282-0.540	-	38.5%d	61.5%d, d=10.5-20.5nm	11,15	[100]

^a33% nonlinear gradient.

^bThis is for a KBA design, discussed later.

^cThis is for a Wolter microscope, discussed later.

However, multilayer mirrors made with uniform layer spacing will have very narrow bandwidths of the order of a few percent of the peak reflected wavelength. To allow for ionization shift of the K_α emission and the varying angles of incidence across the KB mirror surface for large aperture systems, bandwidths on the order of 10% of the peak wavelength are required. Using calculations of reflectivities that include the

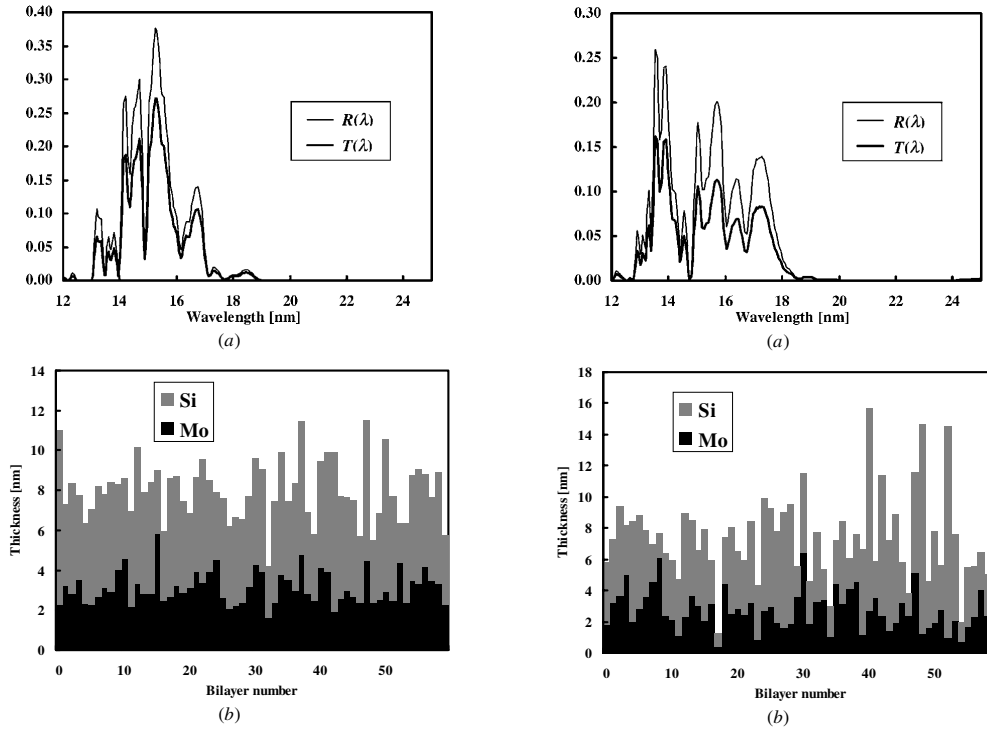


Figure 4.14: Reflectivity R , and throughput T (reflectivity times source spectrum, which is the bremsstrahlung emission from a laser plasma source with a rhenium target, from 12-25 nm) vs. energy (top) and coating thicknesses for Mo/Si multilayered mirrors (bottom) [97].

addition of a roughness factor to the Fresnel equations (the Debye-Waller factor and Nevot-Croce factor [101]), larger bandwidths are obtained [99]. In addition random thickness patterns with the multilayers can be used to give broadband reflectivity, leading to the seemingly arbitrary thicknesses shown in Figure 4.14 and the corresponding large range in layer thicknesses in some cases in Table 4.2. If the spectral range needs to be broadened or fine-tuned to a large extent, this technique is useful.

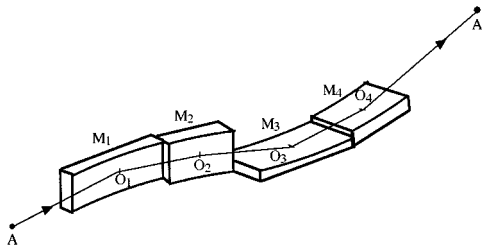


Figure 4.15: KBA Design [102].

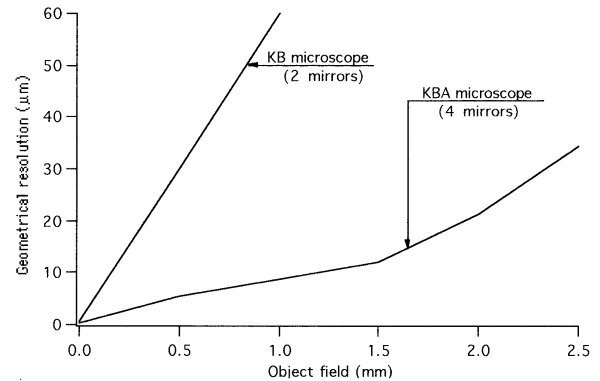


Figure 4.16: Theoretical Resolution comparison of KB and KBA microscopes [102].

4.8 Improving the KB

In 1952, Dyson suggested using two mirrors in series to eliminate the field obliquity [82]. In 1997, R. Sauneuf et al. [102] realized this design, which effectively enhances the field of view while still retaining a high resolution. They quoted a normal KB as having a 3-5 micron resolution over a field radius of 100 microns, but claimed that the adjunction of two similar mirrors can increase the useful field to a resolution of better than 10 microns over a 1-mm field radius. Figure 4.15 illustrates the idea, while Figure 4.16 shows the corresponding improvement in resolution vs. field of view. The design is called a KBA, where the A stands for “améliorée”, French for “improved”.

The field of view increase is a direct result of the cancelation of field obliquity. Each of the two mirrors in series provide equal and opposite field obliquity. As Figure 4.17 illustrates, the angular change of two different rays hitting the same spot on the first mirror is identical for geometrical reasons [102]. In a singlet lens, two rays incident on one point of the lens are deviated by the same angle primarily because they are affected by a lens of a fixed focal length, as illustrated in Figure 4.18. Thus the KBA has one of the principle properties of an ideal focusing lens which a single

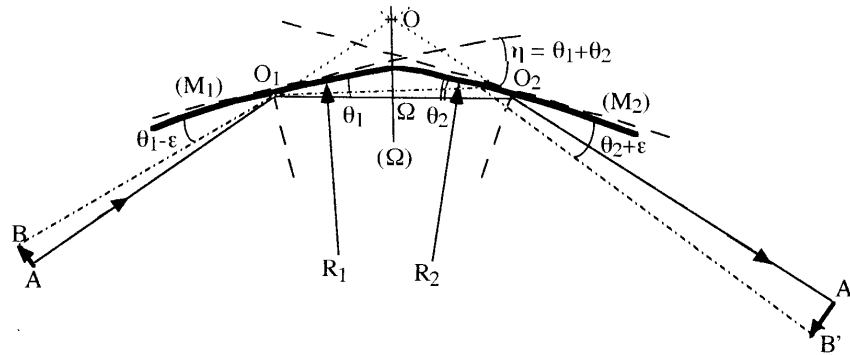


Figure 4.17: The double mirror design in KBA leads to identical angular change for two different incident rays. That is, the difference between AO_1 and O_2A' is the same (2η) as the difference between BO_1 and O_2B' [102]. This roughly means that their focal distance is the same.

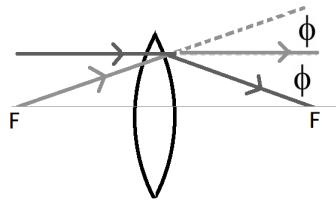


Figure 4.18: Example of two rays on a singlet lens being deflected by the same angle as a result of the fixed focal length.

grazing incidence mirror does not. The second property is that the angular deviation is linearly dependent upon the distance from the center axis of the imaging system, a property which the curved mirrors also possess to first order. The first mirror (called the field mirror) is usually longer than the second (called the aperture mirror) to ensure the majority of incident rays are striking the first mirror and filling up the entire second mirror, whose length defines the aperture size [102].

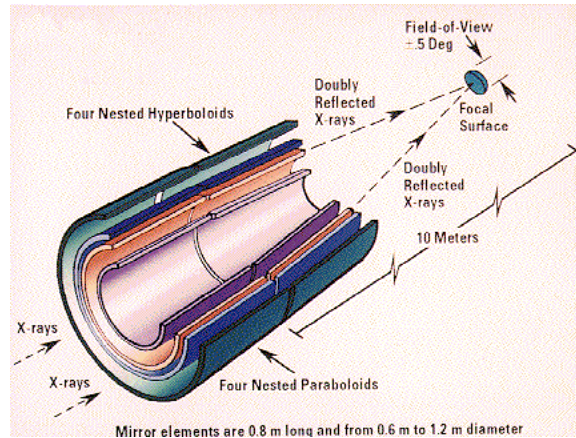


Figure 4.19: A Wolter type I optic for NASA's Advanced X-ray Astrophysics Facility (AXAF), with ellipsoidal followed by hyperboloidal mirrors [103].

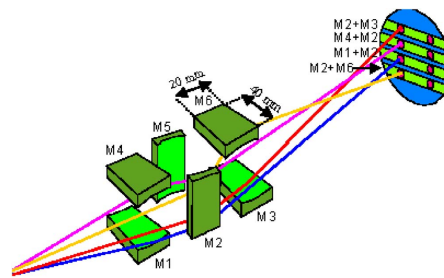


Figure 4.20: The 8-image toroidal mirror design of the Ligne d'Intégration Laser (LIL) facility [83].

4.9 Other Advances

It was mentioned earlier that spherical aberrations could be eliminated through the use of aspherical mirrors. One of the most popular choices is to use an ellipsoidal mirror followed by a hyperbolic mirror, usually in a mirror tube as shown in Figure 4.19. Such a design is called a Wolter I, named after the scientist who made three such designs in 1951 [72]. The difficulty with this design is that the fabrication is extremely difficult, requiring a very odd shape and low roughness. Table 4.3 shows some of the Wolter design parameters for multilayer mirrors used in Korea.

Table 4.3: Various Wolter-I mirror parameters used at the Wonkwang University Institute for Radiological Imaging Science [104]. These examples have an aspect ratio of 2 (i.e., mirror length/intersection diameter=2).

Parameter	D6	D7
Magnification	1/4	1/4
Central grazing incidence angle (°)	6	7
Object-to-image distance (mm)	290	290
Mirror-length (mm)	71.14	82.01
Eccentricity: Ellipsoid	0.9947	0.9927
Eccentricity: Hyperboloid	1.0209	1.0280
Diameter (mm): Front	37.07	42.98
Diameter (mm): Intersection	35.57	41.01
Diameter (mm): Rear	21.34	22.37

Finally, another option to enable better focusing is to have vastly different radii of curvature in each plane (meridian and sagittal). Such a mirror surface is toroidal, and has been used extensively in France. Table 4.4 summarizes the parameters used in “Systèmes d’imagerie X” (SIX) that are being developed for the Laser Megajoule Project in France [105]. Table 4.5 shows the different radii of curvature for the PIXEL diagnostic using three mirrors in sequence as shown in Figure 4.20.

Table 4.4: Design Specifications of SIX Mirror Systems [105]

Optic	Geometry p(cm) q(m), M, i (deg.)	Photon Energy (keV)	Resolution (μm) / Field (mm)	Opening (mrad)
Sténopé (pinhole) LIL	8, 0.4, 5, n/a	≥ 1	20/10	0.25
KBA Silice (silica)	25, 2.5, 10, 2	≤ 0.86	7/2	2
KBA Multicouche (multilayer)	23, 3.3, 12, 2.16	3.1-4	7/2	2
Pseudo-Wolter	24, 4, 16, 0.6	0.1-6	3/0.5	0.8
Sphère-Tore (spherical-toroidal) 1.05	72, 4.13, 4.7, 0.85	1-5	30/3	0.5
Sphère-Tore (spherical-toroidal) 1.08	75, 4.13, 5.5, 1.8	0.1-1	30/3	1
MKB 1.06	40, 1.6, 8, 0.8	1-5	10/1	0.5
MKB 1.09	40, 3.2, 16, 1.8	0.1-1	10/1	0.5
PIXEL (LIL)	83, 7.85, 9, 0.6	0.1-10	5/0.5	0.8
PIXEL (LMJ)	79, 13.4, 15, 0.6	0.1-10	5/0.5	0.8

Table 4.5: PIXEL Mirror Parameters [105]

Mirrors	Type	R_m (m)	R_s (mm)
Ma151-1	Biconcave toroidal	574	62
Ma151-2	Biconcave toroidal	348	36
Ma151-3	Biconcave toroidal	639	78

Chapter 5

Design and Characterization

This chapter outlines the details of how the theoretical KB microscope scheme was implemented into a workable form for use in the Titan laser target area. The overall layout will be discussed along with performance tests of the two most important factors for the microscope's performance, namely, reflectivity and resolution.

5.1 Re-entrant assembly

The KB assembly is a re-entrant module designed to mount on a chamber flange, made up of two tubes connected with an O-ring seal to allow slight pivoting of the inner tube for alignment adjustment, as show in Figure 5.1. It is made entirely out of aluminum to minimize activation after high-intensity laser shots. The central tube holds the high-energy X-ray collimators and the magnetic shields against charged particles. The mirror assembly houses the two perpendicular mirrors, and is mounted at the inside end of the tube. This central tube sits on a large O-ring seal inside a larger tube that is mounted to the chamber flange. The central tube is free to pivot about the O-ring over a small angular range, and is controlled via micrometers which

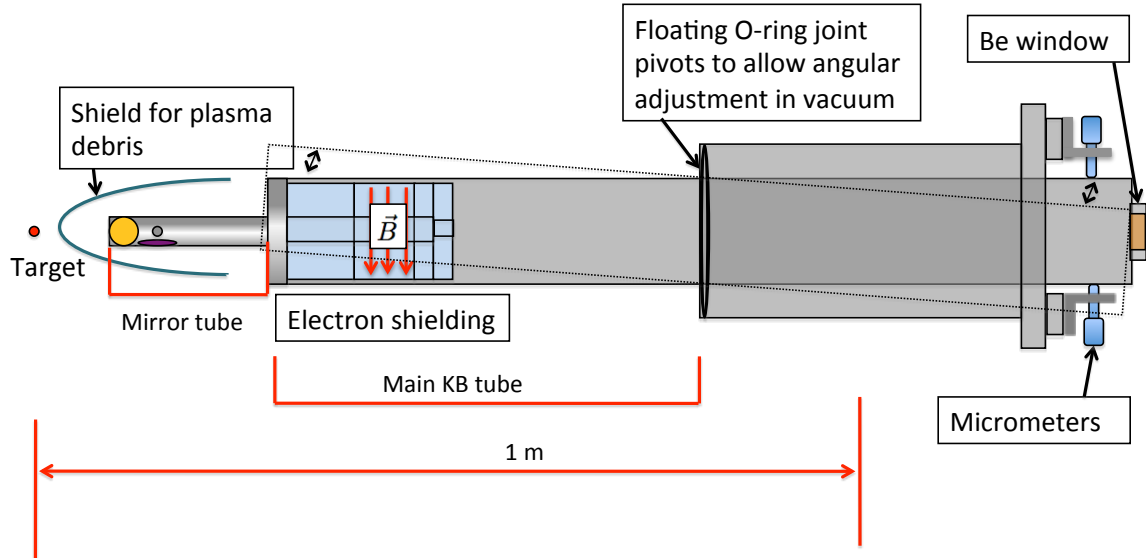


Figure 5.1: Outline of the re-entrant KB microscope.

push against a square collar at the outside end of the tube. Spring plungers (model 33705A21 from McMaster-Carr) were used with a 3.75" long-travel hex-nose plungers with a thread size of 3/4"-10 and a force range of 4 to 35 lbs. It was found that between 20 to 30 pounds of pressure were required to ensure that the microscope tracked the adjustment micrometer. The collimators and magnetic shields could be slid in and out with the microscope mounted in place, using a long rod by removing a beryllium window. A major advantage of the re-entrant design is that the majority of changes to alignment, filtering and shielding can be carried out without entering the chamber, and angular alignment adjustments can be performed without breaking the chamber vacuum.

The mirror tube which houses the platinum-coated mirrors is approximately 20 cm in length, and the mirrors sit in recessed cylindrical holes facing toward the central axis. The mirrors each sit on three press-fit aluminum pins which provide a reliable three-point mounting surface and can be fabricated for different configurations or

incident angles depending on the pin heights. Opposing the mirror surfaces are two 1/4" diameter tungsten rods offset from the mirror surfaces by 0.69 mm and 0.92 mm plus the pin height, which serve to block the direct light from the target which would otherwise overlap with the reflected image. As will be discussed in the alignment section, these two rods combined block three-quarters of the field of view, allowing one quadrant of X-rays through which is useful for verifying alignment from shot-to-shot.

5.2 Mirrors and Coating Results

The substrates were 25.4 mm (1") diameter superpolished ($<1 \text{ \AA}$ rms roughness) spherical fused silica substrates with a radius of curvature of 20 m and a 6.35 mm (0.25") thickness (Gooch & Housego Inc.). The curvature values were tested using a long focal length test with a HeNe laser, and shown to be accurate to within a meter. The mirrors were sputtered with platinum using a magnetron sputtering system. A power of 75 W with a 7 mTorr pressure of argon were used. A chromium adhesion layer was sputtered first for 30 seconds, resulting in an estimated film thickness of 5 nm. Platinum was sputtered at these power and pressure settings for 12 minutes, resulting in a 45 nm coating (measured using an AlphaStep Profilometer). Finally, the roughness was measured to be approximately 1.7 \AA using a white-light interferometer (ZYGO), as shown in Figures 5.2 and 5.3. This method of roughness measurement only measures roughness of large lateral features of the order of a micron due to the use of visible light, and as such is not a completely accurate value. Four mirrors were coated during this run, and are referred to as M1, M2, M3, and M4.

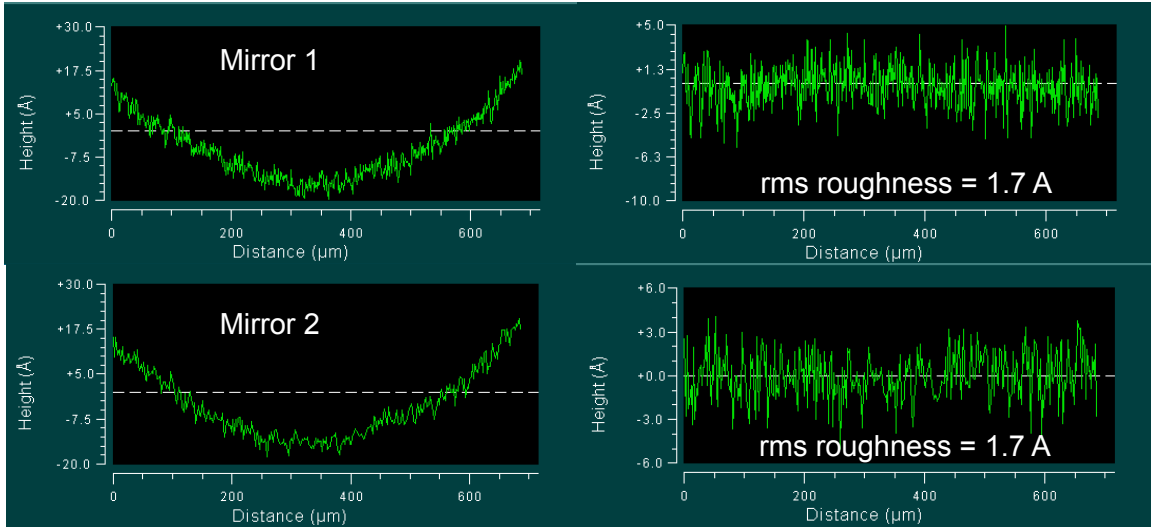


Figure 5.2: Lineouts of the roughness measured with the white-light interferometer (ZYGO) for mirrors 1 and 2. The lineout on the right is high-pass filtered.

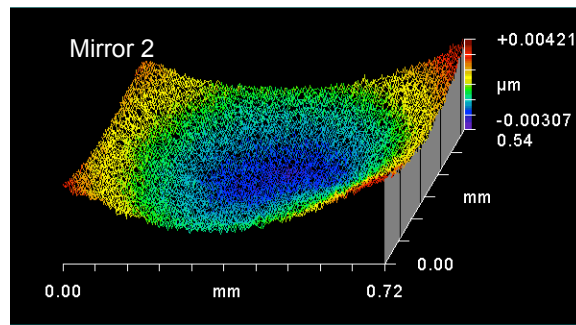


Figure 5.3: 3D surface plot of the area seen in the white-light interferometer (ZYGO) for mirror 2.

5.3 Shielding

Four rare earth magnets, 2.5 cm X 2.5 cm X 0.635 cm arranged in pairs, separated by 2.5 cm, were used to shield against electrons. The peak field strength was 0.5 T as measured with a gaussmeter. The expanding plasma was prevented from coating the mirror surfaces by enclosing the mirror assembly in a thin mylar plastic wrapping. The complete shielding package consisted of an aluminum cylinder, followed by magnets, followed by another longer aluminum cylinder (the electron shielding package in Figure 5.1), all located at the end of the main tube closest to target chamber center (TCC). At the back end a 500 μm thick beryllium window was used to allow the X-rays to exit into air onto a detector (see Section 6.5 for discussion of detectors).

5.4 Measuring incident angles

A sample image is shown in Figure 5.4. There is a large spot which corresponds to broadband, unfiltered light from TCC (which is called the zero-order image). This corresponds to the quarter of the total beam that the tungsten rods do not block. The separation between the zero-order and the 1D line images allows an in-situ measurement of the incident angles on the mirrors for every shot. The known incident angles then allow for correction of the mirror reflectivity versus angle of incidence across the entire field of view, resulting in an accurate transmission correction for each image individually. The equations to determine the angle of incidence are derived below.

As shown in Figure 5.5, the tungsten rods are offset from the mirror surface by a known amount δ . The additional offset of the emission position from the mirror surface is denoted by ϵ , and the grazing angle of incidence by θ_i . The distance from the source to the mirror surface is given by p and the distance from the mirror to the

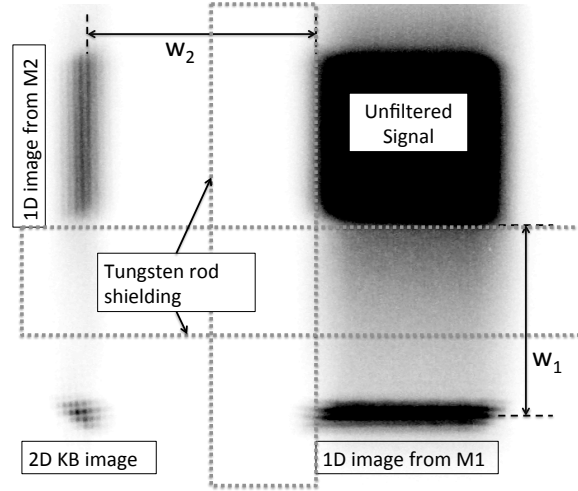


Figure 5.4: How the KB microscope forms images.

image plane is q . The axial reference direction is defined by the line tangent to the tungsten rod and perpendicular to the offset distance δ . From the geometric layout one can determine that

$$\tan \theta_i = \frac{\delta + \epsilon}{p} = \frac{y_i + \delta}{q} \quad (5.1)$$

and

$$\tan \beta = \frac{\epsilon}{p} = \frac{y_0}{q} \quad (5.2)$$

Recalling that image magnification is given by $M = q/p$, one can derive the following:

$$\epsilon = p \tan \theta_i - \delta \quad (5.3)$$

$$y_i = M(\delta + \epsilon) - \delta \quad (5.4)$$

$$y_0 = -M\epsilon \quad (5.5)$$

The negative sign in y_0 was included since under normal circumstances ($\epsilon > 0$) and the zero-order offset is in the negative direction. The expression for w_j , the separation between the zero-order and 1D line image, is thus

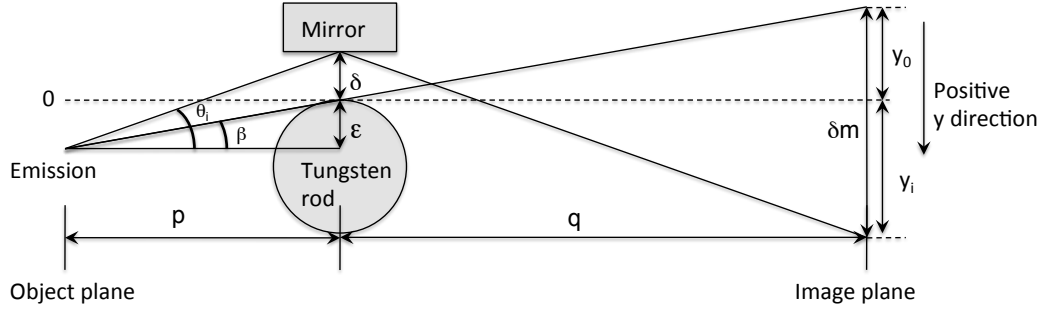


Figure 5.5: The geometry involved in inferring incident angle from the image separation from the zero-order image. The zero axis is chosen for convenience and the down direction is positive.

$$\begin{aligned} w_j &= y_i - y_0 \\ &= 2M\epsilon + \delta(M - 1) \end{aligned} \quad (5.6)$$

Therefore, from a given image's w_j one can calculate the incident angle:

$$\epsilon = \frac{w_j - \delta(M - 1)}{2M} \quad (5.7)$$

$$\theta_i = \tan^{-1} \left(\frac{\epsilon + \delta}{p} \right) \quad (5.8)$$

$$\theta_i = \tan^{-1} \left(\frac{1}{p} \left[\frac{w_j - \delta(M - 1)}{2M} + \delta \right] \right) \quad (5.9)$$

In practice w_j is measured from the half-maximum of the edge of the zero-order image (since that is where the tungsten rod is cutting the image off) to the peak of the one-dimensional image. A large X-ray source size will lead to a sloped cut-off at the tungsten edge and will thus introduce a larger error in the measurement of w_j . However, this system is still significantly better than many KB alignment systems where no absolute measurement alignment from shot-to-shot is available [84, 106],

with the exception of the continuous synchrotron sources where live X-ray images can be adjusted and put into focus [42].

5.5 Adjusting the alignment

Precision alignment is carried out via micrometers at the rear of the KB. The ideal image separation to ensure image focus can be determined from the equations for ϵ and w_j given above.

The pivot point for the KB is at the O-ring where the large tube meets the main tube (see Figure 5.1). The distance from the image plane to the O-ring (d_i) is 55 ± 1 cm (80 ± 1 cm with the camera installed) and the distance from TCC to the O-ring (d_0) is 74 ± 1 cm for ports TS1 and TS4 on the Titan chamber. From these values the leverage ratio of the mirror motion with respect to the image plane is defined:

$$R_L = \frac{p - d_0}{d_i} \quad (5.10)$$

Knowing this leverage ratio the viewing position can be readjusted after any shot to correct misalignment or to reimage a new target position.

5.6 Alignment

The alignment of the KB is nontrivial, since the focal length is sensitively dependent upon the incident angle. For example, a small change in angle of 2 mrad from 8.73 mrad to 6.73 mrad changes the focal length from 87.3 mm to 67.3 mm, a 23% change. Furthermore, grazing incident angles are difficult to set up, since a large throw distance is required to adequately measure the incident angles. Stability of the mirrors

is another key concern. It should be mentioned that traditional mirror mounts are not good in this situation because the very high radii of curvature can be distorted by such a side force from the set screw.

The alignment is carried out using a point source of light mounted at the exact target position. The source consisted of a multimode fiber optic cable glued into the end of a hypodermic needle which supports the exposed fiber in a robust package. In order to make the fiber tip viewable by alignment cameras while still being protected, a V-shaped groove was cut into the end. This light source was mounted on a 6-axis target positioning mount. A green diode laser was coupled into the multimode fiber via a microscope objective. The fiber could then be pointed in any direction and was aligned to the target position (shown in Figure 5.6). However, since each mirror acts as a slit reflector there is substantial diffraction in the optically imaged beams. The optical method can, however, be used to adjust the separation distance between the zero-order and 1D images, which sets the mirror angles. This is adequate to determine focus (as is described in Section 5.6) if the distance parameters are measured accurately, and the technique proved to be a reliable alignment method.

The fiber is usually placed in the target position at air pressure. Since the KB microscope is mounted on one of the ports, its pointing shifts slightly as the chamber flexes when evacuated (to 10^{-5} torr). The displacement of the mirrors was measured to be approximately $700 \mu m$ when evacuated. This corresponds to an angular change on each mirror of approximately $6.11 - 6.46$ mrad and was reproducible to within 0.7 mrad. This change, when unaccounted for, is enough to shift both the 1D images and the 2D image out of the field of view. The microscope is designed to position the inner corner of the zero-order image approximately at the center of the field of view. The microscope could thus be adjusted under vacuum to correct for the misalignment once an X-ray image was taken, even if only the zero-order image was produced. Measuring

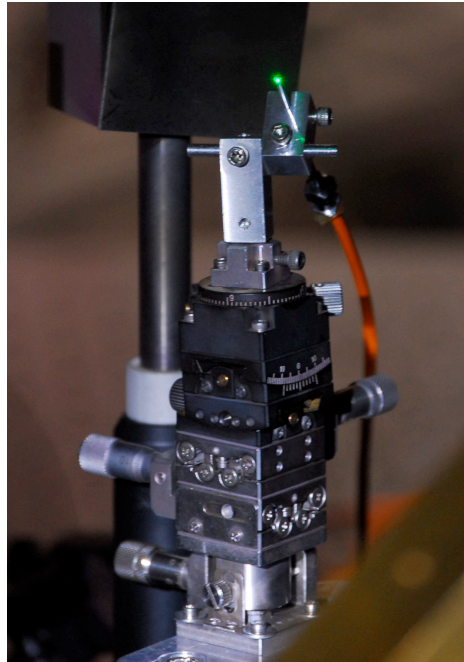


Figure 5.6: The fiber optic alignment setup used to serve as a point source at Target Chamber Center (TCC).

the vacuum shift with a few test shots before the experiment allowed a reproducible correction to be applied.

The stability of alignment shot-to-shot averaged 0.5 mrad ($\sigma = 0.5$ mrad) for the closer mirror, and 0.4 mrad ($\sigma = 0.35$ mrad) for the second mirror. This result was obtained by averaging the measured angular shifts in emission for over 40 shots where the microscope went unmoved. Therefore it is a convolution of the stability of the KB, the positioning of the target, and the pointing of the beam.

This reveals another use of this microscope design. Because of its ability to focus on an absolute position in space, the shifting of emission can be tracked for motions greater than the 50 μm pointing stability of the KB microscope.



Figure 5.7: The X-ray copper reflection tube (Moxtek) along with the 40 kV power supply and controller [107].

5.7 Moxtek X-ray Tube

The cw X-ray source from Moxtek provided a reliable X-ray lightbulb with which to carry out the various imaging tests. The tube itself is a 4 watt, 40 kV, 100 μ A copper anode reflection tube (Moxtek ELC00215) with a controller (Moxtek FTC-200). The analog control voltages that set the tube voltage and emission current are viewable on the controller's LCD screen, and adjusted using a rotary encoder. The actual X-rays emerge from a circular aperture roughly 5 mm in diameter covered by a beryllium window. The source size is specified to be approximately 300 μ m wide. It was measured by the KB microscope to have a FWHM size of $180 \pm 10 \mu$ m wide by $110 \pm 10 \mu$ m tall. The wings of the source ($1/e^2$ of peak value) extended the size to $325 \pm 15 \mu$ m wide by $160 \pm 10 \mu$ m tall, averaged over 9 shots. A sample image is shown in Figure 5.8.

The tube was housed in a 3.175 mm thick steel box that was lined on the inside with 1.6 mm of aluminum to minimize the fluorescence of iron K_α at 6.4 keV [90] that is present inside the box. In contrast, the aluminum K_α fluorescence is 1.49 keV [90]

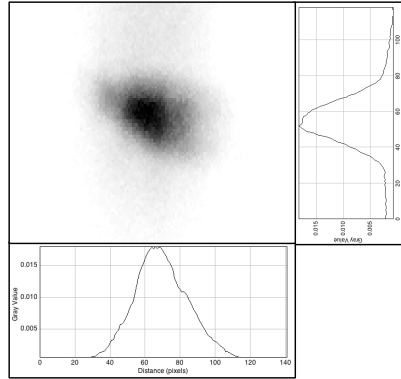


Figure 5.8: A sample image of the Moxtek X-ray source formed using the KB microscope. The first mirror focused vertically ($p=108.3\text{mm}$, $q=1354.5\text{mm}$, $M=9.94$) and the second mirror focused horizontally ($p=133.7\text{mm}$, $q=1329.1\text{mm}$, $M=12.51$). At these settings each mirror focuses at 10.03 mrad and 12.14 mrad respectively. This image was at 8.05 mrad and 10.23 mrad with FWHM $171 \times 112\mu\text{m}$, with wings extending to $322 \times 168\mu\text{m}$. The source size was much larger than the resolution so images a little out of focus were still limited by the source size. The Moxtek tube was set at 15 kV , $100\ \mu\text{A}$ for a 17 min. exposure and a 51 minute decay on BAS-MS IP#4. Exposure #4 on 2011.05.08.

and will only penetrate a few centimeters of air. One larger box was attached by a long tube to a second, smaller box, the dimensions of which are in Figure 5.10. This gave a total working distance of approximately 1.4 m , enough to work at high magnification and test the capabilities of various X-ray imaging diagnostics. A picture is shown in Figure 5.9, where it can be seen that a buffer region with offset slots allowed for cables to be fed into the box without allowing any radiation to escape. The interlock system was set up with contact switches so that the tube controller would only supply voltage and current when the lids were on properly. The entire enclosure was radiation leak-tested and approved by the University of Alberta Radiation Safety Officer.

The spectrum of the cw X-ray source was measured using a solid-state CdTe detector and pulse height spectrometer (XR-100T-CdTe, Amptek, Inc.). The active area of the spectrometer is a Cadmium Telluride (CdTe) diode of $3 \times 3\text{ mm}$ area

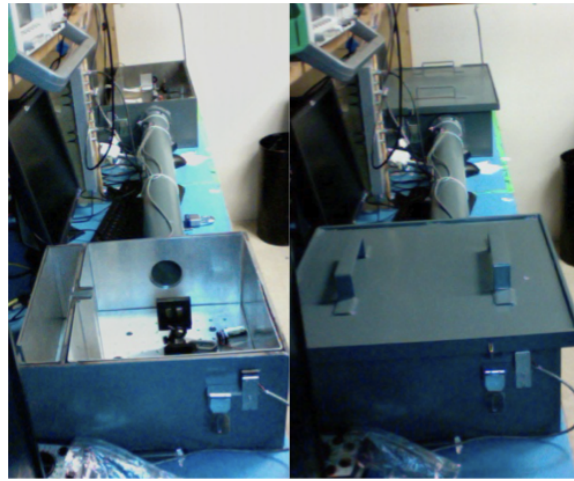


Figure 5.9: The X-ray box with and without the lids on.

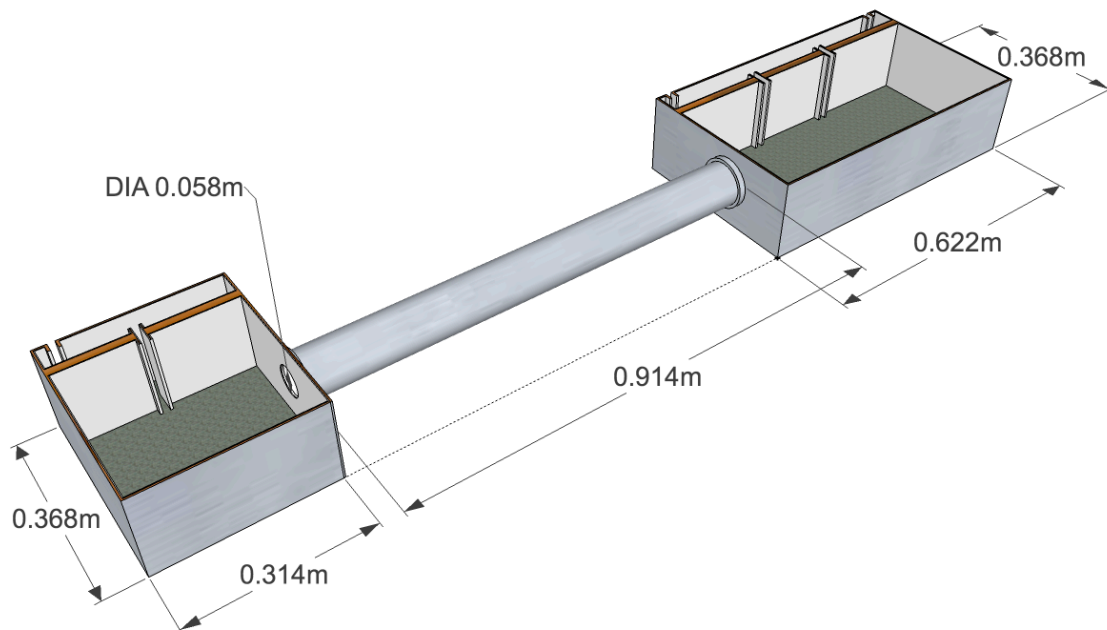


Figure 5.10: A schematic of the X-ray box to shield the Moxtek X-ray source. The larger box typically contained the source and optics, and the smaller box contained the detector.

by 1 mm thickness [108]. Incident X-rays create one electron-hole pair (EHP) per 4.43 eV of deposited photon energy. Energy loss in the CdTe crystal varies with wavelength and is dominated by the photoelectric effect or Compton scattering [109]. A bias voltage of 400 - 500 volts across the CdTe improves the responsivity and collection of EHPs. To minimize the losses from leakage current the spectrometer is thermoelectrically cooled [109].

Electrons and holes drift under the applied field to opposite electrodes of the CdTe detector producing the output pulse measured. However, interactions near the rear of the crystal where some of the charge is lost produce charge collection time fluctuations, and to minimize these a Rise Time Discrimination (RTD) circuit can be used to reject such pulses. Basically its function is to only pass on full charge collection events onto the Multichannel Analyzer (MCA) for spectrum acquisition and analysis [109]. The final spectrum is output to a PC in a pulse height histogram.

The CdTe detector operates on the principle of single photon detection, and so will output a signal proportional to the energy absorbed during the readout time. Therefore if multiple photons interact with the detector during the readout time, the histogram will reflect this with a count as a multiple of the original photon energy. This phenomenon is called pile-up and was minimized during the calibration of the X-ray source. This was done by increasing the distance from the source, by placing a lead pinhole in front of the detector, and by decreasing the tube current. The detector was covered with a 100 um thick beryllium window to protect the detector from dust, to maintain a vacuum environment to avoid water condensation when cooled, and to block low energy photons.

For the calibrations the CdTe detector was placed 101.6 cm away from the source, and covered with a 500 um diameter lead pinhole (which was approximately 5 mm thick). The following corrections needed to be applied, and the representative curves

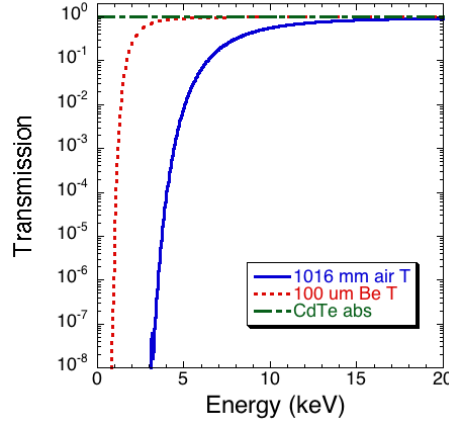


Figure 5.11: Plot of transmission and absorption of Be, air and CdTe versus energy.

are plotted in Figure 5.11.

First, the transmission of air needed to be taken into account. For this, tabulated values from the NIST website [110] were used, assuming an air pressure of 760 torr, and temperature of 298 K. Secondly, the transmission of the 100 μm beryllium window needed to be taken into account. Both of these transmission factors were divided out to obtain the actual photon flux. Finally, the photoabsorption of 1 mm CdTe needed to be taken into account. The mass photoabsorption coefficients were obtained from the NIST tables, and calculated via the following formula:

$$\text{Absorption} = 1 - e^{-(\mu/\rho)\rho l} \quad (5.11)$$

where (μ/ρ) is the photoabsorption coefficient, ρ is the material density (taken to be $6.2 \text{ g} \cdot \text{cm}^{-3}$ [111]), and l is the path length through the material.

For a tube voltage of 15 kV and 10 μA , with an exposure time of 1 minute, the results are shown in Figure 5.12. The trough between the two visible peaks (at approximately 8.5 keV) is used to define the edge of the K_α peak. The width is

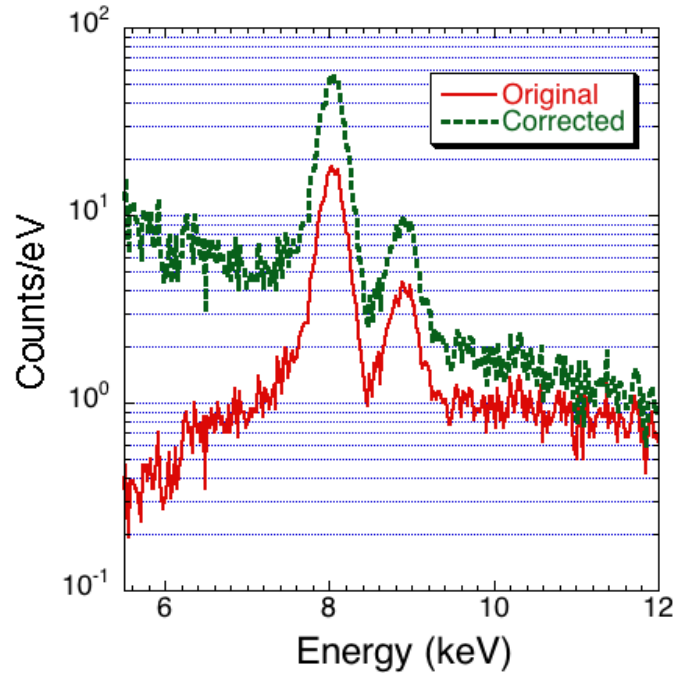


Figure 5.12: Effect of transmission on the observed X-ray spectra. The solid red curve is the original spectrum obtained on the Amptek. The dashed green curve is the spectrum after taking all transmission factors into account. Spectrum #16 on Nov. 17, 2010. 15 kV 10 μ A for 60 s. at a distance of 99.6 cm. RTD ON, threshold 150, gain 6. 500 μ m pinhole on Amptek.

defined as twice the distance between the K_α peak and the trough, and the total number of photons within this region define the number of K_α photons. Therefore, photons from 7.5-8.5 keV are considered K_α photons. Similarly, the distance between the K_β peak and the trough is doubled in order to define the width of the K_β peak. Therefore, photons from 8.5-9.3 keV are considered K_β photons.

Two final spectra are shown in Figure 5.14, where the signals have been normalized by the tube current, time, and solid angle subtended by the detector. The absolute number of K_α and K_β photons for various tube voltages is plotted in Figure 5.13.

In order to further validate these spectra, a cross-calibration was carried out with a PIN (positive-intrinsic-negative) diode. The active area was 25mm^2 and the thickness

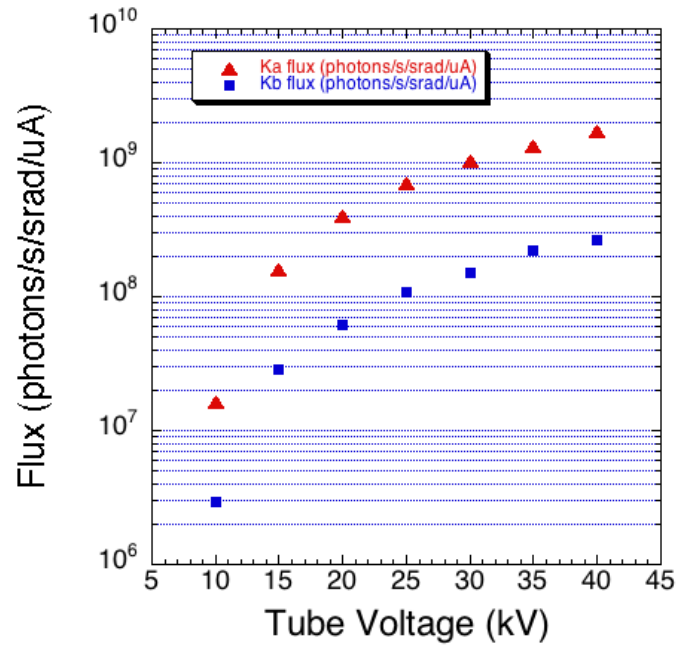


Figure 5.13: Flux of K_α (red triangles) and K_β (blue squares) photons for various tube voltages.

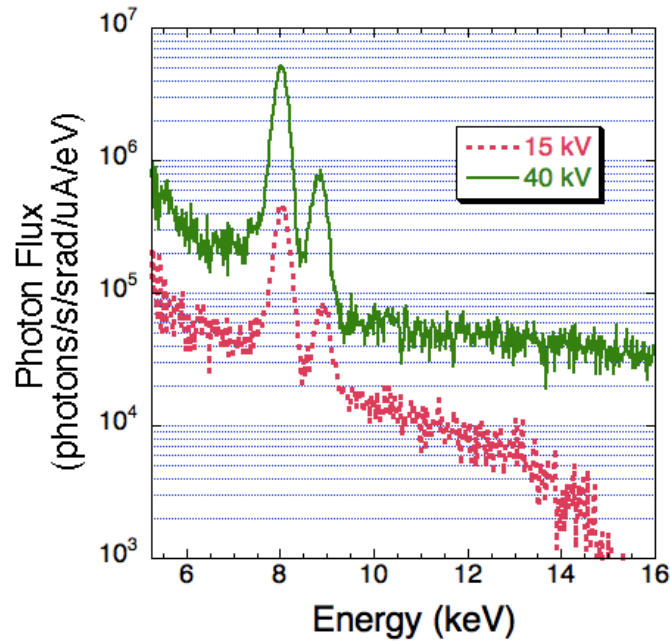


Figure 5.14: Final corrected spectra for the output of the Moxtek cw X-ray source.

of silicon $250\mu\text{m}$. It was biased with 300 V and used in conjunction with a chopper in order to measure an AC signal on an oscilloscope (Tektronix TDS 220 with an internal resistance of $1\text{M}\Omega$).

For the corrections to the PIN diode data, the following need to be considered. First, the transmission of X-rays through air. Secondly, the efficiency of the silicon ($250\mu\text{m}$ thick) to each incident X-ray, which is calculated via the same photoabsorption equation used for the CdTe detector. The transmission of air and efficiency of Si are plotted in Figure 5.15. The diode will generate a current proportional to the total amount of energy, so more current for harder X-rays and less current for softer X-rays. Therefore to compute the current of photons, the Amptek spectrum is taken and weighted by the energy of each photon bin. This energy value is then divided by 3.6 eV per EHP generated in Si, then multiplied by the charge per electron to get the current in C/s. The current is then multiplied by the scope resistance ($1\text{M}\Omega$) and a factor of 1000 to convert it to mV. The results are summarized in Table 5.1, which shows good agreement between the Amptek spectra and the measurements on the PIN diode.

In the low energy limit, the transmission factors approach zero, and division by increasingly small transmission values tends to amplify noise from low counts. Therefore a cutoff was inserted into the spectra, forcing all counts below 6.36 keV to be zero. It can be seen in Table 5.1 that such a cutoff was appropriate for higher tube voltages, but underestimated the flux for lower tube voltages.

A linearity test of the X-ray source was also carried out. This was done using a highly-oriented pyrolytic graphite crystal (HOPG). The crystal basically has a mosaic-like random orientation of crystal planes so that the crystal's surface can be a broadband, high-reflectivity spectrometer selective to X-ray energy. In fact, in Fast Ignition experiments it is often used as a spectrometer. The author designed a

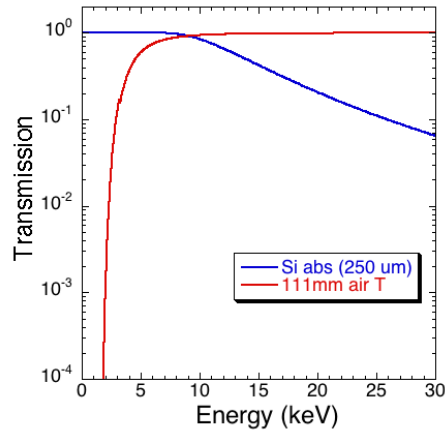


Figure 5.15: The transmission of 111 mm of air and the photoabsorptive efficiency of 250 μm Si versus energy.

housing for use on Titan of the same HOPG crystal that was used in this linearity test.

The setup is shown in Figure 5.16. The Image Plates were scanned using the University of Alberta IP reader (discussed in Section 6.5). For reference the camera used was a Chameleon camera, the LED flash time was 0.520 s and the camera exposure was 0.5 s with the 24 dB filter setting. The lens used had a 6 mm focal length (Fujinon DF6HA-1B). The HOPG will separate the various X-ray energies into different locations because the Bragg condition is satisfied at different angles of incidence. Therefore the K_α peak is effectively filtered out and can be measured easily on any broadband detector (in this case, an image plate). Absolute numbers are estimated from measured calibration factors and source fluxes, and theoretical HOPG reflectivity and angular acceptanceⁱ. Some calibration factors have a large uncertainty and therefore quantitatively these results should be considered preliminary. The results are plotted in Figures 5.17 and 5.18. The linearity of the response with time is indicative that the image plates have a linear response to cumulative K_α exposure

ⁱA reflectivity of 0.4 was assumed with an angular acceptance of ≈ 10 mrad.

Table 5.1: PIN diode measurements vs. Amptek results

kV	μA	V measured on PIN (mV)	V predicted by Amptek (mV)	% error
15	50	13.6 ± 1	10.0	35.7
15	25	5.8 ± 1	5.0	15.7
15	75	18.2 ± 1	15.0	21.1
15	100	22.8 ± 1	20.0	13.7
15	10	3.0 ± 1	2.0	51.6
25	100	79.2 ± 2	77.5	2.3
30	100	111 ± 4	110.4	0.5
35	100	148 ± 4	146.7	0.9
40	100	178 ± 4	177.8	0.1
20	100	50.4 ± 2	45.1	11.7
10	100	5.3 ± 1	3.0	75.3

(with a 12% error), which is a basic assumption for many other results in this thesis.

5.8 Resolution

The resolution of the microscope was tested using a $5 \mu\text{m}$ thick gold mesh with a period of $34 \mu\text{m}$ (Structure Probe, Inc.) backlit by the cw X-ray tube. To quantify the resolution a $50.8 \mu\text{m}$ tantalum foil (Goodfellow, 99.9% purity) was used to obtain edge measurements and infer the Modulation Transfer Function (MTF). The results are plotted at the end of this section in Figure 5.27, showing better than $30 \mu\text{m}$ resolution over a $300 \mu\text{m}$ field of view, reaching as low as $15 \mu\text{m}$. The theoretically predicted resolution was computed using commercial ray tracing software (ZEMAX). ZEMAX is an optical ray tracing code which is applicable in this case since the diffraction spot size is submicron making diffraction effects negligible. The steps to obtain the resolution are outlined below.

Any imaging system has an inherent image spread, either limited by geometrical properties or diffraction effects. In other words, any imaging system will not form a

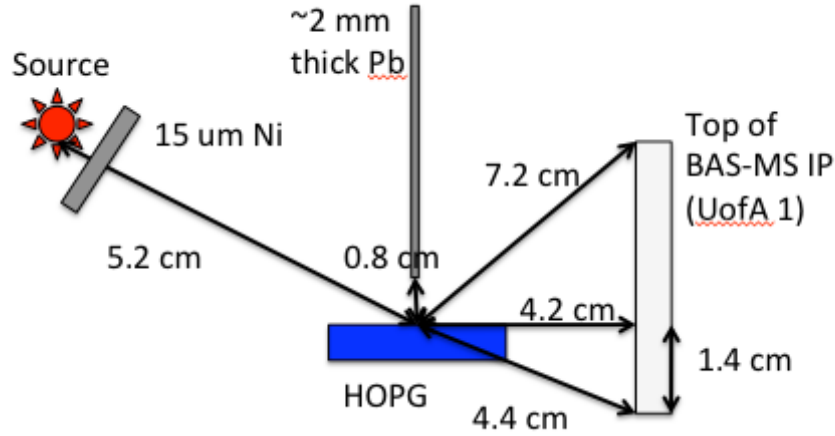


Figure 5.16: The setup for the linearity test using the HOPG crystal done on 2010.10.15.

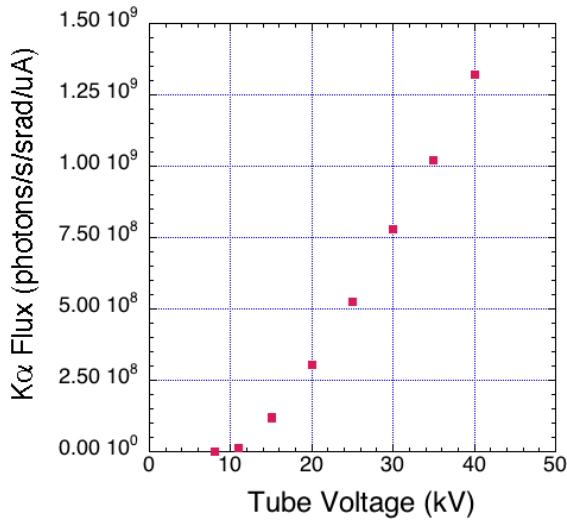


Figure 5.17: The results from the HOPG voltage scan done on 2010.10.15. Fluxes are based on preliminary calibration values.

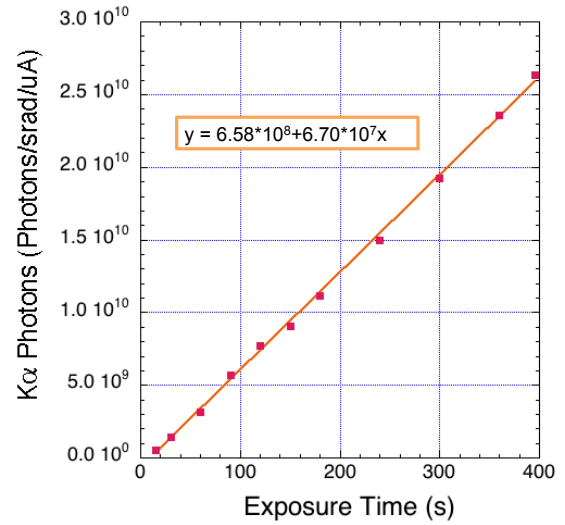


Figure 5.18: The results from the IP linearity test done on 2010.10.15. Fluxes are based on preliminary calibration values. The standard deviation of the fit is 1.4×10^9 photons/srad/μA, or 12% of the average photon signal.

perfect point image of a point source. The image formed from a δ -function source in such circumstances is called a point-spread function (PSF) (plotted in Figure 4.8 in Chapter 4), and is one way of characterizing the performance of an imaging system [73].

Since we do not have access to a very small point source, the δ -function has to be created indirectly, as outlined below. However, there was one image from an experiment on Titan that was small enough to demonstrate qualities of the PSF. The KB microscope was on port TS1, looking at the target from behind (a simulation of the view is given in Figure 6.33). The target was a buried cone depicted in Figure 5.19. It was a shot with 112 J in 0.7 ps in a 10 μm size spot (the prepulse monitor was not run, so it is unknown, but the intrinsic prepulse is expected to be ≈ 10 mJ in 1.5 ns). The detector used to obtain the KB image was a Princeton Instruments CCD camera (see Section 6.5). If the K_α emission from the copper layer was weak, the KB microscope typically didn't see any of the fluorescence from the copper layer (the signal on the Bragg crystal K_α imager was ≈ 1.2 PSL, indicating weak emission). There were some uncertainties about cone alignment and from the weak K_α signal it was surmised that the shot hit the cone wall, producing a small and bright Bremsstrahlung spot visible by the KB microscope.

The image obtained was first smoothed in ImageJ, which involves averaging the pixel value in a 3x3 neighbourhood. The smoothed image, shown in Figure 5.20 had a FWHM size of 8 ± 2 μm horizontally and 6 ± 2 μm vertically (obtained using linewidths of 5 pixels for the lineouts). The vertical angle (first mirror) was 9.3 ± 0.7 mrad, and the horizontal angle (second mirror) was 10.1 ± 0.7 mrad. The imaging parameters were $p_1=94.1$ mm, $p_2=119.5$ mm, $q_1=1289.2$ mm, $q_2=1278.7$ mm for magnifications of 13.7 and 10.7 respectively. The lineouts resemble the expected PSF, and in order to try and reproduce this effect, the same conditions were set in the ZEMAX ray

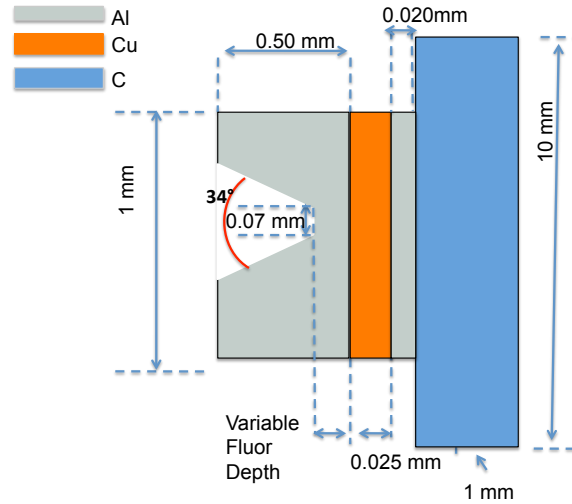


Figure 5.19: The target shot for 2011.06.01 shot#3 on Titan. The fluor depth is $100 \mu\text{m}$.

tracing code, with a source spot size of $10 \mu\text{m}$. The spot obtained and the lineouts are also shown in Figure 5.20. The ZEMAX spot had a FWHM of $11 \mu\text{m}$ horizontally and $9 \mu\text{m}$ vertically. The lineshapes for both experimental and theoretical images are similar, and a direct comparison of the vertical lineouts is shown in Figure 5.21. The PSF of the KB microscope seems consistent with the lineshape, but the noisiness of the image prevents a stronger conclusion. Since such small source sizes are rare and of very low signal level in laser-plasma experiments, another test of the KB microscope's resolution must be used.

When the source is in fact a line emitter, the point spread function becomes what is called the line-spread function (LSF). It is essentially the response to a delta function in one dimension [112]. The frequency domain of the line spread function describes how a modulation of a given frequency will be transmitted through the imaging system. This frequency domain information is also useful, because one can decide on an imaging system that has good imaging properties for the frequencies or

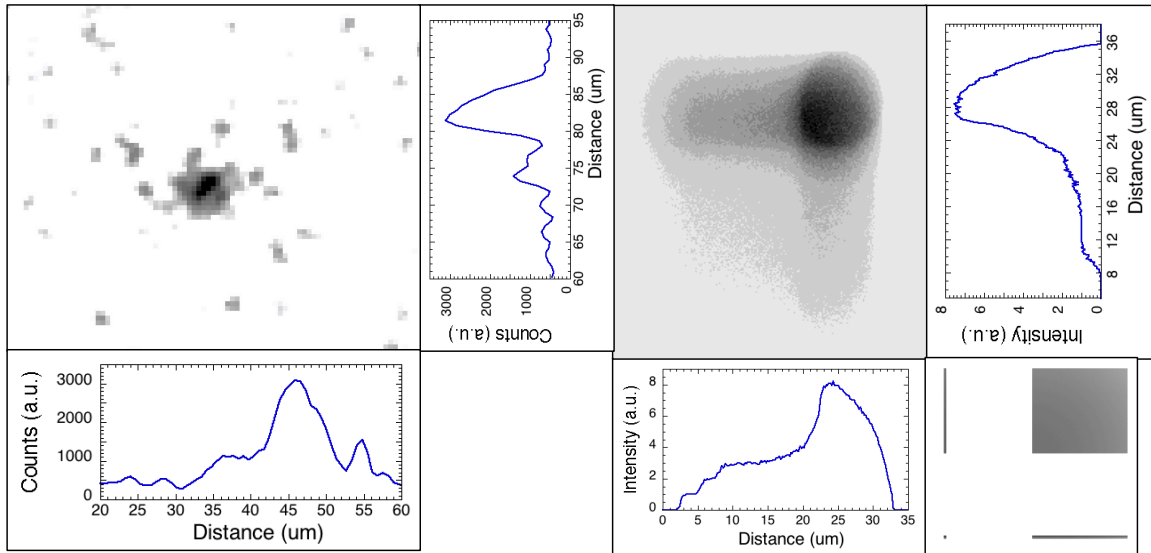


Figure 5.20: Left: Experimental image and lineouts (linewidth=5) obtained with the KB microscope on 2011.06.01 shot#3 on Titan. The KB diagnostic was run by Mianzhen Mo and Shaun Kerr for this experiment. Zero-order and 1D image orientation shown in bottom right. Right: Theoretical image and lineouts obtained using ZEMAX with a $10 \mu\text{m}$ diameter source and the same angles in the image on the left.

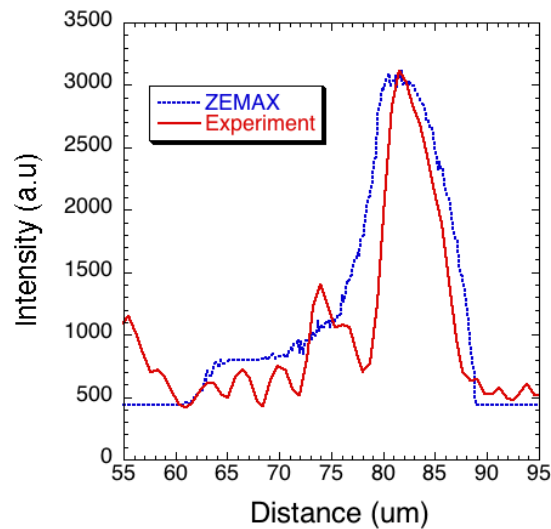


Figure 5.21: A plot of the vertical lineouts (experimental and theoretical) through the images in Figure 5.20. The ZEMAX lineout has been scaled arbitrarily.

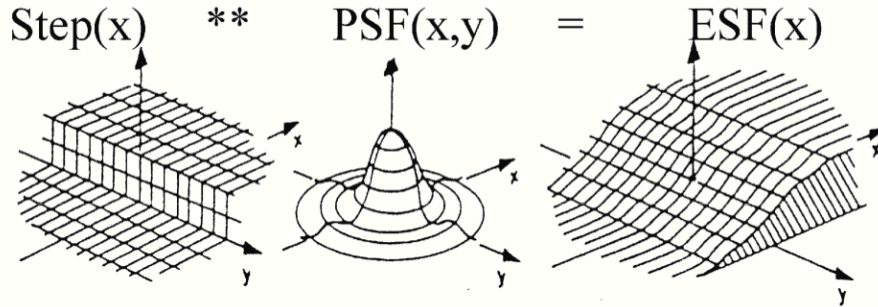


Figure 5.22: How the edge spread function (ESF) is related to the point spread function (PSF). [112]

modulations of interest. The function describing how an imaging system will transfer modulations of varying frequencies is called the modulation transfer function (MTF). Rigorously it is defined as [112]

$$MTF(k) = \int_{-\infty}^{\infty} LSF(x) e^{2\pi i k x} dx \quad (5.12)$$

That is, the MTF in one dimension is the fourier transform of the LSF.

In order to obtain the LSF from which one can obtain the MTF, an edge is first imaged. The convolution of the edge with the PSF produces an edge spread function (ESF) [112], as shown in Figure 5.22. The ESF is related to the LSF by

$$ESF(x) = \int_{-\infty}^x LSF(x') dx' \quad (5.13)$$

or, in other words, as shown in Figure 5.23 [112]

$$LSF(x) = \frac{d}{dx} ESF(x). \quad (5.14)$$

The above steps were carried out numerically, after obtaining a lineout of the edge

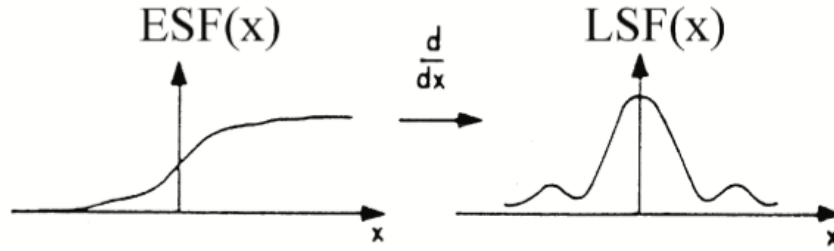


Figure 5.23: How the edge spread function (ESF) is related to the line spread function (LSF). [112]

spread function (ESF) from the image of the edge of the tantalum foil. The derivative was carried out using a finite difference formula:

$$LSF(x_i) = \frac{ESF(x_{i+1}) - ESF(x_{i-1}))}{x_{i+1} - x_{i-1}} \quad (5.15)$$

and was normalized by dividing by the peak value.

The Fast-Fourier Transform (FFT) algorithm in MATLAB was used, whose output is not normalized and so needs to be divided by the number of points. In addition, the numerical LSF used was padded with zeros so that the total number of points would be a power of 2. This speeds up the computation considerably because the algorithm for the FFT relies upon the assumption that the number of points is a power of 2 [113].

Experimentally, the tantalum foil was positioned by trial-and-error using micrometer translation stages. It began clipping the images as shown in Figure 5.24.

In order to correctly visualize and understand the behaviour of the KB in this imaging setup, it was modeled using a commercial ray-tracing code (ZEMAX). A circular source with a diameter of $300 \mu\text{m}$ was used, the first mirror 108.26 mm from it as in the experiment. The tantalum foil was placed at 14.95 mm from the source,

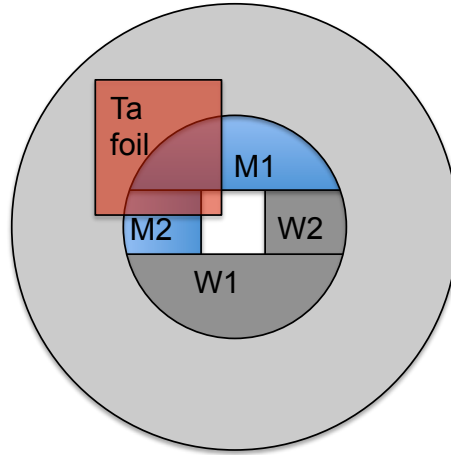


Figure 5.24: How the tantalum foil was positioned relative to the mirrors.

making the object distance for the first mirror 93.31 mm. The image distance for the first mirror was 1354.5 mm for a magnification of 14.5. For the second mirror, the object distance, image distance and magnification were 118.71 mm, 1329.1 mm and 11.2, respectively.

The tungsten rods were modeled using the "ABSORB" material in ZEMAX, and placed at the identical offsets as in experiment (0.94 mm and 1.17 mm, respectively). More details about the ZEMAX simulations can be found in Appendix A.6.1.

A sample image, along with the lineout for the ESF, and the calculated LSF and MTF, is shown in Figures 5.25 and 5.26. For the resolution calculations the FWHM of the LSF is used. The MTF was also calculated to provide additional information for future reference. The amount of modulation, for reference, is defined as [73]

$$Modulation \equiv \frac{I_{max} - I_{min}}{I_{max} + I_{min}} \quad (5.16)$$

Every single LSF was inspected and fit with a gaussian function using a least-squares Levenberg-Marquardt algorithm, until the shape was an accurate representation of

the performance. For some of the higher angles of incidence where the signals were very noisy due to low reflectivity and low signal levels, some smoothingⁱⁱ was applied through ImageJ.

The results from the angular scans in this dimension are shown in Figure 5.27. What is quite remarkable is that M2 had a black damage spot on it where the coating had been removed, yet seemed to perform well in terms of focusing X-rays. For larger angles less of the mirror is used since portions of the mirror are in the low reflectivity regime. To illustrate this effect, a plot of effective mirror size for different threshold reflectivities is included in Figure 5.28. For example, at 14 mrad only a quarter of the mirror surface ($\approx 8mm$) is reflecting more than 5 % of incident X-rays. A smaller mirror size results in a better resolution, which is probably why some points above 8.73 mrad have a resolution that appears better than the theoretical ZEMAX. They have better than 30 μm resolution over a relatively large angular aperture from 6 to 12 mrad, with resolution as good as 15 μm in some cases.

In order to obtain the resolution results from ZEMAX, a macro was written. Since ZEMAX is not built to work at grazing incidence, there is no straightforward way to optimize the number of rays going through the system at a specific angle. Therefore the Footprint window was used, which calculates the percentage of rays traced that succeed in making it to the image plane. It was found that in the majority of cases, a footprint above 60 % meant that the rays from the cone source were not filling the aperture of the mirror. Below 40 %, and not enough rays were being traced to give an accurate measurement of the spot size. What the macro did, for each angle of interest for each mirror, was find an appropriate angular aperture whose footprint was between 40 and 60 percent. The ZEMAX Programming Language (ZPL) was used.

ⁱⁱThe smoothing made every pixel the average of its 3X3 pixel neighbourhood.

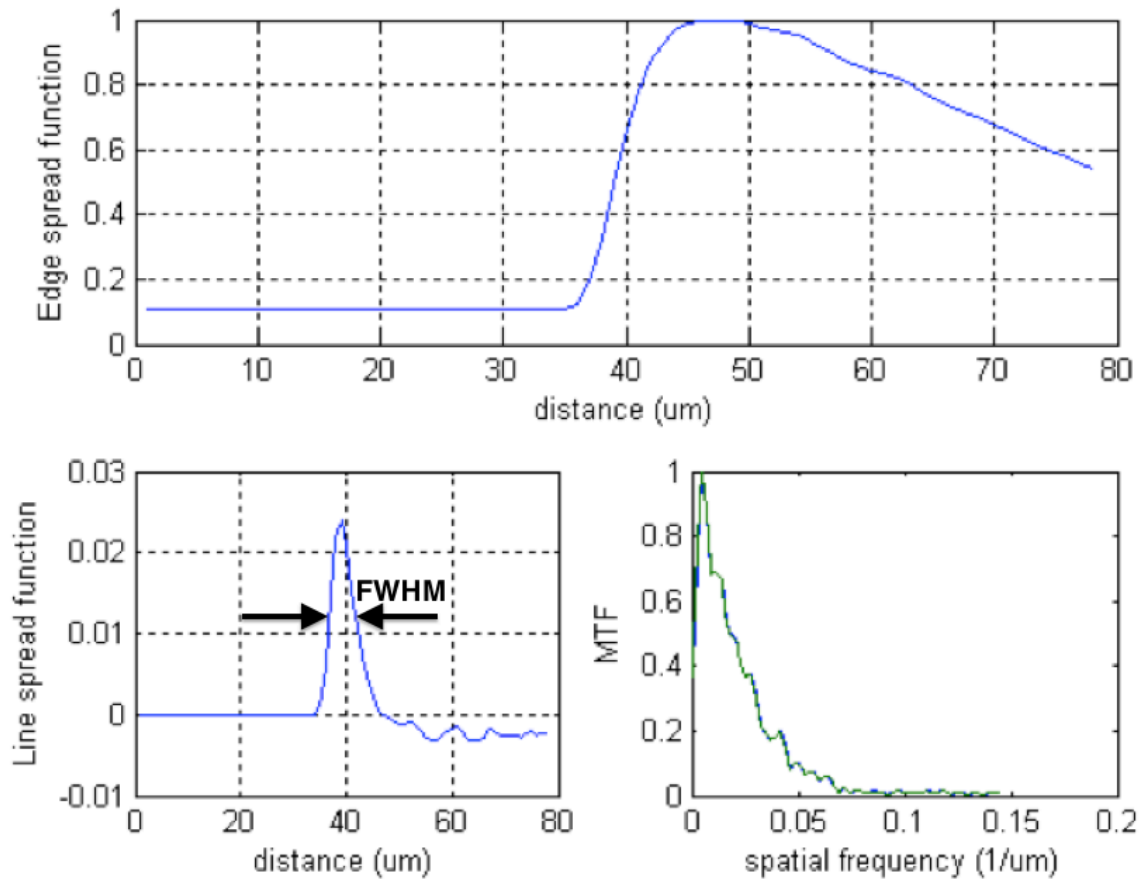


Figure 5.25: A sample ESF, LSF and MTF measured for M1. Image plate #7 was used, and the X-ray tube was set at 15 keV, 100 μA . The exposure was 41 mins. and the delay before scanning was 28 mins., scanned on the FLA-5000. The FWHM of the LSF is 17 μm . The MTF reaches the value of 0.1 at 0.0456 μm^{-1} which corresponds to a resolution of 22 μm . The green curve on the MTF shows how well the interpolation function matches the output. This is the edge obtained for the image shown at the far right of Figure 7.20, at 8.58 mrad.

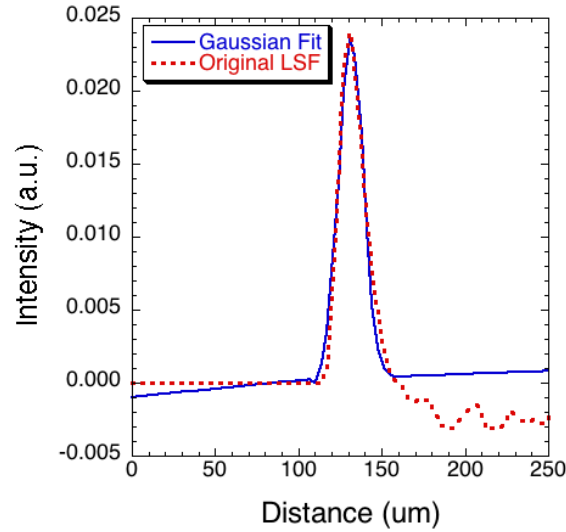


Figure 5.26: A sample LSF and the gaussian fit for the image shown at the far right of Figure 7.20, at 8.58 mrad. The FWHM is $17 \mu m$.

In addition to the LSF scans, a qualitative assessment of the resolution was done using a gold mesh normally used to calibrate SEM and LMs (Structure Probe, Inc.). The entire mesh was between 2.5 to $5.0 \mu m$ thick, and the specifications were a $25 \mu m$ hole size, $8.6 \mu m$ wire width for a mesh period of $33.6 \mu m$ (part no. 02799G-AB). When measured in the precalibrated Light Microscope, the wires were found to be $14 \pm 1.3 \mu m$ wide, and the holes $21 \pm 1.3 \mu m$ for a total mesh period of $35 \pm 1.8 \mu m$. The wires are assumed to be flat, not rounded, since the width is roughly three times the depth.

A $15 \mu m$ nickel filter was used, and the X-ray tube set to 15 kV, $100 \mu A$. For roughly 30 minute exposures, the images were collected on image plates (BAS-MS) and scanned on the FLA-5000 (Fujifilm image plate scanner). The results for an angular scan for mirrors M1 and M3ⁱⁱⁱ are shown in Figure 5.31. One can qualitatively see the defocusing of the microscope as the angle is increased or decreased out of

ⁱⁱⁱFor explanation of M1-M4, see Section 5.2.

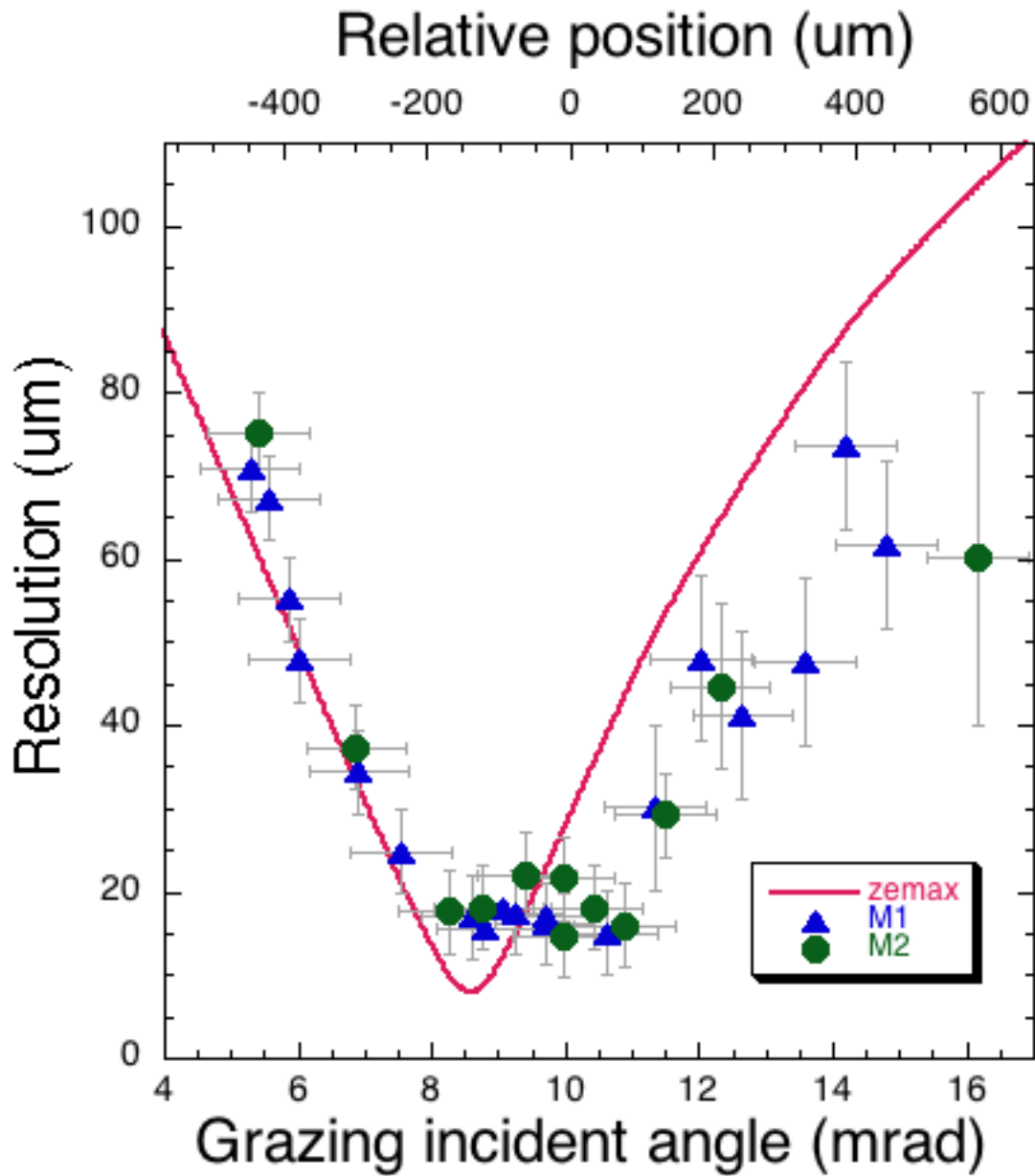


Figure 5.27: Resolution of the KB microscope using a Ta edge and the calculated MTF.

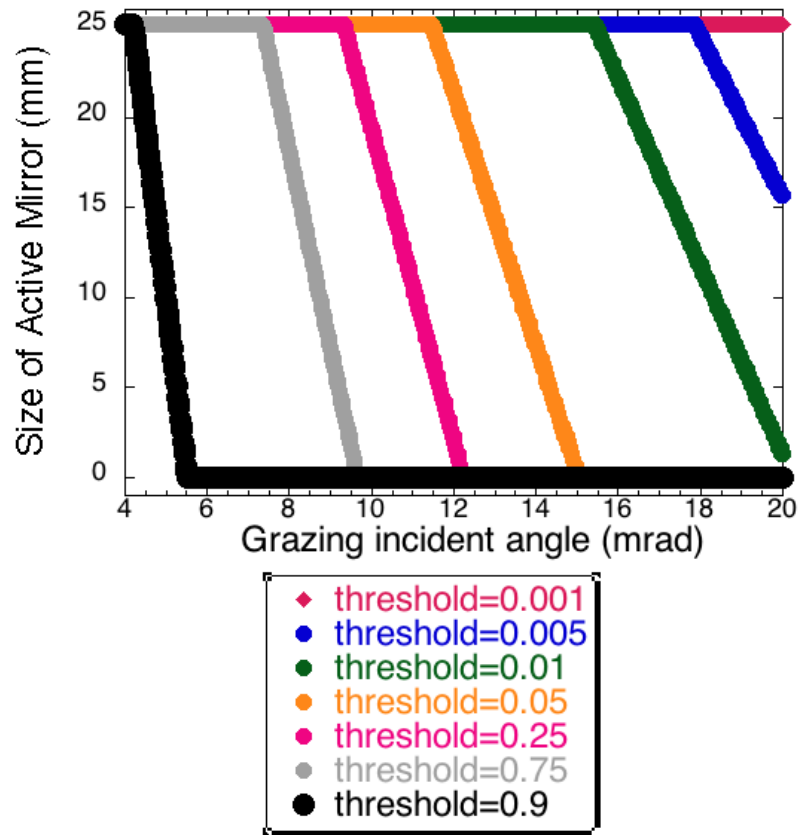


Figure 5.28: Effective size of the mirror versus angle for different threshold reflectivities, assuming a flat 25.4 mm diameter mirror for simplicity.

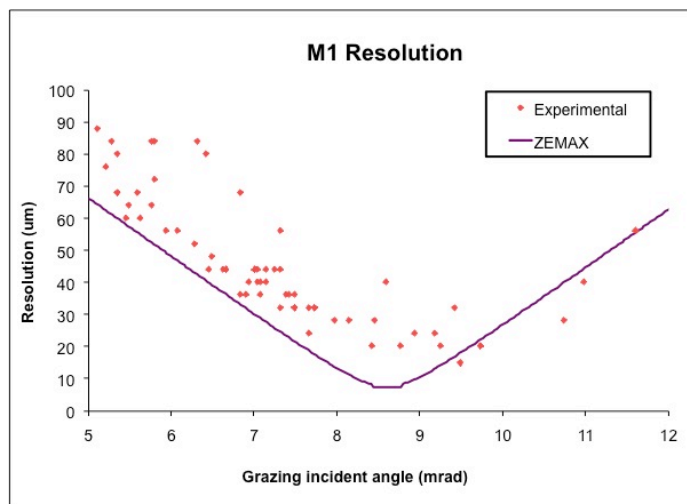


Figure 5.29: The spot sizes of the KB microscope obtained during fast electron experiments on Titan, compared against that predicted by ZEMAX.

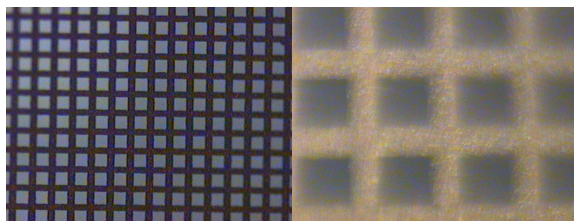


Figure 5.30: Two pictures of Gold mesh used for qualitative image testing, at different magnifications. Pictures taken using light microscope.

best focus. For the best focus, the measured mesh periods were $33\pm 2\mu m$ vertically, and $36\pm 2\mu m$ horizontally. The vertical focusing mirror (M1) was the first mirror, which is why the best focus occurs around 8.73 mrad for it, and 10.35 mrad for the second mirror (M3). A similar scan was carried out for M2 (vertical focusing, first mirror) and M4 (horizontal focusing, second mirror), and the measured mesh period was $33\pm 2\mu m$ vertically, and $36\pm 4\mu m$ horizontally. Although the quantitative LSF was not done for M3 and M4, the indication from experiments as well as from this qualitative resolution assessment is that they perform comparably to the other two mirrors.

The effective transmission of the gold wires is calculated by taking the source spectrum, multiplying by the appropriate filter factors for air, Ni, and Al; multiplying by the reflectivity curve versus energy for a Platinum mirror at 8.73 mrad; then computing the average energy using the spectrum as a weighting function. The transmission of gold for the energy obtained is then used as the effective transmission for the gold wires of the mesh. The weighted average energy computed was 8.003 keV, which corresponded to a transmission of 0.13416 ($5\mu m$ Au) to 0.44777 ($2\mu m$ Au). Since the depth of the mesh is unknown, both cases are investigated below.

The transmission through the mesh was then plotted as function of position for ten mesh periods (of $35\mu m$), depicted in Figure 5.33. The source was then modeled using a gaussian function with a FWHM of $180\mu m$, which was multiplied by the mesh transmission to produce the curve in Figure 5.34. This function then needed to be convolved with the PSF of the KB microscope.

The shape of the PSF is known from Figure 4.8, but it was modeled again in ZEMAX for the identical conditions for the mesh imaging. A preliminary investigation of the change of the PSF with angle was done by considering two cases: $200\mu m$ (≈ 2 mrad) higher or lower in the field of view. It was found that, as a first approximation,

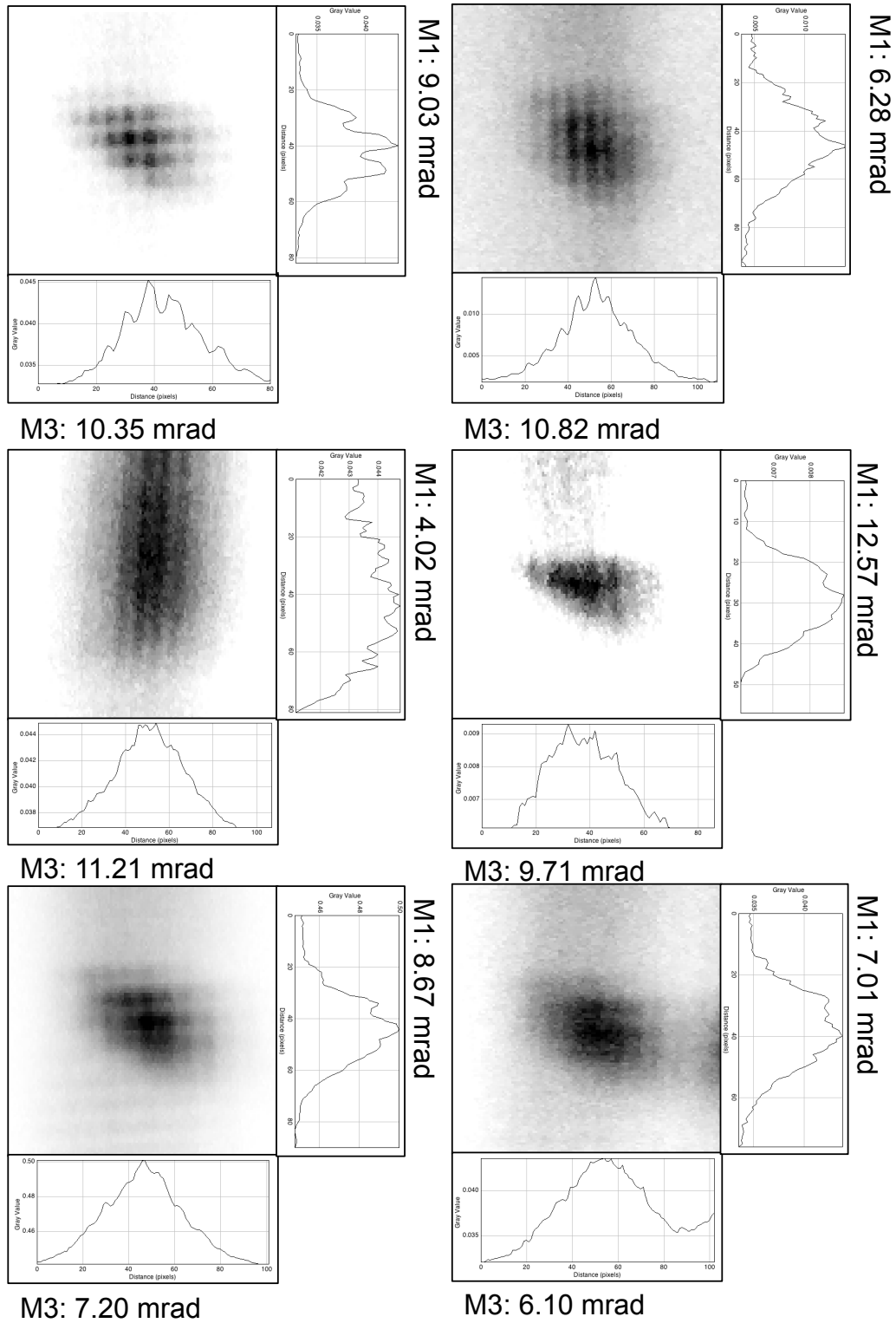


Figure 5.31: X-ray mesh images obtained using M1 and M3 during the qualitative resolution angular scan. Lineouts taken with linewidth=4 pixels. M1 is closer to the source.

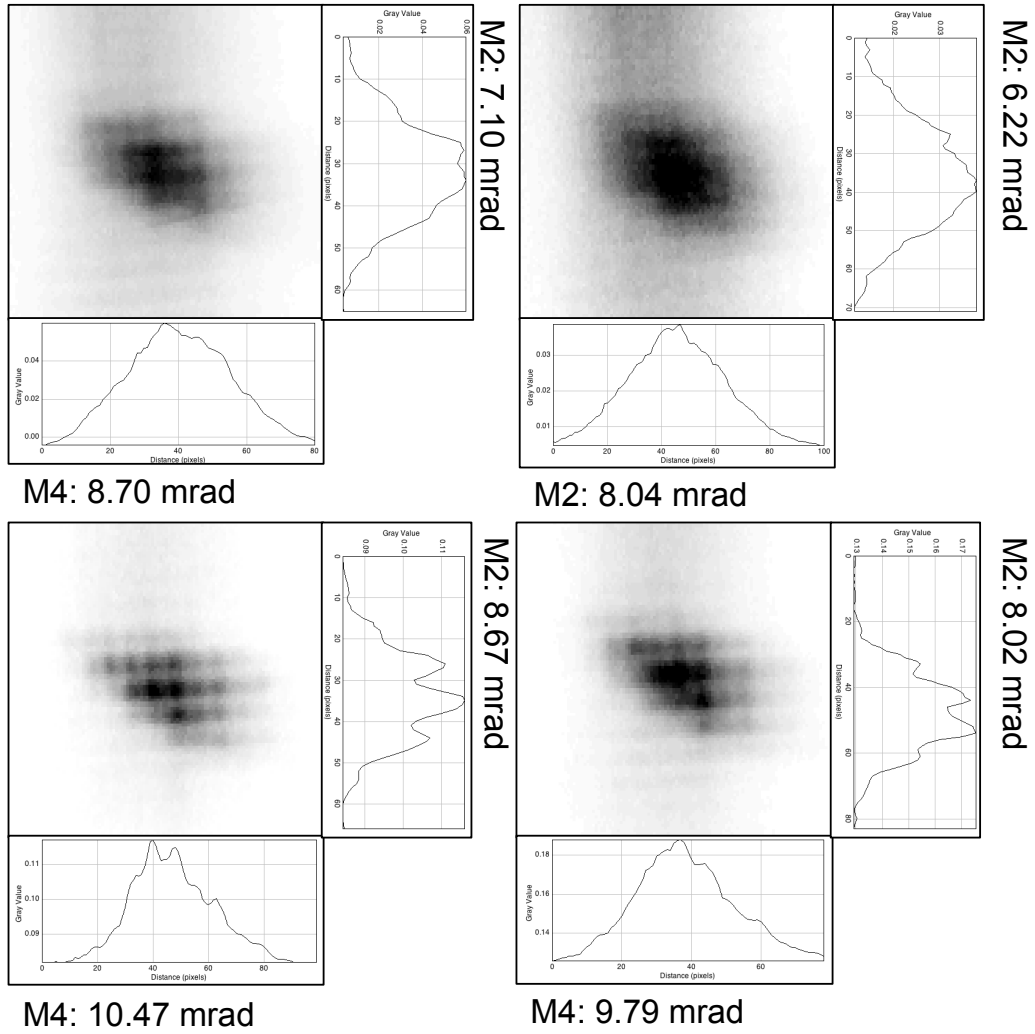


Figure 5.32: X-ray mesh images obtained using M2 and M4 during the qualitative resolution angular scan. Lineouts taken with linewidth=4 pixels. M2 is closer to the source.

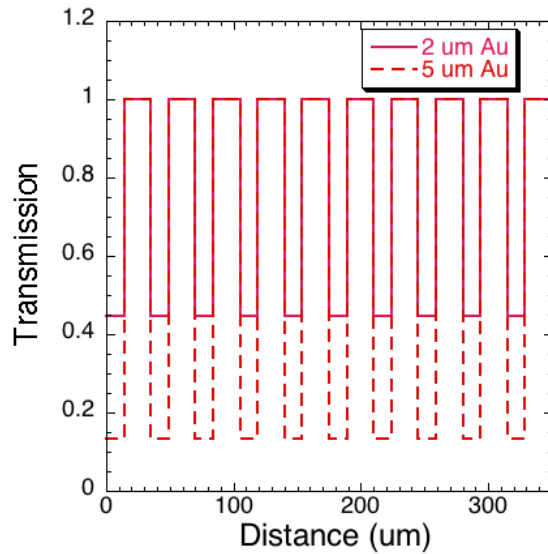


Figure 5.33: The mesh transmission functions for $2\ \mu\text{m}$ and $5\ \mu\text{m}$ Au, after taking a weighted average of the source spectrum and looking up the tabulated transmission of Au.

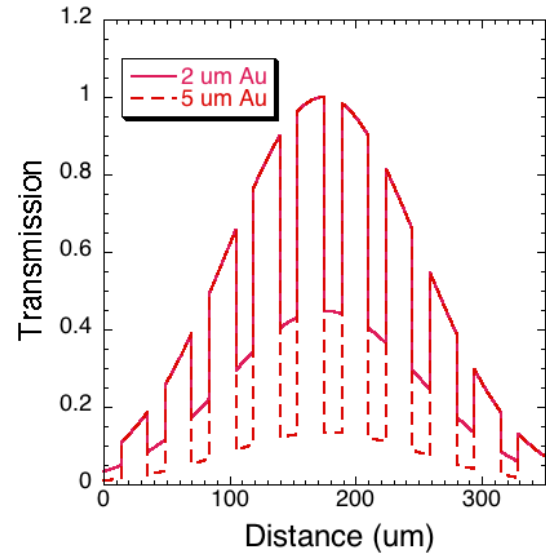


Figure 5.34: The gold transmission curves multiplied by a $180\ \mu\text{m}$ FWHM gaussian function to represent the X-ray source.

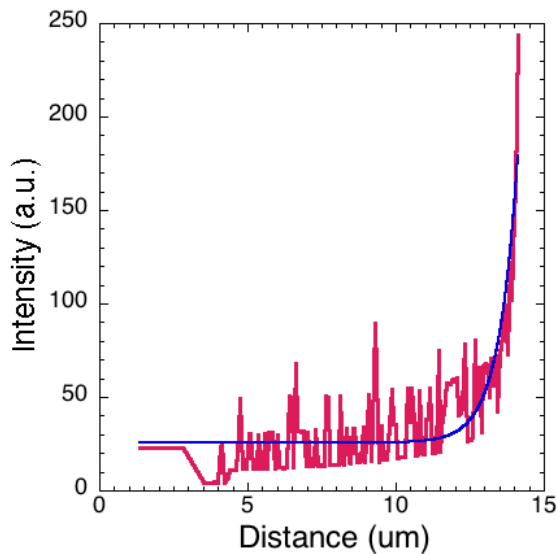


Figure 5.35: A sample exponential fit of the PSF for $8.73\ \text{mrad}$ angle of incidence. The raw PSF was generated in ZEMAX. The curve fit had an $R=0.82$.

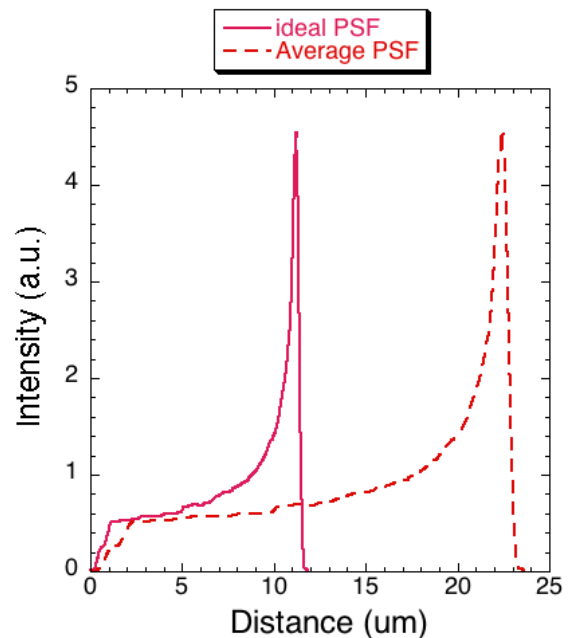


Figure 5.36: The ideal PSF (from ZEMAX) and the average PSF obtained by doubling its lateral size.

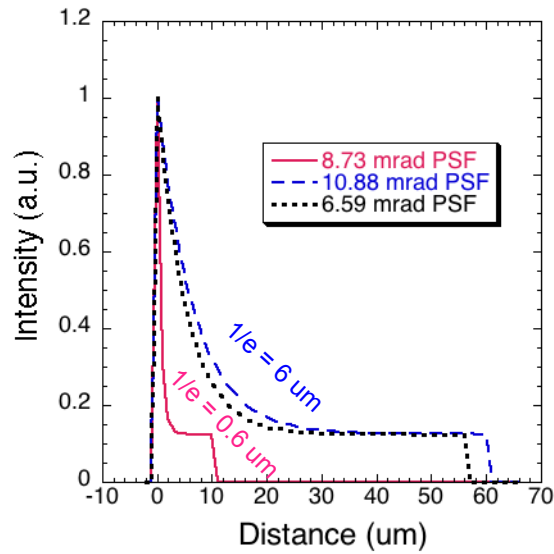


Figure 5.37: The increase in $1/e$ scalelength and tail length observed by changing the position in the field of view by $200 \mu\text{m}$ in each direction from best focus.

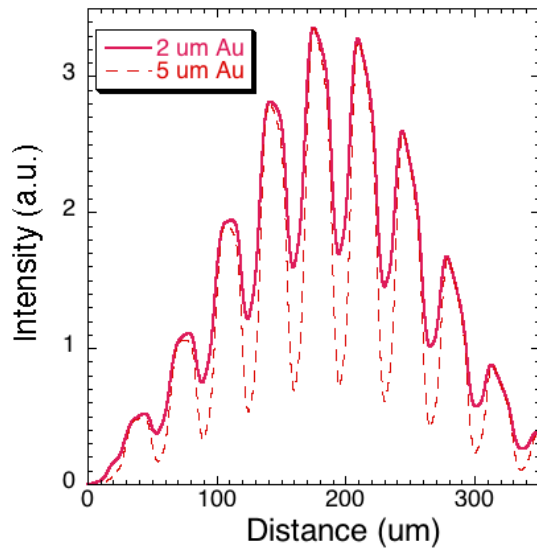


Figure 5.38: The lineshape obtained by convolving Figure 5.34 with the ideal PSF. The maximum contrast is 2.0 and 4.3 for the $2 \mu\text{m}$ and $5 \mu\text{m}$ cases, respectively.

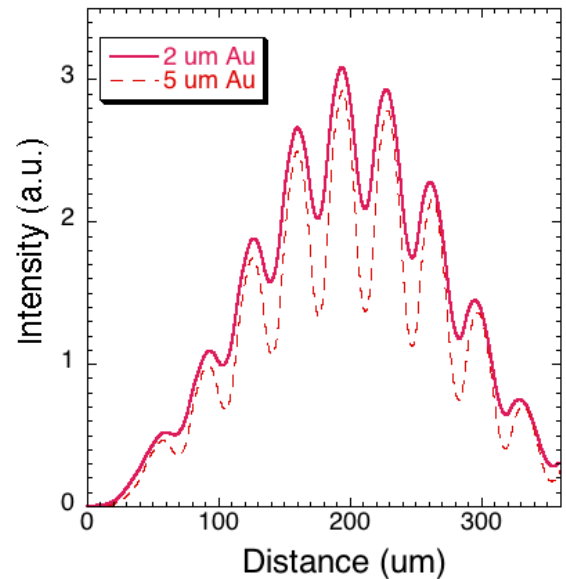


Figure 5.39: The lineshape obtained by convolving Figure 5.34 with the average PSF. The maximum contrast is 1.5 and 2.3 for the $2 \mu\text{m}$ and $5 \mu\text{m}$ cases, respectively.

the PSF can be modeled by a step function with an exponential decay to a flat tail. When the length of the tail changed by a factor γ , the $1/e$ scalelength of the PSF changed by 1.7γ . A sample exponential fit is given in Figure 5.35, and the modeled exponential functions in Figure 5.37, where the PSF stretches by a factor of 6 in the tail, and a factor of 10 in the $1/e$ scalelength.

The best-focus PSF was then convolved with the mesh and source transmission (from Figure 5.34) to produce the lineshape in Figure 5.38. This image has a maximum peak-to-valley contrast of 2.0 for the $2\ \mu\text{m}$ Au case, and 4.3 for the $5\ \mu\text{m}$ Au case. This image represents an ideal case of the image possible if the KB were in good focus across the field of view. The inferred mesh period remains, on average $35\ \mu\text{m}$; however, the sharp front edge of the PSF makes the transmission peaks have an edge (the rightmost peaks of Figure 5.38) which increases the error in the mesh period to approximately $2\ \mu\text{m}$.

A more realistic model is to take an average PSF that represents the angular changes across the view of the mesh, and convolve that with Figure 5.34. A sample PSF was constructed by doubling the $1/e$ scalelength of the best focus PSF and doubling the length of the tail, as shown in Figure 5.36. This may slightly overestimate the length of the tail. It remains for future work to obtain a more accurate model for the average PSF. The result of the convolution of this average PSF is shown in Figure 5.39. The maximum peak-to-valley contrast in this case is 1.5 for the $2\ \mu\text{m}$ Au case, and 2.3 for the $5\ \mu\text{m}$ Au case. The inferred mesh period in this case is in fact better despite the lower contrast. The inferred period is $35\ \mu\text{m} \pm 1\ \mu\text{m}$. A possible explanation is that the longer tail of the average PSF tends to spatially average the sharp front edge of the PSF as it is convolved with the curve.

In comparison, the best contrast achieved in the experimental mesh images was 1.6 ± 0.2 . The experimental performance seems to agree with the $2\ \mu\text{m}$ case, but a

measurement of the exact mesh thickness is needed in order to determine whether the poor contrast is due to the mesh or the focusing capability of the KB microscope.

A final note is that the exposures were 30 minutes long, meaning that the KB microscope needed to be stable over that length of time in forming the images. Therefore the experimental qualitative resolution may be better than shown in these images.

5.9 Incident Angle and Reflectivity

Since Cu tracer layers are widely used in Fast Ignition experiments to characterize the hot electron source and transport, the microscope was designed for an X-ray energy of 8 keV, the Cu K_α line. The theoretical reflectivity at 8.05 keV based on Fresnel reflection is plotted in Figure 5.40. A refractive index of $n=0.9999-4.9374 \times 10^{-6}i$ was used based on scattering coefficients from NIST tables [110]. A balance must be struck between the decrease in solid collection angle of the mirror at lower angles and the increased reflectivity. The product of solid angle and reflectivity is shown in Figure 5.40, where it is clear that the chosen value of a 0.5° angle of incidence optimizes throughput. Note that with a fixed curvature for the two KB mirrors, and a fixed angle of incidence, the focal length will be identical for both mirrors. Since the two mirrors cannot be located at the same distance to the image, only one mirror would be in best focus at this optimal angle at any given time. Often two different angles are employed to put each mirror in focus, but this is at the cost of lower reflectivity. This sacrifice must be considered carefully, since under normal circumstances the KB microscope suffers from low throughput, possessing a solid angle of $3.4 \mu\text{srad}$ with a reflectivity of $(0.7)^2=0.5$ (two mirrors) for an effective solid angle of $1.7 \mu\text{srad}$, compared to 4.4 mrad of the typical Bragg crystal with a reflectivity of 0.04 for an effective solid angle of 0.2 mrad , 2 orders of magnitude higher [114].

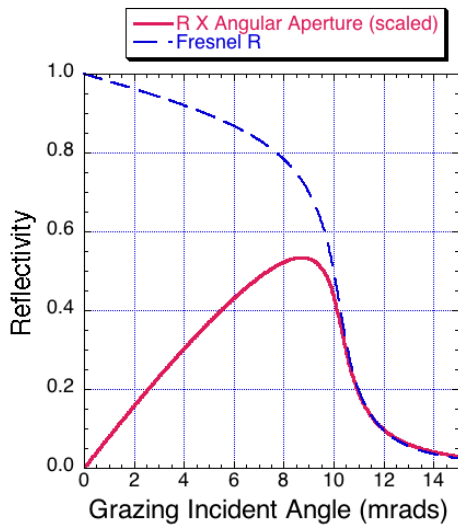


Figure 5.40: Reflectivity at 8.05 keV of the platinum coated mirrors according to Fresnel theory. The solid line depicts an arbitrarily scaled reflectivity times angular aperture for a fixed diameter mirror (25.4 mm), showing that there is an optimal region around 0.5° angle of incidence.

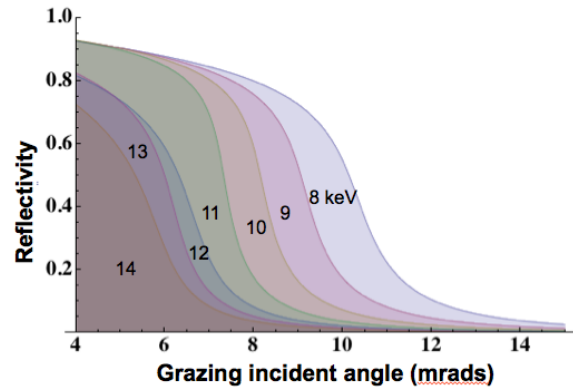


Figure 5.41: The reflection versus grazing incident angle for different X-ray energies, in keV.

The measurement of reflectivity involved using the source at a distance of 108 mm from the first mirror.^{iv} X-ray Image Plates (Fujifilm BAS-MS) were used, covered with 20 μm of aluminum foil. They were scanned on the FLA-5000 scanner, which has been calibrated with the FLA-7000 scanner (Fujifilm) used in Livermore.

The procedure for calibration was to expose an image plate to the cw X-ray source, take it down to Livermore and scan it at a known time on the FLA-7000, and repeat the procedure at the University of Alberta FLA-5000 scanner. The amount of absorbed radiation during transit was also tested and found to be significantly lower than the signal (an average signal of 0.0002 PSL for the extra radiation in transit). The FLA-5000 was approximately 155 times less sensitive than the FLA-7000, based on the average of 7 calibration measurements.

Furthermore, the decay time of the metastable state of the IPs was characterized by another grad student (Mianzhen Mo), as can be seen in Figure 5.42. The best fit is obtained with a double-exponential function,

$$\text{Intensity} = Ae^{-\ln 2t/T_1} + Be^{-\ln 2t/T_2} \quad (5.17)$$

where $A=0.19\pm 0.03$, $T_1=19\pm 8$ min, $B=0.81\pm 0.03$, and $T_2=4400\pm 1800$ minutes. The χ^2 value (sum of the squared errors) is 0.002. The single exponential decay reported in [117] was

$$I = A \exp\left(\frac{-t}{\tau}\right) + B \quad (5.18)$$

where $A=0.231 \pm 0.015$, $B=0.779 \pm 0.117$, and $\tau=107 \pm 19$ minutes. However, this was carried out on a FLA-3000 scanner. A single exponential fit to M. Mo's data gives $A=0.25\pm 0.03$, $B=0.72\pm 0.03$, and $\tau=78\pm 32$, with a χ^2 of 0.004. From the χ^2

^{iv}This was done instead of the optimal distance because the tests were done back-to-back with the resolution tests, and the tantalum foil was translated out of the way so that it could be repositioned again for the second set of mirrors.

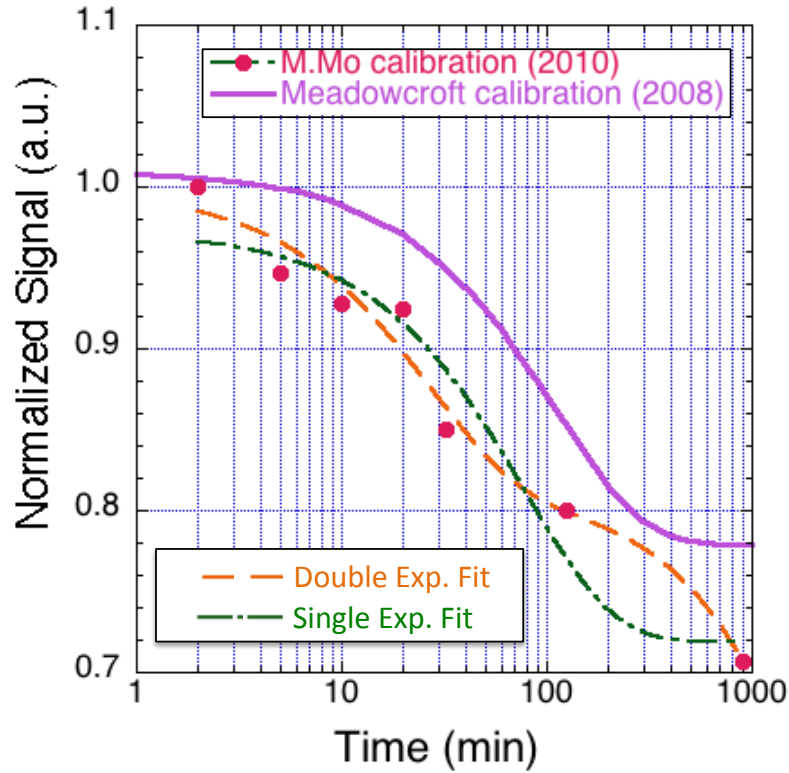


Figure 5.42: The decay of the BAS-MS type Fujifilm IP versus time. The dashed curve represents the double exponential fit, and the dot-dash curve represents the single exponential fit. Data collected by Mianzhen Mo, 2010.

values we conclude that the double exponential is a better fit to the data. Chen made a similar observation of a two-stage decay, but does not list the time constants he obtained [115]. This decay was taken into account in order to determine the original absorbed X-ray flux.

The IP sensitivity to Cu K_α X-rays was measured by Meadowcroft et al. using discrete X-ray line energies generated at the Excalibur soft X-ray facility [117]. The measured sensitivity is given by the following formula as a function of deposited X-ray energy E (in keV):

$$\psi_j = \eta(m_j E + c_j) \quad (5.19)$$

where ψ_j is the sensitivity in mPSL, η is the absorption efficiency, and m_j and c_j are fitted constants with values 0.61 ± 0.02 mPSL/keV and 1.92 ± 0.21 mPSL, respectively. η was determined using a model of the IP composition and using photoabsorption coefficients. In the end the absolute sensitivity to 8.05 keV X-rays for the BAS-MS IP was 1.33 MeV/PSL [117]. This value is a convolution of the absorption efficiency as well as the readout efficiency for de-exciting the metastable state. Similar measurements have been made by Chen [115] giving a sensitivity value of 2.0 ± 0.3 MeV/PSL. This sensitivity value was measured on the scanner that has been calibrated for the experiments (FLA-7000 which was cross-calibrated against the FLA-5000), and so this sensitivity value was used to eliminate any dependence the sensitivity value may have on the scanner type.

The transmission factors for 15 μm nickel, 20 μm aluminum and 144.9 cm of air needed to be taken into account. They are shown in Figure 5.44. The spectra obtained with the Amptek CdTe detector before and after these filter factors are shown in Figure 5.45. The principal purpose of the filtering is to try and make the spectrum primarily copper K_α at 8.05 keV. The spectra reveal that the percentage of K_α in the original spectrum in the range of 7.5 to 8.5 keV is 36 ± 2 %, whereas after the above filtering the percentage of K_α is 68 ± 2 %.

For the analysis the first mirror has a 1D reflection that had a FWHM in the unfocused direction of 219 pixels. Therefore a lineout of a slightly larger girth was taken (320 pixels). The width of the 1D image is determined by the tungsten rod and mirror surface of the opposing mirror. The second mirror has a 1D reflection with a FWHM of 212 pixels (actual lineout size was therefore 270 pixels), but dividing each by the magnification for the opposite mirror (14.52 and 11.196) gives the first and second mirror widths for the 1D image: 980 ± 30 μm and 730 ± 30 μm respectively. These quantities, depicted in Figure 5.43 are crucial for the appropriate calculations

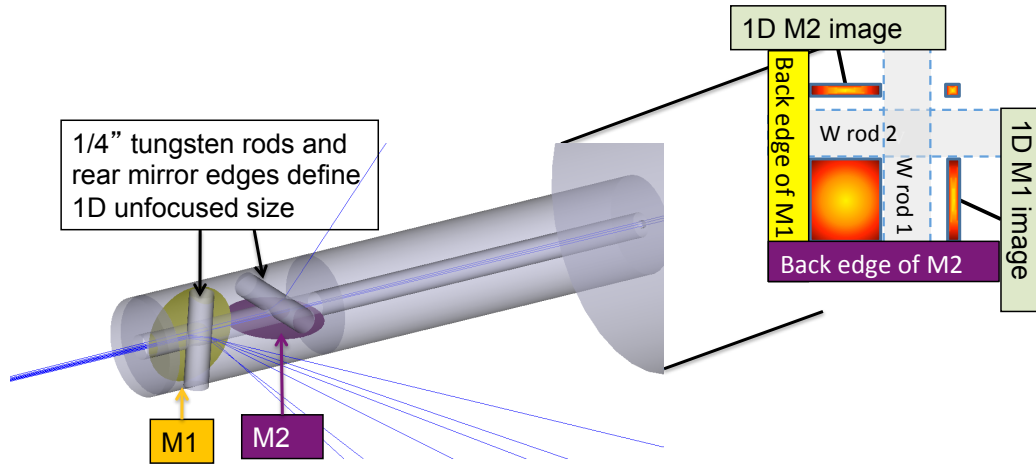


Figure 5.43: The tungsten rods and the rear mirror surfaces define the size of the zero-order as well as the size of the 1D images in the unfocused dimension.

of solid angles.

For the solid angle of the first mirror, the width of the 1D reflection is determined by the *back* edge of the second mirror, and the position of the *second* tungsten rod. For the second mirror, the width is determined by the *back* edge of the first mirror, and the position of the *first* tungsten rod. Since the mirrors are so close to the source the differences in calculation if the wrong distance values are used can be up to 25 %.

Finally, in computing the reflectivity, it is assumed that the mirrors reflect no X-rays above 8.5 keV. This assumption is valid if one investigates the theoretical curves for higher X-ray energies, shown in Figure 5.41. These were computed using f_1 and f_2 scattering factors from NIST [110]. Thus for the denominator in the calculation of reflected signal versus original signal, we take only the X-ray spectrum up to 8.5 keV (70.46% of the total spectrum).

However, for signals below 6 mrad, this assumption is no longer valid, since a significant portion of the higher energy X-rays are reflected at these angles. Therefore an extra factor of $1/0.7046=1.419$ is included for the reflectivities at these low angles.

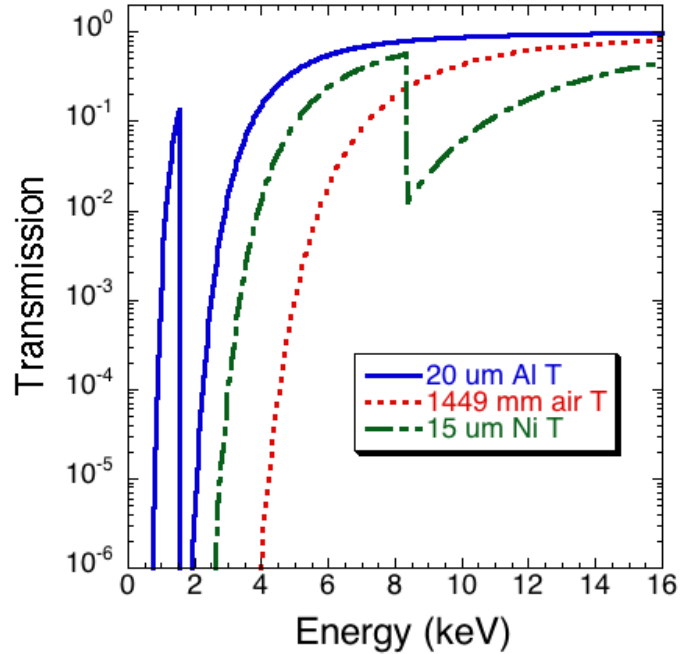


Figure 5.44: Transmission curves for the materials in the reflectivity calibration. The solid (blue) curve is for 20 μm of aluminum. The dash-dot (green) curve is for 15 μm nickel. The dashed (red) curve is for 144.9 cm of air at 760 torr, 298 K.

In addition, work by Chen [115] showed that X-ray energies closer to 20 keV have an IP sensitivity of 1.6 MeV/PSL (for the Mo, Ag, and BaO K_α lines of 17.5, 22.2 and 32.2 keV, respectively). Therefore this sensitivity value was used instead of the 2 MeV/PSL used for the 8 keV X-rays. Since all of these reflectivity values lay in the region of the zero-order which makes background subtraction significantly more difficult, the error bars are significantly larger in this region. Under normal circumstances the KB microscope is not operated at these angles, so the uncertainty in the reflectivity in this region is not a major concern.

In integrating the peaks, a gaussian fit was applied. We then use knowledge of

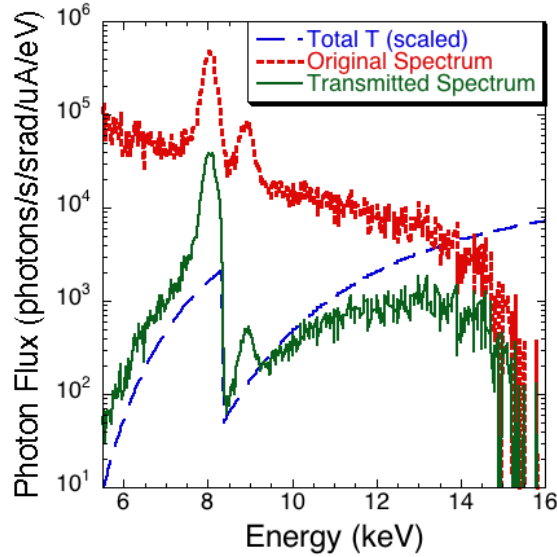


Figure 5.45: The photon flux before and after air, nickel and aluminum transmission. The dashed curve is the total transmission scaled by 2×10^5 for visibility. The edge above 8 keV corresponds to the K edge of Ni and serves to filter a significant amount of the K_β radiation at 8.9 keV.

the definite integral of a gaussian [116]:

$$\int_0^\infty e^{-ax^2} dx = \frac{1}{2} \sqrt{\frac{\pi}{a}} \quad (5.20)$$

Therefore the full integral is simply $\sqrt{\frac{\pi}{a}}$. Since the fit is defined in order to output the FWHM,

$$a = \frac{2.77256}{FWHM^2} \quad (5.21)$$

the equation for the integral becomes (adding the amplitude A)

$$A \int_{-\infty}^{\infty} e^{-ax^2} dx = A \sqrt{\frac{\pi}{a}} = A \frac{FWHM \sqrt{\pi}}{\sqrt{2.77256}} \approx 1.06447 \times A \times FWHM \quad (5.22)$$

The traces from a series of data at various incident angles were fit with a Gaussian

function using a least-squares Levenberg-Marquardt algorithm. The Gaussian function was an arbitrary choice that seemed to match the data reasonably well. Each fit was inspected individually as a script proceeded through the data series. A sample image is shown in Figure 5.48. The final fits had a χ^2 value less than 10^{-3} , where χ^2 is defined as the sum of the squared errors of all the points. In the cases where one mirror reflection was embedded in the zero-order image (as in Figure 5.48), a zero-order background from another image was used and scaled horizontally and vertically in order to provide accurate subtraction of the non-uniform background. It was observed that the size of the zero-order changes slightly depending upon incident angle, since the viewed separation of the rear mirror surface and the tungsten rod (which clip the beam to form two sides of the zero-order) changes with incident angle. That way a clean zero-order image, from another incident angle where the 1D reflection was not embedded, could be used and scaled appropriately where needed. The scaling of the zero-order size is shown in Figure 5.46 and a sample zero-order subtraction is shown in Figure 5.47.

The results for all four mirrors are shown in Figure 5.50 along with a comparison to theoretically predicted Fresnel reflectivity of perfect smoothness (calculated using scattering factors from NIST [110]). The lower angle measurements have a larger uncertainty because the reflections were embedded in the zero-order, and despite the above attempts to accurately model it, the fits were generally less accurate than other cases. Unlike the Titan experiment where the zero-order tended to have a flat-top profile in the majority of cases, the zero-order in these experiments tended to be convolved with the large source function size.

The mirror reflectivities match Fresnel theory fairly well above 9 mrad, and below that they are approximately 10-20 % lower. X-ray specular reflection, for cases where the roughness is much smaller than the wavelength, is dominated by the roughness

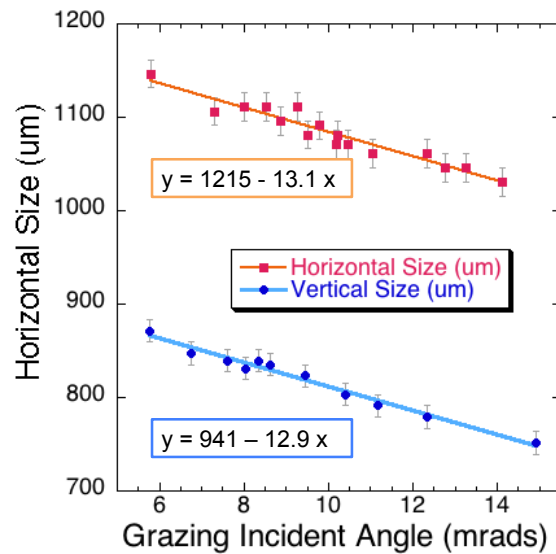


Figure 5.46: The size of the zero-order (FWHM) versus incident angle, measured on images where the 1D reflection was not embedded. The vertical magnification was 12.51, and the horizontal magnification was 9.94.

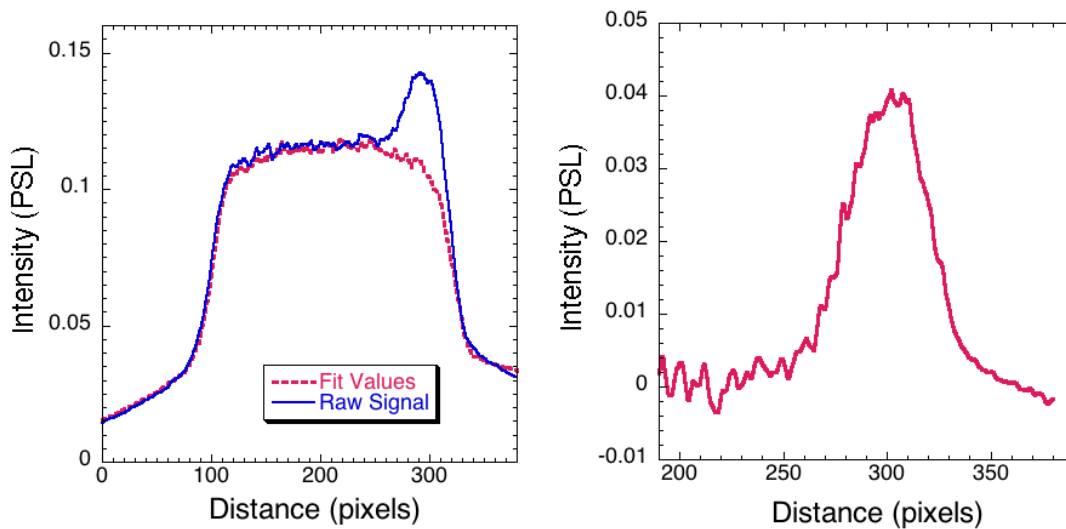


Figure 5.47: A zero-order background taken from another image is scaled horizontally using the results from Figure 5.46 and vertically (arbitrarily) to provide an adequate background for subtraction (left). The image on the right shows the result of subtraction (taken on 2011.05.09 #5, for M2 focusing vertically as first mirror).

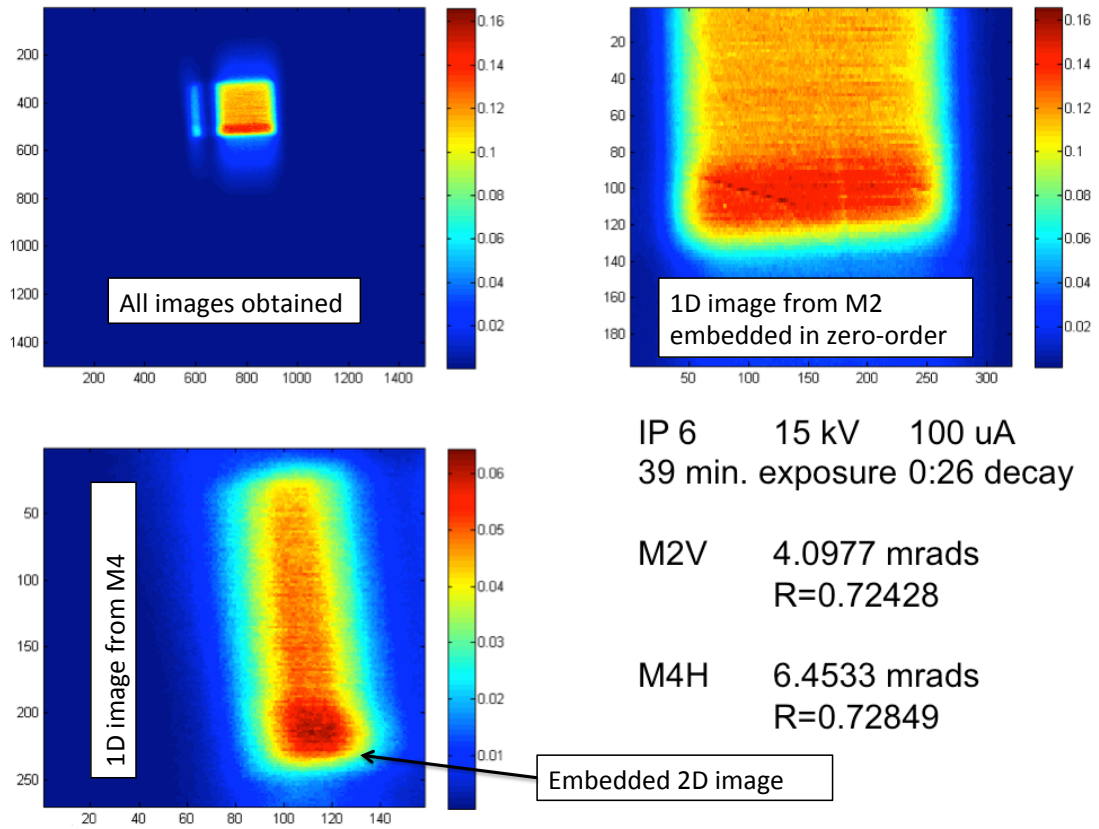


Figure 5.48: A sample image obtained during the reflectivity measurements (2011.05.09 exposure #5). In this case the 2D image is embedded in the horizontal reflection from M4 since the angle for M2 is too small – in such cases the lineout was taken through the unaffected region.

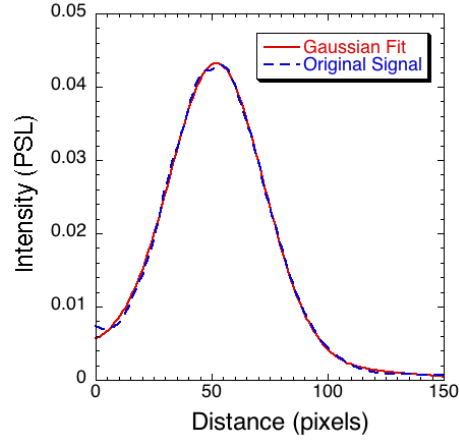


Figure 5.49: Sample fit of the reflected lineshape for the M4H reflection given in Figure 5.48.

[118]. A statistical scattering theory developed by Davies [119] can be applied where the diffuse scattering is proportional to $(\sigma_{rms}/\lambda)^4$ where σ_{rms} is the root-mean-square roughness and λ the wavelength [118]. As one moves to longer wavelengths, the diffuse scattering term vanishes, and this scheme was in fact proposed by Bennett as a way of characterizing surface roughness. The specular reflection is given by the following factor [119]:

$$\exp\left(-\frac{16\pi^2\sigma_{rms}^2}{\lambda^2}\cos^2\psi\right) \quad (5.23)$$

where ψ is the grazing scattered angle. In the case of grazing incidence ψ approaches zero, and $\cos\psi \rightarrow 1$. Therefore the reflectivity will be multiplied (and thus decreased) by this factor which depends on roughness and wavelength. To compute the roughness, the measured reflectivity values (R) were all divided by the Fresnel reflectivity (R_0), and the following rearrangement of Expression 5.23 (equating it with R/R_0) gives the roughness:

$$\sigma = \sqrt{\frac{\lambda^2 \ln\left(\frac{R_0}{R}\right)}{16\pi^2 \cos^2\psi}}. \quad (5.24)$$

Taking the average of all the data gives an average roughness of $0.06\text{\AA} \pm 0.14\text{\AA}$. A pessimistic scenario of Fresnel reflectivity with a roughness of 0.55\AA is plotted in Figure 5.50. Similar measurements on Pt mirrors were carried out by Bilderback [120], and he achieved good agreement when he modified the Fresnel reflectivity in this way, obtaining a surface roughness of $\sigma_{rms} = 15\text{\AA}$ for a $2.5\text{cm} \times 11\text{cm} \times 2.5\text{cm}$ thick fused silica mirror coated (by evaporation) with $> 500\text{\AA}$ platinum.

Another possible reason for the discrepancy between the theoretical and experimental reflectivities is that the sputtered platinum does not form a uniform layer at solid density. Parratt [121] found that evaporated films were anywhere from 70-90 % solid density. His results were based on thick (2000\AA) coatings of copper deposited by evaporation from pieces of $625\ \mu\text{m}$ Cu wire for 20 minutes, from an array of four $375\ \mu\text{m}$ Ta helical filaments 20 cm from the substrate. However, his principal arguments for porosity or island formation do not apply in the case of platinum sputtering (see Section 5.2 for parameters). His conjectures primarily revolve around the formation of oxides which lower the bulk density through disturbances in the crystalline structure, but in the case of platinum oxide formation is non-existent. To illustrate that such a density argument is invalid, Fresnel reflectivity assuming a bulk density of 80 % platinum solid density is plotted in Figure 5.50. It is evident that such a model does not match the data well.

Some other things are worthy of note. These measurements were made on May 8-9, 2011, and the mirrors were sputtered with platinum on February 11, 2009, over 2 years earlier. Therefore the mirror coatings are stable and appear to perform well for lengthy periods of time. The second remarkable result is that the mirrors appear to be more or less the same as far as reflectivity goes, despite obvious optical differences. For example, M2 had a black spot where there was a hole in the coating. M1 had some coating from plasma expansion. M3 and M4 had much less use and were in very good

*5.10. Adjustment of Focal Length by Bending
the Second Mirror*

Hal Friesen

condition. Despite these visible differences in optical quality, in the X-ray regime the mirrors appear to be equivalent (M2 did not have a lower reflectivity on average). A thin optically visible coating of 10's nm is much shallower than the penetration depth of 8 keV X-rays and thus is effectively transparent to X-rays.

5.10 Adjustment of Focal Length by Bending the Second Mirror

The second mirror is necessarily at a different object distance, because it must be placed after the first by nature of the KB microscope design. Since this new object distance requires a different focal length, either the radius of curvature must be changed or the incident angle changed (since $f = R \sin i/2$). In the case of the initial design the available mirror curvatures eliminated the option of selecting different radii of curvature for 8.73 mrad (0.5°) grazing angle of incidence for both mirrors. Therefore the second mirror actually forms a focus at around 10.8 mrad, which is less than ideal since the mirrors are already on the falling edge of the reflectivity curve, and such a higher angle results in a significant loss of signal. A proposed solution was to mechanically alter the radius of curvature by applying a force to the back of the mirror to increase the radius of curvature so that the incident angle could remain at 8.73 mrad (0.5°). In order to measure the applied force so that any bending effects could be reproduced, transducers (or subminiature load cells) were used. However, before they could be used reliably, they required calibration.

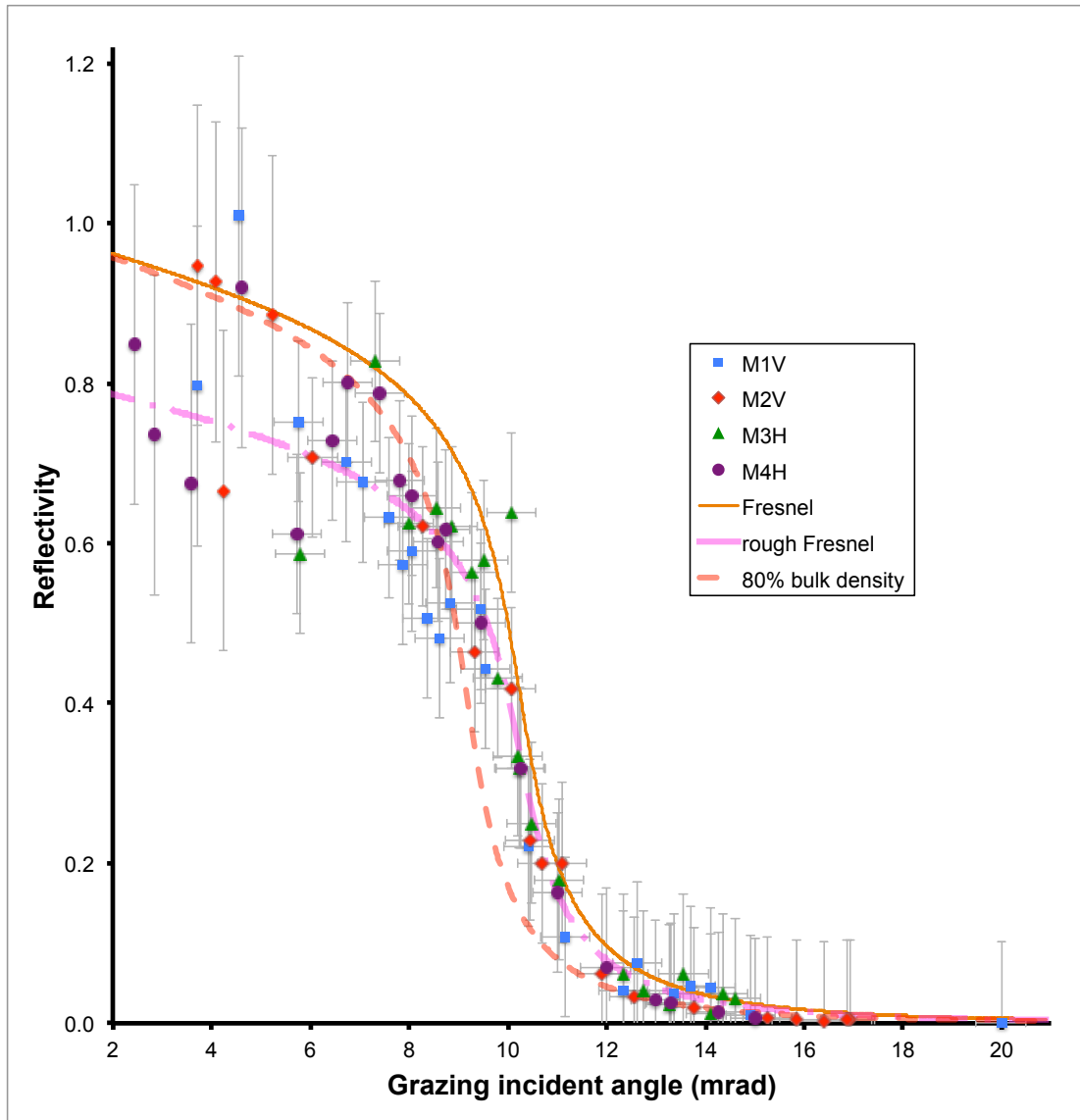


Figure 5.50: Experimentally obtained reflectivity versus angle, compared to Fresnel theory. The other curves are modified versions of Fresnel assuming, respectively, 0.55 Å rms roughness, and 80% Platinum solid density.

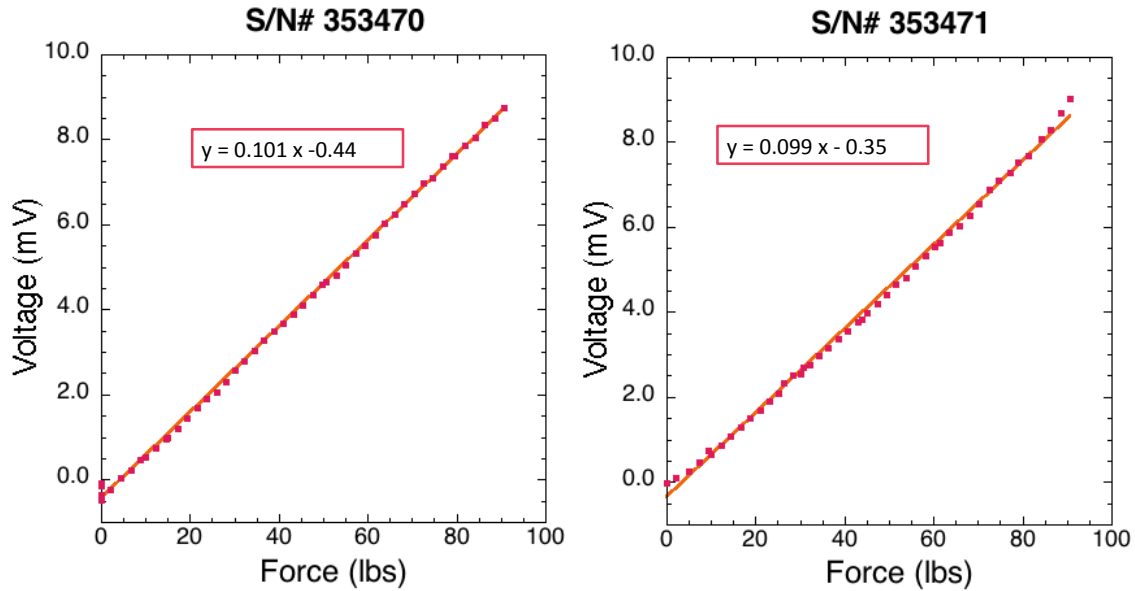


Figure 5.51: Calibration curves for the transducers.

5.10.1 Transducer Calibrations

Strain gauge transducers were used to measure the applied force (Cooper Instruments model no. LPM-510) They had a resistance which varied with load up to a maximum capacity of 100 lbs (445 N). (they are accurate to as low as 10% of that). To calibrate the transducers, a large steel platform ($\approx 10\text{cm} \times 25\text{cm} \times 1\text{cm}$) was placed with its center on each transducer. Small $\approx 5\text{cm} \times 5\text{cm} \times 5\text{cm}$ weights were slowly stacked in such a way to maintain the balance on the contact point, and the voltage at the output terminals measured directly using an oscilloscope. The bias voltage across each transducer was 5 VDC, provided by a DC power supply damped with a voltage regulator (Fairchild LM7805) and capacitors to ensure a stable bias. The results of the calibration are shown in Figure 5.51.

From the calibration Figure 5.51 it can be seen that approximately 0.1 mV is generated per 4.45 N (1 pound) of pressure. This implies approximately 10 mV for

*5.10. Adjustment of Focal Length by Bending
the Second Mirror*

Hal Friesen

100 lbs. (445 N) of pressure (the maximum capacity). This can also be written as 2 mV per Volt of input. This is the standard way in which transducer response is described. The measured values are 2.02 ± 0.01 mV/V (S/N 353470) and 1.98 ± 0.02 mV/V (S/N 353471). The data sheet received with the transducers which specified their response as 1.931 and 1.939 mV/V respectively. One possible reason for the discrepancy is that the transducers require a re-calibration 1 year after their shipping date, and the tests were carried out ≈ 3 months prior to the specified recalibration date (2011.07.21). Another possible reason is that a voltage divider was not used to measure the signal, and thus small voltage fluctuations could have affected the measurements, even with averaging turned on on the oscilloscope.

The transducer used for the bending tests was serial no. 353470 with a calibration factor of 0.101 ± 0.0005 mV/lb based on the calibration given in Figure 5.51.

5.10.2 Mirror Bending tests

The setup for carrying out the bending tests of the second mirror is shown in Figure 5.52. The X-ray tube settings were 15 kV, 100 μ A , and a 15 μ m nickel filter was used to ensure the beam was primarily K_{α} . The exposures were between 15 and 30 minutes. A different mirror holder was used than the one used for all other experiments and tests due to constraints on the original one being required in LLNL. The major differences of this holder were a smaller through hole size for the X-ray beam in the center, part of the first mirror protruding unsupported beyond the front end of the holder to minimize the obstructed solid angle, and no precision pins to rest on. The lack of pins meant that the bending would occur against 3 random points rather than the known pins, which increases the risk of angular shift during bending if the mirror reseats against new contact points.

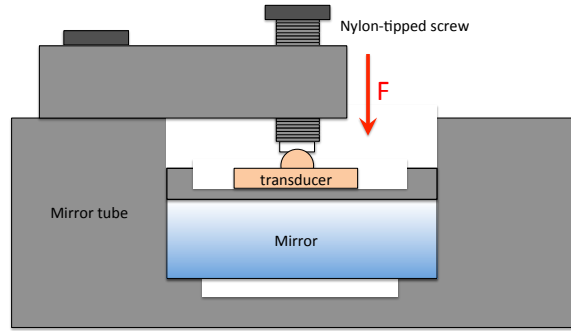


Figure 5.52: Setup for bending the 2nd mirror.

A simple model of the mirror bending is needed in order to analyze the results. First, we recognize that the edges of the mirrors are raised up from the center by the following amount:

$$d = R - \sqrt{R^2 - x^2} \quad (5.25)$$

where R is the radius of curvature, and x is the radius of the mirror (in our case, 12.7 mm). For a 20 m ROC, $d=4.03 \mu\text{m} \equiv C_0$. Therefore the deflection of the center when the mirror is bent to a new radius R is given by

$$\Delta d = C_0 - R + \sqrt{R^2 - x^2}. \quad (5.26)$$

This assumes that the mirror deforms in the center into a spherical shape.

Similarly, if one wants the curvature for a given amount of deflection, a bit of algebra gives

$$R = -\frac{(F^2 + x^2)}{2F} \quad (5.27)$$

where

$$F = \Delta d - C_0. \quad (5.28)$$

If we assume that the load on the mirror is uniformly distributed, and that the

5.10. Adjustment of Focal Length by Bending
the Second Mirror

Hal Friesen

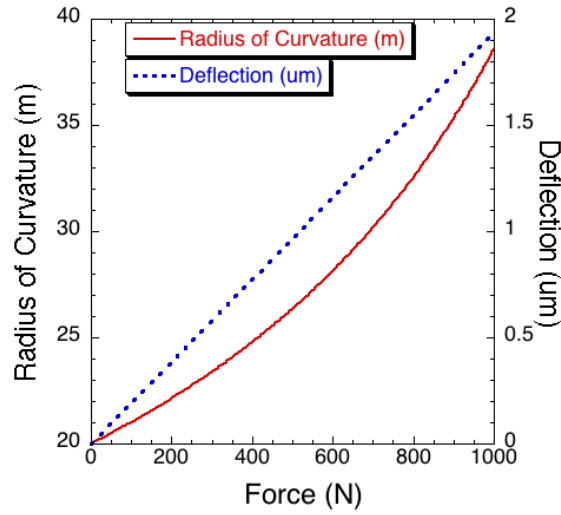


Figure 5.53: A plot of maximum deflection (y_M) versus applied uniform force calculated using Equation 5.29, along with inferred radius of curvature using Equation 5.27 and assuming the mirror bends into a spherical shape.

mirror is a circular plate supported freely on its edge, we can calculate the maximum deflection y_M of the mirror center using the following formula from [122]:

$$y_M = k_1 \frac{wx^4}{Et^3} \quad (5.29)$$

where w is the weight in units of pressure, E is Young's Elastic Modulus (72.0 GPa for fused silica [123]), x is the radius of the circular slab (12.7mm), t is the thickness of the slab (6.35mm) and k_1 is a tabulated bending factor which varies depending upon the support setup and geometry of how the slab is bent. In the case of a circular slab supported freely on its edges, $k_1=0.696$ [122]. Again, it is assumed that the mirror bends into a spherical shape with the new radius of curvature determined by the deflection of the mirror center. Using Equations 5.27 and 5.29, the radius of curvature can then be plotted versus applied force, as shown in Figure 5.53.

After comparing Figure 5.53 to the forces applied during the bending tests, we

*5.10. Adjustment of Focal Length by Bending
the Second Mirror*

Hal Friesen

can make a plot of Resolution versus incident angle, and compare it to the theoretical resolution of different mirror curvature radii. During the experiment, force was gradually increased, then gradually released. The two parts of the experiment exhibited different characteristics. In general, the edge spread functions (ESFs) produced during the bending were much blurrier by eye than the regular (unbent) case. A possible explanation for this is that the bending system was not entirely stable, and since the exposures were all from 15-60 minutes long, the images are averages over long periods where the whole system was possibly shifting. Indeed, some images seemed to have image shadows where the mirror reflection may have drifted during the course of the exposure. Although more work with a more stable bending system is required to establish reliable quantitative bending, the initial tests done here still show some understandable and encouraging trends. The resolution was calculated using the same methods described in Section 5.8. The LSFs obtained were noisier but useful data could still be extracted. A sample image is shown in Figure 5.54 with its corresponding fit in Figure 5.55.

5.10. Adjustment of Focal Length by Bending the Second Mirror

Hal Friesen

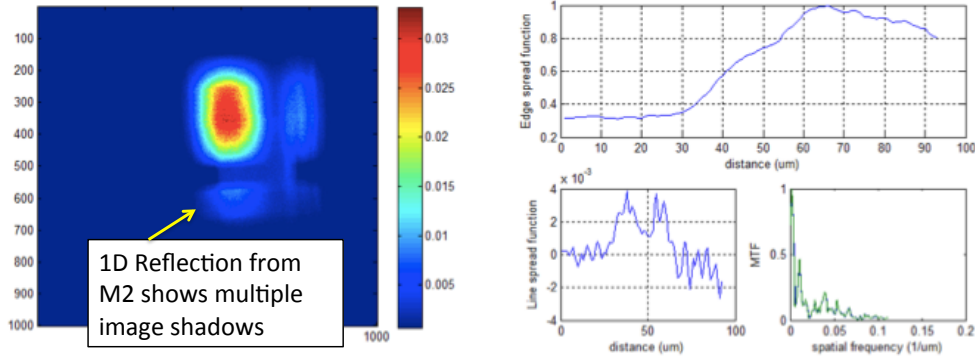


Figure 5.54: A sample image obtained during the bending tests where M2 is the second mirror focusing vertically. There is evidence of multiple image shadows which are pronounced enough to produce two peaks in the LSF. The image corresponds to a measured applied force of 410 ± 10 N (92 ± 2 lbs.). The image was obtained using IP #6, with X-ray tube settings of 15 kV, 100 μA for a 1 hour long exposure, and 90 minute decay.

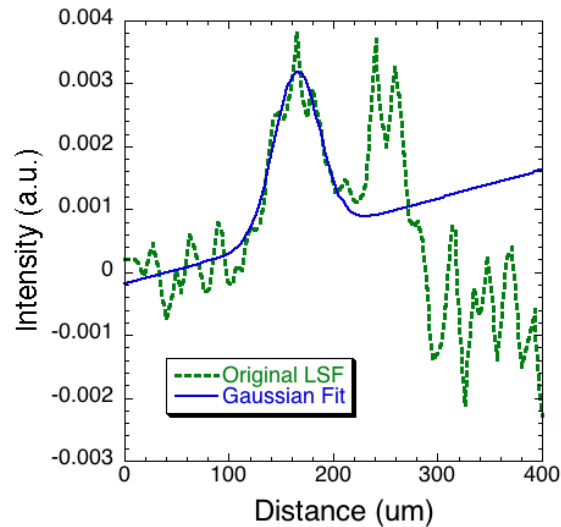


Figure 5.55: Two peaks are found in the LSF from Figure 5.54, likely due to mechanical shifting during the time-integrated exposure resulting in two edges in the ESF. The worst peak from the LSF in Figure 5.54 is fit with a Gaussian function to give a FWHM of 44 ± 10 μm .

5.10. Adjustment of Focal Length by Bending the Second Mirror

Hal Friesen

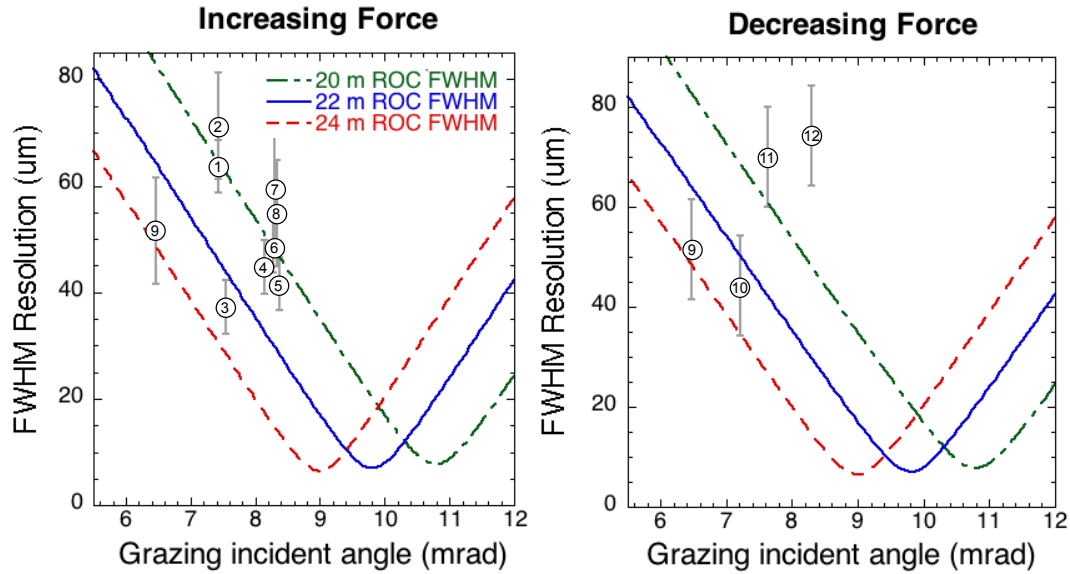


Figure 5.56: Experimental results for bending the 2nd mirror. The theoretical curves for the various radii of curvature were calculated using ZEMAX, and the details about each point are given in Table 5.2.

Table 5.2: Summary of Bending Results

Point #	Applied Force (N)	Applied Force (lbs)	Predicted ROC (m)
1	0	0	20.0
2	$\approx 0^a$	≈ 0	20.0
3	192 ± 10	43 ± 2	22.1
4	79 ± 10	18 ± 2	20.8
5	188 ± 10	42 ± 2	22.0
6	227 ± 10	51 ± 2	22.5
7	251 ± 10	56 ± 2	22.8
8	304 ± 10	68 ± 2	23.4
9	410 ± 10	92 ± 2	24.9
10	194 ± 10	44 ± 2	22.1
11	101 ± 10	23 ± 2	21.0
12	49 ± 10	11 ± 2	20.5

^aSmall pressure applied below measurement capacity of transducer.

*5.10. Adjustment of Focal Length by Bending
the Second Mirror*

Hal Friesen

While the force was gradually applied (as shown in the left of Figure 5.56), the resolution improved going from 0 to 190 N, with the 190 N resolution point (#3) lying within error of the predicted 22 m ROC resolution curve (calculated in ZEMAX). After that, the force was decreased to try and get an intermediate point, resulting in the 79 N resolution point (#4) that is within error of the region where the 21 m ROC resolution curve would be. The following points (5 to 8) all fall more or less on the 20 ROC resolution curve. An explanation for this behaviour is that the bending system may have slipped, since the balancing of the nylon-tipped screw on the knob of the force transducer was a bit unstable, due to the curved contact surface depicted in Figure 5.52. Therefore, the additional force may have been bending the aluminum support rod in Figure 5.52, for example. At a certain point the system may have stabilized after enough applied force, resulting in the 410 N resolution point (#9) lying within error where the 25 m ROC curve would be. Note that the large error bars are a product of the image blurriness produced by long integration times and a bending system that wasn't completely stable.

While the force was gradually released (as shown in the right of Figure 5.56), the 194 N resolution point (#10) lay within error of the predicted 22 m ROC resolution curve. As the force was released further, the resolution was in fact worse than predicted (points 11 and 12). A possible explanation is that the mirror was mechanically relaxing throughout the course of the exposure, resulting in a more blurry edge from the reflection shifting as well as moving into different focus levels. It seems that mechanical relaxation is worse when the force is released than when it is applied, but more work is required to make a definite conclusion in this regard.

It is worth noting that between the first and last exposures, the baseline voltage ("zero" force reading) drifted from 5.19 mV to 6.28 mV, a change of 1.09 mV, or approximately 45 N (10 lbs). This was over the course of seven hours of data collection,

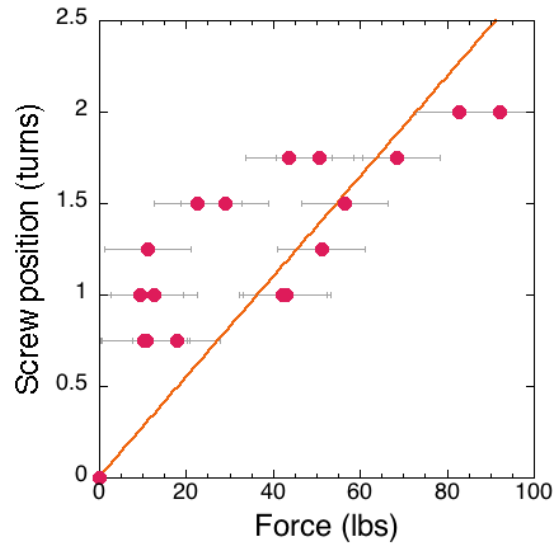


Figure 5.57: Calibration for number of screw turns versus pounds of force.

and was not taken into account in the above results. It is unknown whether it is a constant and linear process, or whether it is affected by the bending and relaxation of the load cell itself. Further work is required to characterize this effect.

For convenience, in the cases where a transducer is not available, the number of screw turns was recorded and is plotted as a function of the measured force in Figure 5.57. The screw used was a steel Imperial 1/4"-20 screw, which consists of a 6.35 mm diameter screw with 1.27 mm/thread. The fit through the points is 0.027 turns per pound of force, which corresponds to approximately a quarter turn for 10 pounds of force. The points lying above the line seem to have a comparable slope, but may just have a slightly different offset from zero, since the zero on the transducer tends to drift a small amount. Therefore approximately two full turns on the screw will provide the force required to bend the mirror appropriately, but further tests with a stable bending system are required to establish confidence in this value.

Finally, a qualitative assessment of the bending performance was carried out using

*5.10. Adjustment of Focal Length by Bending
the Second Mirror*

Hal Friesen

the fine gold mesh from previous resolution tests. Unfortunately there was only a single mirror available for the test (M2), so the results are only viewable for the line focusing, and not the qualitative effect on the 2D image. The object distance to the center of the mirror was 119 ± 1 mm with a magnification of 11.20 ± 0.1 , and it was in the second mount hole of the KB mirror holder. The settings on the X-ray tube were 15 kV, 100 μ A, with exposures between 30-60 minutes. A 15 μ m Ni filter was used once again to limit the spectrum as much as possible to Cu K_α . The results are shown in Figure 5.58.

The mesh appears to be faintly apparent in all images, which is remarkable because even during equilibrium (non-bending) scenarios the mirror had to be close to focus in order to see hints of the mesh. This indicates that the mirror bending was reasonably stable over the 30-60 minute integration times. The best image was obtained with 115 N at 7.72 mrad in Figure 5.59, which gave a measured mesh period of 31 ± 5 μ m with a peak-to-valley contrast of 1.09 ± 0.03 . The discrepancy between this measured period and the actual period is likely due to slight image movement due to the bending system. Referring back to Figure 5.56, it is clear that at 7.72 mrad the mirror will be in best focus for a radius of curvature of 28.2 m. At the force applied (115 N), the predicted radius of curvature is 21.2 m, which at 7.72 mrad corresponds to a resolution of approximately 50 μ m. Theoretically one would expect the mesh to get sharper as more force is applied at the angle of incidence. A possible explanation is that the bending system was only mechanically stable up to a certain threshold force (possibly close to 115 N) which is why this image has the most resolved mesh.

An average of the peak-to-valley contrast for the all the images where above 50 N of force was applied is 1.08 ± 0.17 . Although this contrast is only slightly greater than one, it is nevertheless an improvement over the 0 N case, where no transmission peaks were visible. A preliminary conclusion is that this simple method demonstrates

5.10. Adjustment of Focal Length by Bending the Second Mirror

Hal Friesen

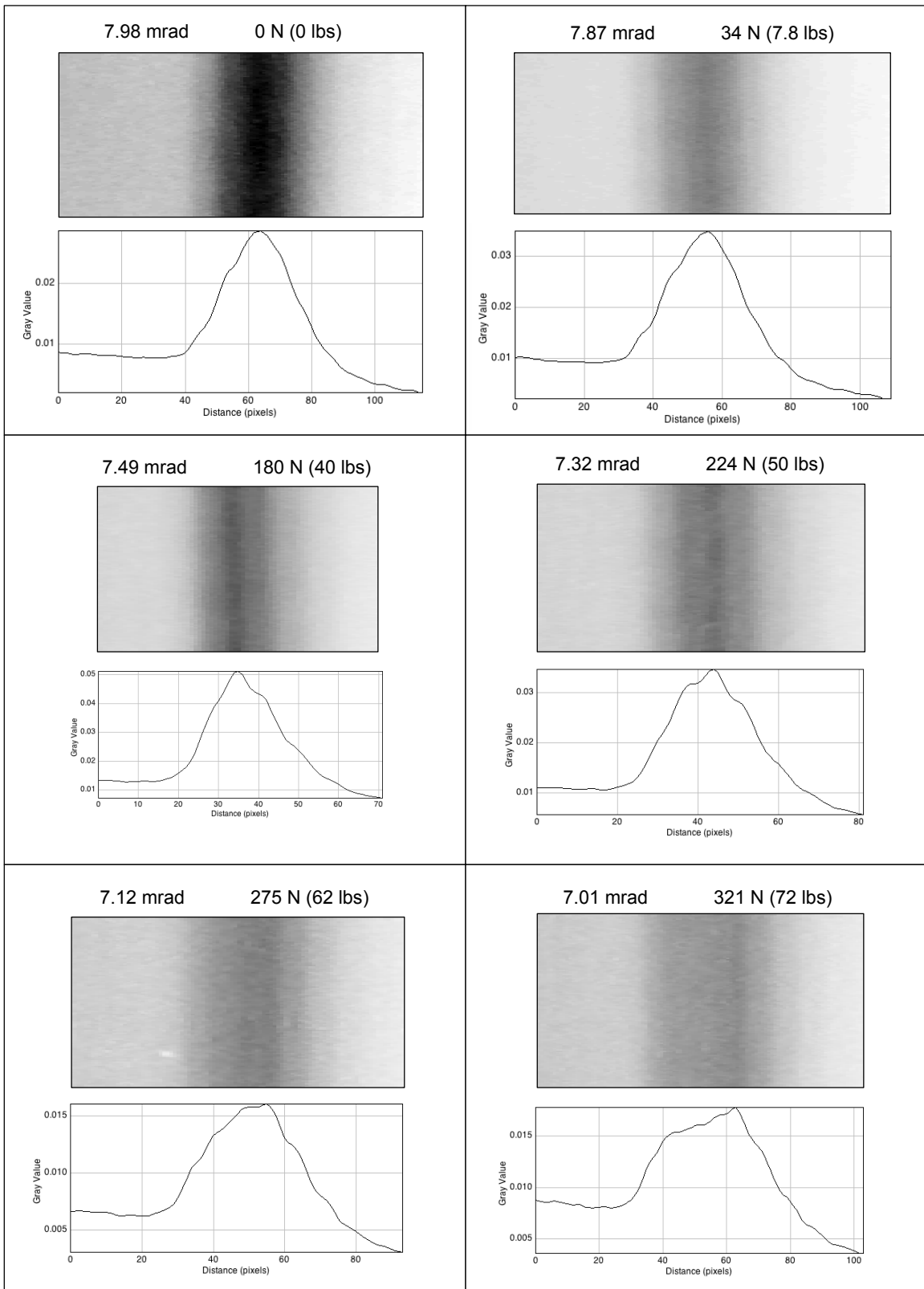


Figure 5.58: 1D images of gold mesh obtained during the bending test.

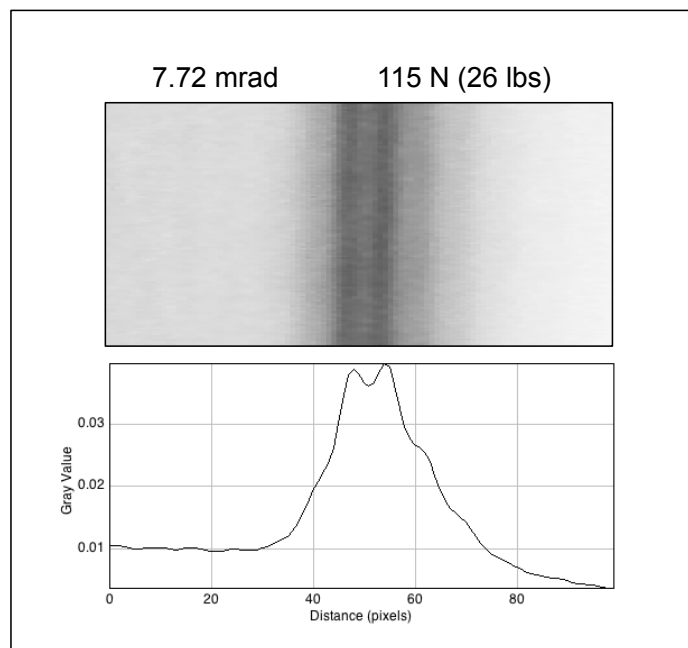


Figure 5.59: The best mesh image obtained during the bending test, exposure #5 on 2011.05.16. The inferred mesh period is $31\mu m \pm 5\mu m$, and the predicted radius of curvature at this force is 21.2 m, which would have a theoretical resolution of approximately $50\mu m$.

*5.10. Adjustment of Focal Length by Bending
the Second Mirror*

Hal Friesen

potential to put the second KB mirror into focus and improve the resolution in this dimension without purchasing very specific radii of curvature. Future work to test the bending more rigorously with a stable bending system would help establish whether aberrations are a significant effect and develop reproducible bending where, ideally, little to no change in angle would be introduced.

Chapter 6

Prepulse Scan on Titan

This chapter explains the formation of a prepulse and why it is important to study for fast ignition. It goes through the experimental parameters on the Titan laser beamline, followed by the background necessary to understand the codes and arguments used in data analysis. The chapter finishes with the physical results to demonstrate a powerful application of the KB microscope.

6.1 Fast Ignition Experimental Setup

All the laser-plasma experiments were carried out using the Titan laser beamline at the Jupiter Laser Facility (JLF) at the Lawrence Livermore National Laboratory (LLNL). This is a short pulse laser beamline that allows for investigation of high-intensity laser plasma interactions and regimes of physics which were previously unreachable. In order to appreciate the scale and technological achievement of a high-intensity laser system of this class, some background will be discussed regarding laser advances leading to such a sophisticated light generation system.

6.2 Laser History

Since the invention of the laser in 1960, there have been incredible advances in all areas from amplification, to wavelength tunability, to mode selection and choice of gain medium. The most notable advance for Fast Ignition is that of Chirped Pulse Amplification (CPA), in 1985, which allowed lasers to reach much higher intensities than before [31]. Previously the damage threshold of optics and gain media limited the amount of amplification that could take place. Attempts to sidestep this issue by spreading out the beam required expensive optics that were impractical. CPA uses gratings to stretch out the pulse temporally prior to amplification, effectively reducing the intensity on the optics. This is done by making the longer wavelengths travel a different distance from the shorter wavelengths. After amplification occurs, a second set of gratings is used to recompress the beam prior to final focusing. The amount of stretch in time is on the order of $10^3 - 10^5$ [115].

Optical Parametric Amplification (OPA) is a technique invented in 1979 [124] that uses a non-linear crystal as a gain medium, and a higher frequency pump laser. The pump laser's photons are converted into the signal laser's energy via the nonlinear effect of the crystal, and results in amplification. This technique provides higher gain per unit volume than a standard gain medium [115]. Another advantage is that the pulselength of the pump laser can be matched to the signal pulse, and amplification will only occur when the signal beam is passing through. This reduces spontaneous emission and provides a higher intensity contrast in the pulse.

6.3 Titan Description

The Titan laser system at LLNL makes use of both of the above techniques in what is called Optical Parametric Chirped Pulse Amplification (OPCPA) [115], and can reach intensities up to $9 \times 10^{19} \text{W/cm}^2$. A schematic is shown in Figure 6.1. A seed pulse of 100-200 fs at 1053 nm is provided by a commercial master oscillator (Time Bandwidth Products GLX-200) [115]. An Offner Pulse Stretcher [125] is used to stretch the pulse to 1.6 ns while minimizing beam aberrations. A set of BBO crystals (BaB_2O_4) is pumped by a 532 nm beam, which originates from a frequency-doubled 1.06 μm beam amplified through YLF. This makes up the OPCPA preamplifier, where the seed pulse is amplified up to a few mJ [115]. The beam is then sent through 25 and 50 mm flashlamp-pumped rod amplifiers, raising the energy to approximately 5 J. A double pass through 9.4 cm disk amplifiers is followed by a pockels cell switch, then a pass through 9.4 and 15 cm disk amplifiers to raise the beam to full energy (roughly 150 J for the shortest pulse). Two 40X80 cm Multilayer Dielectric diffraction gratings recompress the beam to 0.7 ps, where it is then directed by two turning mirrors prior to being focused by an f/3 off-axis dielectric parabola to a best spot size of 7 μm FWHM [115].

6.4 Laser Diagnostics

Leakage light through the final turning mirror is sent through an equivalent plane monitor (EPM) for on-target intensity data and a far-field monitor for beam pointing. Leakage from the compressor is used for the prepulse monitor, which is a water breakdown cell that has a nonlinear response to strongly filter higher intensities to protect the sensitive photodiode. The compressor leakage light is also used for the

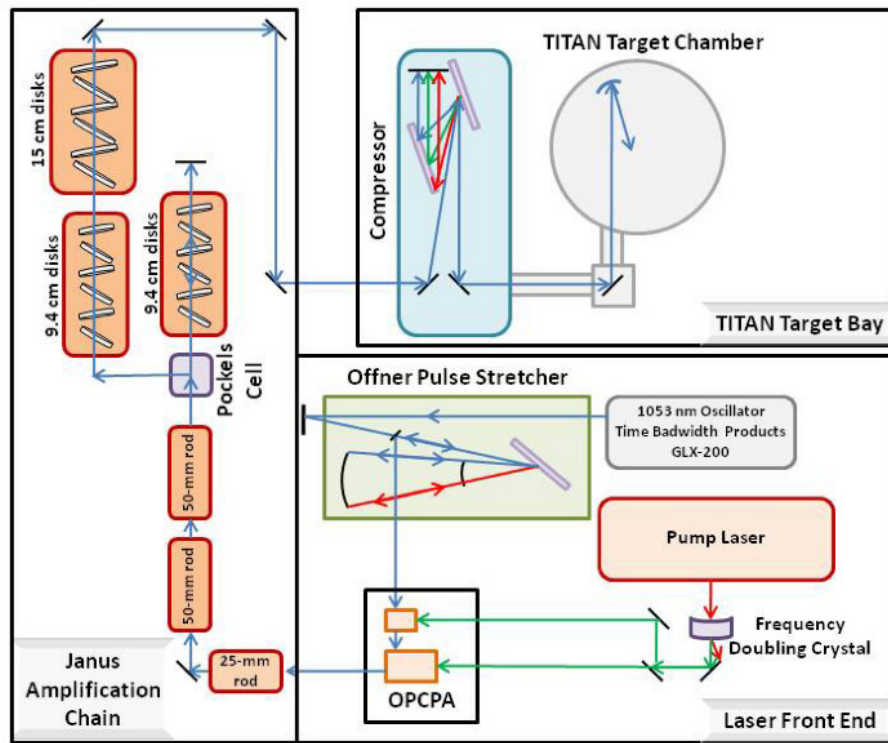


Figure 6.1: Titan Laser in the Jupiter Laser Facility at LLNL [115].

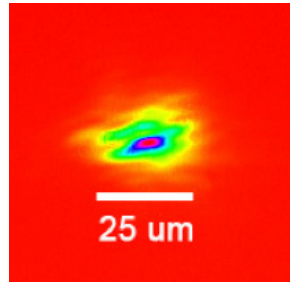


Figure 6.2: A sample focal spot on Titan using the 16-bit camera [115].

autocorrelator, which uses second harmonic generation to measure the pulse length.

A carbon wire target is placed in the chamber initially, and the parabola adjusted to minimize the astigmatism and ensure the low-power laser spot is in focus at the wire (imaged using an 8-bit camera). The focal spot was then imaged in the 16-bit EPM camera (Apogee Alta U2000). The camera chip is 1600X1200 pixels with $7.4 \mu\text{m}$ pixels [115]. A spot is shown in Figure 6.2. As shown by Chen [115], if the elliptical FWHM of the focal spot is mapped onto a circular distribution of equal area, the focal spot diameter is $7 \mu\text{m}$ and contains 15% of the laser energy.

6.5 Diagnostic Techniques

The detectors used in the experiments were Fujifilm Image Plates and Princeton CCD cameras. A CID camera was tested at one point but the noise level was very high resulting in images with low signal-to-noise.

6.5.1 Image Plates

Imaging Plates (IP) were first invented in the 1980s in order to replace one-time use X-ray film [126]. The Fujifilm image plates come in several varieties and were designed for medical applications. The type used on the KB was the BAS-MS ("more

sensitive”, with a thicker fluor layer) type. Image plates have the advantage of being highly durable and reusable. They can be used extensively without significant degradation and are not affected by electromagnetic pulses (EMP) generated by high-flux electron currents produced in high-intensity laser shots [115], in contrast to electronic CCD camera systems. The dynamic range of IPs is good (almost five orders of magnitude [126]), although they are not as sensitive as CCD cameras and are slightly more noisy.

The image plates have several layers: a surface layer of polyethyleneterephthalate (PET) (9 μm), a phosphor layer described below (115 μm), a back plastic layer (12 μm) a base layer of PET (190 μm) a ferrite layer (consisting of MnO , ZnO Fe_2O_3 and plastic, 80 μm), and a back protective layer of PET (25 μm) [115]. The phosphor layer consists of phosphor:urethane ratio of 25:1, with the phosphor $\text{BaFBr}_{0.85}\text{I}_{0.15} : \text{Eu}^{2+}$ and an organic resin as a binder [126]. The purpose of the magnetic backing is to allow the image plate to adhere to the metal scanning tray that is inserted into the Fujifilm scanner. In LLNL the scanner used was FLA-7000, and at the University of Alberta the FLA-5000 was used alongside a homemade University of Alberta IP Reader. As mentioned previously, the FLA-5000 was 155 times less sensitive than the FLA-7000.

Incident radiation or particles can create electron-hole pairs (EHP) in the phosphor layer. Some of these pairs recombine immediately to scintillate, but the rest are trapped in metastable centers in the crystal [126]. Exposure to red light (633 nm, provided by a HeNe laser in the scanner and by an LED in the University of Alberta IP reader) excites the electrons out of the metastable states, whereupon they recombine to emit blue light around 390 nm [126]. The process is called photo-stimulated luminescence (PSL), and Fuji in fact uses PSL as a unit to quantify the amount of absorbed radiation in Fujifilm IPs. The signal is quantized by an analog to digital

converter (ADC) and the produced images are in a 16-bit pixel format, with the resolution adjustable between 25, 50 and 100 μm . For the scanner one can also adjust the sensitivity (s1000,s4000,s10000) which is related to the gain on the PMT, and the latitude (L4,L5) which determines the dynamic range of the PMT. The actual scanner output is in logarithmic data units Fuji calls “Quantum Levels” and are dependent on the scanner settings. Fuji supplies the following formula to convert to their linear PSL unit [115]:

$$PSL = \left(\frac{\text{Resolution}}{100} \right)^2 \times \frac{4000}{\text{Sensitivity}} \times 10^{\text{Latitude} \times \left(\frac{QL}{G} - \frac{1}{2} \right)} \quad (6.1)$$

where G is the Gradation (G=255 for 8-bit output and G=65535 for 16-bit output) [115] and QL is the Quantum Level output by the scanner. It should be noted that the laser spot size is approximately 70 μm and therefore some periphery signal is lost, particularly when a higher resolution setting is used, as the laser scans across the surface of the IP [115]. This effect can be corrected for.

Signal fading is a phenomenon associated with IPs, and is basically the spontaneous decay of electrons trapped in the metastable state [127]. It is dependent upon the type of IP and the ambient temperature [127]. Previous work has shown that the fading characteristics of the IP is independent of the exposure level (at least for detection of electrons) [128]. This decay was discussed in Section 5.9.

6.5.2 University of Alberta IP Reader

In order to try and speed up the image scanning process and lower costs, a homemade IP reader was constructed, basically consisting of an array of red LEDs with an imaging system, appropriate filtering and a CCD camera in a light-tight box. This system has been developed primarily by another graduate student, Mianzhen Mo.

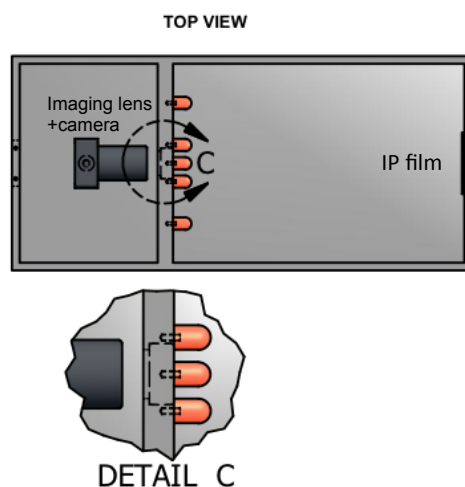


Figure 6.3: Schematic Diagram of the University Alberta IP reader. The CCD camera and lenses are on the left, and the image plate is on the right attached to a magnetic backing to hold it in place. The LED array and filters are in between. Figure courtesy of Mianzhen Mo 2011.

The thesis author assisted in many of the calibration tests.

The maximum resolution of this IP reader is much lower than the IP scanner made by Fuji; however, the speed of scanning is practically instantaneous in comparison. The IP reader uses a single flash, lasting a fraction of a second, of a red LED array and collects the emitted light stimulated by the excitation of the metastable states over the entire IP.

6.5.3 Princeton CCD Cameras

The CCD camera used (Princeton Instruments model no. 7381-0002) had a pixel size of 20 μm and a chip area of one square inch (1340 X 1300 pixels). It has a much higher SNR than the Image Plates by a factor of ≈ 2.5 for weak signals and ≈ 30 for stronger signals. The camera was employed wherever possible. The only disadvantage was the setup involved, requiring vacuum pumps and appropriate shielding from the

EMP generated during a shot. In fact, in some cases the Titan shots generated such a great EMP that the cameras did not behave reliably for some of the X-ray diagnostics. However, the bulk of the KB microscope design seemed to be an advantage in this regard, since there were almost never any camera failures due to EMP for the KB microscope system.

6.6 Prepulse Formation

High power laser systems such as Titan always have a low level of leakage light through the system prior to the main pulse. Spontaneous Emission (ASE) from the front end is amplified through the laser chain propagating ahead of the main pulse, competing with the main pulse for gain. Sometimes spurious reflections of scattered light from the main pulse can be amplified as a short pulse prior to the main pulse. The ASE and any spurious prepulse typically are on the order of millijoules of energy, on the order of a nanosecond in advance of the main pulse. The net result is a preformed plasma at target that modifies the coupling of the main pulse laser energy into hot electrons [129].ⁱ

6.7 Experimental Parameters

A typical Titan prepulse is shown in Figure 6.4, which was measured using a water breakdown cell [131]. The intrinsic prepulse was on the order of 1-10 mJ approximately 1.5 ns prior to the main pulse. For the prepulse scan an injected prepulse of 10 to 1000 mJ was added colinear to the beam and approximately 3 ns prior to the main pulse.

ⁱThis paragraph was published previously in [130].

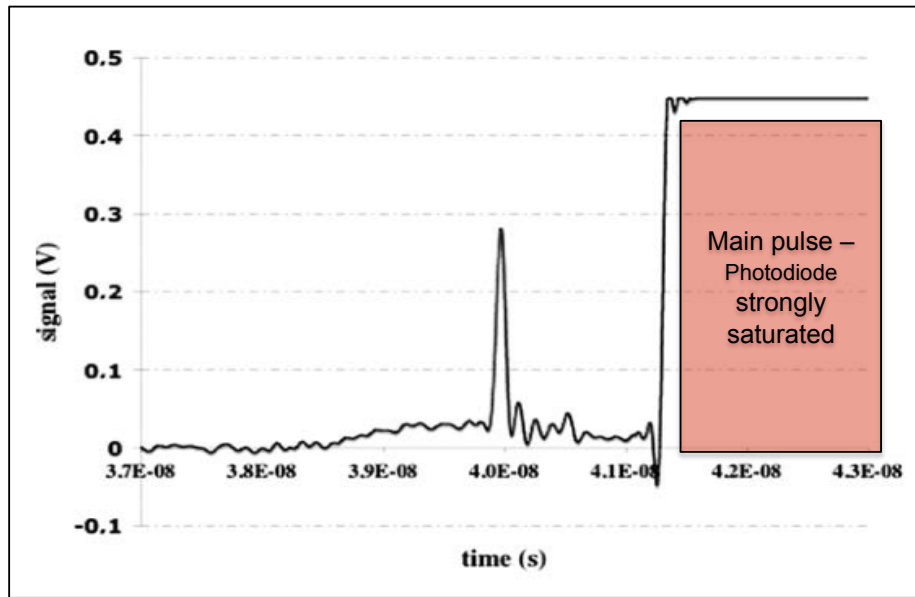


Figure 6.4: A typical Titan prepulse [131].

The targets were gold cones attached to copper wires. The cones were $20\ \mu\text{m}$ thick with a tip thickness of $10\ \mu\text{m}$ and an opening angle of 30 degrees. The copper wire was $40\ \mu\text{m}$ thick and 1.5 mm long. A picture is shown in Figure 6.6. The KB microscope was unique in that it was the only diagnostic that could image the emission from both the cone and the wire simultaneously. A summary of the shots analyzed is provided in Table 6.1. Note that the information about focus is chronological and refers to comparison to a previous shot in the scan. For all shots the KB images were filtered by $50\ \mu\text{m}$ aluminized mylar, $500\ \mu\text{m}$ Be, and $26\ \mu\text{m}$ Al.

6.8 FLYCHK

Since the grazing-incidence reflection of superpolished platinum occurs for a broad spectrum of energies to various degrees, it is difficult to know exactly the spectrum that one is seeing in an image of the emission from the inside of a gold cone that is

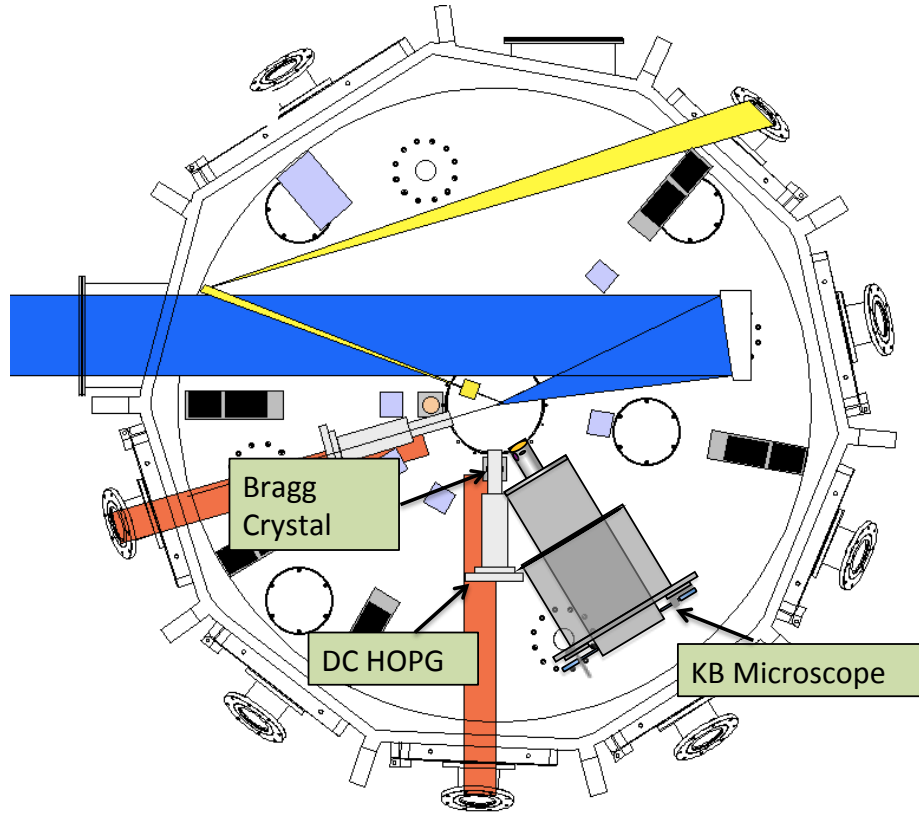


Figure 6.5: The layout of relevant diagnostics in the Titan chamber. The large blue beam is the laser pulse. The KB microscope was mounted on port TS4 on the roof of the chamber pointing down at TCC with a 40° angle with respect to horizontal.

Table 6.1: Experimental Parameters for Prepulse Scan on Titan.

Shot Date & No.	E (J)	τ (ps)	ϕ (μm)	Prepulse Energy E (mJ)	KB focus
2009.08.18 #2	145	0.7	7	7 mJ intrinsic	-
2009.08.18 #6	149	0.7	7	30 mJ injected	Focus shifted by $\approx 200 \mu\text{m}$ down wire.
2009.08.17 #2	165	0.7	7	100 mJ injected	Focus shifted by $\approx 100 \mu\text{m}$ down wire.
2009.08.17 #3	154	0.7	7	500 mJ injected	-
2009.08.17 #4	141	0.7	7	1000 mJ injected	-

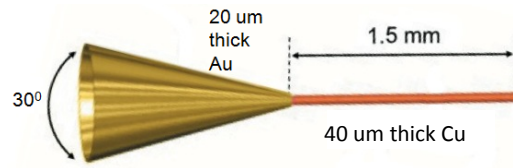


Figure 6.6: A cone-wire used in the prepulse scan [129].

filled with preplasma. In order to correctly assess the spectral emission peaks and their locations within the cone, the X-ray emission was predicted using FLYCHK (see Section 6.11.4) [65]. In order to do so one requires the electron energy distribution function and hydrodynamic model of the plasma to give the input variables for the CR code.

For plasma spectroscopy, a suite of computer codes is available at the NIST Atomic Spectroscopy websiteⁱⁱ. The original time-dependent code FLY and its predecessors were K-shell based and used successfully for the study of hot dense plasmas, but could only do so for low Z ions from helium to iron ($Z=26$) [65]. As plasma research moved into warm dense matter and other regimes of temperature-density phase space with higher Z ions, FLYCHK was developed with similar philosophies of ease-of-use, speed and portability, but for higher Z regimes. FLY included atomic data, continuum lowering and radiation trapping effects (or opacity) [65]. It can use an LTE, or a collisional radiative (CR) code.

For mid to high Z atoms, the CR code uses an average-atom model, UTA model, super configuration radiative and collisional model and Monte Carlo DCA [65]. The UTA model is an Unresolved Transition Array model ideal for regions that consist of numerous closely packed lines. The model uses intensity-weighted distributions of transition energies along with simple mean and variance of the weighted distribution to model these unresolved lines [132]. The super configuration model is a class of code

ⁱⁱ<http://nlte.nist.gov/FLY>

that can treat the “overwhelming multiplicity of excited levels of heavy elements in hot and dense plasmas” [133] where the coupling cannot be calculated properly by a regular CR code. The Monte Carlo DCA is a detailed configuration accounting code that does not average any of the configurations for the atoms, but has very precise atomic data for transitions [134].

Coefficients for collisional and radiative processes are computed by atomic physics codes. The rate equation for atomic level i [65] is

$$\frac{dn_i}{dt} = -n_i \sum_{j \neq i}^{N_L} W_{ij} + \sum_{j \neq i}^{N_L} n_j W_{ji}, \quad 1 \leq i \leq N_L \quad (6.2)$$

For upward transitions we have

$$W_{ij} = B_{ij} \bar{J}_{ij} + n_e C_{ij} + \beta_{ij} + n_e \gamma_{ij} + \sigma_{ij} + I_{ij} \quad (6.3)$$

and for downward transitions,

$$W_{ij} = A_{ji} + B_{ji} \bar{J}_{ji} + n_e D_{ji} + \alpha_{ji}^{RR} + n_e \kappa_{ji}^{EC} + n_e^2 \delta_{ji} \quad (6.4)$$

where the various atomic processes that are included via rate coefficients are listed in Table 6.2 [65]. The quantity N_L is the number of levels in the calculation. This is calculated for each charge state by continuum lowering models [65].

The radiation transport equation used in FLYCHK is [65]

$$\left[\frac{1}{c} \frac{\partial}{\partial t} + \mathbf{n} \cdot \nabla \right] I(\mathbf{r}, \mathbf{n}, \nu, t) = \eta(r, n, \nu, t) - \chi(r, n, \nu, t) I(r, n, \nu, t) \quad (6.5)$$

where $I(\mathbf{r}, \mathbf{n}, \nu, t)$ is the specific intensity of radiation at position \mathbf{r} in direction \mathbf{n} with frequency ν . Specifically, it is defined as the amount of energy $\delta\epsilon$ that is carried by

Table 6.2: Rate Coefficients in Collisional-Radiative Model [65].

A_{ij} spontaneous emission	α_{ij} radiative recombination
B_{ij} stimulated absorption ($i < j$) or emission ($i > j$)	β_{ij} photoionization plus stimulated recombination
C_{ij} collisional excitation	γ_{ij} collisional ionization
D_{ij} collisional deexcitation	δ_{ji} collisional recombination
I_{ij} beam and non-thermal electron collisions	κ_{ji} electron capture
	σ_{ij} autoionization

the radiation in the frequency interval ν to $\nu+d\nu$ across a surface element $d\mathbf{S}$ into a solid angle $d\Omega$ in time dt :

$$\delta\epsilon = I(r, n, \nu, t)n \cdot d\mathbf{S}d\Omega d\nu dt \quad (6.6)$$

The other variables in Equation 6.5 are $\eta(r, n\nu, t)$, which is an emission coefficient or emissivity, and $\chi(r, n, \nu, t)$ is an absorption coefficient or opacity. $\eta(r, n, \nu, t)$ is written in terms of the absorption cross sections for bound-bound, free-bound and free-free transitions [65].

The main parameters for a FLYCHK run are

1. The atomic element of choice (from 1 to 79).
2. The electron temperature.
3. The electron density.
4. The radiation temperature (defaulted to zero).
5. Ion temperature (default is to be equal to the electron temperature).
6. Opacity (default assumes optically thin plasma. Specification of length gives the path length the radiation must travel in order to escape the plasma).

7. Option of a mixture to dilute the main species with other ions.
8. Fraction of hot electrons (given when the plasma has two temperature electron distributions). The user specifies the fraction of the total density and the other energy which is given a Maxwellian distribution.
9. The f_e input option that specifies a beam or non-Maxwellian energy distribution. FLYCHK assumes Maxwellian distributions for all calculations unless otherwise specified in an input file. When two temperatures are given, with one a fraction of the total density, two Maxwellian temperatures are used with the appropriate fraction given. The f_e option can also be used to load a text file with an electron beam distribution as a function of energy in eV. This input file can also be used alone without a background Maxwellian distribution.
10. The option to choose how the calculations are propagated, whether as a steady state solution, LTE or a time-dependent version.
11. The option to initialize from an input spatial distribution.
12. The option to initialize from a hydrodynamic data file, incorporating all the variables mentioned above and allowing them to be specified on a grid as well as a function of t .

FLYCHK is “zero-dimensional” in the sense that there is no information on plasma conditions outside the local conditions, and no geometrical considerations beyond a scale length for opacity and radiation escape calculations. Radiation transfer is very sensitive to geometry and so for calculations which are very sensitive to radiation transfer FLYCHK is probably best only as a rough estimate.

6.9 Bremsstrahlung

The Bremsstrahlung power emitted from a hydrogen-like plasma is [135]

$$P_{Br} = 1.69 \times 10^{-32} N_e T_e^{1/2} \sum_Z [Z^2 N(Z)] \text{watt/cm}^3 \quad (6.7)$$

where the sum is over all ionization states. What is important from this equation is the proportionality to the electron density squared (since $\sum_Z Z \times N(Z) = N_e$), which comes from the collisional nature of Bremsstrahlung radiation. Since Bremsstrahlung is produced collisionally, it is reasonable to use it as a basic correlation to plasma density squared which will be done shortly.

The conversion efficiency of laser energy into X-rays for high-Z plasmas can be given approximately by

$$\epsilon \approx 2.5 \times 10^{-5} R A^{0.5} T_e^{0.35} \quad (6.8)$$

where R is the radiation factor (ratio of total radiation to free-free radiation) with values of 35 at 1 keV down to 2.5 at 10 keV [136]. Taking $T_e=1$ keV and $A=79$ (gold) gives $\epsilon \approx 2.5\%$ (i.e. for 150 J laser energy, 3.75 J of X-ray emission).

6.10 Analysis Steps

Since the KB microscope is a fairly complex instrument and has unique focusing, spectral and geometrical properties, the analysis of images is a complex task which requires special and careful consideration of these factors. Therefore it is instructive and necessary to outline the steps taken to correct and obtain accurate information from the raw images.

6.11 Background Subtraction

The disadvantage to allowing a significant amount of unfiltered plasma emission to strike the image plane of the KB microscope is that it produces a high background that tends to fall off toward and into the images. This effect is worsened by electrons that manage to make it to the image plane and strike near the zero-order image. The net effect is a non-uniform background that has some hot-spots throughout, as can be seen in Figure 6.9. In order to assess the image signal level and size properly, this background must be subtracted. However, it is nontrivial to try and fit a curve or a function to a such a non-uniform background that varies from shot to shot. ImageJ, a Java-based image processing and analysis program, was used for the majority of image analysis. The program has a background subtraction function that is based on a rolling ball algorithm described in an article by Stanley Sternberg [137], and paraphrased in Appendix A.1.

The maximum dimension of the target of interest (a gold cone attached to a copper wire) is the opening of the cone which is about 500 μm . At the KB's magnification of approximately 10, this means a 5 mm size on the image plate, which is one hundred 50 μm pixels. Therefore the rolling ball radius is chosen to be at least 50 pixels for the background subtraction. If one investigates the background created by such a radius, it can be seen that there are portions of the cone-wire emission that are still included in the background. This means that the ball dips into the features of the wire a small amount, and so the rolling ball radius should be increased until this observed effect is minimized. This effect is a disadvantage of the rolling ball algorithm – the depth that the ball penetrates seems to be related to the pixel size, whereas the actual signal strength of the image will vary greatly and in general have no correlation to the pixel size. The way around this problem is to visually assure that the background created

does not have traces of any of the features of interest. This method is significantly better than a smooth visual fit to the background, however, since it acts in two dimensions to produce a corrected image rather than only a corrected lineout.

The rolling ball algorithm is very similar to a Fourier filter, and a comparison is given between two images in Figure 6.7. The Fourier filter used was the FFT Bandpass Filter in ImageJ which filtered structures down to a specified size, which was chosen as 100 pixels. The images in Figure 6.7 are very similar, but a slightly stronger background seems evident. A lineout through both central cone regions (of linewidth=4 pixels, left in Figure 6.8) reveals that the Fourier filter left a substantial background compared to the rolling ball algorithm, but it was nevertheless a flat background. Shifting the lineouts to coincide with one another (right in Figure 6.8) shows that, despite the fact that the Fourier filter left a higher background than the rolling ball algorithm, the wire signal falls off more quickly, which has a strong impact on the $1/e$ scalelength (discussed later). Aside from that the lineouts are essentially identical, and it would seem that the rolling ball algorithm may just be slightly better at retaining the lower-frequency portion of the wire fall-off as the signal decreases to nothing.

It was found for this data set that a rolling ball radius of 300 pixels modelled the background quite well without tracing any of the imaged emissions, as seen in Figure 6.11. If the ball radius was increased beyond this the background was not adequately traced, resulting in a residual non-uniform background. As can be seen in Figure 6.13, the resulting region of interest is sharp and background-free.

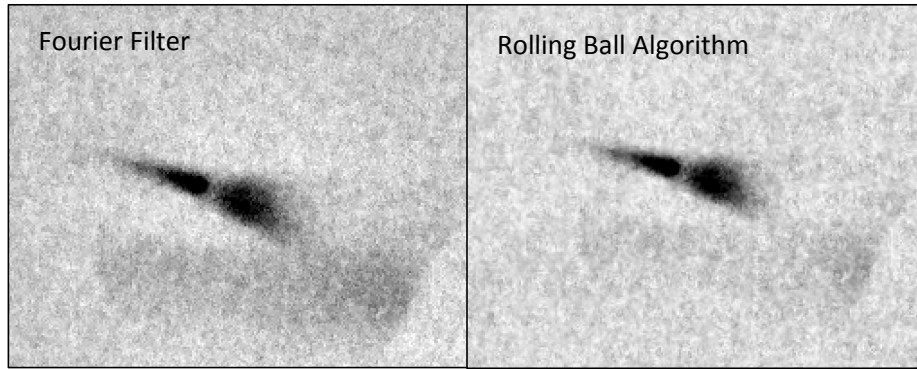


Figure 6.7: KB microscope image (2009.10.18 shot #2) after background subtraction using the Fourier filter in ImageJ for structures down to 100 pixels (left), and the rolling ball algorithm using a pixel radius of 50 pixels (right).

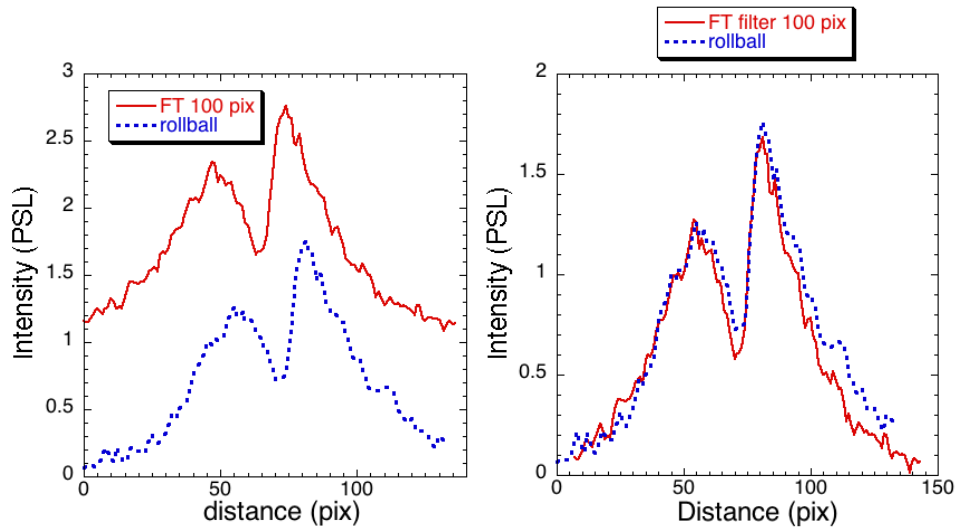


Figure 6.8: Comparison of lineouts (2009.10.18 shot #2) after background subtraction using the Fourier filter and the rolling ball algorithm. Left: The raw lineouts reveal that the Fourier filter leaves a substantial background, but it is still flat. Right: After shifting the lineouts to overlap, the Fourier filtered image has a faster fall-off for the signal from the wire region.

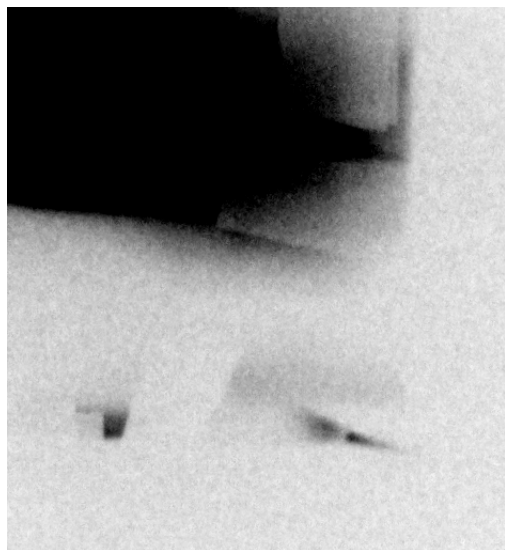


Figure 6.9: Sample KB microscope image of a gold-cone copper wire shot using the Titan Laser at LLNL. Shot number 2 on August 18, 2009.

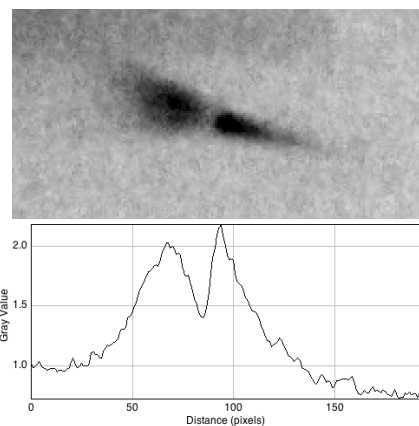


Figure 6.10: Sample region of interest of a KB microscope image of a gold-cone copper wire shot using the Titan Laser at LLNL. Shot number 2 on August 18, 2009. The plot shows a lineout of emission intensity along the central axis of the cone (linewidth=10 pixels).

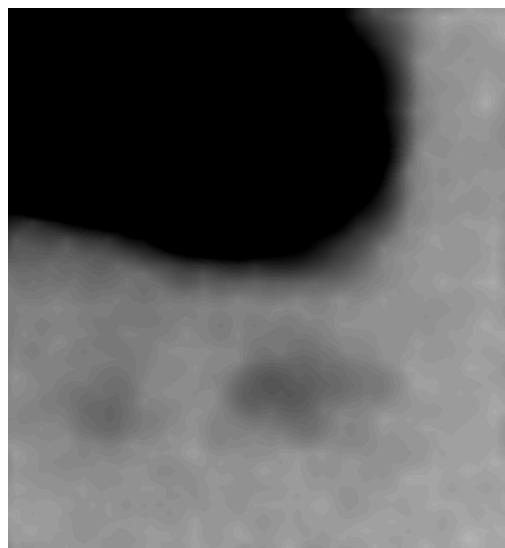


Figure 6.11: Background using ImageJ's rolling ball algorithm ($r=300$ pixels, no smoothing). Shot number 2 on August 18, 2009.

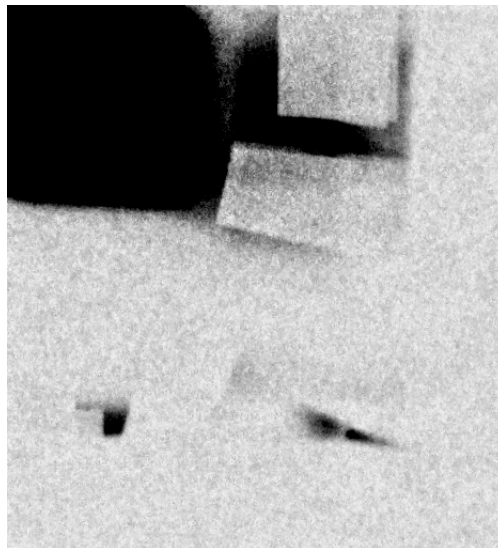


Figure 6.12: KB microscope image after background subtraction using rolling ball algorithm. Shot number 2 on August 18, 2009.

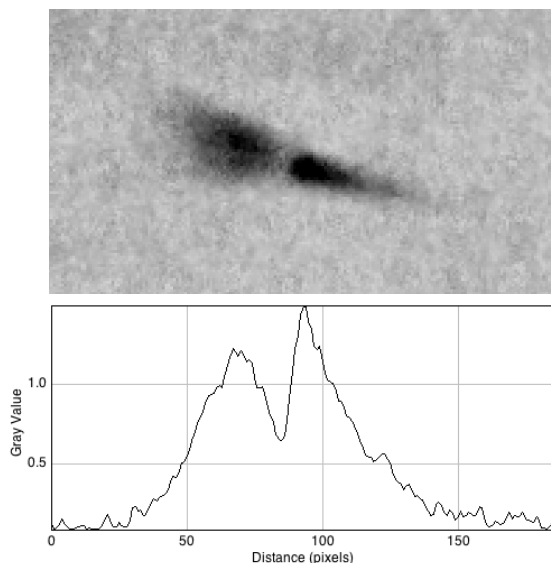


Figure 6.13: KB microscope image region of interest after background subtraction using rolling ball algorithm. Note the removal of the non-uniform background and the clarity of the image. The lower portion of the plot is a lineout (linewidth=10 pixels) through the central axis of the cone.

6.11.1 KB Linearity

Prior to doing any analysis, the KB microscope's linearity with respect to the HOPG was checked to ensure that the scaling with different energies was due to K_α yield differences and not some extraneous emissions that the KB would see without being able to discriminate. For this test 50 μm thick copper disks were shot and the total integrated signal on the KB was compared to the integrated K_α line on the HOPG. The results are plotted in Figure 6.14, showing that indeed the KB microscope response is linear with respect to the HOPG.

6.11.2 Image Rotation

First the image is rotated and cropped so that any tilt of the mirror reflections is removed. it was found in tests (performed by another graduate student, Mianzhen

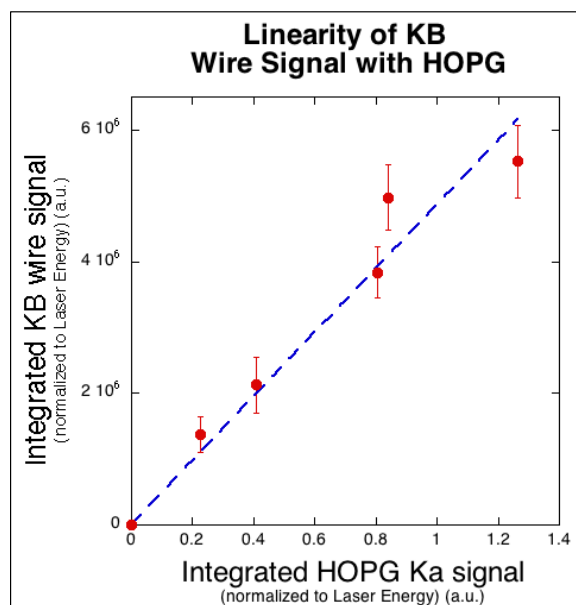


Figure 6.14: KB microscope linearity with respect to the HOPG, with a least-squares curve fit passing through zero. The fit had a 6% error.

Mo) that the bilinear interpolation used in ImageJ can introduce an error of as much as 4 %. This prepares the image for the use of a macro that will step through horizontally and vertically and calculate the appropriate reflectivity correction for each pixel in the image.

6.11.3 Gaussian Blur

In order to smooth out some of the hard hits and noise spikes that are present in many images of the KB microscope, a gaussian blur was then applied to the image. It basically constitutes a two dimensional convolution of a gaussian function with the image function. The HWHM of the gaussian is specified by a pixel radius.

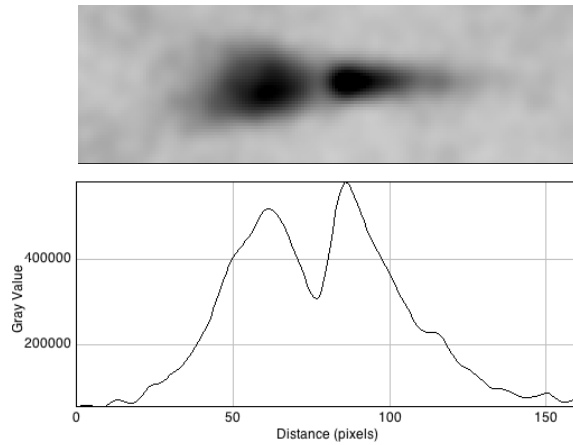


Figure 6.15: KB microscope image region of interest after background subtraction and reflectivity correction assuming 8 keV X-rays. Shot number 2 on August 18, 2009.

6.11.4 Reflectivity Correction

The edges of the zero-order image are found by finding the maximum within the quadrant of interest (specified at the beginning of a KB macro), then stepping in each direction until it reaches half of the maximum value for a pixel. The initial maximum is an average over a small region of the zero-order, and the half-maximum test is done pixel by pixel. Despite the lack of line averaging it performed well in tests and marked the half-max point accurately. This marks the edges of the zero-order, at which point every pixel can be assigned an angle of incidence on the KB mirror based on the alignment equations defined in Chapter 5. If the angle of incidence for a pixel is known, then so is the reflectivity from the KB mirror, and thus a correction can be applied over the entire image (an ImageJ macro was written that does just that). For the data analysis here, however, the start and end pixels/angles were recorded for the lineouts drawn, and separate analysis done using mathematica. This allowed for an additional reflectivity correction for the preplasma emission which has multiple wavelengths, discussed below.

For the preplasma region, since it is emitting a broad spectrum, the assumed platinum reflectivity at 8 keV was not necessarily correct. To try and obtain a sample spectrum, FLYCHK was used. The parameters were chosen to try and be an average emission for the gold as it is ionized by the high-intensity pulse (simulations by Mishra et al. [138] for example, showed that the gold is nearly fully ionized early on in the pulse for a 10^{20} W/cm² pulse). Therefore the temperature of the plasma is rapidly changing, as well as the density and average ionization state. The gold (A=79) plasma temperature was set to 10 keV. The electron density was 10^{21} cm⁻³ (critical density) with an opacity of 0.01 cm (100 μ m). A second electron temperature of 2 MeV was used with a 10% fractional density of the main plasma (therefore a density of 10^{20} cm⁻³). The spectrum was then multiplied by the transmission function for 23.7 μ m gold (20 μ m wall thickness corrected for a slant angle of 15° (cone half-angle) +17.29° (KB viewing angle)=32.3°) to give the final values after the gold's self-shielding. A volumetric emission was assumed from a 400 square pixel area (10 000 square microns) from a 100 μ m thick plasma. Also, it was assumed that a constant reflected angle of 6.98 mrad (0.4°) was in effect for the spectrum to simulate it passing through the KB microscope, and the effective reflection of two mirrors was simulated. The reflectivity across the energy spectrum is approximately 0.6-0.7 for this angle of incidence, affecting the throughput by a factor of 0.36-0.49.

The output emissivity from FLYCHK is in erg/s/srad/Hz/cm³, so the spectra had to be multiplied by 1×10^{-7} to get J, e/h (e is elementary charge and h is Planck's constant) to go from Hz to eV, and multiply by the emitting volume to obtain final units of J/s/srad/eV.

It was found that the gold was practically unaffected by the presence of the hot electrons, and there was no difference in the output spectrum if the fractional population were present or not. The separate free-free, bound-free and bound-bound

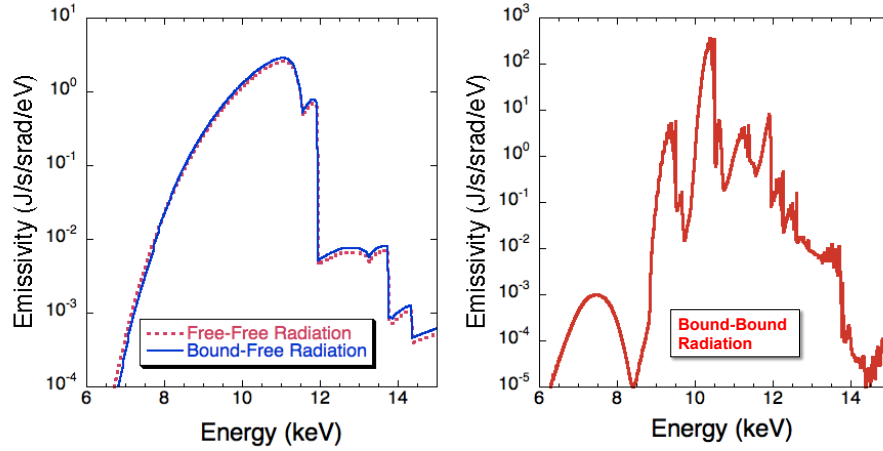


Figure 6.16: The comparison of bound-bound, bound-free and free-free radiation from a 10 keV gold plasma at $n_e=10^{21}\text{cm}^{-3}$. The radiation is that is viewable by the KB microscope after transmission through 23.7 μm Au and two mirror reflections at 0.4° .

transition radiations that make it to the KB microscope after reflection and transmission through the gold wall are plotted in Figure 6.16. The results indicate that the majority of emission from the gold region is from bound-bound transitions.

As a sanity check, the copper emission was also modeled using the same hot electron population. The copper ($A=29$) temperature was set to 0.03 eV to simulate the cold copper wire, and the density was $8.47 \times 10^{22}\text{cm}^{-3}$. The hot electron population was 0.1% of the bulk density, yielding a 10^{20}cm^{-3} population as in the gold case. The volumetric emission was assumed to be from a 260 square pixel region (6500 square microns) from a 40 μm thick plasma (an opacity of 40 μm or 0.004 cm was chosen).

The total emitted energy from the Cu plasma that reaches the KB microscope image plane was integrated from the spectrum by summation of the peaks multiplied by dE . The total gold emission was found to be 6.24×10^4 J/s/srad, and the total copper emission was found to be 1.77×10^6 J/s/srad, larger by a factor of 28. The order of magnitude difference is reasonable for such a rough simulation of the experimental conditions. The simulations provide a preliminary verification of what was seen on the

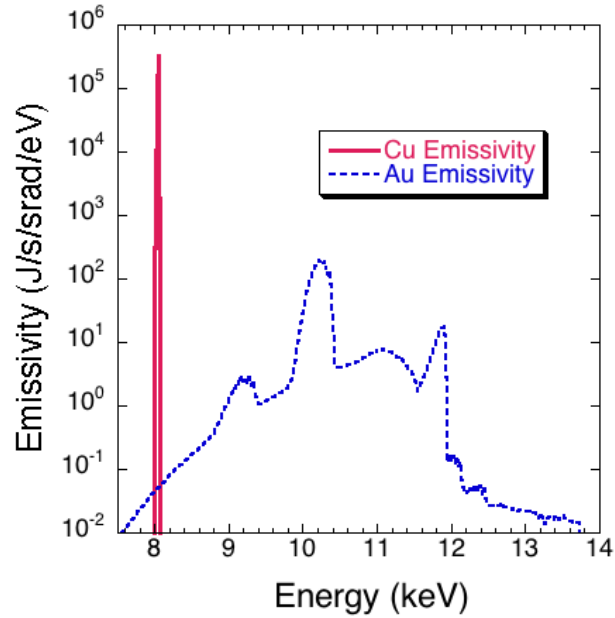


Figure 6.17: The emissivity of two plasmas versus energy. The sharp peak on the left is cold copper, and the rest of the spectrum is hot gold. They both have the same hot electron population of 10^{20} cm^{-3} .

KB microscope images, where the two emissions were of the same order of magnitude. A comparison of the two is in Figure 6.17, where it can be seen that the copper emission is larger by an order of magnitude.

From the FLYCHK simulations it was found that 4.5% of the gold emission was between 9-10 keV, 84.2% between 10-11 keV, and 10.8% between 11-12 keV for the spectrum in Figure 6.17. The weighted reflectivity function was calculated using these values. Different output spectra for different Au plasma temperatures were analyzed for the % of the spectrum in different energy segments (shown in Table 6.3). As the table shows the main emission occurs between 9 and 12 keV, and even though the proportions change with the plasma temperature the effective reflectivity remains within 15 % of its value. Therefore the assumption of gold plasma temperature does not need to be exact in order to validate the correction to the preplasma region. In

Table 6.3: The percentage of emission in different bandwidths (in keV) for different Au plasma temperatures. Generated in FLYCHK.

T_e	<6	6-7	7-8	8-9	9-10	10-11	11-12	12-13	13-14	>14
1	<0.0001	< 0.0001	0.0044	0.427	89.1	2.16	8.22	0.0284	0.002	<0.0001
2	0.0003	0.0044	0.235	2.83	53.2	25.9	17.8	0.056	0.022	<0.0001
5	0.0001	0.0013	0.09	1.58	52.2	25.1	21.0	0.069	0.041	<0.0001
10	<0.0001	0.0004	0.020	0.419	4.81	84.9	9.73	0.077	0.021	<0.0001

the end the effective reflectivity was different from the assumed 8 keV reflectivity as shown in Figure 6.18, and this difference was accounted for. The change to obtain the final corrected lineout is shown in Figure 6.19. This procedure was carried out for all images from 7 mJ, 30 mJ, 100 mJ, 500 mJ, 1 J prepulse energy. All the corrected lineouts are plotted in Figure 6.25.

6.12 Wire Transport

The coupling into the wire was observed to decrease as the prepulse energy increased. This was because of a larger standoff distance between the source of the hot electrons and the wire. It was noted by T. Ma [129] that the decrease in signal by 8X is larger than a simple geometrical argument based on source displacement. There are other effects at play, such as filamentation at 100 mJ that scatters electrons through multiple filaments into the sides of the cone [139].

The principle stopping factors at play for the electrons in the wire are as follows. At lower electron currents collisional stopping is expected to dominate [129]. For larger prepulses, the hot electron number and temperature tend to be higher, which results in larger electron currents. As this current is increased it is expected that ohmic stopping due to self-generated electric and magnetic fields has an increased

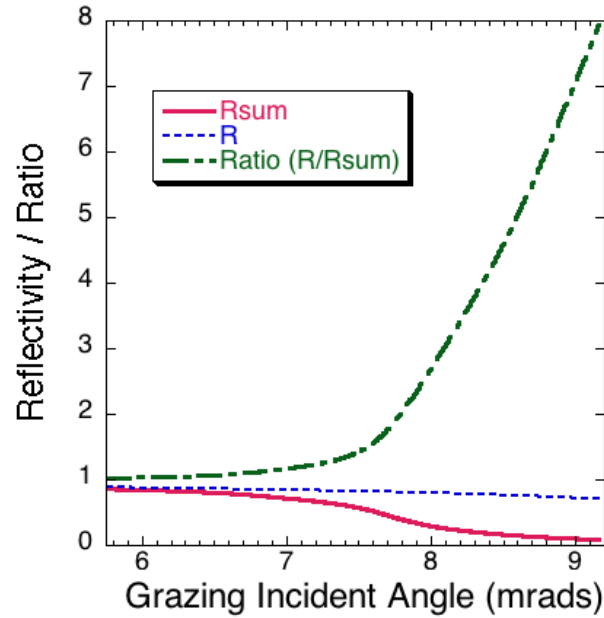


Figure 6.18: The difference in reflectivity over the lineout of the image from 8 keV (dashed, R) to the weighted reflectivity calculated using FLYCHK spectra (line, R_{sum}). R_{sum} is the Fresnel reflectivity using the weighting 4.8% 9.5 keV reflectivity, 84.9% 10.5 keV reflectivity, and 9.7% 11.5 keV reflectivity. The ratio of 8 keV to the weighted reflectivity (R/R_{sum}) is plotted as well (dash-dot, Ratio).

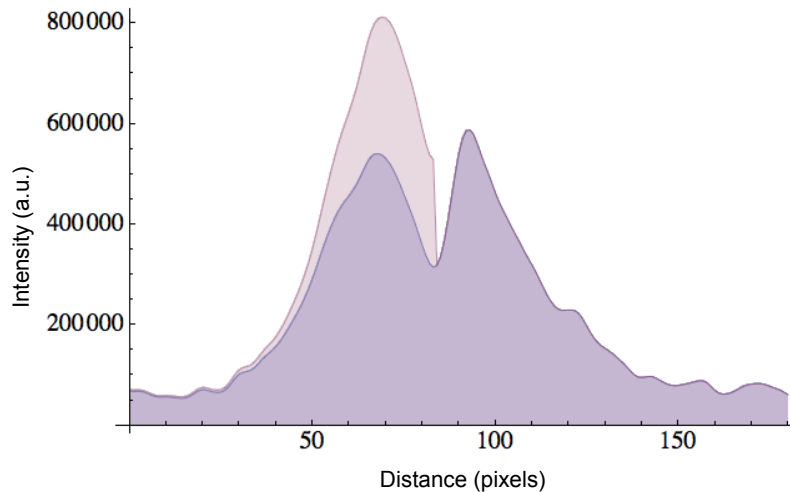


Figure 6.19: The final axial lineout (top) after correcting for background, reflectivity and the specific reflectivity of the preplasma region. The lower curve is the axial lineout prior to the weighted reflectivity correction.

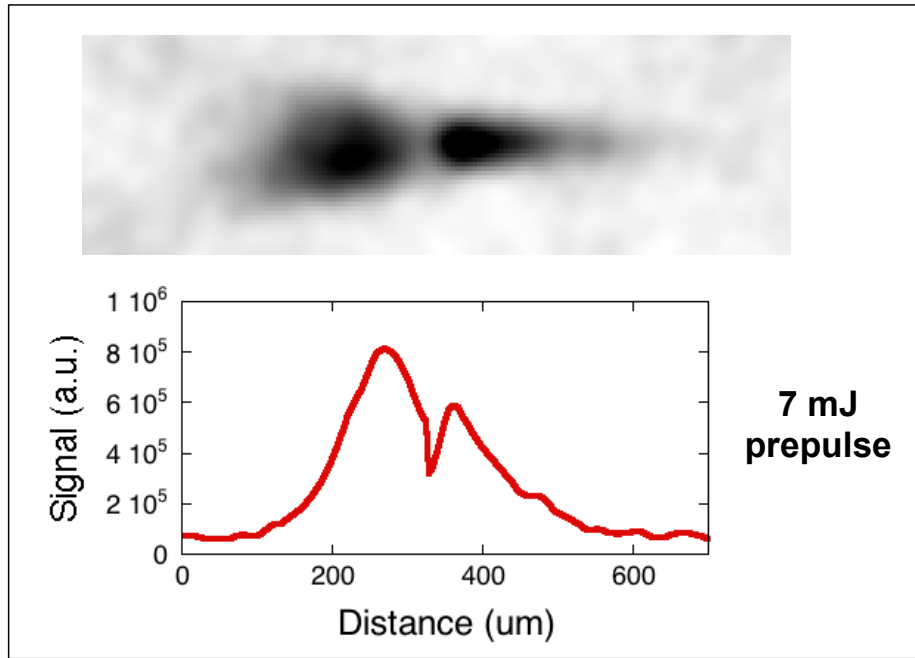


Figure 6.20: The corrected image and lineout (10 pixel linewidth) for shot #2 on 2009.08.18, for an intrinsic prepulse of 7 mJ in 1.5 ns.

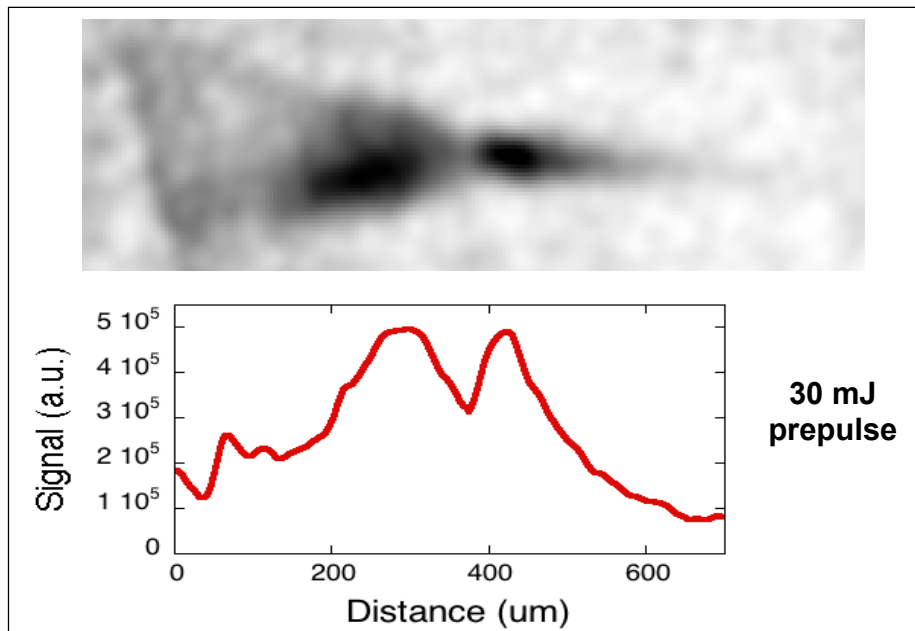


Figure 6.21: The corrected image and lineout (10 pixel linewidth) for shot #6 on 2009.08.18, for an injected prepulse of 30 mJ in 3 ns.

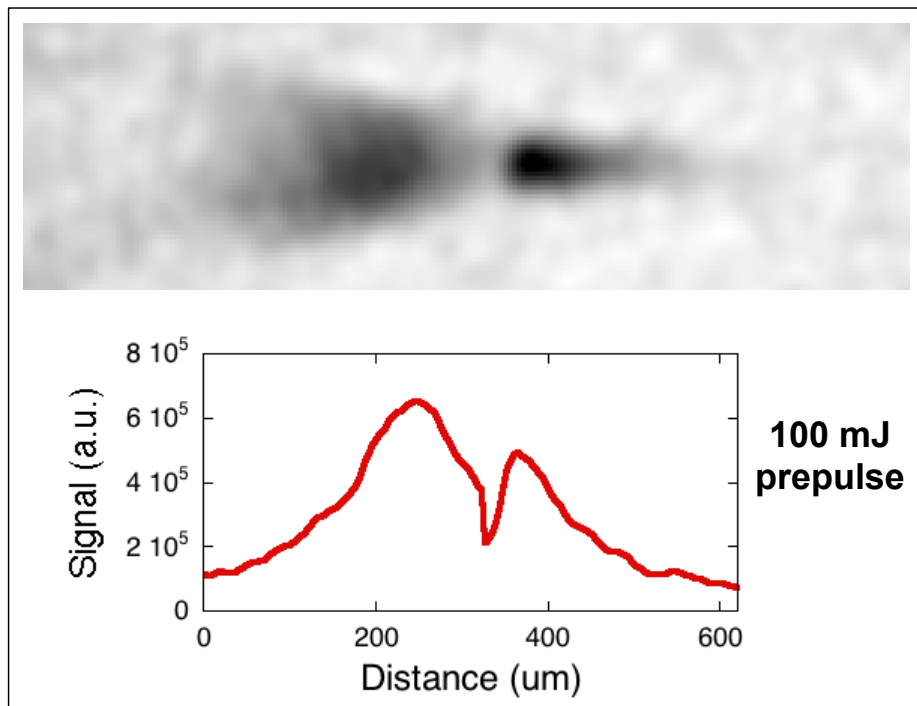


Figure 6.22: The corrected image and lineout (10 pixel linewidth) for shot #2 on 2009.08.17, for an injected prepulse of 100 mJ in 3 ns.

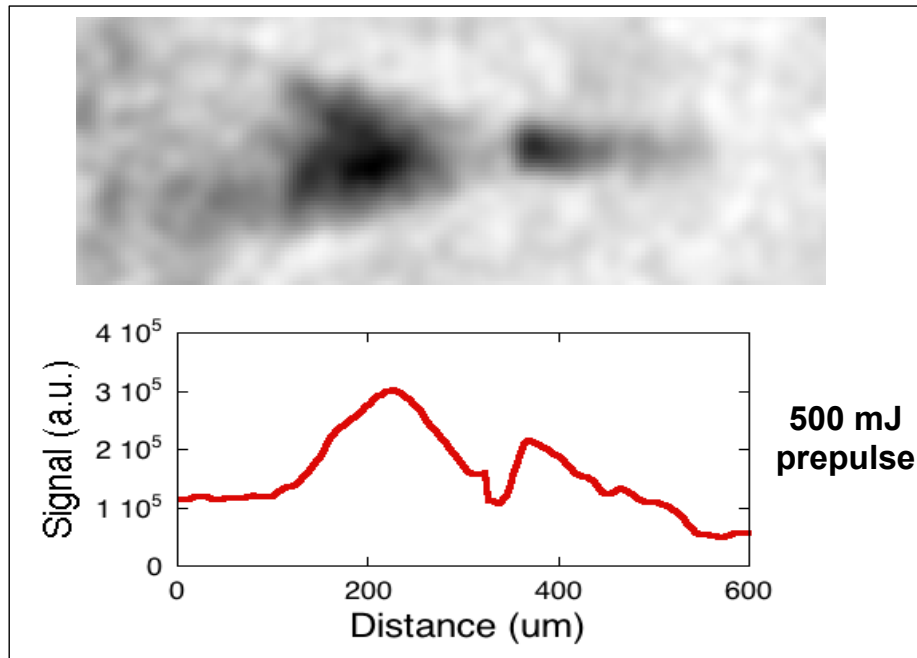


Figure 6.23: The corrected image and lineout (10 pixel linewidth) for shot #3 on 2009.08.17, for an injected prepulse of 500 mJ in 3 ns.

effect, which is why the coupling becomes poorer at higher prepulse energies. Work by T. Ma for the same set of data revealed that the electron temperatures required to reproduce the results in simulation were from 400-500 keV [129]. A comparison of the $1/e$ scalelengths from the KB microscope and the Bragg crystal imager is shown in Figure 6.27. The two results agree within error but there appears to be a systematic discrepancy. The principal reason for the discrepancy is believed to be artifacts introduced during smoothing, since small changes to the peak value can have a large impact on the fitted $1/e$ scalelength.

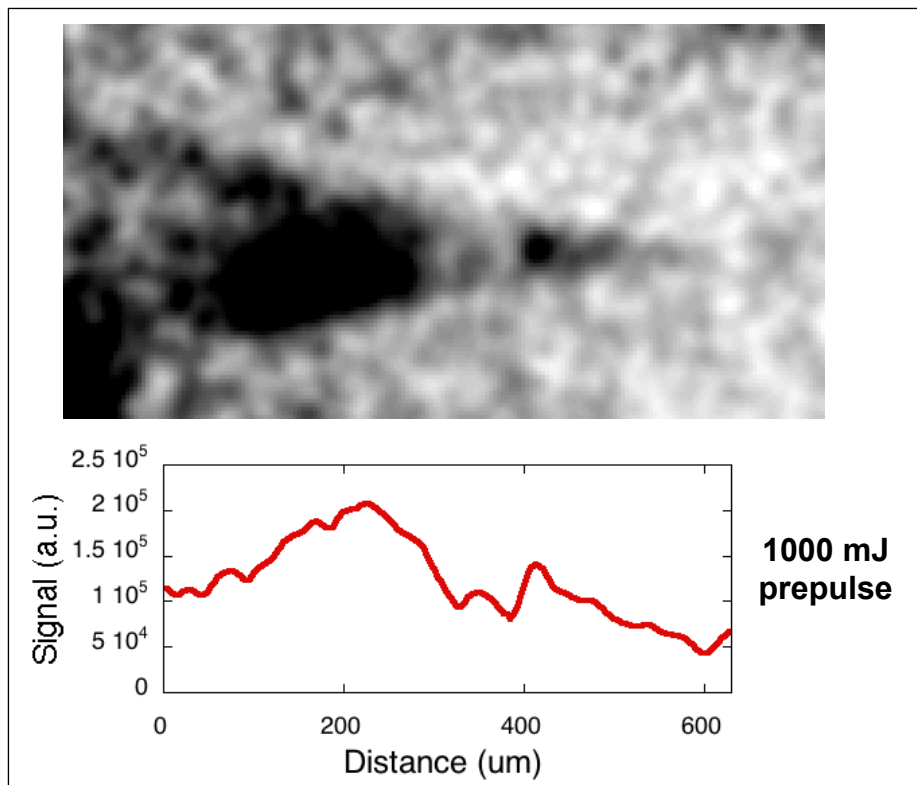


Figure 6.24: The corrected image and lineout (10 pixel linewidth) for shot #4 on 2009.08.17, for an injected prepulse of 1000 mJ in 3 ns.

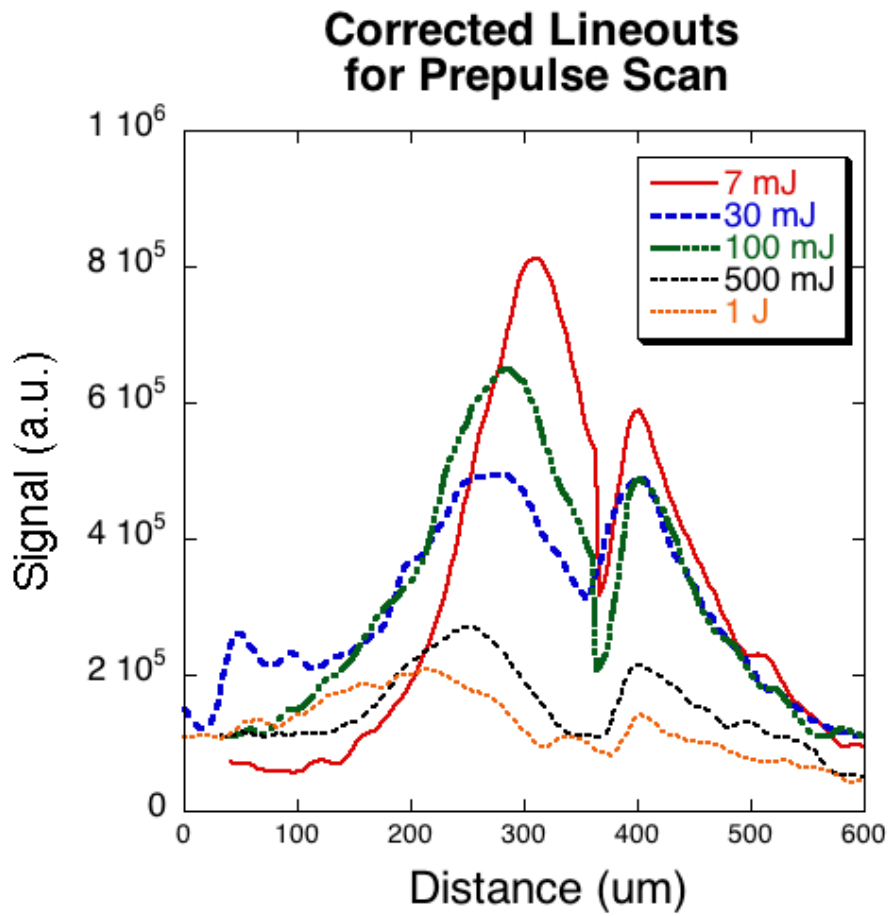


Figure 6.25: The final corrected lineouts from the prepulse scan on Titan.

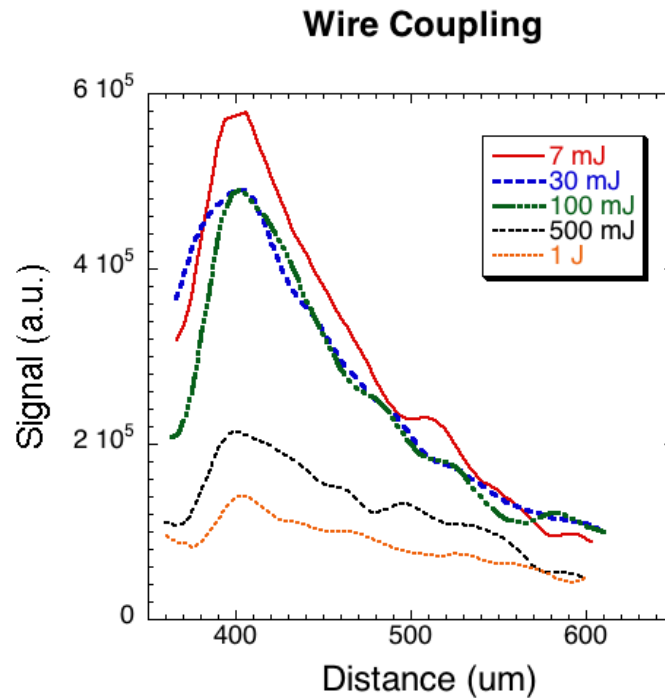


Figure 6.26: Coupling into the copper wire for different prepulse energies.

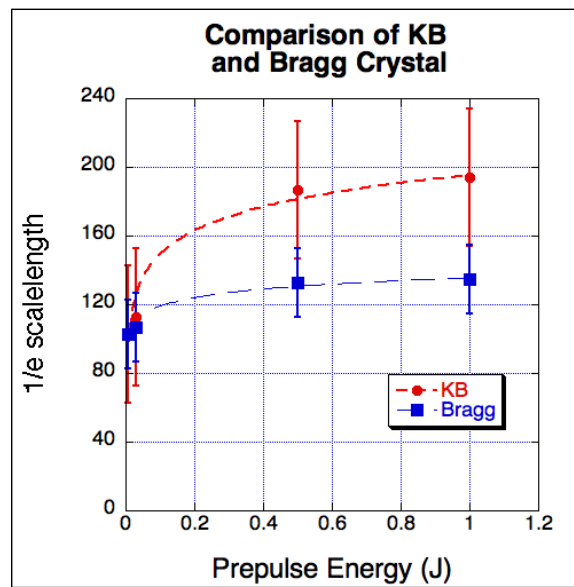


Figure 6.27: Comparison of the KB microscope 1/e scalelengths to those obtained by the Bragg crystal imager

6.13 Preplasma scaling

The preplasma scale lengths were computed by measuring the distance of the peak Bremsstrahlung emission to the trough between the cone and the wire, which was assumed to be the cone tip. A further assumption that the peak Bremsstrahlung emission occurs at the critical density was made in order to compare to simulation results.

Two simulations were done. The first was a 1D HYADES code (run by John Pasley), with the following parameters. The gold equation of state was replicated using SESAME tables, and the code itself uses a multigroup radiation diffusion approximation, with 40 groups. The target was 15 μm thick. For the intrinsic prepulse simulations (8 mJ and 10 mJ) the spot size used was 10 μm with a pulselength of 1.5 ns and flat-top intensities of $6.8\text{-}8.5 \times 10^{12}$ W/cm², respectively. For the injected prepulse cases, a 40 μm spot size was used and a 3 ns pulselength used. 1.5 ns was at the injected intensity, and 1.5 ns was at the injected intensity + intrinsic. The distance from the tip of the cone to the critical density was recorded at 3 ns and plotted in Figure 6.28.

To estimate the expansion in the cone tip the above result was modified as follows. The volume of the plasma column in a 1D cylindrical expansion is

$$V = d \times \pi \left(\frac{\text{spotsize}}{2} \right)^2 \quad (6.9)$$

If we keep this same volume and pack it into a conical volume in the shape of the cone tip (whose diameter was 40 μm), the new equation for the volume is

$$V_0 = \frac{1}{3} \pi \left(d^3 \tan^2 \theta - \frac{r_0^3}{\tan \theta} \right) \quad (6.10)$$

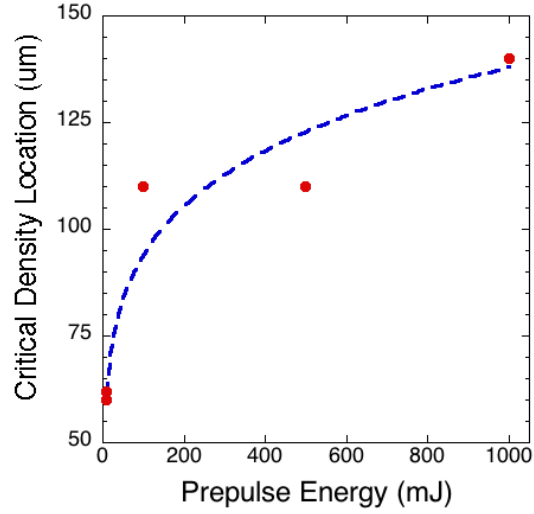


Figure 6.28: The original critical density distances from the target surface obtained through 1D HYADES simulations. The dashed line is a power law fit with a scaling of $\approx E^{1/6}$.

where $\theta = 15^\circ$ half-angle and $r_0=20\mu m$. The subtraction is because of the fact that the tip of the cone target doesn't actually go to zero diameter, and this overcalculation has to be accounted for (call this volume V_0). Assume the same plasma volume is produced for the cone tip case. The new distance from the cone tip to the critical density surface is

$$d' = \sqrt[3]{\frac{3}{\pi \tan^2 \theta} \left(d \times \pi \left(\frac{\text{spot size}}{2} \right)^2 + V_0 \right)} \quad (6.11)$$

The distances are calculated accordingly and plotted versus experimental results in Figure 6.29.

For another comparison, Mora's model for self-regulating expansion of the plasma [141] was used as a starting point. It involves 1D planar isothermal self-similar expansion and has the following scalings. The spot-size was taken to be $40 \mu m$ for the cases of injected prepulse, and $10 \mu m$ for intrinsic prepulse. First of all, the plasma

expands proportionally to the expansion velocity, which is taken to be the speed of sound, c_s .

$$L \propto c_s \quad (6.12)$$

The plasma speed of sound scales with temperature as [13]

$$c_s \propto T_e^{1/2} \quad (6.13)$$

Secondly, for planar expansion the plasma temperature scales as follows with laser intensity [141, 142]:

$$T_e \propto I^{1/2} \quad (6.14)$$

Since intensity is linearly proportional to laser energy, we can write that the expansion distance scales as follows with the laser energy, taking the combined effects of the above scalings into account.

$$d \propto L \propto E_L^{1/4} \quad (6.15)$$

We assume that the plasma critical density is at this scale length $c_s\tau$, and we pack this expanded plasma into a cone of the equivalent volume as derived above. As shown above, the plasma expansion distance scales as the third power of the volume, assuming that the cone tip region is negligible:

$$d \propto V^{1/3} \propto L^{1/3} \quad (6.16)$$

This gives a final net scaling of

$$d \propto E_L^{1/12} \quad (6.17)$$

This is a very weak scaling with laser energy, and is obviously quite simplified. In the

real case the plasma ablation away from the cone walls results in a plasma jet along the cone axis, for example. Therefore this estimate provides a lower bound for the minimum plasma distance given ideal expansion and perfect packing of the plasma into the volume of the cone.

The second set of simulations performed was using a two-dimensional HYDRA code (run by Tammy Ma). It involved a double gaussian pulse, with 50% of the energy in a $7\ \mu\text{m}$ FWHM spot, and 75% in a $15\ \mu\text{m}$ FWHM spot. There is a 0.25 ns linear rise, a 2.5 ns flat top, and a 0.25 ns linear decay. The 2D modeling predicts a plasma jet along the axis of the cone (see Figure 6.30), and so provides an upper bound for the distance the plasma expands.

As can be seen in Figure 6.29, the actual experimentally measured distances lie somewhere in between the rough 1D estimate and the full 2D modeling. This raises the question of what is missing or misrepresented in the 2D simulations to give such an incorrect estimate of the plasma expansion. However, the assumption that the Bremsstrahlung peak emission occurs at the critical density is not necessarily valid given the strong scaling of emission with density squared. Further work is required to investigate these effects in detail.

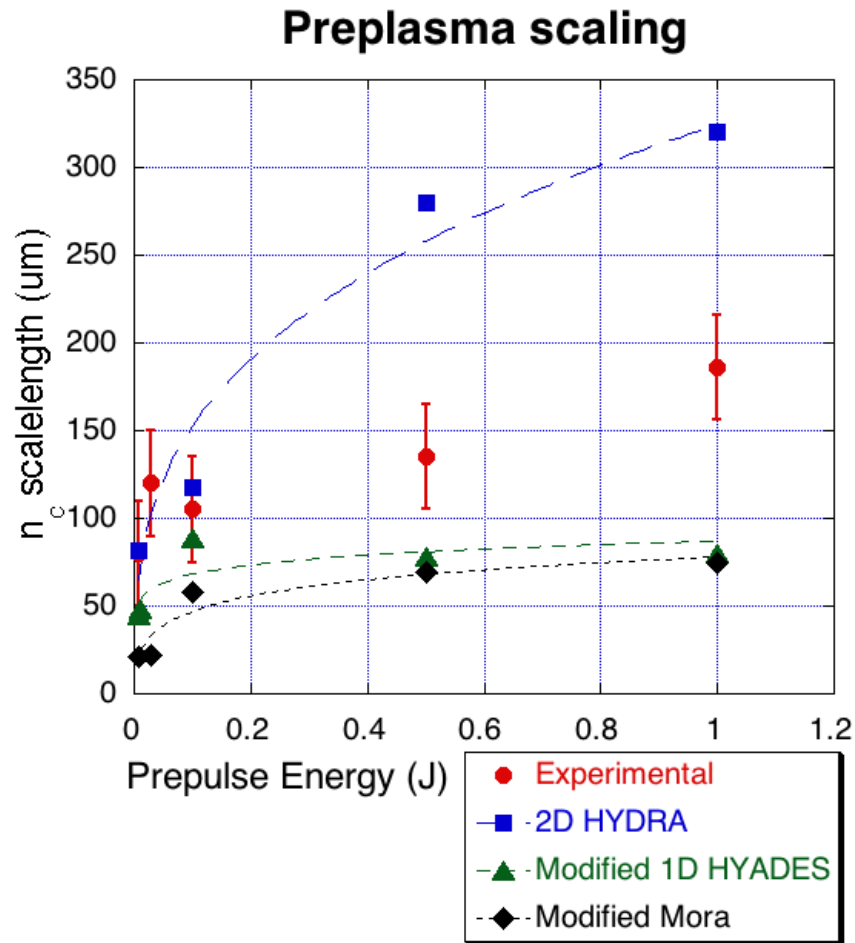


Figure 6.29: The scale length of preplasma versus prepulse energy. Experimental is compared against 2D HYDRA modeling and extended 1D modeling (from both Mora's model and HYADES), which provide upper and lower bounds. The dashed line through the 2D data is a power law fit of $1/3$ scaling, and the dashed line through the 1D data is a power law fit of $1/12$ scaling.

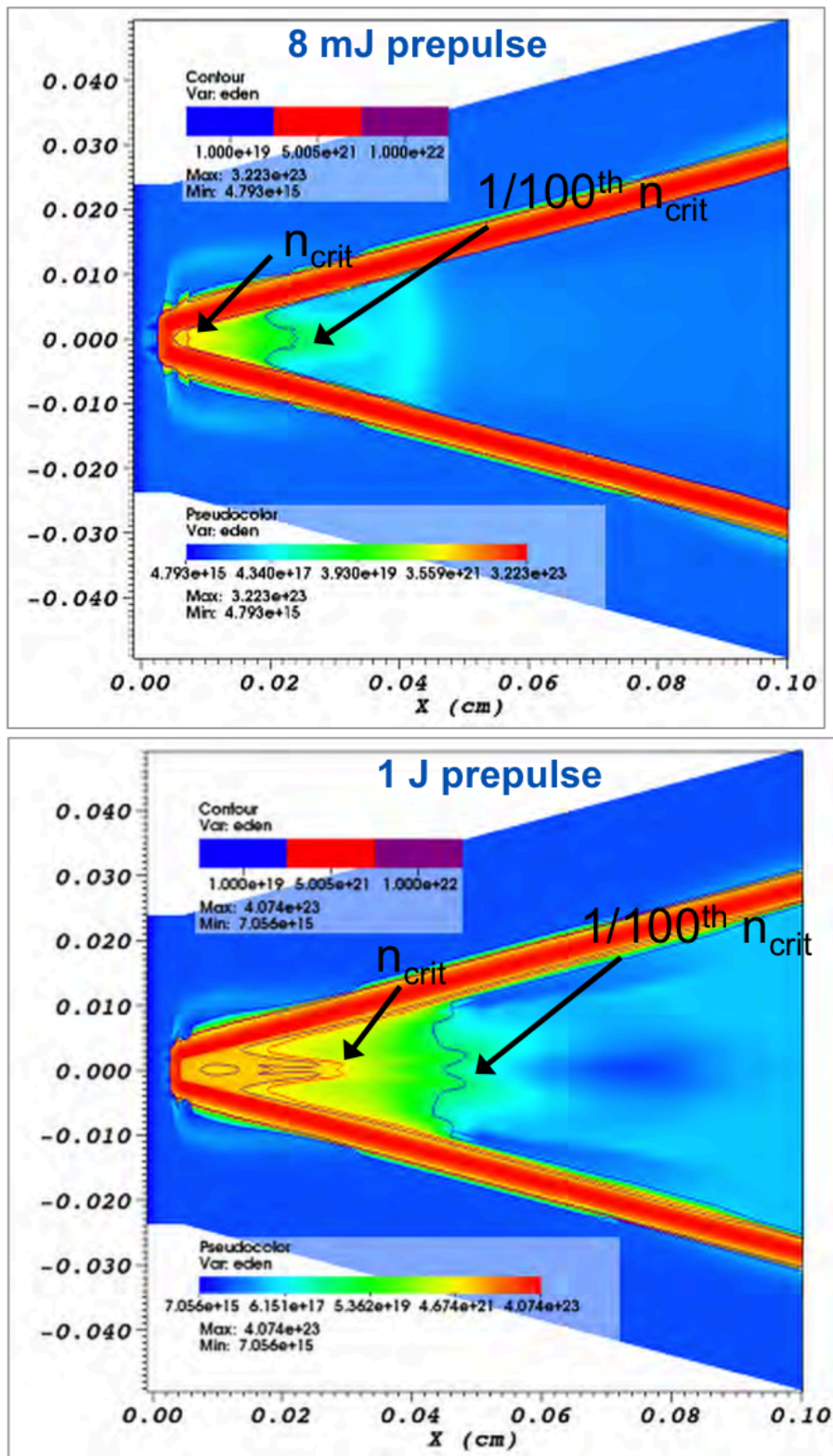


Figure 6.30: The 2D cylindrical HYDRA code simulation results for 8 mJ prepulse and 1J prepulse, showing evidence of a plasma jet along the central axis [143].

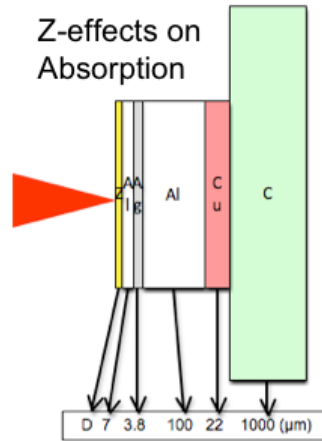


Figure 6.31: One of the targets shot during the Z effect study on Titan [64].

6.14 Preplasma emission from other targets

The KB microscope's broadband nature compared to traditional Bragg crystal imagers used in Fast Ignition experiments led to some unique images during other experiments as well. As alluded to in Chapter 3, the KB microscope was used in an experiment investigating the effects of the nuclear charge (Z) or resistivity on the propagation of hot electrons. One of the targets investigated is depicted in Figure 6.31. The first layer was of varying material, either plastic (CH), aluminum, molybdenum, or gold. The thickness was adjusted for each to so that the shock transit time was the same based on hydrodynamic simulations done by M.S. Wei. For CH, Al, Mo, and Au, the thicknesses were 2.5, 0, 0.6 and 1.1 μm respectively (the lower Mo thickness was a target manufacturing error). This particular target investigated the effects of laser absorption on hot electron generation and transport, which is why the changing layer was at the front surface of the target. The KB microscope's position in the chamber was on Titan port TS1, whose view of the target is shown in Figures 6.33 and 6.34.

Two spots were in fact seen for shot 6 on May 18, 2010 as shown in Figure 6.34. The shot was 135 J with a pulselength of 0.7 ps and a prepulse of 13 mJ on a target with a $0.6 \mu m$ Mo front layer. The measured separation of 23 ± 2 pixels peak-to-peak at an angle of 48° from horizontal needs to be corrected for magnification and viewing angle.

First a correction is made for the differing horizontal and vertical magnifications. The horizontal and vertical lengths are given, respectively, by

$$\frac{23 \cos 48^\circ \times 50 \mu m}{13.87} = 55.5 \mu m \quad (6.18)$$

$$\frac{23 \sin 48^\circ \times 50 \mu m}{10.72} = 79.7 \mu m \quad (6.19)$$

where 13.87 and 10.72 are the horizontal and vertical magnifications, respectively. Thus the net separation from the center of one spot to the center of the second spot in the object plane is, via pythagorus,

$$\sqrt{55.5^2 + 79.7^2} = 97 \pm 11 \mu m \quad (6.20)$$

Next, the viewing angle of the KB relative to the target normal needs to be considered as well. A diagram of the two vectors, one going through the target rear normal and one going to the KB microscope, is shown in Figure 6.32. The vector for the target normal is given by $(0,-1,0)$. The vector for the KB microscope is given by

$$[\sin (17.29^\circ) \cos (40^\circ), -\cos (17.29^\circ) \cos (40^\circ), \sin (40^\circ)] \quad (6.21)$$

where 17.29° is the horizontal angle between the KB microscope and the target normal, and 40° is the vertical angle between the KB microscope and the target

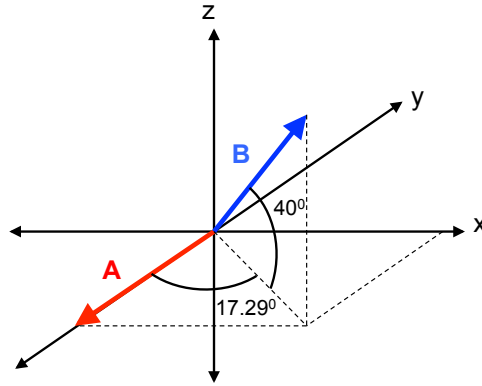


Figure 6.32: The vectors defining target normal (**A**) and the view of the KB microscope (**B**).

normal. Denoting the target normal as **A** and the normalized KB microscope vector as **B**, we recall the definition of dot product:

$$\mathbf{A} \cdot \mathbf{B} = |\mathbf{A}||\mathbf{B}| \cos \theta = (\cos (17.29^\circ))(\cos (40^\circ)) \quad (6.22)$$

Computing the $|\mathbf{A}||\mathbf{B}|$ term of the above equation gives

$$|\mathbf{A}||\mathbf{B}| = 1 \cdot \sqrt{\cos^2 (40^\circ)(\sin^2 (17.29^\circ) + \cos^2 (17.29^\circ)) + \sin^2 (40^\circ)} = 1 \quad (6.23)$$

Thus we can obtain the separation angle

$$\cos \theta = \frac{\mathbf{A} \cdot \mathbf{B}}{|\mathbf{A}||\mathbf{B}|} = 0.731 \quad (6.24)$$

$$\theta = 43.0^\circ \quad (6.25)$$

Correcting for the projection angle gives a final separation distance of

$$\frac{97 \mu m}{0.802} = 130 \mu m \pm 15 \mu m \quad (6.26)$$

The net separation between the front surface of the target and the copper layer from the target specifications is $0.6+7+3.8+100=111\ \mu\text{m}$. If we assume a preplasma scalelength of $10\ \mu\text{m}$ for a 13 mJ prepulse (obtained for critical density distance in simulations for ≈ 15 mJ on a planar target in [144]), that brings the separation to approximately $121\ \mu\text{m}$. If we assume the viewed emission comes from roughly the center of the copper layer, we get an additional distance of $11\ \mu\text{m}$, for a final separation of $132\ \mu\text{m}$. Thus the experimentally obtained separation is almost in agreement with that predicted by modeling. The smaller distance for the KB microscope is likely due in part to the fact that emission further into the target will be less attenuated by target opacity effects and thus the peak emission will be seen further into the target than expected. Also, by overlapping the KB microscope image with the image predicted by visrad simulations, it can be seen that the expected and observed emissions are in good agreement. However, they are not perfect, and such a situation illustrates the KB microscope's capacity to be used as a secondary alignment diagnostic.

What was particularly interesting for this set of shots was that the double emission was observed only for molybdenum targets. A plausible explanation for this is that molybdenum had the right balance of high enough Z to generate substantial front surface Bremsstrahlung emission, while being thin enough and not absorbent enough (low enough Z) to allow the emission to pass through to the back of the target without a large attenuation. In the cases of aluminum and CH, the low Z did not generate substantial frontal surface emission, while for the gold case substantial frontal surface emission was generated, but the gold layer was too thick and attenuating for it to make it to the rear of the target. The image in Figure 6.34 is only a sample image of double emissions obtained by the KB microscope. For a complete list of shots where double emission was observed, see Appendix A.2.

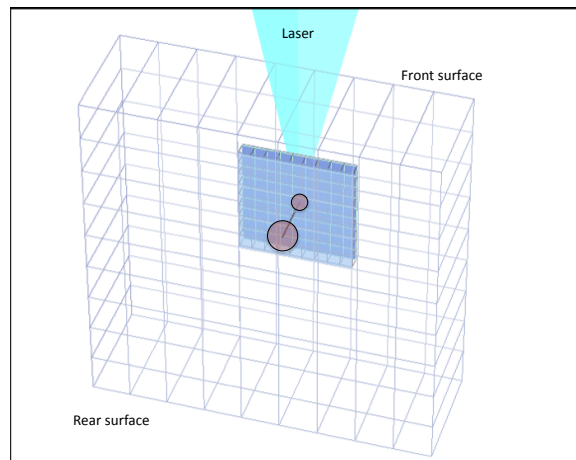


Figure 6.33: The target as seen by the KB microscope on Titan Port TS1. The grey circles indicate where front surface emission is positioned relative to layer emission for electrons traveling normal to the target surface. Generated using visrad by Hiroshi Sawada (UCSD).

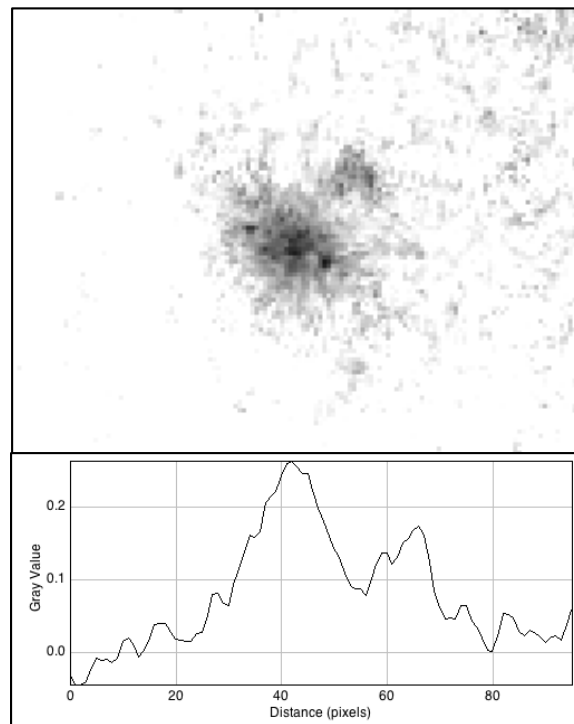


Figure 6.34: The double emission seen by the KB microscope for shot 6 on May 18, 2010. The plot is a lineout 5 pixels wide taken through the two peaks at an angle of 48° .

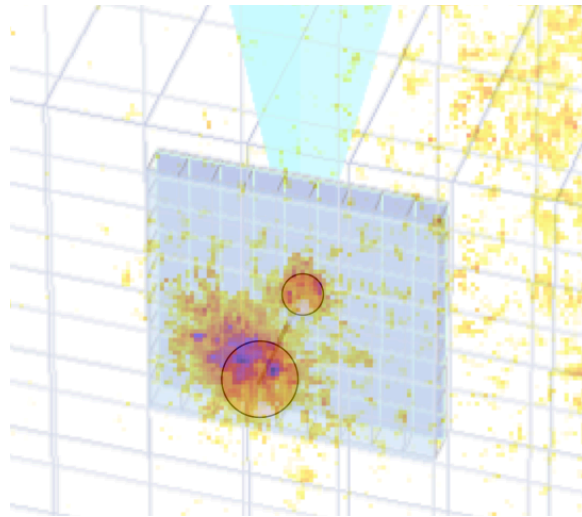


Figure 6.35: The double emission seen by the KB microscope for shot 6 on May 18, 2010 overlain on the image generated using visrad. The emission lies roughly within the circles predicted by visrad.

Chapter 7

Current Developments and Future Work

This chapter will discuss some research that is still in progress at the time of writing, and center around the key issues needed to develop the next generation KB microscope. These are mainly the mirror bender, which aims to bend a long superpolished slab into a large radius of curvature necessary for KB imaging; and multilayer coatings which will allow for a higher reflectivity and higher angles of incidence for hard X-rays.

7.1 Mirror Bender and Multilayer Mirrors

The motivation for the mirror bender is two-fold. Firstly, the cost of large radius-of-curvature superpolished mirrors is high, particularly if one desires an aspheric shape for better resolution. Flat superpolished slabs, however, are much more reasonably priced and thus a cost-effective starting point in the design of an X-ray imaging system. Secondly, as discussed previously, each mirror in the KB microscope always

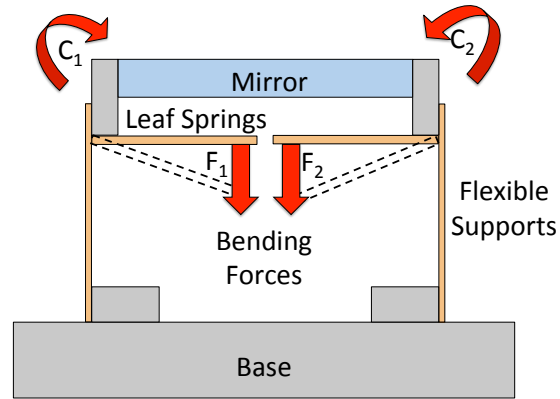


Figure 7.1: Concept of the mirror bender (modified from [145]).

requires a different radius of curvature in order to be in focus at the same angle. The ability to adjust the second mirror would be very beneficial, as well as opening up the possibility of having an adaptable KB microscope that can be tweaked for different imaging conditions and X-ray energies.

The design attempted was based on that of Howells et al. [145]. Basically a slab is either glued or clamped at both ends, and levers underneath apply coupling torques up and inward on both sides, as shown in Figure 7.1. This design has the advantage of being simple, but the disadvantage of coupled focusing and aberration correction (another design in the same paper puts the mirror in tension and can alter both parameters independently).

According to Howells the bending couples necessary for a radius of curvature R_0 obey the following equation:

$$\frac{C_1 + C_2}{2} = \frac{EI_0}{R_0} \quad (7.1)$$

where E is Young's Modulus, I_0 is the moment of inertia of the beam cross section, and C_1 and C_2 are coupling torques. The assumption is made that the support bars are very flexible and do not affect the torque. The moment of inertia of the beam

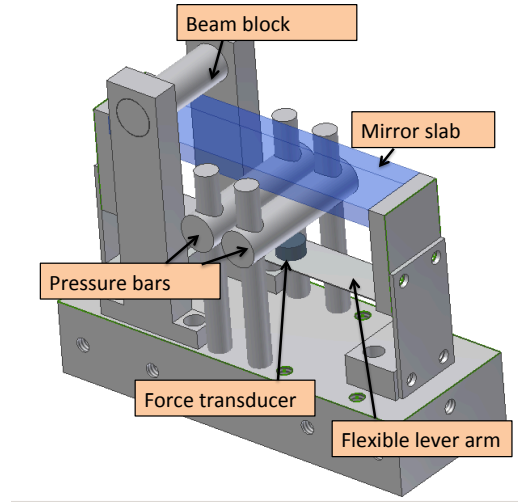


Figure 7.2: First mirror bender design.

cross section is actually what is normally called the second moment of area, and is defined as

$$I_{xy} = \int \int xy dA. \quad (7.2)$$

The initial constructed design is shown in Figure 7.2.

In order to test the design, the bender was set up in a large aperture Michelson interferometer. The setup is given in Figure 7.3.

A 20X microscope objective was used to expand the laser beam, and an 80 cm FL 102 mm diameter lens to re-collimate it. The interferometric patterns were captured on a CCD camera (Chameleon). Preliminary tests have indicated that the support bars are too stiff and that the mirror is not yet bending as much as expected. An exploration of different support lengths and strengths will follow. Further work is needed to quantify the mirror bender's performance.

In order to begin the development of mirror coatings, tungsten and boron carbide multilayer coatings were sputtered onto silicon wafers in the nanofabrication lab by

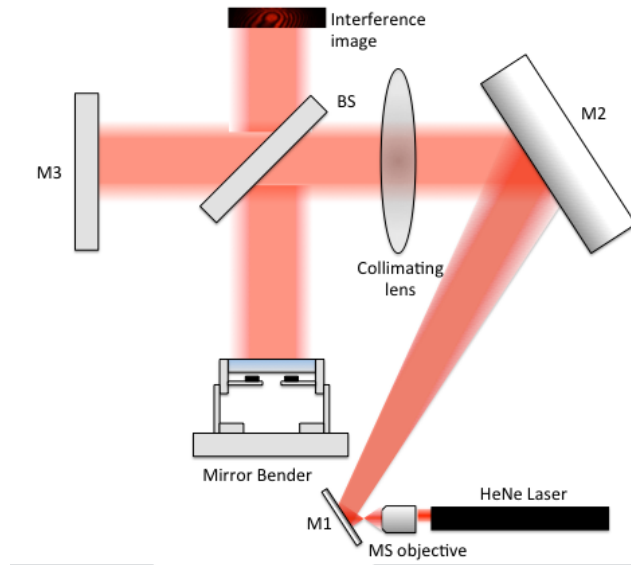


Figure 7.3: Interferometer used to measure mirror bending. All mirrors are flat. M1 is 25.4 mm diameter. M2 is 190.5 mm diameter. M3 and BS are 127 mm diameter. The lens has a focal length of 80 cm and a diameter of 101.6 mm. The lens sets the vertical size limit and the beamsplitter sets the horizontal size limit.

Allan Beaudry, a summer student, using a magnetron sputtering system. The deposition rates were characterized but further work is required to assess the reflectivity, roughness and interlayer diffusion of the multilayers prior to coating any superpolished optics.

7.2 Next Generation KB

Ultimately these coatings can be used on superpolished 2.5X10 cm zerodur slabs that can be used to make a large throughput KB – the length increases the solid angle by increasing the only dimension that matters for the KB imaging. Zerodur is a glass with a very low thermal expansion coefficient, and so is ideal for mirror bending in the vacuum conditions of a given target chamber. The bending curvatures of interest are between 20 m and 120 m, and the mirror bender shows promise for achieving just

that. More advanced bending will involve varying the couples on either end of the mirror in order to create an aspherical surface for even higher resolution.

7.3 Conclusions

A Kirkpatrick-Baez X-ray microscope has been designed and characterized to image the K_α emission of copper at 8.05 keV from tracer layers in Fast Ignition experiments. A resolution better than $30\ \mu\text{m}$ over a $300\ \mu\text{m}$ field of view was demonstrated through tests on a cw X-ray source, with a best resolution of $15\ \mu\text{m}$, a factor of 2 worse than the ideal theoretical resolution (calculated using ZEMAX). The reflectivity was measured to be 20% lower on average than perfectly smooth Fresnel reflectivity, and corresponded to an rms roughness of $0.55\ \text{\AA}$. The imaging capabilities were also demonstrated using a fine gold mesh of $35\ \mu\text{m}$ period, and a qualitative image was obtained whose lineshape matched that of experiments, using transmission functions and an effective PSF of the KB microscope. Improvement in resolution of the second mirror was demonstrated by bending the second mirror via external force applied to the mirror back, and the resolution of the bent mirror tested. The results were in qualitative agreement with theoretical calculations of circular slab bending, that $\approx 410\ \text{N}$ (92 lbs.) of force is necessary to bend the second mirror to a radius of curvature of 25 m and put it into focus at an incident angle of 8.73 mrad (0.5°). The preliminary results are encouraging but a more stable bending system is required to establish confidence and reliable bending. This result is significant because it allows for more flexibility in the initial curvature of the mirror purchased which can decrease the cost of the imaging system substantially.

The KB microscope was tested on the Titan laser system at LLNL in Fast Ignition experiments. The alignment procedure was refined using an optical fiber source in the

target position. The shift in alignment from air to vacuum could be measured prior to experiment and accounted for, since it was consistent within 0.7 mrad. The overall alignment stability of the microscope was 0.5 mrad, where angles were inferred based on the separation between the one-dimensional images and the edge of the zero-order image clipped by the tungsten rods.

As a demonstration of its application and usefulness in Fast Ignition experiments, a detailed analysis was carried out on prepulse scan data from Titan. The preformed plasma has significant effects on the transport of hot electrons, and it was shown that the coupling into the wire was decreased beyond the pure geometrical effects involved by moving the critical surface further away through a larger preplasma. The inferred plasma distance from the imaged Bremsstrahlung in the gold cone region showed a scaling with prepulse energy that lay somewhere between simple one-dimensional estimations and full two-dimensional hydrodynamics simulations. The inferred $1/e$ scale lengths for wire transport were within error of those found by another diagnostic (the Bragg crystal imager), but demonstrated a systematic discrepancy. The KB microscope is the only diagnostic that could image the preplasma emission and the K_α generation simultaneously, which to the author's knowledge has never been done before.

A further demonstration of the KB microscope's unique imaging capacities was shown with some sample images from foil and buried cone targets viewed from behind where both front surface emission and tracer layer K_α emission were observed. The emission separation distance was consistent with the target specifications of layer depths, and in some cases the geometrical positioning of the imaging could be used to assess the accuracy of alignment within the cone tip.

Future work and progress on the development of this diagnostic includes an in-situ experimental test of the bending of the second mirror, since it was only studied

in-depth outside of Fast Ignition experiments. A refinement of the alignment system could be obtained by using a camera with a chip large enough to image all four image spots (zero-order, 2 one-dimensional images and the 2D image). The fiber source could be placed at TCC and the chamber evacuated in order to align under vacuum conditions using the same method described in this work. A mirror bender was constructed and multilayer mirror slabs coated as steps toward the next generation KB microscope. Further development in these two areas could result in the production of a high-throughput KB microscope for use on future Titan as well as OMEGA-EP experiments, which are approaching the energy regimes of full scale Fast Ignition tests.

As the energy is ramped up and hotter plasmas generated, harder X-rays are necessary to escape the plasma without significant attenuation. The KB microscope is capable of imaging these X-rays well without being sensitive to temperature shifts due to target heating. It is therefore a useful diagnostic capable of investigating the crucial aspects of hot electron transport. The physics of electron transport, including divergence, energy spectrum, scattering and absorption are still in the process of being understood. Having improved diagnostic capabilities allows the understanding of fast ignition processes to be refined and helps move toward the realisation of fusion energy on Earth.

Bibliography

- [1] Sheffield, J. et. al. (2004). Energy Options for the Future. *Journal of Fusion Energy*. 23, 63.
- [2] Energy Information Administration (U.S. Department of Energy) (2006). *International Energy Outlook, Report No: DOE/EIA-0484*.
- [3] Fedosejevs, R. (2008). *Laser Fusion A Route to a Sustainable Energy Future*. Presentation for the Canadian Association of Physicists Annual Congress, Moncton, June 7-10, 2009.
- [4] Schultz, K.R. (2003). Production of Hydrogen by Fusion Energy: A Review and Perspective. *Fusion Science and Technology* 44, 393.
- [5] International Fusion Research Council (IFRC) (2005). Status Report on Fusion Research, *Nuclear Fusion* 45, A1.
- [6] Tabak, M., Hammer, J., Glinksy, M. E. et al. (1994). Ignition and high gain with ultrapowerful lasers. *Physics of Plasmas* 1 (5), 1626-1634.
- [7] Moses, E., Boyd, R., Remington, B. Keane, C. and Al-Ayat, R. (2009). The National Ignition Facility: Ushering in an new age for high-energy density science. *Physics of Plasmas*, 16(041006), 1-13.
- [8] Moses, E. (2009) *The National Ignition Facility – Status and Future Directions*. Presentation to the Fusion Power Associates, Dec. 2, 2009.
- [9] Landen, O.L. et al (1999). Indirect-Drive Time Dependent Symmetry Diagnosis at NIF-scale. *Article presented at First International Conference on Inertial Fusion Sciences and Applications, Bordeaux, France..*
- [10] Palmer, J. BBC News. *Laser fusion test results raise energy hopes* [Online] February 22, 2010. (<http://news.bbc.co.uk/2/hi/8485669.stm>).
- [11] Fusion Energy: NIF & Photon Science [Online] July 12, 2011. (https://lasers.llnl.gov/about/missions/energy_for_the_future/life/).

- [12] HiPER Project. [Online] February 22, 2010. (<http://www.hiper-laser.org/>).
- [13] Chen, F. (2006). *Introduction to plasma physics and controlled fusion*. New York: Springer.
- [14] Tayal, D.C. (2009) *Nuclear Physics*, Himalaya Publishing House: Mumbai. [Online] July 12, 2011.
- [15] Pfalzner, S. (2006). *An Introduction to Inertial Confinement Fusion*. Taylor & Francis: London.
- [16] Mahdavi, M. and Kaleji, B. (2009). Deuterium/helium-3 fusion reactors with lithium seeding. *Plasma Physics and Controlled Fusion* 51 (085003), 1-11.
- [17] Siegel, J. (2006). In Brief. *Bulletin of the Atomic Scientists* 62 (2), 8-13.
- [18] Kulcinski, G.L. and Schmitt, H.H. (1992). Fusion Power from Lunar Resources. *Fusion Technology* 21(4), 2221-2229.
- [19] Lawson, J. D.(1957). Some Criteria for a Power Producing Thermonuclear Reactor. *Proceedings of the Physical Society, Section B* 70 (1), 6-10.
- [20] Atzeni, S. and Meyer-ter-vehn, J. (2004). *The Physics of Inertial Fusion: Beam Plasma Interaction, Hydrodynamics, Hot Dense Matter*. Oxford Press: Oxford.
- [21] Rosen, M.D. (1999). The physics issues that determine inertial confinement fusion target gain and driver requirements: A tutorial. *Physics of Plasmas* 6(5), 1690-1699.
- [22] Edwards, J. et al. (2000). Turbulent hydrodynamics experiments using a new plasma piston. *Physics of Plasmas* 7(5), 2099-2107.
- [23] Marinak, M.M. et al. (2001). Three-dimensional HYDRA simulations of National Ignition Facility targets. *Physics of Plasmas* 8 (5), 2275-2280.
- [24] MacPhee, A.G., et al. (2008). Diagnostics for fast ignition science (invited). *Review of Scientific Instruments*, 79, 1-5.
- [25] Gibbon, P. (2005). *Short pulse laser interactions with matter: An introduction*. London: Imperial College Press.
- [26] Griffiths, D. J. (1999). *Introduction to Electrodynamics*, Prentice Hall: New Jersey.
- [27] Krueer, W. L. (2003). *The Physics of Laser Plasma Interactions*, Westview: Colorado.

- [28] Wilks, S.C. and Kruer, W.L. (1997). Absorption of Ultrashort, Ultra-Intense Laser Light by Solids and Overdense Plasmas. *IEEE Journal of Quantum Electronics*, 33(11), 1954-1968.
- [29] Langdon, A.B. (1980). Non-linear Inverse Bremsstrahlung and Heated Electron Distributions. *Physical Review Letters* 44(9), 575-579.
- [30] Kosarev, I. N. (2006). Kinetic theory of plasma and gas. interaction of high-intensity laser pulses with plasmas. *Physics-Uspokhi*, 49(12), 1239-1252.
- [31] Strickland, D. and Mourou, G. (1985). Compression of amplified chirped optical pulses. *Optics Communications* 55(6), 447449.
- [32] Key, M. H. (2007). Status of and prospects for the fast ignition inertial fusion concept. *Physics of Plasmas* 14(5), 055502.
- [33] Snavely, R.A. et al. (2000). Intense High-Energy Proton Beams from Petawatt-Laser Irradiation of Solids. *Physical Review Letters* 85(14), 2945-2948.
- [34] Eliezer, S. (2002). *The interaction of high-power lasers with plasmas*. Institute of Physics Pub.: Bristol.
- [35] Key, M.H., Cable, M.D., Cowan, T.E., Estabrook, K.G., Hammel, B.A., Hatchett, S.P., et al. (1998). Hot electron production and heating by hot electrons in fast ignitor research. *Physics of Plasmas*, 5(5), 1966-1972.
- [36] Honrubia, J.J., and Meyer-ter-Vehn, J. (2008). Ignition of pre-compressed fusion targets by fast electrons. *Journal of Physics: Conference Series*, 112, 022055.
- [37] Nilson, P.M. et a. (2010). Scaling Hot-Electron Generation to High-Power, Kilojoule-Class Laser-Solid Interactions. *Physical Review Letters* 105(23), 235001.
- [38] Kritcher, A.L., Neumayer, P., Urry, M.K., Robey, H., Niemann, C., Landen, O.L., Morse, E. and Glenzer, S.H. (2007). K-alpha conversion efficiency measurements for X-ray scattering in inertial confinement fusion plasmas. *High Energy Density Physics*, 3, 156-162.
- [39] Eder, D.C. et al. (2000). Spatial characteristics of K_α radiation from weakly relativistic laser plasmas. *Applied Physics B: Lasers and Optics* 70, 211-217.
- [40] Marshall, F. J., & Su, Q. C. (1995). Quantitative measurements with X-ray microscopes in laser-fusion experiments. *Review of Scientific Instruments*, 66(1), 725-727.
- [41] Kirkpatrick, P., & Baez, A. V. (1948). Formation of optical images by X-rays. *Journal of the Optical Society of America*, 38(9), 766-774.

- [42] Dabin, Y., Rostaing, G., Hignette, O., Rommeveaux, A., & Freund, A. K. (2002). The present state of kirkpatrick-baez mirror systems at the ESRF, *Proceedings of SPIE*, 4782(1) 235-245.
- [43] Ping, Y., Shepherd, R., Lasinski, B. F., Tabak, M., Chen, H., Chung, H. K., et al. (2008). Absorption of short laser pulses on solid targets in the ultrarelativistic regime. *Physical Review Letters*, 100(8).
- [44] Nakai, S., & Mima, K. (2004). Laser driven inertial fusion energy: Present and prospective. *Reports on Progress in Physics*, 67(3), 321-349.
- [45] Ashcroft, N.W. and Mermin, D.N. (1976). *Solid State Physics*, Harcourt College Publishers: Orlando.
- [46] Y. Tsui, *ECE 673: Laser Applications*, lecture notes, (University of Alberta, Winter 2009).
- [47] Price, D. F., More, R. M., Walling, R. S., Guethlein, G., Shepherd, R. L., Stewart, R. E., et al. (1995). Absorption of ultrashort laser-pulses by solid targets heated rapidly to temperatures 1-1000 ev. *Physical Review Letters*, 75(2), 252-255.
- [48] Fedosejevs, R. et al. (1990). Absorption of Subpicosecond Ultraviolet Laser Pulses in High-Density Laser Pulses in High-Density Plasma. *Applied Physics B: Photophysics and Laser Chemistry* 50, 79-99.
- [49] Fedosejevs, R. et al. (1990). Absorption of Femtosecond Laser Pulses in High-Density Plasma. *Physical Review Letters* 64(11), 1250-1253.
- [50] Kitagawa, Y., Fujita, H., Kodama, R., Yoshida, H., Matsuo, S., Jitsuno, T., et al. (2004). Prepulse-free petawatt laser for a fast ignitor. *IEEE Journal of Quantum Electronics*, 40(3), 281-293.
- [51] Cornolti, F., Mulser, P., & Hahn, M. (1991). Absorption of ultrashort laser-pulses in solid targets. *Laser and Particle Beams*, 9(2), 465-475.
- [52] Estabrook, K.G., Valeo, E.J., and Kruer, W.L. (1975). Two-dimensional relativistic simulations of resonance absorption. *Physics of Fluids* 18(9), 1151-1159.
- [53] Thomson, J.J., Kruer, W.L., Langdon, A.B., Max, C.E. and Mead, W.C. (1978). Theoretical interpretation of angle- and polarization-dependent laser light absorption measurements. *Physics of Fluids* 21(4), 707-708.
- [54] Salamin, Y. I., Hu, S. X., Hatsagortsyan, K. Z., & Keitel, C. H. (2006). Relativistic high-power laser-matter interactions. *Physics Reports-Review Section of Physics Letters*, 427, 41-155.

- [55] Brunel, F. (1987). Not-So-Resonant, Resonant Absorption. *Physical Review Letters* 59(1), 52-55.
- [56] Wilks, S.C., Kruer, W.L., Tabak, M. and Langdon, A.B. (1992). Absorption of Ultra-Intense Laser Pulses. *Physical Review Letters* 69(9), 1383-1386.
- [57] Alfvén, H. (1939). On the Motion of Cosmic Rays in Interstellar Space. *The Physical Review* 55(5), 425-429.
- [58] Davies, J.R. (2004). Alfvén limit in fast ignition. *Physical Review E* 69, 065402.
- [59] Atzeni, S. (1999). Inertial fusion fast ignitor: Igniting pulse parameter window vs the penetration depth of the heating particles and the density of the precompressed fuel. *Physics of Plasmas* 6(8), 3316-3326.
- [60] Bell, A.R., Davies, J.R., Guerin, S., and Ruhl, H. (1997). Fast-electron transport in high-intensity short-pulse laser-solid experiments. *Plasma Physics and Controlled Fusion* 39, 653-659.
- [61] Beg, F.N. et al. (1996). A study of picosecond laser-solid interactions up to 10^{19}W cm^{-2} . *Physics of Plasmas* 4(2), 447-457.
- [62] Milchberg, H.M. Freeman, R.R., Davey, S.C. Davey, and More, R.M. (1988). Resistivity of a Simple Metal from Room Temperature to 10^6 K. *Physical Review Letters* 61(20), 2364-2367.
- [63] Robinson, A.P.L. (2010). Guiding Fast Electrons Using Resistivity Gradients to Generate Magnetic Fields. *Presentation at the Fusion Science Centre Meeting 2010*. Location: LLNL. Affiliation: Central Laser Facility, Rutherford-Appleton Lab.
- [64] Chawla, S. et al. (Nov. 8, 2010). Z Effects on Laser Energy Absorption and Fast Electron Transport in Fast Ignition ICF. *Presentation at APS DPP Annual Meeting in Chicago, Illinois*.
- [65] Chung, H.-K., Morgan, W.L. and Lee, R.W. (2003). FLYCHK: an extension to the K-shell spectroscopy kinetics model FLY. *Journal of Quantitative Spectroscopy & Radiative Transfer* 81, 107-115.
- [66] Bradt, H. (2008). Supplement to Chapter 4 of *Astrophysics Processes*. Cambridge University Press: Cambridge.
- [67] Griem, H.R. (1963). Validity of Local Thermal Equilibrium in Plasma Spectroscopy. *Physical Review* 131(3), 1170-1176.

- [68] Stambulchik, E. et al. (2009). Progress in line-shape modeling of K-shell transitions in warm dense titanium plasmas. *Journal of Physics A: Mathematical and Theoretical* 42, 214056.
- [69] Davies, J.R. (2002). How wrong is collisional Monte Carlo modeling of fast electron transport in high-intensity laser-solid interactions? *Physical Review E* 65, 026407.
- [70] Akli, K.U. et al. (2007). Temperature sensitivity of Cu K_α imaging efficiency using a spherical Bragg reflecting crystal. *Physics of Plasmas* 14, 023102.
- [71] Debayle, A., Honrubia, J.J., d'Humières, E. and Tikhonchuk, V.T. (2010). Divergence of laser-driven relativistic electron beams. *Physical Review E* 82, 036405.
- [72] Hu, J. S., Zhao, L. L., Li, X., & Bai, Y. H. (2006). Imaging quality analysis of a KBA X-ray microscope working at grazing incidence. *Optical Engineering*, 45(4).
- [73] Hecht, E. (2002). *Optics, 4th Ed.* Pearson Education Inc.: San Francisco.
- [74] Underwood, J. H., & Barbee, T. W. (1981). Soft-X-ray imaging with a normal incidence mirror. *Nature*, 294(5840), 429-431.
- [75] Pak, A. Gregori, G, Knight, J. Campbell, K., Price, D., Hammel, B. et a. (2004). X-ray line measurements with high efficiency Bragg crystals. *Review of Scientific Instruments*, 75(10), 3747-3749.
- [76] Ross, P.A. (1928). A new method of spectroscopy for faint X-ray radiations. *Journal of the Optical Society of America* 16, 433-437.
- [77] Chen, Y.T. et al. (2008). Full-field hard X-ray microscopy below 30 nm: a challenging nanofabrication achievement. *Nanotechnology* 19, 395302.
- [78] Chon, K.S., Namba, Y., & Yoon, K.H. (2006). Wolter type I X-ray focusing mirror using multilayer coatings. *Applied Optics* 45(19), 4609-4616.
- [79] Prince, E. (1950). The Resolving Power of an X-ray Microscope. *Journal of Applied Physics*, 698.
- [80] Bridou, F., Mercier, R., Raynal, A., Clotaire, J. Y., Colas, C., Fournet, P., et al. (2002). Large field double kirkpatrick-baez microscope with nonperiodic multilayers for laser plasma imaging. *Review of Scientific Instruments*, 73(11), 3789-3795.
- [81] Gotchev, O. V., Jaanimagi, P. A., Knauer, J. P., Marshall, F. J., & Meyerhofer, D. D. (2004). KB-PJX - A streaked imager based on a versatile X-ray microscope coupled to a high-current streak tube (invited). *Review of Scientific Instruments*, 75(10) 4063-4068.

- [82] Dyson, J. (1952). Optics of the focusing X-ray microscope. *Proceedings of the Physical Society of London Section B*, 65(392), 580-589.
- [83] Rosch, R., Boutin, J. Y., le Breton, J. P., Gontier, D., Jadaud, J. P., Reverdin, C., et al. (2007). X-ray imaging with grazing-incidence microscopes developed for the LIL program. *Review of Scientific Instruments*, 78(3).
- [84] Marshall, F. J., & Oertel, J. A. (1997). Framed monochromatic X-ray microscope for ICF (invited). *Review of Scientific Instruments*, 68(1), 735-739.
- [85] Gotchev, O. V., Jaanimagi, P. A., Knauer, J. P., Marshall, F. J., Meyerhofer, D. D., Bassett, N. L., et al. (2003). High-throughput, high-resolution kirkpatrick-baez microscope for advanced streaked imaging of ICF experiments on OMEGA. *Review of Scientific Instruments*, 74(3), 2178-2181.
- [86] Witteles, E.M., et al. (1995). Multilayer structures for high performance hard X-ray optics. *Proceedings of SPIE*, 25, 494-505.
- [87] Mori, Y., Yamamura, K., & Sano, Y. (2000). The study of fabrication of the X-ray mirror by numerically controlled plasma chemical vaporization machining: Development of the machine for the X-ray mirror fabrication. *Review of Scientific Instruments*, 71(12), 4620-4626.
- [88] Liu, C., Conley, R., & Macrander, A. T. (2004). Functional profile coatings and film stress. *Journal of Vacuum Science & Technology a*, 22(4), 1610-1614.
- [89] Park, H.-S., Chambers, D.M., Chung, H.-K., Clarke, R. J., Eagleton, R., Giraldez, E., et al. (2006). High Energy K(alpha) Radiography Using High-intensity, Short-pulse Lasers. *Physics of Plasmas*, 13 056309.
- [90] Harvard Medical School. *X-ray Emission Lines* [Online] July 14, 2009. (<http://www.med.harvard.edu/JPNM/physics/refs/xrayemis.html>).
- [91] Windt, D. L. (2007). Reduction of stress and roughness by reactive sputtering in W/B₄C multilayer films., 6688(1) 66880R.
- [92] Seely, J. F., Kowalski, M. P., Hunter, W. R., & Gutman, G. (1996). Reflectance of a wideband multilayer X-ray mirror at normal and grazing incidences. *Applied Optics*, 35(22), 4408-4412.
- [93] Rech, G., Lee, J. Norman, E.B. Larimer, R.-M. & Guthrie, L. The Isotopes Project (Lawrence Berkeley Laboratory). *Viewing the Periodic Table of the Elements with X-rays* [Online] July 14, 2009. (<http://ie.lbl.gov/xray/>).
- [94] Marshall, F. J., & Bennett, G. R. (1999). A high-energy X-ray microscope for inertial confinement fusion. *Review of Scientific Instruments*, 70(1), 617-619.

- [95] Gotchev, O. V., Hayes, L. J., Jaanimagi, P. A., Knauer, J. P., Marshall, F. J., & Meyerhofer, D. D. (2003). Large-grazing-angle, multi-image kirkpatrick-baez microscope as the front end to a high-resolution streak camera for OMEGA. *Review of Scientific Instruments*, 74(12), 5065-5069.
- [96] Hignette, O., Cloetens, P., Rostaing, G., Bernard, P., & Morawe, C. (2005). Efficient sub 100 nm focusing of hard x rays. *Review of Scientific Instruments*, 76(6).
- [97] Wang, Z., & Michette, A. G. (2000). Broadband multilayer mirrors for optimum use of soft X-ray source output. *Journal of Optics A-Pure and Applied Optics*, 2(5), 452-457.
- [98] Wang, Z. S., Cao, J. L., & Michette, A. G. (2000). Depth-graded multilayer X-ray optics with broad angular response. *Optics Communications*, 177(1-6), 25-32.
- [99] Windt, D. L., Christensen, F. E., Craig, W. W., Hailey, C., Harrison, F. A., Jimenez-Garate, M., et al. (2000). Growth, structure, and performance of depth-graded W/Si multilayers for hard X-ray optics. *Journal of Applied Physics*, 88(1), 460-470.
- [100] Chon, K. S., Namba, Y., & Yoon, K. H. (2006). Wolter type I X-ray focusing mirror using multilayer coatings. *Applied Optics*, 45(19), 4609-4616.
- [101] Stoev, K. and Sakurai, K. (1997). Recent Theoretical Models in Grazing Incidence X-ray Reflectometry, *The Rigaku Journal*, 14(2), 22-37.
- [102] Sauneuf, R., Dalmaso, J. M., Jalinaud, T., LeBreton, J. P., Schirmann, D., Marioge, J. P., et al. (1997). Large-field high-resolution X-ray microscope for studying laser plasmas. *Review of Scientific Instruments*, 68(9), 3412-3420.
- [103] NASA. Wolter.gif. [Online] August 4, 2009. http://science.nasa.gov/newhome/headlines/axaf_cal/wolter.gif.
- [104] Chon, K. S., Namba, Y., & Yoon, K. H. (2006). Wolter type I X-ray focusing mirror using multilayer coatings. *Applied Optics*, 45(19), 4609-4616.
- [105] Champeaux, J.-Ph., Troussel, Ph., Boutin, J.-Y., Lidove, G., Marmoret, R., Souille, G., et Rosch, R. (2006). Systèmes d'imagerie à haute résolution dans le domaine des Rayons X pour le Laser Megajoule. *Journal de Physique IV*, 138, 285-295.
- [106] Mu, B., Wang, Z., Huang, S., Yi, S., & Shen, Z. (2007). Design and fabrication of X-ray kirkpatrick-baez microscope for ICF. *Proceedings of SPIE*, 6722(1), 67220S.

- [107] Moxtek Inc. (2009). *FTC-200 X-ray Tube Controller Users Manual Rev. A*. Orem, Utah.
- [108] Amptek, Inc. X-ray and GAMMA RAY DETECTOR HIGH RESOLUTION CdTe CADMIUM TELLURIDE. Data Sheet for XR-100T-CdTe. Bedford, Massachusetts.
- [109] Ali, A. (2010). Femtosecond Laser based X-ray Sources and their Applications in Phase Contrast Imaging. *MSc. thesis*, 1-139.
- [110] National Institute of Standards and Technology. *X-ray Form factor, Attenuation and Scattering Tables*. [Online] August 7, 2011. (<http://www.nist.gov/pml/data/ffast/index.cfm>).
- [111] Haynes, W.M., and Lide, D. R. (2011). *CRC Handbook of Chemistry and Physics, 91st Ed*. Web. Accessed on August 7, 2011.
- [112] Boreman, G.D. (2001). *Modulation transfer function in optical and electro-optical systems*. SPIE Press: Washington.
- [113] Faires, J.D. and Burden, R.L. (2003). *Numerical Analysis*, Thomson Higher Education: California.
- [114] Friesen, H. (2009). Internal Notes from Titan Experiments. June-August.
- [115] Chen, C.D. (2009). Spectrum and Conversion Efficiency Measurements of Suprathermal Electrons from Relativistic Laser Plasma Interactions. *PhD Thesis*, Massachusetts Institute of Technology.
- [116] Spiegel, M.R. and Liu, J. (1999). *Mathematical Handbook of Formulas and Tables, 2nd Ed.*. Schaum's Outline Series. McGraw-Hill: New York.
- [117] Meadowcroft, A.L., Bentley, C.D., and Stott, E.N. (2008). Evaluation of the sensitivity and fading characteristics of an image plate system for X-ray diagnostics. *Review of Scientific Instruments* 79, 1-4.
- [118] Bennett, H.E. and Porteus, J.O. (1961). Relation Between Surface Roughness and Specular Reflectance at Normal Incidence. *Journal of the Optical Society of America* 51(2), 123-129.
- [119] Davies, H. (1954). The Reflection of Electromagnetic Waves From a Rough Surface. *Monograph: Radio Section* 90, 209-214.
- [120] Bilderback, D.H. and Hubbard, S. (1982). X-ray Mirror Reflectivities From 3.8 to 50 keV (3.3 TO 0.25 .) Part II—Pt, Si and other materials. *Nuclear Instruments and Methods* 195, 91-95.

- [121] Parratt, L.G. (1954). Surface Studies of Solids by Total Reflection of X-rays. *Physical Review* 95(2), 359-369.
- [122] Avallone, E.A., Baumeister, T. and Sadegh, A. *Marks' Standard Handbook for Mechanical Engineers, 11th Ed.* McGraw-Hill: Web. Accessed on May 31, 2011.
- [123] Oliver, W.C., and Pharr, G.M. (2004). Measurements of hardness and elastic modulus by instrumented indentation: Advances in understanding and refinements to methodology. *Journal of Materials Research* 19(1), 3-20.
- [124] Baumgartner, R. and Byer, R. (1979). Optical parametric amplification. *IEEE Journal of Quantum Electronics*, 15(6), 432444.
- [125] Cheriaux, G. et al. (1996). Aberration-free stretcher design for ultrashort-pulse amplification. *Optics Letters* 21(6), 414416.
- [126] Izumi, Snavel, R., Gregroi, G. et al. (2006). Application of imaging plates to X-ray imaging and spectroscopy in laser plasma experiments (invited). *Review of Scientific Instruments*, 77(10E325), 1-5.
- [127] Tanaka, K. Yabuuchi, T., Sato, T. et al. (2005). Calibration of imaging plate for high energy electron spectrometer. *Review of Scientific Instruments*, 76(013507), 1-5.
- [128] Taniyama, A. Shindo, D., and Oikawa, T. (1996). Sensitivity and fading characteristics of the 25 μ m pixel size imaging plate for transmission electron microscopes. *Journal of Electron Microscopy* 45(3), 232-235.
- [129] Ma, T. (2010). Electron Generation and Transport in Intense Relativistic Laser-Plasma Interactions Relevant to Fast Ignition ICF. *PhD Thesis*, 1-192.
- [130] Friesen, H. et al. (2010). Investigation of Preplasma Formation and Hot-electron Transport in Cone-wire Targets. *Poster Presented at the 2010 Shanghai Fast Ignition Workshop*, October 2010.
- [131] LePape, S. et al. (2009). Characterization of the preformed plasma for high-intensity laser-plasma interaction. *Optics Letters* 34(19), 2997-2999.
- [132] Zigler, A. et al. (1987). Use of unresolved transition arrays for plasma diagnostics. *Physical Review A* 35(1), 280-285.
- [133] Bar-Shalom, A., Oerg, J. and Klapisch, M. (1997). Non-LTE Superconfiguration Collisional Radiative Model. *Journal of Quantum Spectroscopy and Radiation Transfer*, 58(4-6), 427-439.

- [134] Rosen, M.D. et al. (2011). The role of a detailed configuration accounting (DCA) atomic physics package in explaining the energy balance in ignition-scale hohlraums. *High Energy Density Physics* 7, 180-190.
- [135] Huba, J.D. (2009) *NRL Plasma Formulary*. Naval Research Laboratory: Washington.
- [136] Bernstein, M. J. and Comisar, G. G. (1970). X-ray Production in Laser-Heated Plasmas. *Journal of Applied Physics*, 41 (2), 729-733.
- [137] Sternberg, S.R. (1983). Biomedical Image Processing. *IEEE Computer*, 0018-9162/83/0100-0022, 22-34.
- [138] Mishra, R. Sentoku, Y. and Kemp, A.J. (2009). Hot electron generation forming a steep interface in superintense laser-matter interaction. *Physics of Plasmas* 16, 112704.
- [139] MacPhee et al. (2010). Limitation on Prepulse Level for Cone-Guided Fast-Ignition Inertial Confinement Fusion. *Physical Review Letters* 104(055002), 1-4.
- [140] Harms, A., Schoepf, K., Miley, G. and Kingdon, D. (2000). *Principles of Fusion Energy*. World Scientific: Singapore.
- [141] Mora, P. (1982). Theoretical model of absorption of laser light by a plasma. *Physics of Fluids* 25(6), 1051-1056.
- [142] Krokhin, O.N. and Lebedev, P.N. (1965). Self-Regulating Regime of Plasma Heating by Laser Radiation. *Proceedings of the International Symposium on Laser-Physics and Applications* 16, 123-124.
- [143] Ma, T. (2010). Fast Electron Coupling Efficiency Scaling with Prepulse for Cone-Guided Fast Ignition. *Presentation at the First Student and Postdoctoral HEDP Workshop*. UC San Diego, June 29 .
- [144] Baton, S.D. et al. (2008). Inhibition of fast electron energy deposition due to preplasma filling of cone-attached targets. *Physics of Plasmas* 15, 042706.
- [145] Howells, M.R. et al. (2000). Theory and practice of elliptically bent X-ray mirrors. *Optical Engineering*, 39(10).
- [146] Pacific Silicon Sensor Quadrant Series Data Sheet, Part Description QP20-6-T08.

Appendices

A.1 Rolling Ball Algorithm

ImageJ, a Java-based image processing and analysis program, was used for the majority of image analysis. The program has a background subtraction function that is based on a rolling ball algorithm described in an article by Stanley Sternberg [137]. The description here is paraphrased from his article.

The entire algorithm is based on mathematical morphology, which basically carries out image analysis through the use of structuring elements. The idea is best explained with a binary image, but extends easily to digital images where the pixel values range from say 0 to 255. We start with two morphological transformations: erosion and dilation.

Erosion of a region A (Figure 7.5) by a structure element B1 (left in Figure 7.4) consists of setting any pixel to 0 if any cells in the neighbourhood defined by B1

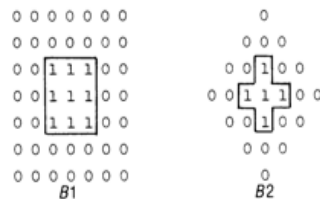


Figure 7.4: Structuring elements used for erosion and dilation [137].



Figure 7.5: Sample binary image A [137].

are 0. It is essentially applying "AND" logic to all the cells in the window. For the case shown in Figure 7.6, where B_1 is a 3 by 3 square, the erosion of A (Figure 7.5) basically sets most of the boundary pixels equal to zero. For the second case (B_2) (right in Figure 7.4), the erosion in Figure 7.7 doesn't include the corner neighbouring cells. Algebraically, the two erosions needed to define C in Figure 7.7 can be written as

$$C = (A \ominus B_1) \ominus B_2 \quad (7.3)$$

where the \ominus symbol is used to denote erosion. Rigorously, erosion is "the determination of those pixels p of A to which the origin of the structuring element B_k can be translated and still be entirely contained within A" [137]:

$$A \ominus B_k = \{p : B_{k_p} \subset A\} \quad (7.4)$$

The second transformation to look at is that of dilation. Basically dilation consists of applying an "OR" rule to all cells in the neighbourhood defined by the structure element B_k . That is, if any cell is non-zero in a translation of the structure element



Figure 7.6: Result after first erosion of A by B1 [137].

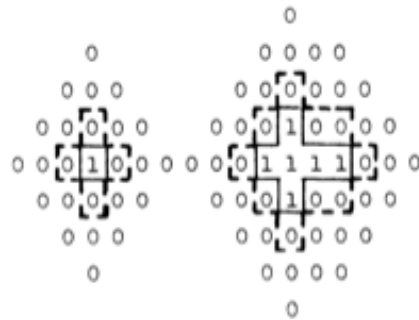


Figure 7.7: Result after second erosion of A by B2 : denote this as C [137].

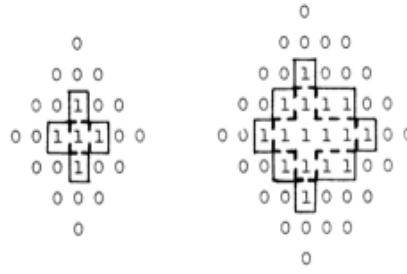


Figure 7.8: Result after first dilation of C by B2 [137].

B2, for example, all the cells are transformed to 1, as shown in Figure 7.8. The second dilation of C by B2 is shown in Figure 7.9, and the entire process can be written as

$$D = (C \oplus B2) \oplus B1 \quad (7.5)$$

where the \oplus symbol has been used to denote dilation. Rigorously, the dilation of C by Bk is “the union of translations of the structuring element Bk to the points of C” [137]:

$$C \oplus Bk = \cup_{p \in C} Bk_p \quad (7.6)$$

The process of erosion and dilation by the same sequence of structuring elements is defined as opening [137]. Visually the opening process can be seen and understood in Figure 7.10. The opening of an image A by $B = B1 \oplus B2$ is a new image containing those pixels which were “1 in A and can be covered by at least one placement of B entirely in A” [137]. That is to say, wherever B fits inside of A is retained and the rest is set to zero.

If we extend this idea to a gray-scale image, whose pixel values range from say 0 to 255, the range of intensity values must be taken into account. It can be visualized as though the value of the pixel were the height of the image at a position x,y in the

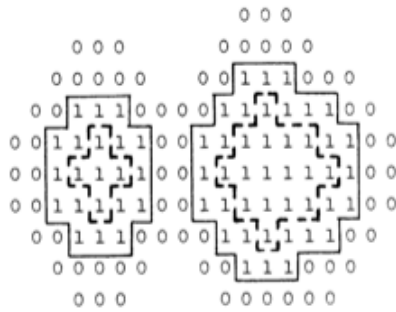


Figure 7.9: Result after second dilation of C by B1 [137].

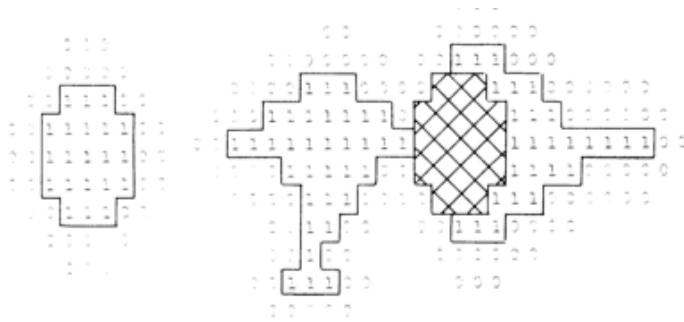


Figure 7.10: Net result of 2 erosions and 2 dilations of image A. We can remark that the entire process is identical to placing the structure element $B = B1 \oplus B2$ inside the region and only retaining those portions where it fits [137].

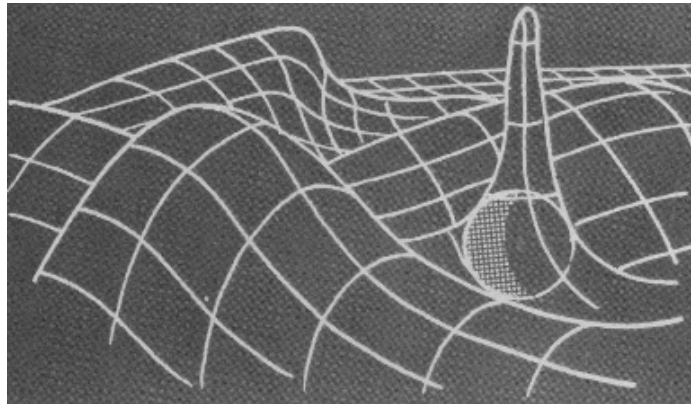


Figure 7.11: Application of the rolling ball algorithm to a gray-scale image is akin to using a three-dimensional structure element and rolling it across the umbra (cubical pixels in a 3D volume) [137].

image, giving a landscape of peaks and valleys called an umbra [137]. The structuring element for opening is three dimensional now, and in ImageJ is either a sphere or a paraboloid. Rolling this sphere across the bottom of the three dimensional surface, and only retaining where it fits, is what the rolling ball algorithm does in creating the background. It can be visualized in Figure 7.11. Rigorously, the opening of an image to create a background is “the union of all translations of the 3D structuring element that can be entirely contained within the ... image umbra” [137].

As long as the 3D structuring element’s size is chosen so that it is never smaller than any peaks or features of interest, the rolling ball algorithm is thus an effective way to model a non-uniform background in a rigorous and reproducible way. A sample image and background for which this algorithm was carried out are shown in Section 6.11. It should be noted that in ImageJ the default setting is to smooth (average over 3 by 3 pixels) during the background subtraction, but this option was turned off for the analysis in this thesis.

A.2 List of Shots and Parameters where Preplasma Emission was observed

In addition to the cone-wire targets discussed in Chapter 6 (on Titan Port TS4), preplasma emission as well as Cu layer emission was observed on the following shots on Titan. Note that all shots were at the shortest pulselength on Titan, approximately 0.7 ps.

*A.2. List of Shots and Parameters where
Preplasma Emission was observed*

Date/Shot	Target	E (J)	λ (nm)	Prepulse (mJ)	Detector	Port
20100517.s4	Multilayer Slab: A01-3, Au transport, 3 Al/10 Au/7 Al/3.8 Ag/100 Al/25 Cu/1000 C	147.4	1054	16	BAS- MS IP	TS1
20100518.s5	Multilayer Slab: C04-1, Al absorption, 7 Al/3.8 Ag/100 Al/22 Cu/1000 C	139.5	1054	10	BAS- MS IP	TS1
20100518.s6	Multilayer Slab: C02-5, Mo absorption, 0.6 Mo/7 Al/3.8 Ag/100 Al/22 Cu/1000 C	135	1054	13	BAS- MS IP	TS1
20100519.s3	Multilayer Slab: C02-1, Mo absorption, 0.6 Mo/7 Al/3.8 Ag/100 Al/22 Cu/1000 C	146.9	1054	11	BAS- MS IP	TS1
20100520.s2	Multilayer Slab: C02-2, Mo absorption, 0.6 Mo/7 Al/3.8 Ag/100 Al/22 Cu/1000 C	48	1054	3	BAS- MS IP	TS1
20100720.s2	Multilayer Slab: A02-2, 0 degree; 100 Al/21 Cu/26 Al/1mm CH	114	1054	18	BAS- MS IP	TS1

*A.2. List of Shots and Parameters where
Preplasma Emission was observed*

Date/Shot	Target	E (J)	λ (nm)	Prepulse (mJ)	Detector	Port
20100726.s4	Buried Cone: B02-4, 19 degrees; 100 Al/25 Cu/25 Al/25 Al/1mm CH	142.6	1054	10	PI CCD	TS1
20100727.s6	Buried Cone: B03-4, 16 degrees; 200 Al/25 Cu/28 Al/1mm CH	159	1054	9	PI CCD	TS1
20100824.s1	Multilayer Slab: A02-2 50 Al/20 Cu/22 B-doped Al/1 mm CH, 0 degree tilt	53.8	527	<10 μ J	PI CCD	TS1
20100824.s6	Multilayer Slab: A03-2 100 Al/25 Cu/22 B-doped Al/ 1 mm CH, 0 degree tilt	43.3	527	<10 μ J	PI CCD	TS1
20100831.s2	B02-1 Buried Cone 50 Al/25 Cu/45 B-doped Al/1 mm CH, 15.2 degrees tilt CCW	47.1	527	<10 μ J	PI CCD	TS1
20100831.s3	B03-1 Buried Cone 100 Al/25 Cu/45 B-doped Al/1 mm CH, 15.2 degrees tilt CCW	47.7	527	<10 μ J	PI CCD	TS1

*A.2. List of Shots and Parameters where
Preplasma Emission was observed*

Date/Shot	Target	E (J)	λ (nm)	Prepulse (mJ)	Detector	Port
20100901.s5	B03-4 Buried Cone 100 Al/25 Cu/45 B-doped Al/1 mm CH, 15.2 degrees tilt CCW	50.3	527	<10 μ J	PI CCD	TS1
20100901.s7	B03-5 Buried Cone 100 Al/25 Cu/45 B-doped Al/1 mm CH, 15.2 degrees tilt CCW	50.9	527	<10 μ J	PI CCD	TS1
20100902.s3	cone-foil target, 2-AF. (30 um tip diameter, 10 um tip thickness, 34 inside an- gle, attached to 50 um Al/25 um Cu/30 B-doped Al, 1 mm CH). Tiny dent in cone.	42.5	527	<10 μ J	PI CCD	TS1
20100902.s4	cone-wire #2 (34 degree opening angle, Al cone, 20 um wall thickness, 30 um tip diameter, 10 um tip thickness, 40 um wire thickness) (2nd best cone- wire target)	51.5	527	<10 μ J	PI CCD	TS1

Date/Shot	Target	E (J)	λ (nm)	Prepulse (mJ)	Detector	Port
20100902.s5	cone-wire #1 (34 degree opening angle, Al cone, 20 um wall thickness, 30 um tip diameter, 10 um tip thickness, 40 um wire thickness) (BEST cone-wire target)	51	527	<10 μ J	PI CCD	TS1
20100902.s6	cone-wire #3 (34 degree opening angle, Al cone, 20 um wall thickness, 30 um tip diameter, 10 um tip thickness, 40 um wire thickness) (WORST cone-wire target)	52.5	527	10 J 1054 nm in 3 ns re- quested	BAS- MS IP	TS1

A.3 Alignment Guide

A.3.1 Initial Setup

The Kirkpatrick-Baez (KB) Microscope design employed is re-entrant, meaning that it inserts from outside the chamber on one of Titan's numerous ports. After the KB microscope main tube has been inserted, the following steps should be taken:

1. Ensure steel collar at back (to which micrometers will push) is level.
2. Attach micrometers and spring plungers at back for alignment. Ensure that they

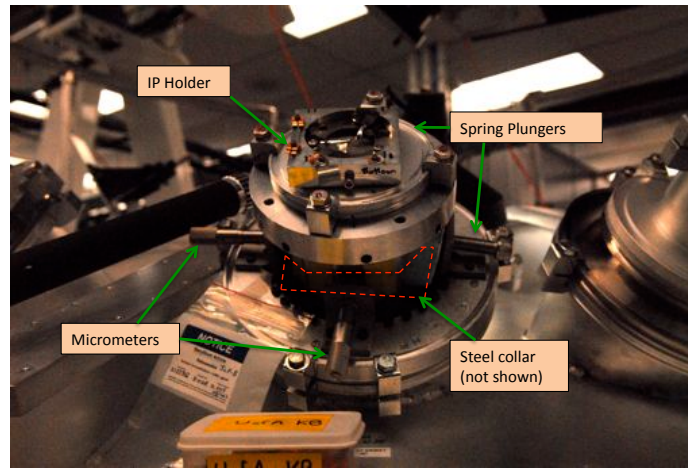


Figure 7.12: Picture taken during August 2009 experiments showing back of KB microscope, outside the Titan target chamber.

- are level. Choose micrometer position so that natural weight of KB pushes it against the vertical micrometer face.
3. Insert mirror tube and adjust length to mm accuracy using caliper from TCC. Tighten collar to mark this position.
 4. Level the KB using the slot and flat piece that allow for a larger level to be used accordingly. Whether horizontal or vertical will depend on desired configuration of mirrors.

A.3.2 Alignment at air

The KB can be aligned at air with visible light because it is an achromatic imaging system.

1. Insert fiber optic point source at TCC. This will require a combination of target jig alignment as well as chamber tests to get it pointing in the correct direction.

2. Turn on point source that should illuminate the KB and form images at the image plane. Using a piece of paper taped across the chamber port opening, adjust the micrometers until the four spots have the desired separation (see the subsequent section on checking alignment).

A.3.3 Preparing for vacuum

1. Ensure tungsten rods are in mirror tube.
2. Wrap front of KB from tip all the way to the adjoining tube in mylar. This is not only a blast shield but prevents the expanding plasma from coating the mirrors. Although the coating won't greatly affect the hard X-rays in question, it should still be avoided.
3. Put magnetic shield and aluminum collimator in main KB tube, noting the orientation of the magnetic field. If possible, adjust orientation so that electrons are deflected in the opposite direction of image formation.
4. Attached Be window to back of KB. May require mating flange that changes the image distance a small amount. This is not substantial because the KB has a large depth of focus in the image plane.
5. Attach an IP (image plate) holder to the back of the Be window, and make sure it is level.
6. Put a clean IP wrapped in Al foil on the IP holder. Ensure that its active face is toward TCC.

A.3.4 Adjusting the alignment

Precision alignment is carried out via micrometers at the rear of the KB. The ideal image separation to ensure image focus can be determined from the equations for ϵ and w_j given above.

The pivot point for the KB is at the O-ring where the large tube meets the main tube (see Figure 5.1). The distance from the image plane to the O-ring (d_i) is 55 ± 1 cm (80 ± 1 cm with the camera installed) and the distance from TCC to the O-ring (d_0) is 74 ± 1 cm for ports TS1 and TS4 on the Titan chamber. From these values the leverage ratio of the mirror motion with respect to the image plane is defined:

$$R_L = \frac{p - d_0}{d_i} \quad (7.7)$$

To calculate the required motion at the rear of the KB, the following steps need to be taken:

1. Determine ϵ_{actual} via

$$\epsilon_{actual} = \frac{\delta m - \delta(M - 1)}{2M} \quad (7.8)$$

2. Determine ϵ_{ideal} for the desired incident angle of the KB microscope via

$$\epsilon_{ideal} = p \tan \theta_i - \delta \quad (7.9)$$

3. Determine movement at the rear of the KB from

$$\Delta\epsilon = \epsilon_{ideal} - \epsilon_{actual} \quad (7.10)$$

$$\delta\mu = \frac{\Delta\epsilon}{R_L} \quad (7.11)$$

A.4 Other Alignment Techniques

This section contains a detailed explanation of other alignment techniques attempted during the development of the KB microscope, and outlines in each case why they weren't implemented in the end.

A.4.1 First Alignment Scheme

A separate plate was made with optics for shining a laser backward through the KB system. The intent was to have the lasers cross exactly at the target, which would indicate that the microscope is in alignment. However, this scheme is very insensitive to small corrections of alignment, since the beams will still appear to be overlapping for a fairly large angular range around the optimum.

In the end what was useful of this alignment scheme was that the reference beam that didn't strike the mirrors could be used as a pointer on target. Since the KB was designed for the mirrors to be appropriately spaced when the axis is centered on target, this was a reasonable way of getting close to alignment.

However, when the Titan Chamber is brought to vacuum (10^{-5} torr) the roof of the chamber flexes (upon which the KB was nearly always mounted), and the breadboard on which the target sits also moves. This is enough to bring an initially well-aligned microscope (at air) out of alignment in vacuum. This alignment scheme, since it required a separate plate to be put on the back, could not be carried out in vacuum and thus it was a hunting process of trying to find the image once full system shots began. In general the zero-order image was still visible after the vacuum shift, so it was reasonably straightforward to hunt around for the image when the zero-order was visible. However, when rapid alignment is necessary to not miss out on shots, this alignment scheme was inadequate.

A.4.2 Second Alignment Scheme

The second alignment scheme involved various iterations of a point light source placed in the target position. At first it was a bare fiber optic cable pointed in the correct direction and mounted on one of the 6-axis target mounts. A green diode laser was coupled into the multimode fiber via a microscope objective. The bare fiber optic cable proved to be very fragile and easily breakable, so finally the end of a hypodermic needle was used, and the fiber glued inside. The end was carefully adjusted so that a V-shaped groove in the hypodermic metal needle allowed the fiber to be viewable from the sides while still being protected from any bumps or jarring. After being put in a freely rotating mount, the fiber could then be pointed in any direction, as shown in Figure 5.6. Using the target alignment area with 4 cameras to position the tip exactly where the target will be (an alignment done with any target), the fiber could then serve as a stable, nearly indestructible point source for aligning the KB optically. The KB microscope has the advantage of being achromatic. However, since each mirror is only reflecting over an effective area of about $200 \mu m$, each mirror acts as a slit and there is substantial diffraction. Therefore the optical method can only be used to adjust the separation distance, and the actual focus of the 2D spot unfortunately cannot be used in order to determine where the position of best focus is.

This scheme could align the KB virtually perfectly at air. However, as before, the shift of the chamber going from air to vacuum makes it so that there is still a process of hunting around for the image after pumping down to vacuum. In light of this, further developments were attempted.

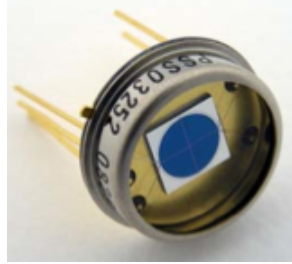


Figure 7.13: The Quad Photodiode (QPD) used to track alignment. The differential voltage between two opposing quadrants was zeroed in order center the beam on the detector [146].

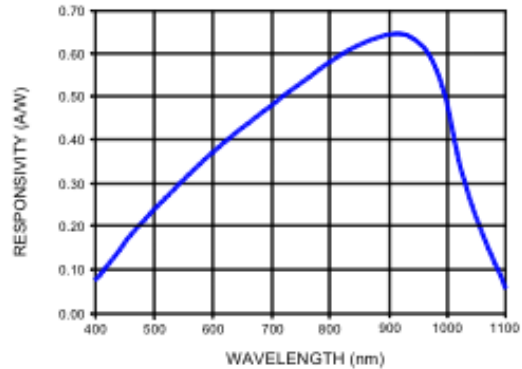


Figure 7.14: The response function of the QPD used [146].

A.4.3 Third Alignment Scheme

This scheme used tracking laser alignment beams to establish a way of tracking the motion of the KB from air to vacuum, enabling live correction. A quadrant photodiode from Pacific Silicon Sensor (part # QP20-6-TO8) with an active area of 4 X 4.9 mm², shown in Figure [?], was used to enable positional tracking of a beam of light. It was positioned to be almost in the same vector as the KB-TCC, and housed in a long black plastic cylinder to block stray light from the actual target itself. The QPD's response is shown in Figure 7.14. The four output signals from the four photodiodes could be used as desired, either to equalize the voltage reading on each, or to minimize the differential voltage from opposing quadrants.

The light source used was a fiber optic mounted via a split-ring clamp to the main tube of the KB microscope. The light from the fiber was collimated using a Gradient-Index (GRIN) lensⁱ mounted in a special SM1 mount on a tip-tilt stage. The intent was to use a 633 nm pigtailed fiber laser coupled into the chamber through a fiber vacuum feedthrough. However, the laser diodes both burnt out when appropriate

ⁱF230 SMA-B from THORLABS: 633 nm, beam 0.91 mm diameter, divergence 0.051 deg., NA=0.55

power supplies were used. A green diode laser was then used to couple into a fiber via a microscope objective. Testing the QPD revealed that it was reasonably sensitive to the position of the laser. However, this was done when the laser was coupled directly inside the chamber. When we attempted to couple light from outside the chamber, into a fiber and into the GRIN lens, there was very low output. This was primarily because the fiber feedthrough was for an SM style multimode fiber, and the fiber used for the collimators was a single mode FC style fiber. Therefore a tremendous amount of light was lost going from multimode to a single mode fiber. It was found that the QPD's response to such low levels of light was inadequate to obtain reasonable positional sensing.

A.4.4 Fourth Alignment Scheme

Finally an autocollimator (ThetaScan Dual Axis Angle Measurement, T100 head from Micro-Radian Instruments) was used to try and track the motion of the KB. Basically a mirror was mounted on the KB, and the autocollimator mounted outside the chamber facing in through a window. The autocollimator functions by emitting a certain wavelength of light and quantifying the amount of specularly reflected light. In this manner the autocollimator is sensitive to mirror tilt, and can give an estimate of the microradians of mirror tilt suspected.

It was demonstrated to be sensitive enough to detect the change in the mirror when it was well-aligned. There was a quantifiable drift that was tested prior to actual movements which was quantified to be $-2.6 \mu\text{rad}/\text{min}$ in the azimuthal (AZ) axis, and $0.63 \mu\text{rad}/\text{min}$ in the equatorial (EL) axis.

The intent was to have the autocollimator well-aligned on the mirror, and to maintain this tip-tilt alignment as the chamber pressure decreases to vacuum. This way,

in theory, the KB would still be in the same configuration with respect to the target after all is said and done. Prior to testing the net movement of the KB microscope was measured on the autocollimator during pumpdown. It seemed reasonably consistent from two runs once the system had gone through a few iterations of pumping and airing. The average change, once drift had been taken into account, was $-863 \mu\text{rad}$ AZ, and $189 \mu\text{rad}$ EL.

In the end, on the final day of experiments, after the KB was moved, the autocollimator was put to the test. After being aligned via the fiber optic source while the chamber was at air, the KB was adjusted so that the tip-tilt on the autocollimator was identical (after accounting for the drift in the two axes), no image was obtained – not even the zero-order. This suggests that the KB was moved drastically out of alignment with the mirror.

For completeness, the autocollimator was looking through one of the chamber windows, about 12.3 cm away on a tower that was as stable as possible. The mirror on the KB microscope was 86 cm away from the window, with the collar 23.5 cm down the KB tube from the o-ring. The T100 head is optimized to be within 1 m of the mirror in question, where it has a measuring range of $\approx \pm 5.8 \text{ mrad}$ (0.33°). As this distance is increased to the maximum recommended working distance of 3 m, the range is reduced to 1.93 mrad (0.11°). Therefore it is possible that since we were at about 1 m, the autocollimator did not have the angular range to be able to track the movements that we made with the KB microscope to try and maintain alignment. This is because during initial attempts angles were overshot quite often.

Another possible explanation is that the fixtures used to clamp the mirror onto the KB were subject to more shift than the chamber was. The hoped-for precision is on the order of milliradians at the mirror surfaces. The mirror for the autocollimator, however, for practical reasons and constraints due to the window positions, was

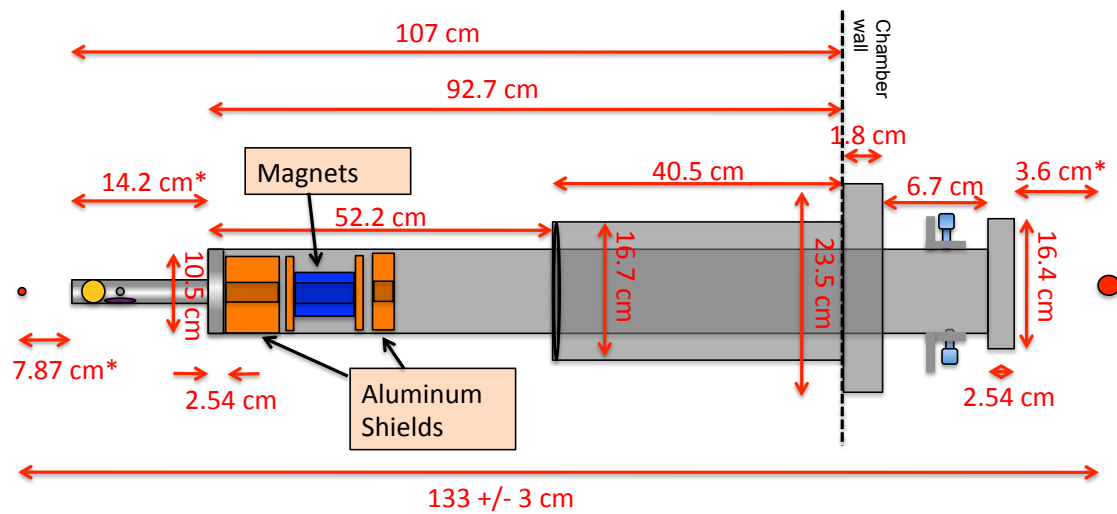
mounted very close to the pivot point, raising the precision level required in order to maintain mirror alignment (probably around 100s of μrad). Therefore a small shift due to the numerous joints and posts needed to point the mirror in the right direction could result in a massive misalignment at the KB mirror surfaces.

It is difficult to say whether or not the motion resulted from the KB microscope or the mirror itself. A more careful test where very small motions are carried out would be able to determine the success for certain, but because of the small margin for error even if this alignment method is successful it may not be good to rely upon.

Basically the difficulty in tracking the KB is that anything you use to try and track it needs to have more stability than the KB microscope. Therefore such tracking may be more difficult than one originally expects.

A.4.5 Fifth Alignment Scheme

The final scheme attempted was to put the fiber optic source at TCC and pump the chamber down, carrying out the reliable alignment in vacuum. This can be done early morning or late at night so as not to disrupt the shot cycle. Normally when this is done at air the back of the KB microscope is open and the spots investigated via grid paper. A glass window is used in the vacuum case, and a fiber-feedthrough used to couple the laser light in to the source at TCC. This method is devoid of any positional problems. However, the reason it did not work was because of very low light levels coupled into the chamber. If a single-mode fiber feedthrough were used this probably wouldn't have been an issue. Because the light levels were so low, a camera was positioned behind the glass window. The difficulty is that the four spots of interest for the KB take up approximately a square inch, and most camera chips are much smaller than that. Therefore with the cameras on hand the spots couldn't



NOTE: The distances with * are for 8 keV imaging, and with an IP loaded behind a Be window on an IP holder. These values could change for imaging different energies or for different detector at the back of the KB. These are also for the Titan upper TS ports with a TCC distance of 45.23"=114.9 cm
Also, the order of the shields can be altered.

Figure 7.15: Measurements of the KB microscope.

be visualized simultaneously, and as such the microscope could not be aligned.

This alignment scheme shows some promise. The likely fix is to have the proper fiber feedthrough which can then couple sufficiently light into the chamber and allow the spots to be seen by eye, which would remove the requirement for a large-chip camera.

A.5 Instrument Dimensions and Vacuum Shifts Measured

A.5.1 Instrument Dimensions

See Figures 7.15 and 7.16.

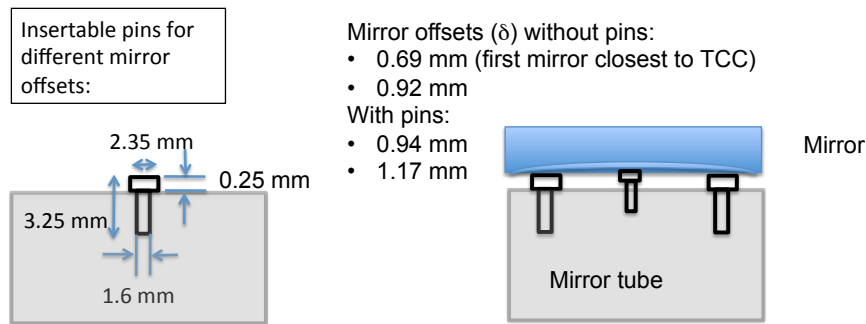


Figure 7.16: Dimensions of the mirror pins used to define a reproducible surface on the KB microscope.

A.5.2 Vacuum Shifts

TS1:

KB mirror tube tends to move (as viewed from outside the chamber looking down tube):

LEFT 0.8 mm (0.0315") (therefore to correct need to move RIGHT)

DOWN 0.95 mm (0.0375") (therefore to correct need to move UP)

These are averaged from 0.028", 0.035" and 0.033", 0.040" respectively.

TS4:

KB mirror tube tends to move (as viewed from outside the chamber looking down tube):

LEFT 0.3 mm (0.012") (therefore to correct need to move RIGHT)

DOWN 0.33 mm (0.013") (therefore to correct need to move UP)

These values are not as reliable, since they are based on a single set of measurements and a different alignment method. However, it does seem to be consistent with the observation that there is less shift on this port. Also, this measurement was done with much heavier shielding collimators, so the weight distribution is different.

A.5.3 Port Information

TS1:

The values listed in the TABLE of the Titan chart for the angles are wrong. The angles indicated on the drawings, however, are correct. On the chamber, its also labeled incorrectly.

TL1:

This port is a few inches further back compared to other ports (this is likely the same for all TL ports). Thus the extension tube for the KB needs to be used here. Recommend keeping the extension tube close by for the entire experiment just in case its needed, or using it for the entire experiment. There is also a non-magnetic steel endcap that can extend the tube even more – good to have onhand as well.

A.6 ZEMAX Simulations

This Appendix contains some detailed descriptions of investigations carried out using ZEMAX.

A.6.1 Imaging Ta Foil

Three detectors were used in order to investigate the clipping by the tantalum foil. One detector viewed the entire 4 images (zero-order, the two 1D images and the 2D image). The other two detectors viewed slices of the respective 1D images. A cross sectional lineout through one line of each of these detectors was taken, with a smoothing of 4 (since there was no straightforward way for zemax to vertically or horizontally average).

Figure 7.18 shows a few images where the tantalum foil was moved by increments

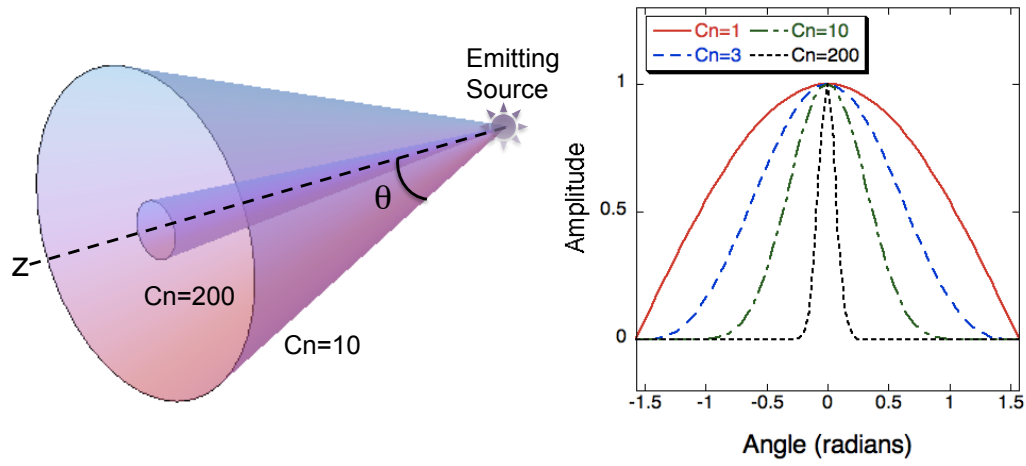


Figure 7.17: The cosine exponent Cn controls the distribution of rays around a polar axis. The graph on the right shows functions $(\cos \theta)^{Cn}$ for different values of Cn , and shows that as Cn is increased, the angular spread of the cone of rays decreases. The image on the left shows a 3-dimensional view of what these spreads imply for the source emission.

of $100 \mu m$ into the beam. The orientation of the tantalum foil was such that the first rays that are blocked are those that form the 2D image, so that is the first image to disappear. Of interest is that in order to emit light in a narrow cone from the entire surface of the circular source, the cosine exponent had to be adjusted, which is a parameter not often mentioned when studying zemax. The cosine exponent is defined as Cn where

$$I = I_0(\cos \theta)^{Cn} \quad (7.12)$$

gives the distribution of rays as a function of the polar angle θ around z . The effect of the cosine exponent is to control the distribution of rays around a polar axis from the source, as illustrated in Figure ???. As the tantalum is moved further in, the cosine exponent Cn was set to 30000 to narrow the cone of rays so that enough of them struck the KB mirrors. Five million analysis rays were traced.

The first insight from these simulations is that only one edge spread function can

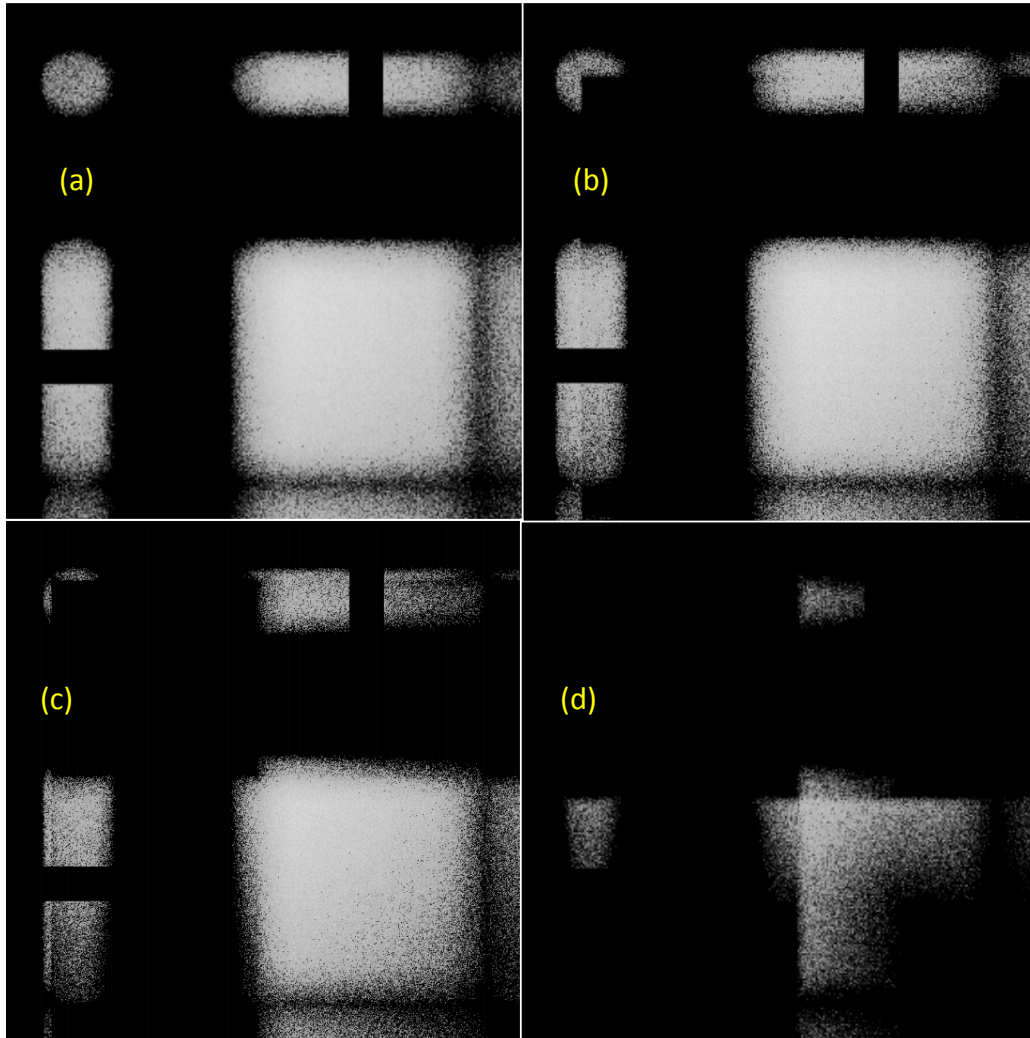


Figure 7.18: ZEMAX output images for various cases. (a): The image produced by a $300\ \mu\text{m}$ diameter source. (b) & (c): The images produced as the tantalum foil is moved further and further into the incident beam. (d): The Ta foil is blocking so much of the beam we do not have an ESF for either mirror. The cross pattern is from the foil taking the place of the tungsten rod for the edge cutoff of the zero-order.

be produced at a time from this geometry. The reason is because in order to clip a significant portion of one edge, the entire image from the other edge is blocked. The only situation where both edges can be formed in this configuration is when the Ta foil is just clipping the 2D image, in which case only the outskirts of each 1D image are affected. This was not done experimentally primarily because the geometrical constraints were not fully understood until after the KB microscope had been shipped back to California for further use in experiments on Titan. Therefore, although an angular scan was carried out in both dimensions for all four mirrors, only one of the dimensions contains valid ESF data and as such only the resolutions of two mirrors were fully characterized using the LSF (M1 and M2).

What is important about these simulations, and illustrated in Figure 7.20 is that in the situation where the tantalum begins to cut only one of the 1D images, *the edge of the zero-order beam is unaffected*. What this means is that although the KB is performing as though there were an edge function at the position of the tantalum foil, the way we measure angles is still dependent on the separation between the zero-order and the edge. Since the position of the zero-order is determined by the distance from the KB to *the source*, the appropriate distance values *to the source* must be used in computing the incident angle. The difference the inappropriate distance produces is about 2 mrad. The situation where one mirror has an ESF and the other does not is shown in Figure 7.19.

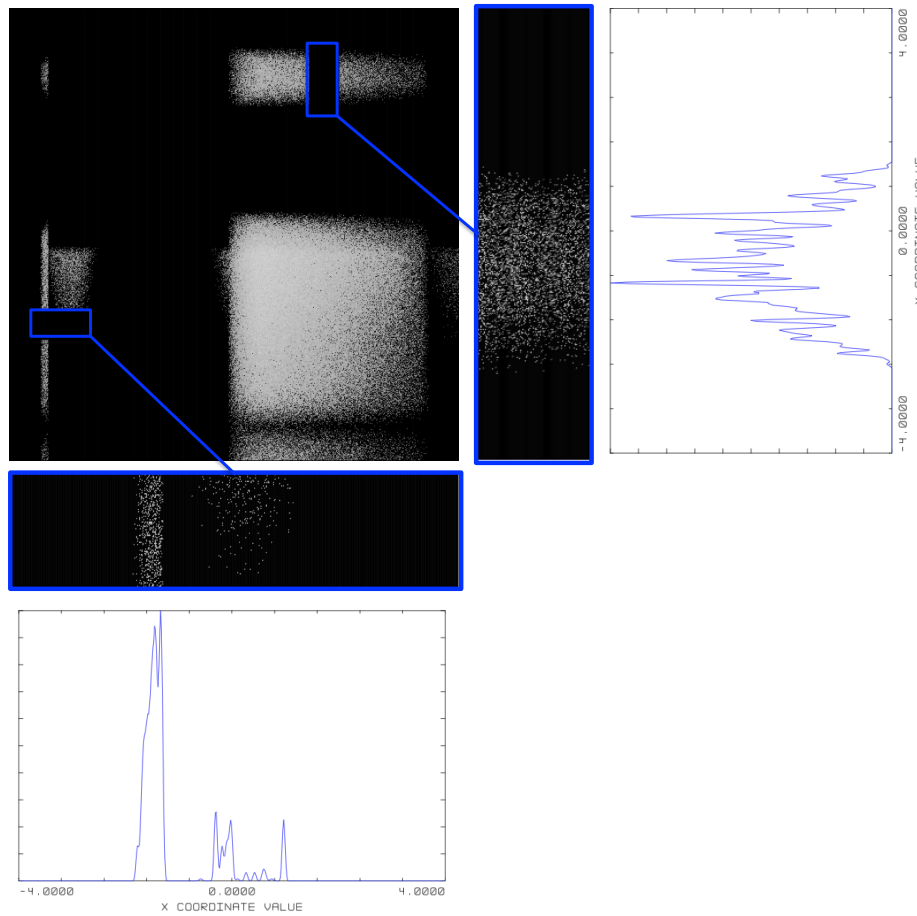


Figure 7.19: The ZEMAX output image for the experimental situation where one mirror's image was well-clipped forming a nice ESF, but the other was still imaging normally.

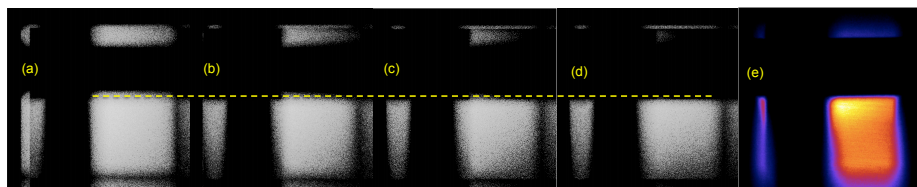


Figure 7.20: The ZEMAX output images demonstrating that as the tantalum is moved further into the beam in (a) through (d) in one dimension only, the edge of the zero-order stays in the same position because it is dependent on the source. The image in (e) was obtained during the experiment.

A.7 Layout of Titan Ports

See Figure 7.21.

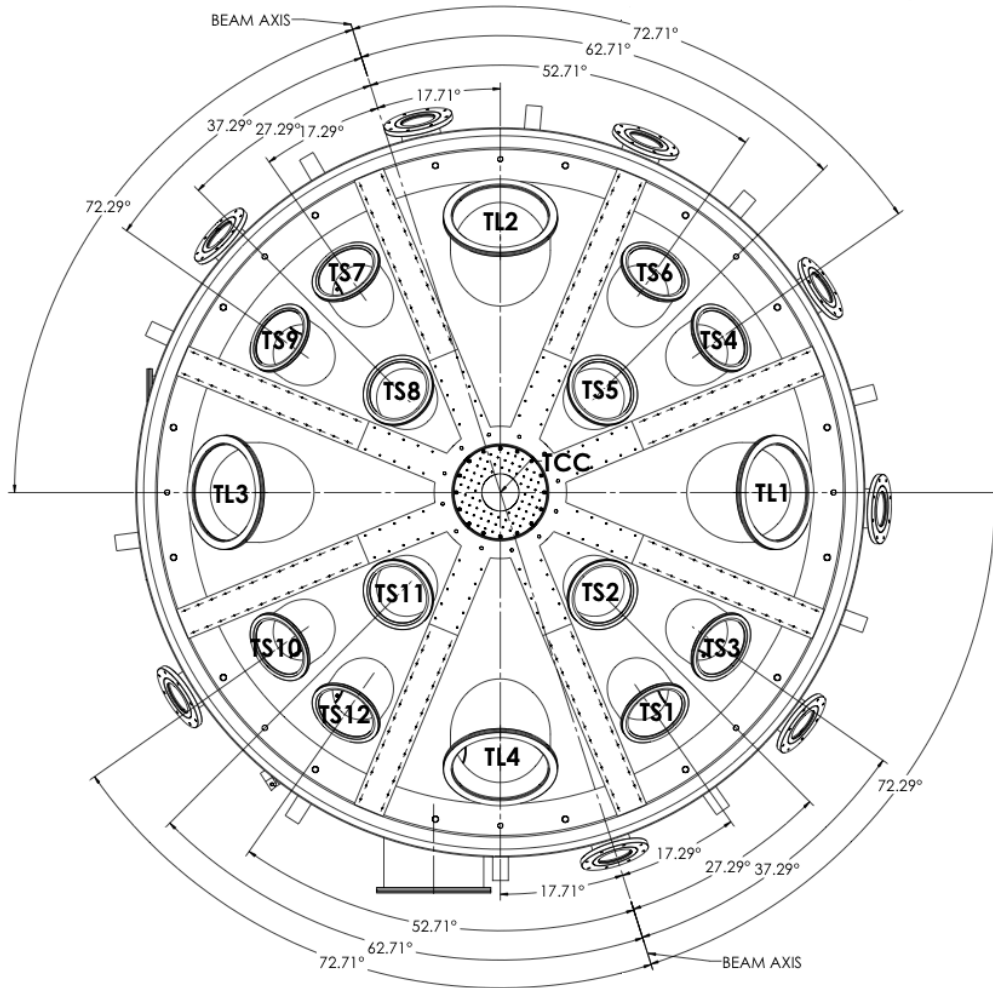


Figure 7.21: The layout of ports on the Titan chamber.